CHARACTERIZATION OF 3D ULTRASTRUCTURE OF PLANT BIOMASS AND DEVELOPMENT OF A TRANSPORT-REACTION MODEL FOR THE PRETREATMENT PROCESS

A THESIS
SUBMITTED TO THE FACULTY OF THE GRADUATE SCHOOL
OF THE UNIVERSITY OF MINNESOTA
BY

Sahana Ramanna

IN PARTIAL FULFILLMENT OF THE REQUIREMENTS
FOR THE DEGREE OF
DOCTOR OF PHILOSOPHY

Shri Ramaswamy, Adviser

May 2021

© Sahana Ramanna 2021

ACKNOWLEDGEMENTS

First and foremost, I would like to thank my advisor Dr. Shri Ramaswamy for giving me this incredible opportunity to carry out this research work and for his constant guidance, support and encouragement without which this dissertation would not have been possible. I sincerely thank my committee members Dr. Ulrike Tschirner, Dr. Huajiang Huang and Dr. Bandaru V. Ramarao for their valuable inputs and timely reviews. I would like to express my gratitude to our collaborators, Dr. Feng Xu from Beijing Forestry University, Dr. Manfred Auer from Lawrence Berkeley National Laboratory and Dr. Ramarao from SUNY-ESF as well as their group members for providing the necessary data and sharing their expertise. I would also like to thank the Characterization Facility at University of Minnesota for their training and suggestions.

I would like to extend my warmest regards to the members of Dr. Ramaswamy's lab and friends from the BBE department for their suggestions and encouragement which made my graduate school experience more enjoyable. I would like to thank the Buckman Graduate Fellowship for supporting this work. Last but not the least I would like to thank my friends and family without whose support and encouragement this would not have been possible. I am indebted to my parents Champaka Ganaganur Krishnappa and Ramanna Nagashrothi and my husband Nitin Shastri who have been my constants and pillars of strength throughout this journey.

Abstract

The complex network of fibers and pore spaces in porous materials such as paper, wood etc., affect their structure, physical properties, and transport characteristics. In the case of wood or plant biomass, the system consists of cellulose fibers enclosed in a matrix of lignin and cellulose with some void spaces enclosed. Biomass is renewable and can be converted to a wide variety of bio-based products including biofuels, biochemicals, bioplastics, paper, wood plastic composites etc. The 3D internal structure of biomass can be related to their material properties. The biomass ultrastructure and how they change during various treatments may play a critical role in influencing the biomass conversion processes. Hence, it is essential to have an overall understanding of the 3D ultrastructure of plant cell walls and its relationship to the properties and how their change influences biomass conversion processes. The first step in biomass conversion processes is the pretreatment which is crucial in terms of the changes it brings to the cell wall architecture which in turn influences the reaction path forward. During this step, degradation of one or more of the cell wall components occur thereby, potentially altering the cell wall architecture. This is achieved with the help of several reagents such as alkali, acid, hot water, ammonia, enzymes, etc. and paves way for further treatment and conversion processes.

While most of the previous work in this regard focuses mainly on 2D structure characterization using techniques such as optical and scanning electron microscopy, Fourier transform infra-red spectroscopy, atomic force microscopy, etc., it is vital that 3D structure characterization techniques are employed to fully explore the ultrastructure in a non-intrusive manner. This is possible with the advent of techniques such as Computed Tomography (CT) using either X-rays or Transmission Electron Microscopy (TEM). The current work uses TEM-CT to visualize the structural evolution of plant biomass and determine changes in properties such as porosity, pore size distribution and surface area, due to pretreatment. The cell wall structure was disrupted during pretreatment which resulted in a more porous structure and greater surface area which made it suitable for further hydrolysis. Additionally, topochemical distribution obtained from Raman spectroscopy was correlated with the TEM-CT structural evolution data in order to provide

a complete understanding of the pretreatment process. In this context, a 3D transport-reaction model was then developed based on stochastic principles and reaction kinetics for lignin dissolution during pretreatment.

The simultaneous transport-reaction occurring within the biomass cell wall structure is modeled using a hybrid random walk process. In our model, the structure and topochemical distribution of the untreated biomass sample obtained using Confocal Laser Scanning Raman Microscopy was used as the initial biomass sample. The diffusion and reaction model, using the actual biomass structure, begins in the cell wall lumen where the reagent particles diffuse through the lumen and other enclosed pore spaces based on a hybrid random walk. Diffusion continues in the pore phase until the fiber phase is encountered, upon which either reaction or further diffusion occurs based on the reaction probability. The reaction probability is determined from the Thiele modulus which encompasses both diffusive and reactive behavior of the system. The changes in lignin concentration in the cell wall is determined by local pseudo first order kinetics where the rate of reaction depends on the lignin concentration. The reagent used for pretreatment is assumed to be available in abundance compared to the lignin in the cell wall. The extent of conversion and thereby the efficiency of the pretreatment process is determined by the rate of transport of the reagents both in the pore and fiber phases, reaction probability, local kinetics, and ratio of diffusivity between the pore and fiber phases. Both the spatial and bulk concentration profiles of lignin as a function of reaction time were determined from the diffusion-reaction simulation. It was shown that the effective rate constant K_{eff} considering both transport and reaction during biomass conversion is a function of biomass composition and, in some cases, also the reaction time. This is in correspondence with prior work reported in the biomass conversion literature. In addition, an overall transport rate co-efficient K_T considering only the bulk and internal diffusion of the reagent in the cell wall system during pretreatment was determined based on walker's survival time.

The transport and reaction model results for different biomass species and pretreatment processes were compared with experimental data and appropriate local transport and reaction rate constants were determined. The relative effects of diffusion and

reaction during biomass conversion for a given biomass species was then studied using various Thiele moduli over an appropriate range. Interestingly, it was found that diffusive transport, in general, played a critical role in the overall biomass dissolution. However, the relative effect of diffusion was found to be more significant at a lower Thiele modulus than at a higher Thiele modulus for the same local rate constant. The critical Thiele modulus may also depend on the biomass species and the biomass treatment conditions. These results indicate that approaches to opening the cell wall prior to any chemical/biochemical treatment, thus increasing their diffusive transport characteristics, may help with improving the efficiency of biomass pretreatment processes and, hence, further conversion. The results from the transport and reaction model may provide additional insights on the relative benefits of thermal, mechanical, and chemical pretreatment processes prior to further biomass conversion. This may help to select appropriate pretreatment processes for effective biomass conversion. The 3D structure visualization, characterization and the transport-reaction model using actual biomass structure developed here can help provide fundamental insights into the structure-property relationships during biomass pretreatment as well gain additional insight in developing improved biomass conversion strategies.

Table of Contents

LIST OF TABLES

List of Figures

1. INTRODUCTION

Plant biomass is a widely used raw material and can be converted to a wide range of bio-based products. They are used in the production of wood products, food additives, pulp and paper, fibers, textiles, bio-composites, bioplastics and biofuels (Moran-Mirabal, 2013). Interest has increased worldwide in improving renewable energy sources such as lignocellulosic biomass and use them as a replacement for fossil fuels, thus decreasing overall CO_2 emissions (Faravelli et al., 2010). Apart from ethanol, about forty other potential products that can be obtained from biomass have been identified (Mosier et al., 2005). The US Energy Independence and Security Act (EISA) of 2007 has further increased the development of biomass to biofuel conversion technologies and establishes a biofuel production benchmark of 36 billion gallons per year of biofuel by 2022 (*Energy Independence and Security Act of 2007 : A Summary of Major Provisions.*, 2007; Morinelly et al., 2009).

Plant cell walls are complex bio-composite materials that have an intricate network of pores and fibers. The bulk properties of such materials are determined not only by elemental composition and molecular connectivity but also by their macromolecular architecture which is retained in plant cell walls even after mechanical particle size reduction processes (Ciesielski et al., 2015). Hence it is of utmost importance that the true ultrastructure be characterized thoroughly to determine its physiochemical properties so that further conversions can be carried out to produce value added products. Conventionally, several characterization techniques, mainly in 2D have been employed to visualize the cell wall architecture and topochemistry. Reddy et. al, studied the structure of cellulose fibers from rice straw using SEM (Reddy and Yang, 2006). Zolfrank et. al used TEM to investigate the ultrastructure of softwood cell walls during pyrolysis (Zollfrank and Fromm, 2009). Donohoe et. al, used a correlative microscopy approach that included light microscopy, TEM and SEM to study the cell wall architecture of raw and pretreated switchgrass (Donohoe et al., 2011). Yu et. al, visualized the arrangement of cellulose microfibrils in wheat straw cell wall using AFM (Yu et al., 2008). Gierlinger et. al and Horvath et. al, used Raman spectroscopy to obtain topochemical information of plant cell

walls (Gierlinger et al., 2012; Horvath et al., 2012). Kacurakova et. al used FTIR to characterize plant cell wall model compounds while Wilson et. al, used FTIR to study the mechanical properties and molecular dynamics of plant cell wall polysaccharides (Kacuráková et al., 2000; Wilson et al., 2000). Cegelski et. al, used NMR to identify in situ protein cross links in plant cell walls (Cegelski et al., 2010).

Although several 2D characterization techniques offer a considerably high resolution and provide a vast amount of information regarding the structure and morphology of cell walls, they have some inherent disadvantages. Many of these techniques are somewhat intrusive to the specimen which could create artifacts during visualization and alter the information thus obtained. More importantly, these techniques provide only 2D and do not account for the third dimension which is significant in determining structure property relationships. Therefore, other relatively non-intrusive 3D characterization techniques are required to fully comprehend the cell wall architecture at the micro and nanoscales. Techniques such as confocal scanning laser microscopy and computer tomography using X-ray, SEM and TEM are used in this regard. Anderson et. al, used confocal microscopy to image the cellulose redistribution (Anderson et al., 2010). Goel, Defrenne et. al, and Rolland du Roscoat et. al, used X-ray CT to visualize and characterize the 3D structure of paper (Defrenne et al., 2017; Goel, 2003; Rolland du Roscoat et al., 2007). Mayo et. al and Svedstom et. al, studied the micro-structure of wood using X-ray CT (Mayo et al., 2010; Svedström et al., 2012). Hughes et al, used serial block face SEM to study the 3D structure of plant cells (Hughes et al., 2014). Sarkar et. al used TEM-CT to study the nanoscale cell wall architecture of Arabidopsis (Sarkar et al., 2014). Chundawat et. al used TEM-CT in correlation with other techniques to characterize the changes in 3D structure of different regions of cell wall during pretreatment (Chundawat et al., 2011). TEM-CT can also be combined with immuno-labeling techniques to detect the presence of certain components (Donohoe et al., 2009a). Thus, these techniques not only preserve the true structure of the specimen but also capture the true structure of the material. X-ray computed tomography provides useful insights into the micron scale 3D structure of the cell wall. However, dimensions inside the cell wall are of the nanoscale order and higher resolution techniques such as TEM-CT and SEM-CT are necessary to probe their ultrastructure.

Plant cell walls encompass the three major components - cellulose, hemicellulose, and lignin in a complex crystalline structure which make it recalcitrant (Keshwani and Cheng, 2010). In order to convert biomass to other useful products, it is necessary to breakdown this recalcitrant structure. The conversion of lignocellulosic biomass is a multi-step process which includes pretreatment, enzymatic hydrolysis, fermentation and product purification (Morinelly et al., 2009). The pretreatment process causes disruption of the recalcitrant cell wall structure by altering the hemicellulose or lignin, reducing cellulose crystallinity and increasing the surface area, pore volume and subsequently the efficiency of the hydrolysis process (Esteghlalian et al., 1997; Morinelly et al., 2009). Cell walls undergo significant structural and topochemical changes during this process which enable further their conversion to other value-added products. Pretreatment can be achieved by mechanical, chemical, thermochemical and enzymatic techniques. Regardless of the pretreatment strategy, the digestibility of biomass is enhanced by making the cellulosic fibers more accessible (Donohoe et al., 2009a). Since the structure and topochemistry of the cell walls significantly change during the pretreatment process, it is extremely important to take a deeper dive and analyze how these changes affect structure property relationships and conversion of cell wall components at the nanoscale. Such an understanding is the key to developing effective pretreatment techniques and further conversion steps.

The current work aims at understanding the structural evolution and changes in topochemical composition during the pretreatment process. The 3D structure and morphology of plant biomass was visualized by TEM-CT. In the earlier work, X-ray CT was used to understand the structural characteristics of paper in 3D (Defrenne, 2008; Goel, 2003). The same approach was extended to the TEM-CT images to study the structural evolution of plant cell walls during pretreatment. The changes in structural properties such as porosity, specific surface area and 3D pore size distribution were determined from the processed TEM images. Additionally, the structural changes in the cell wall during pretreatment was correlated with the topochemistry that was obtained using Raman spectroscopy. The Raman Data was provided by Dr. Feng Xu's group at Beijing Forestry University and Dr. Ramarao's group at SUNY-ESF (S. Chen et al., 2016; Ji et al., 2014;

Ma et al., 2014). This revealed the changes in bulk and spatial concentration of the cell wall components during the course of pretreatment.

A micron scale transport reaction model was developed to predict the lignin dissolution over time for different pretreatment techniques and species and matched with the experimental data from Raman spectroscopy. This is an extension of the earlier work where a diffusion model was developed for the moisture conductivity in fibrous materials (Defrenne, 2008; Defrenne et al., 2019). During pretreatment, the cell wall structure undergoes physiochemical changes which affects its transport and reactive properties. (Chundawat et al., 2011; Donohoe et al., 2011). Biomass species are treated with different reagents such as acid, alkali, hot water, ammonia, enzymes etc. depending on the end result desired (Chundawat et al., 2011; Esteghlalian et al., 1997; Goel, 2003; Keshwani and Cheng, 2010; Ma et al., 2014; Montané et al., 1998). During the pretreatment process, the reagent molecules diffuse through the cell lumen and pore spaces of the cell wall based on a hybrid random walk until they reach a cell wall interface. When they encounter the lignin the cell wall, they either react or diffuse into the cell wall based on the reaction probability and diffusivity of the cell wall. The bulk and spatial concentration profiles, instantaneous reaction rate and the overall rate constant based on transport and reaction were determined for different biomass species and pretreatments. In addition, a transport coefficient was also determined based on the internal diffusion and survival time of the reagent molecules. The effect of changing diffusivity and reactivity on the pretreatment process was also studied which enabled in establishing the parameters for effective conversion. Thus, with the combination of characterization of the structural and topochemical evolution during the pretreatment coupled with the stochastic modelling, a fundamental insight was provided into the pretreatment process.

2. LITERATURE REVIEW

2.1 Biomass Composition

Lignocellulosic biomass has three major components – cellulose, hemicellulose, and lignin. Apart from these components, small amounts of extractives, inorganics, starch, proteins, and alkaloids are also present. Cellulose, hemicellulose and lignin are macromolecules and play a major role in biomass conversion processes (Rowell, 2012).

Cellulose is the most abundant renewable biopolymer (Brinchi et al., 2013). It is the main constituent in plants and has a significant influence on their structure (O'Sullivan, 1997).Cellulose is composed of polymer chains consisting of unbranched β (1,4) linked D-glucopyranosyl units as shown in Figure 1 (Abdul Khalil et al., 2012; Luo et al., 2013). These repeating glucose units are responsible for the specificity, diverse architectures and reactivity of the macromolecule (Poletto et al., 2014). The degree of polymerization of cellulose is about 10,000 for lignocellulosics (John and Thomas, 2008).

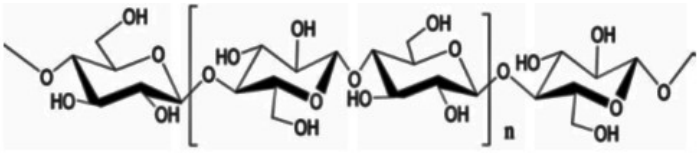

Figure1. Structure of cellulose (Luo et al., 2013)

The hydroxyl groups in the cellulose molecules form intra and inter chain hydrogen bonds which give rise to crystallinity to the cellulose chain and also affects its properties (John and Thomas, 2008). Van der Waal's forces and hydrogen bonding in the cellulose molecules allow parallel stacking of cellulose chains and form elementary fibrils, which then aggregate to form microfibrils in the cell wall (Moon et al., 2011). However, cellulose microfibrils are not perfectly crystalline and exhibit an amorphous character. The properties and conversion of cellulose are highly dependent on its isolation process, number of hydrogen bonds, chain lengths and their distribution, crystallinity and the distribution of functional groups within the molecule (Poletto et al., 2014). The cellulose

microfibrils are aligned along the length of the fibers which provides maximum rigidity, tensile strength and flexural strength (John and Thomas, 2008). Hence, cellulose is a precursor for a wide variety of biobased products. These include biofuels such as ethanol and butanol, bioplastics such as polylactic acid, other cellulose based derivatives such as carboxy methyl cellulose, micro-cellulose crystals, and nanocellulose as well as cellulose based composite materials. Cellulose nanoparticles are ideal materials for the production of next generation cellulose based products and composites that have a wide variety of applications (Moon et al., 2011). Six polymorphs of cellulose are known to exist (I, II, III_I, III_{II}, IV_I and IV_{II}) and can be interconverted as shown in Figure 2 (O'Sullivan, 1997). Figure 3 shows the structure of Cellulose I and II. Native cellulose or cellulose I occurs in two different crystalline forms - I_α and I_β (Abdul Khalil et al., 2012). Cellulose II is rarely found naturally but can be obtained from Cellulose I through a regeneration or mercerization process as shown in Figure 2. Cellulose I has parallel chains while Cellulose II has anti-parallel chains as shown in Figure 3.

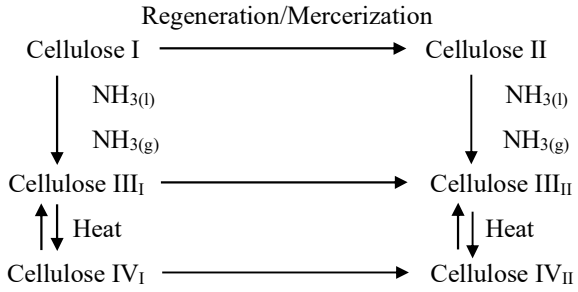

Figure 2. Interconversion of polymorphs of cellulose

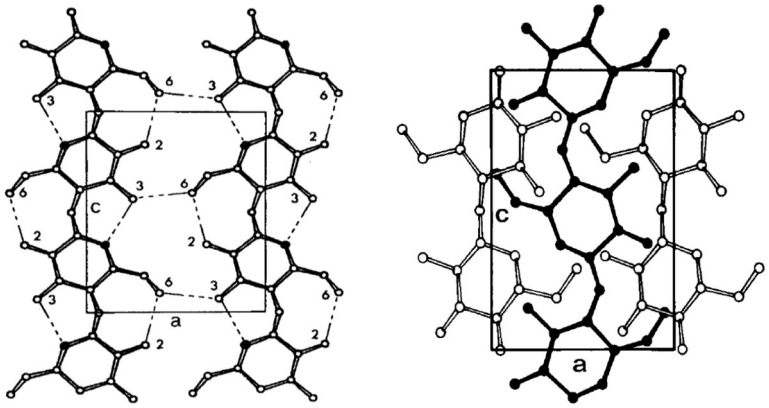

Figure 3. Structure of Cellulose I and Cellulose II (Sjostrom, 1993)

Hemicellulose is also a non-crystalline polymer consisting of 5 and 6 carbon ring sugars and are very hydrophilic (John and Thomas, 2008). Hemicellulose chains are shorter than cellulose and can be either branched or unbranched. They consist of sugars such as D-xylopyranose, D-glucopyransose, D-galactopyranose, L-arabinaofuranose, D-mannopyranose, among others, and have an average degree of polymerization of about 100-200 (Rowell, 2012). Hemicelluloses form a supportive matrix for the cellulose microfibrils (John and Thomas, 2008). The types of hemicelluloses present in hardwoods differ from those in softwoods. Hardwood hemicelluloses comprise of 15-30% glucoronoxylans and 2-5% glucomannans (Rowell, 2012). Xylans are homopolymers of 1,4 linked β-D xylopyranose units. Glucomannans are composed of β-D glucopyranose and β-D mannopyranose units. Softwoods contain about 20% galactoglucomannans and 5-10% arabinoglucoronoxyans (Rowell, 2012). Figures 4 and 5 show the structures of some hardwood and softwood hemicelluloses. Straws and other types of grasses which are ideal for biofuel production have a high content of arabinoglucoronoxylans as shown in Figure 6 (Pauly and Keegstra, 2008). The presence of carboxylate groups in hemicellulose can strongly affect the strength of the primary cell wall (Silveira et al., 2013).

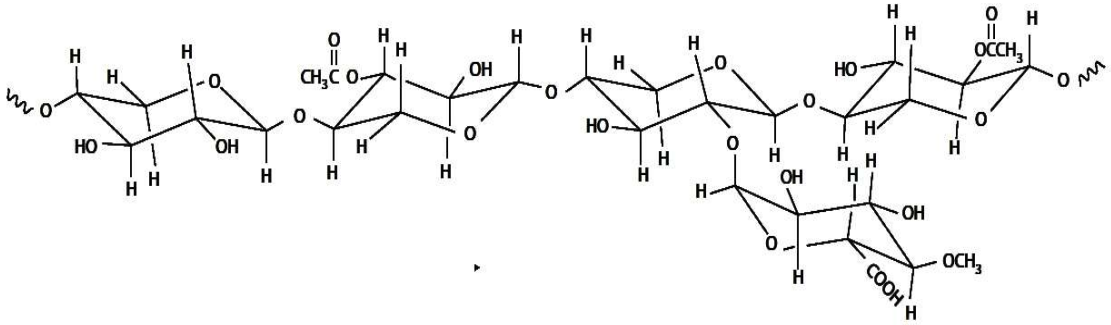

Figure 4. Structure of O-acetyl-4-O-methyl-glucoronoxylan (Rowell, 2012)

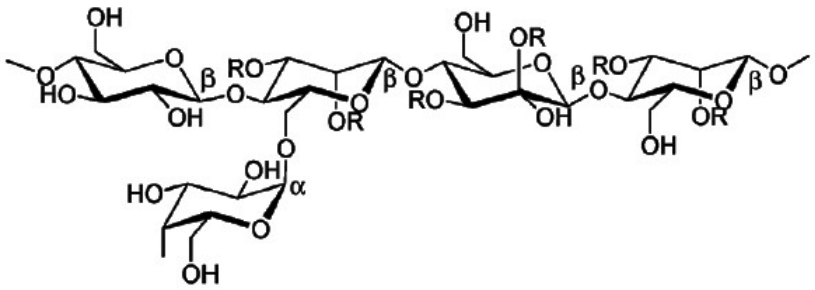

Figure 5. Structure of glucomannan (R - CH_3CO or H) (Dutta et al., 2012)

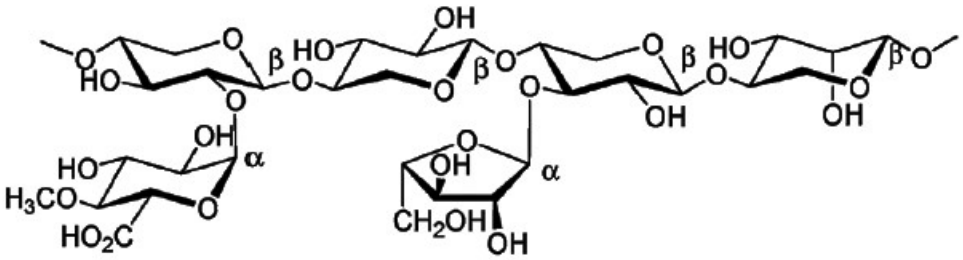

Figure 6. Structure of xylan (R - CH_3CO or H) (Dutta et al., 2012)

Lignin is another major component of a plant cell wall. Lignin is the second most abundant biopolymer on earth after cellulose (Beisl et al., 2017). It provides mechanical strength and is the reason behind recalcitrance of lignocellulosic biomass. Without the presence of lignin and hemicellulose matrices, the cell wall would not stay intact (Sjostrom, 1993). Lignin is a complex amorphous hydrocarbon containing both aliphatic and aromatic components (John and Thomas, 2008). Lignin is a highly irregularly branched polymer that consists of three basic building blocks namely, hydroxyphenyl (H), guaiacyl (G) and syringyl (S) units which are derived from p-coumaryl alcohol, coniferyl alcohol and sinapyl alcohol respectively as seen in Figure 7 (Beisl et al., 2017; Rowell, 2012). The chemical reactivity of lignin varies depending on the amount of G, H and S units present in the wood species (Fromm, 2013). Guaiacyl units are predominant in softwoods and contain a low amount of hydroxyphenyl units while hardwoods contain more syringyl and guaiacyl units with traces of hydroxyphenyl units (Faravelli et al., 2010). Different types of C-C and C-O-C linkages can be found in the lignin matrix such as β-O-4, β-5, and β–β linkages as seen in Figure 7 (Fromm, 2013). Lignin is a highly branched polymer and contains cross-links (Sarkanen and Ludwig, 1971). It bonds covalently with carbohydrates to form lignin-carbohydrate complexes which does not allow easy separation of lignin from the cell wall (Vainio et al., 2004).

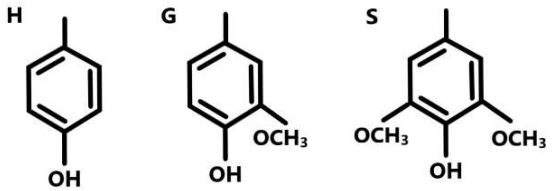

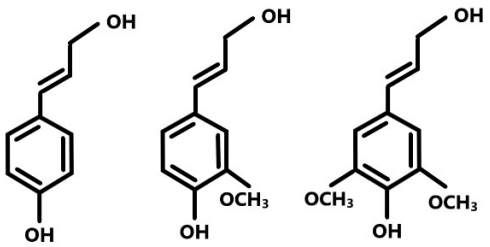

Figure 7. Structure of basic building blocks of lignin (H, G and S - top three) and the respective alcohols from which they are derived (p coumaryl alcohol, coniferyl alcohol and sinapyl alcohol - bottom three) (Shmulsky and Jones, 2011; Vanholme et al., 2010)

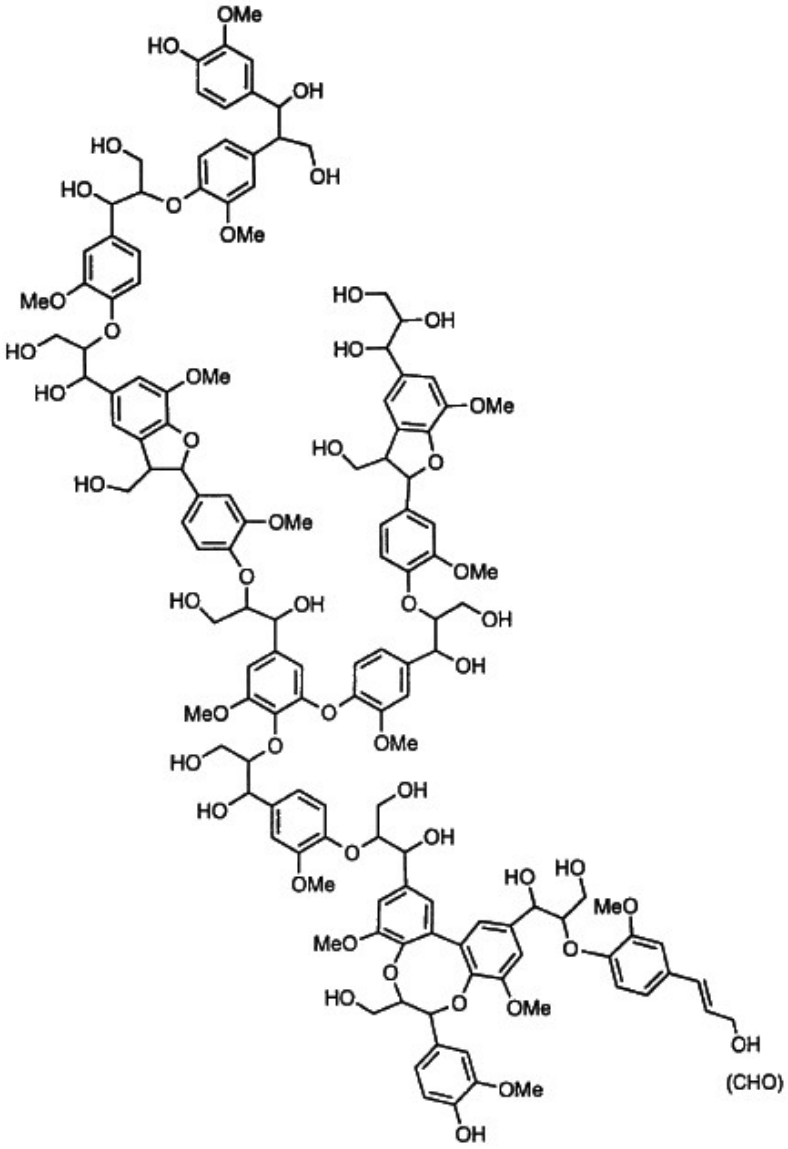

Figure 8. Structure of softwood lignin (adapted) (Brunow et al., 1998)

The composition of cell wall components of softwoods and hardwoods are different as shown in Table 1. The distribution of the cell wall components is also not uniform across the cell wall layers. Plant cell wall architecture is complex and affects the macroscopic properties of wood and hence needs to be understood well. There are three layers in a plant cell wall – primary wall, secondary wall and middle lamella as shown in Figure 9. The middle lamella, which is the outermost layer, is the cell wall material between two adjacent cells and provides adhesion between the cells (Rowell, 2012). The layering of cell wall starts from the middle lamella and proceeds inwards towards the secondary wall. The layer of cell wall interior to the middle lamella is the primary wall. Since the primary wall is thin and indistinguishable from the middle lamella, the primary wall of one cell, middle lamella and the primary wall of the adjacent cell are collectively known as compound middle lamella (CML) (Rowell, 2012). The secondary cell wall, which is located on the inside of the CML, is a combination of three layers – S1, S2 and S3 with S1 being the outermost layer. The S2 layer is the thickest layer of the cell wall and is the most important layer in determining the properties of the cell wall (Rowell, 2012; Shmulsky and Jones, 2011).

Source	Composition (%)		
	Cellulose	Hemicellulose	Lignin
Hardwood	43-47	25-35	16-24
Softwood	40-44	25-29	25-31

Table 1. Composition of plant cell walls in hardwood and softwood species (Fromm, 2013)

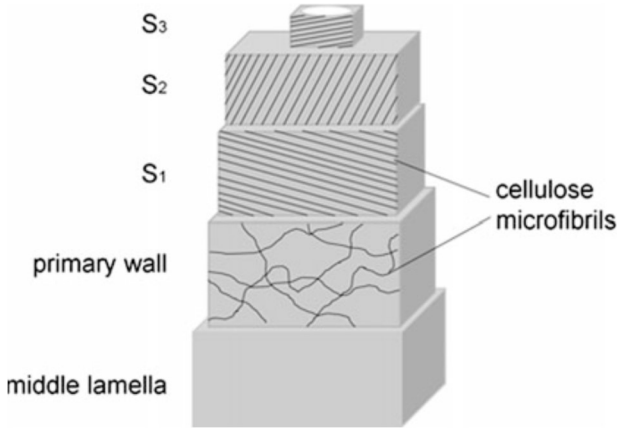

Figure 9. Different layers of plant cell wall (Fromm, 2013)

Each layer has a different proportion of cellulose, hemicellulose and lignin as shown in Figure 10. Initially, before the formation of the secondary wall, the CML is rich in pectin and xyloglucan but in the later stages, it is rich in lignin (Fromm, 2013). Most of the cellulose is present in the secondary cell wall, mainly in the S2 layer as seen from Figure 10 (Shmulsky and Jones, 2011). The cellulose fibers are oriented differently in each layer. The S1 and S3 layers have a relatively flat microfibril angle (60-90°) whereas the S2 layer has a very low microfibril angle (4-30°) and the least amount of lignin (Fromm, 2013; Rowell, 2012). S2 layer is the thickest layer and has the strongest influence on the macroscopic properties (Rowell, 2012). Although the largest concentration of lignin is present in the CML as seen Figure 10, the quantity of overall lignin is highest in the secondary wall as it is the thickest layer (Shmulsky and Jones, 2011).

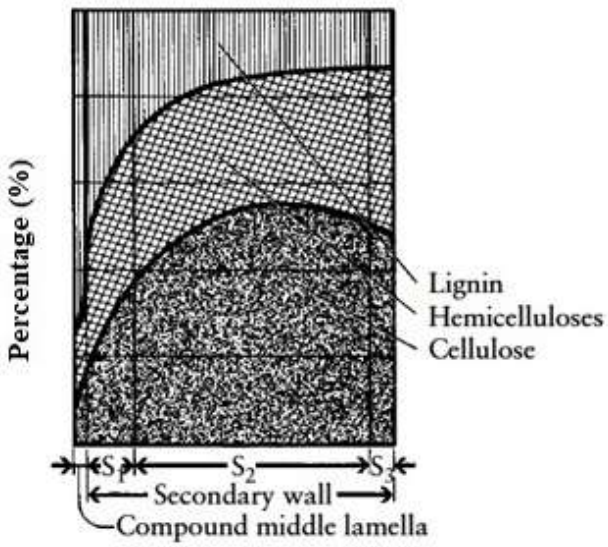

Figure 10. Distribution of lignin, hemicellulose, and cellulose within various cell wall regions (Shmulsky and Jones, 2011)

2.2 Biomass Pretreatment

In order to convert lignocellulosic biomass to other useful bioproducts such as pulp and paper, biofuels, bioplastics, etc., cellulose has to be separated from the rest of the cell wall components and treated further. This is accomplished by a series of steps, in which the first step is the pre-treatment. It is one of the most expensive steps in the bio-refinery

process and affects the upstream feedstock production, particle size reduction and several other key features of the overall process (Morinelly et al., 2009). Plant cell walls are composed of crystalline cellulose fibers embedded in an amorphous matrix of cross-linked lignin and hemicellulose which reduces the accessibility to cellulose and makes it recalcitrant (Chundawat et al., 2011). The pretreatment process aims to break the recalcitrant structure of biomass and disrupt the cellulose crystallinity as shown in Figure 11 (Mosier et al., 2005; Zhao et al., 2014). During the pretreatment process, one or more of the cell wall components are dissolved or degraded. Several pretreatment methods have been developed over the years. They can be physical, chemical, thermochemical or biological in nature. Chemical or physiochemical pretreatment methods are often coupled with mechanical refining or size reduction techniques to reduce energy consumption, preserve the cellulose structure and increase accessibility to enzymes during the subsequent hydrolysis step (Barakat et al., 2013).

Physical pretreatment methods include comminution, steam explosion and hydrothermolysis (Mosier et al., 2005). Thermochemical pretreatments such as hot water and steam explosion pretreatments are carried out at high temperatures and short residence times to enable effective solubilization of hemicelluloses and prevent degradation of solubilized oligomers, thereby increasing the hemicellulose yields. (Kim and Lee, 2006; Montané et al., 1998). Chemical and thermochemical pretreatments involve treating the lignocellulosic biomass with a chemical reagent such as dilute acid, alkali, hydrogen peroxide, ozone, lime, hot water, etc. Pretreatment of biomass with dilute acid dissolves hemicellulose, mainly xylans (Esteghlalian et al., 1997). Alkali pretreatment removes lignin and uronic acid substitutions on hemicellulose and thereby increase the accessibility to the cellulose chains in the subsequent steps (Chang and Holtzapple, 2000).

Another type of chemical pretreatment method is cellulose based fractionation. It involves fractionation of the feedstock by dissolving it in a solvent followed by regeneration of the amorphous cellulose using anti-solvents thereby making it more accessible and easier to hydrolyze by enzymes (Zhao et al., 2017). Cellulose solvents such as alkaline H_2O_2, ozone, organosolv, glycerol, dioxane, phenol ethylene glycol,

concentrated mineral acids, ammonia-based solvents, metal complexes etc., disrupt the structure of cellulose and promote hydrolysis (Mosier et al., 2005; Wood and Saddler, 1988). The organosolv pretreatment recovers cellulose as a solid phase while most of the hemicellulose and lignin are dissolved in the solvent which can later be recovered, thereby achieving a high sugar yield and allowing efficient utilization of all major biomass components (Zhao et al., 2017). A more advanced method of pretreatment known as ammonia fiber expansion (AFEX) has been developed which enhances cell wall digestibility without removing the lignin or hemicellulose into separate streams (Chundawat et al., 2011). It also loosens the cell wall, causes lignin relocation and thereby allows expansion, delamination and nanofibrillation of certain parts of the cell wall (Ciesielski et al., 2013). Recently, the use of ionic liquids for biomass pretreatment have been explored as they are non-volatile, reusable, have low melting points, reduce energy consumption and also enhance enzyme saccharification (Uju et al., 2013). Another method for efficient conversion of biomass is a deacetylation and mechanical refining process (DMR) which resulted in high sugar yield and reduced the energy consumption and recalcitrance of the biomass feedstock while using minimal chemicals (X. Chen et al., 2016).

Several biological methods are also available for pretreatment. These methods involve treatment of biomass with enzymes. Microorganisms such as brown rot fungi attack and degrade the cellulose while white and soft rot fungi attack both the cellulose and lignin in the biomass (Sun and Cheng, 2002). Cellulases degrade cellulose while hemicellulases degrade hemicelluloses (Mosier et al., 2005). Cellulases are a combination of at least three major groups of enzymes – endoglucanases which attack low crystallinity regions of the cellulose fibers, exoglucanases which eliminate the cellobiose units from the free ends of the chain and β-glucosidase which hydrolyze the cellobiose to produce glucose (Sun and Cheng, 2002). Enzymes that degrade the hemicellulose include glucuronidase, acetylesterase, xylanase, b-xylosidase, galactomannanase and glucomannanase (Duff and Murray, 1996). Demethylation of lignin by chemical and enzymatic methods have also been explored to produce several lignin-based products (Ferhan et al., 2013; Venkatesagowda and Dekker, 2019). Thus, several pretreatment options are available for

overcoming cell wall recalcitrance. Based on the end product, energy consumption, biomass species and other factors, the most effective method of pretreatment can be chosen accordingly.

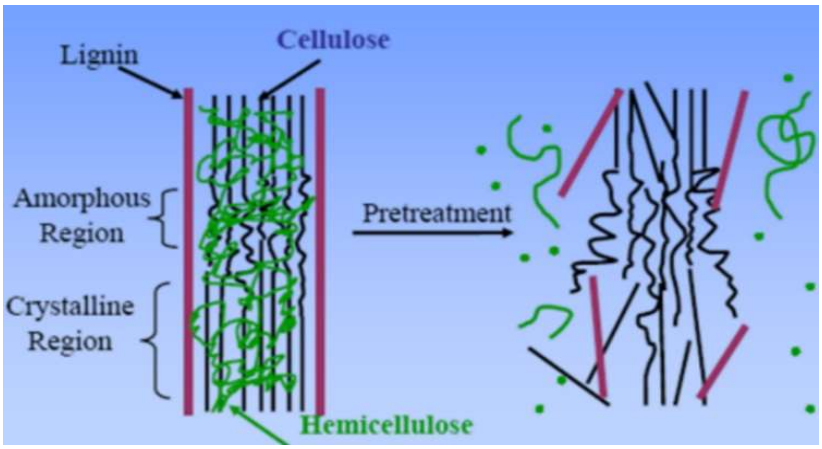

Figure 11. Effect of pretreatment on plant cell wall components (Mosier et al., 2005)

2.3 Biomass Characterization:

The structure and composition of biomass affects its properties and conversion. As mentioned in the previous sections, pretreatment processes alter the nanoscale architecture of the cell wall and changes its composition simultaneously. As a result, the structure of the cell wall evolves during the process and characteristics like porosity, specific surface area and tortuosity change in addition to the spatial chemical composition. These structure-property changes as well as the compositional changes needs to be thoroughly studied in order to gain a fundamental insight into the pretreatment process and thereby determine the efficacy of the process as well as further conversion routes. Hence, there is a necessity for in-depth characterization of lignocellulosic biomass. It must be noted that the characterization techniques used in this regard have to be minimally invasive so as to keep the structure of biomass intact. Several characterization tools are available for this purpose. Techniques such as optical and electron microscopy, Raman Spectroscopy, Fourier Transform Infra-red Spectroscopy (FTIR), Atomic Force Microscopy (AFM), Nuclear Magnetic Resonance Spectroscopy (NMR), High Performance Liquid Chromatography (HPLC), etc., have been popular for characterization (Anderson et al., 2010; Donohoe et

al., 2011; Ghaffar and Fan, 2013; Gierlinger et al., 2012, 2008; Horvath et al., 2012). Most of these are 2D characterization techniques. However, in order to get a true sense of the ultrastructure of wood, it is necessary to probe its 3D structure. X-ray CT is a useful tool for 3D visualization of micron scale structures and has been used to characterize biomass samples previously (Mayo et al., 2010). However, cell wall dimensions are of the order of nanometers and X-ray CT does not provide the required resolution to view the nanoscale ultrastructure. However, TEM-CT has proven to be an effective technique to visualize the structure of the cell wall at this resolution (Chundawat et al., 2011; Sarkar et al., 2014). Some of the characterization techniques have been explained in the further sections.

2.3.1 3D structure from Computed Tomography

X-ray CT has been extensively used to characterize the 3D structure of paper (Defrenne, 2008; Defrenne et al., 2019, 2017; Goel, 2003). Computed tomography was first used in the medical field and later extended to material and biological sciences. The fact that it is a non-invasive technique makes it a very suitable technique at the micron scale. The principle of computed tomography is based on capturing a series of images of the object by rotating it along a single or a dual tilt axis as shown in Figure 12. Using the tilt series, a 3D reconstruction is carried out by a back-projection technique (Saghi and Midgley, 2012). The instrument consists of a target from which the X-rays are emitted and sent through a sample. The transmitted X-rays are measured by the detectors (Wei et al., 2011).

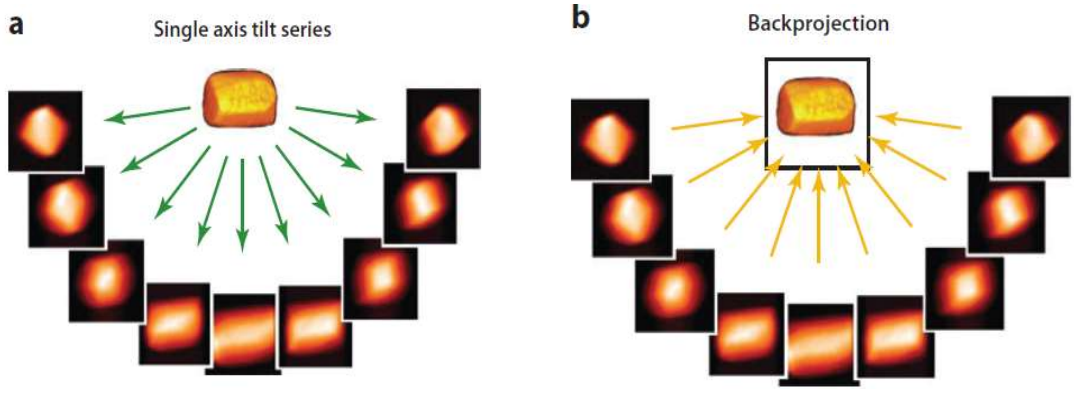

Figure 12. Principle of electron tomography (Saghi and Midgley, 2012)

According to the Rayleigh criterion, the smallest distance resolved is related to the wavelength of the radiation λ (Williams and Carter, 2009) as,

$$\boldsymbol{\delta = \frac{0.61\lambda}{\mu \sin\beta}} \quad (1)$$

where μ is the refractive index of the medium and β is the semi angle of collection of the magnifying lens. Therefore, the resolution of X-ray CT is limited to micron scale resolution. However, to probe plant cell wall architecture, a higher resolution is required. This is achieved by TEM-CT as it uses electrons for imaging which have a much smaller wavelength compared to X-rays. This technique involves a series of sample preparation steps prior to imaging, where the sample is embedded in a resin to preserve its structure during slicing thin sections and further imaging (Abad et al., 1988; Chundawat et al., 2011). The different steps in the TEM-CT sample preparation are explained further.

2.3.2 TEM-CT sample preparation and imaging

The first and most important step in electron tomography is the sample preparation process. Unlike X-ray CT, the sample preparation for TEM-CT is a more elaborate process and not totally non-intrusive. Very thin sections of the material of the order of 70-200 nm are required for imaging. This is challenging for biological specimens since they require a high level of preservation. Conventional methods of sample preparation that are used for hard materials are not applicable to wood as they can damage the structure of the wood fibers. Hence, it is embedded in a resin to preserve the structure and then sectioned to the desired thickness. Bulk of the sample preparation steps are performed under vacuum. The steps for sample preparation are as follows:

i. Fixation – The first step is treatment with a chemical fixative. This stabilizes cellular organizations such that the ultrastructural details of the sample are preserved from damage during further preparation steps and electron beam exposure (Riemersma, 1968). Commonly used fixatives are gluteraldehyde, permanganates or osmium tetroxide (Abad et al., 1988).
ii. Dehydration – The next step is to remove moisture from the wood, since most of the resins used for embedding are not miscible with water. This step is usually carried out

by dehydrating the wood sample with a graded series of acetone or ethanol. There are some changes to the structure during this process as the pores shrink and some of the lipids are extracted by dehydrating agents (Glauert and Lewis, 1998)

iii. Infiltration – Once dehydrated, the pores are infiltrated in graded series of the resin that will be used for embedding (Abad et al., 1988).

iv. Embedding and Polymerization – Soft and fibrous material such as wood are first embedded in a polymer resin before obtaining thin sections as shown in Figure 13. The purpose of embedding a material using a resin is to enable the material to protect its surface from possible damage during the preparation process (Ayache et al., 2010) . The choice of resin for embedding is important and should have some specific attributes. The resin must have low viscosity so that it is miscible with the dehydrating agent, interact minimally with the specimen, harden uniformly and be stable under the electron beam (Glauert and Lewis, 1998).

v. Microtoming – The microtome comprises of a knife which slices the resin embedded specimens into very thin sections of 40-150 nm by inducing a microcrack that progresses based on the least area of resistance (Glauert and Lewis, 1998) as shown in Figure 14. The hardness and plasticity of the specimen are important in this technique (Glauert and Lewis, 1998). Microtome may contain a glass or diamond knife based on the type of specimen that has to be sectioned. Thin sections are then collected on grids.

vi. Staining – In order to increase the contrast of the images obtained, the grids are post-stained. Commonly used stains include heavy metals. In case of wood samples, heavy metal stains such as uranyl acetate and $KMnO_4$ are known to bind to lignin (Chundawat et al., 2011) and these regions appear darker in the images, making their identification possible. Several cell wall components or enzymes are identified similarly by immuno-labelling (Donohoe et al., 2009a). Finally, the TEM grids are stained with gold colloid particles that are used as fiducial markers during imaging and 3D reconstruction.

The grid containing the stained sample is inserted into the specimen holder of the TEM. The specimen holder is tilted either along a single or a dual axis and a series of images at regular intervals typically 1 - 2° are acquired (Saghi and Midgley, 2012). The image series is then aligned with the help of the gold fiducial markers and reconstructed in 3D using image analysis software packages such as IMOD and AMIRA (Kremer et al., 1996).

Figure 13. Wood chips embedded in epoxy resin during TEM-CT sample preparation

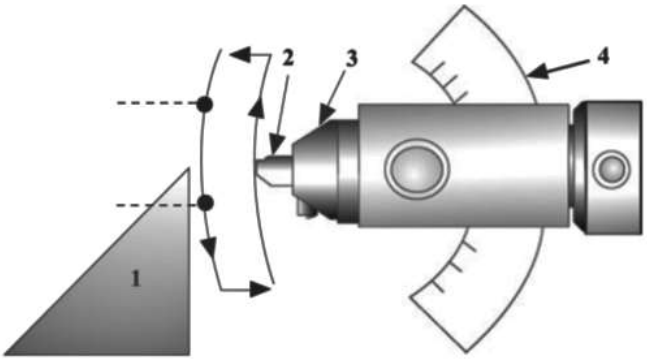

Figure 14. Microtome arm and specimen holder assembly (1 – Knife, 2 – Sample, 3 – Specimen holder and 4 – Goniometer) (Ayache et al., 2010)

2.3.3 Topochemical Distribution from Raman Spectroscopy

Raman Spectroscopy is an excellent 2-D topochemical technique that provides spatial and spectral information about a specimen simultaneously (Batonneau et al., 2001). It is a surface vibrational spectroscopy technique based on the phenomena of Raman scattering (Figure 15). This is an inelastic scattering event where the energy lost by photons is analyzed to detect molecular vibrations (Vickerman and Gilmore, 2009) . An incident photon whose energy is greater than the vibrational quantum energy of the specimen molecule, loses a part of its energy to molecular vibrations that is emitted as another photon of lower energy than the incident photon (Larkin, 2017). A schematic of the Raman spectroscopy instrumentation is shown in Figure 16.

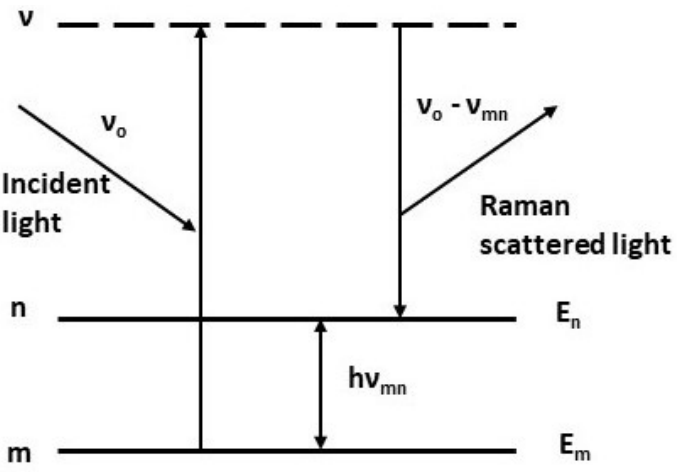

Figure 15. Schematic of Raman scattering (Suëtaka, 1995)

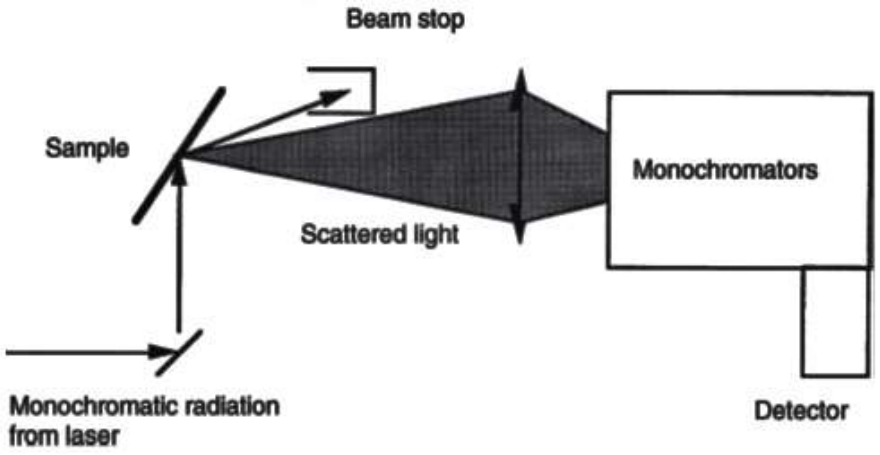

Figure 16. Instrumentation setup for Raman Spectroscopy (Vickerman and Gilmore, 2009)

The topochemical distribution of the cell wall components of biomass, namely cellulose, hemicellulose and lignin can be obtained from Raman spectroscopy. Images showing the spatial distribution of these components in different cell wall layers can also be obtained from the Raman intensities (Gierlinger et al., 2012; Horvath et al., 2012). Gierlinger and Burgert also used Raman spectroscopy in combination with tensile testing to study the spatial composition, molecular orientation, stress-strain behavior and provide a better insight to molecular mechanistic phenomena in Poplar (Gierlinger and Burgert, 2006). The topochemical information obtained over the course of the pretreatment at different time intervals reveal changes in composition of different cell wall components. It

was seen that the rate of dissolution of the cell wall components was different for different regions of the cell wall. The studies of Zhou et al., revealed that dilute acid pretreatment affected the removal of carbohydrates differently in different regions of the cell wall in both compression wood and opposite wood in Pinus bungeana Zucc (Zhou et al., 2014). In case of alkali pretreatment, it was observed that, during the initial stages, there was a preferential delignification in the secondary wall, but for the overall process, the amount of delignification was higher in the middle lamella than the secondary wall (Ji et al., 2014). In case of hydrothermal pretreatment, the amount of delignification in the S2 layer is higher than that of the middle lamella, while hemicellulose dissolution follows the opposite trend (Ma et al., 2014). The studies of Zhang et al., on swelling behavior during ionic liquid pretreatment revealed that the secondary walls were affected at the beginning while the middle lamella and cell corners remain relatively unchanged until a certain degree of swelling and ionic liquid penetration occurred in the cell wall (Zhang et al., 2014).

3. OBJECTIVE

The underlying scientific hypothesis of the current work is that the three-dimensional structure of plant biomass influences their response to biomass pretreatment and conversion processes. Hence, the evolution of the three-dimensional structure of plant biomass as a function of conversion processes and treatment conditions are significantly influenced by the same. Secondly, in addition to three-dimensional structure, topochemical distribution of lignocellulose components also influence their response to biomass conversion processes and treatment conditions, and hence their evolution during conversion. Together, the three-dimensional structure and topochemical distribution synergistically influence the efficiency and effectiveness of overall biomass conversion processes. In order to verify the above hypothesis, the research undertaken here has number of objectives.

Objective 1: Visualization and characterization of the three-dimensional structure of plant cell walls at varying resolutions using different methods as a function of pretreatment and conversion processes

It is necessary to visualize the 3D structure in order to get a wholesome perspective of the nanoscale architecture and understand the layout of cell wall fibers in different regions. Techniques such as X-ray CT and TEM-CT were used for this purpose. Due to inherent limitations of X-ray CT in probing the nanoscale architecture, TEM-CT proved to be a more effective technique for revealing complete structural information of plant cell walls. It was used to elucidate the structural changes and evolution of the three-dimensional structure as a function of biomass pretreatment. It was mentioned earlier that the cell wall components degrade during pretreatment which can alter pore fiber networks affecting the properties of biomass. Thus, structural characteristics such as porosity, surface area and 3D pore size distribution can be altered during pretreatment. As part of this objective, the changes in the structural characteristics of different cell wall regions were determined from TEM-CT images. Understanding these structural changes provided fundamental insights into how the cell wall structure aids in determining the efficacy and severity of the

pretreatment process, how different cell wall regions respond to pretreatment and determine the structure – property and conversion relationships for biomass pretreatment.

Objective 2: Understand the composition and spatial distribution (topochemical distribution) of plant cell wall (lignocellulose) components in different regions of the cell walls and how they change as a function of biomass pretreatment

In the recent years, there have been significant developments in the chemical characterization of biomass components at various topological regions of the cell wall using Confocal Laser Scanning Raman Spectroscopy (Ji et al., 2014; Ma et al., 2014). This technique has also been used to study the changes in topochemical distribution of lignocellulose components during biomass conversion. In order to better understand the role of topochemical distribution on biomass conversion and how the topochemical distribution changes during conversion using the modeling and simulation approach in this work, Raman spectroscopy data and the corresponding images or intensity maps were obtained from the previous work done by Dr. Feng Xu's group at Beijing Forestry university and Dr. Ramarao's group at SUNY-ESF (Ji et al., 2014; Ma et al., 2014). Experimental data on the changes in bulk and spatial composition of lignin, due to dissolution as well as redistribution of these components during the pretreatment process were obtained from the Raman intensity images and compared with the results from the modeling work. The bulk concentration profile for lignin as well as the instantaneous reaction rate of lignin dissolution over the course of the pretreatment process were also determined from the Raman intensity maps by image analysis techniques and compared with the modeling results.

Objective 3: Develop a fundamental model of the transport and reaction processes during biomass pretreatment and conversion processes using the above information and known reaction kinetics

A transport-reaction model was developed using fundamental principles of transport phenomena and reaction kinetics while using the actual biomass structure and

topochemical information described above. As part of this objective, the dissolution of lignin was specifically modelled for different pretreatment methods and biomass species. The transport of the molecules of the reagent used for pretreatment such as acid, alkali, hot water etc., was modeled as diffusion through the cell lumen, pore spaces between the biomass cell walls and through the cell walls itself using a hybrid random walk approach. A similar hybrid random walk approach has been successfully used to predict the simultaneous, pore-fiber diffusion in heterogeneous porous media (Defrenne et al., 2019). At the interface and inside the cell walls where the lignocellulose constituents are present, the reaction between the diffusing reagents and biomass components were modeled using reaction kinetics and reaction probabilities. The local dissolution of the lignocellulose constituents (i.e., lignin) at the cell wall level was modeled as a pseudo first order reaction considering the local concentration of the corresponding component of interest. Due to the combined transport and reaction of the reagent particles, as they traverse and react throughout the cell wall matrix, they can dissolve some of the biomass components and correspondingly alter their physiochemical structure. The changes in the spatial composition of the biomass constituents as well as the changes in the overall bulk concentration of the sample are determined throughout the process. Following the simulation, overall transport and reaction kinetics considering the biomass structure and bulk dissolution were determined as a function of biomass pretreatment. Based on this analysis, the overall transport rate coefficient and the effective reaction rate constant were determined as biomass conversion proceeds. This can lead to developing further insights into the fundamentals of biomass pretreatment and conversion processes. The methodologies used for experiments as well as modeling and simulation in achieving the above research objectives are given in detail in the upcoming sections.

4. 3D STRUCTURE CHARACTERIZATION AND STRUCTURAL EVOLUTION

A complete understanding of the structure of lignocellulosic biomass requires the use of 3D visualization and characterization techniques at the necessary resolution. In the previous work by Goel and Defrenne, X-ray CT was used extensively to characterize the micron scale structure of paper (Defrenne, 2008; Defrenne et al., 2019; Goel, 2003). However, a micron scale resolution did not provide detailed information on the biomass ultrastructure, layout of the cell wall layers and their structural evolution. Thus, in order to better understand the architecture of biomass cell walls, it is necessary to probe the nanoscale structure and its effect on biomass conversion. Nanoscale ultrastructure characterization was accomplished by TEM-CT which follows the same principle as X-ray CT but uses electrons for imaging instead of X-rays, resulting in a higher resolution. This yields further insights into the cell wall architecture. Using the TEM-CT technique, high quality 3D images of different types of pretreated cell walls were obtained after a series of sample preparation, image acquisition and 3D reconstruction steps. The images were then processed using a series of steps to yield a binary image which formed the basis for further analysis of structural characteristics. Using the binary TEM-CT images, characteristics such as porosity, pore size distribution and specific surface area were determined for both untreated and treated images.

4.1 X-Ray Computed Tomography

X-ray CT revealed the micron scale structure of the cell walls. These images were taken on a Skyscan 1172 instrument and had a voxel size of 0.6 μm. As seen in Figure 17, the cell wall and lumen can be clearly visualized. However, due to inherent limitations of this technique, a higher resolution visualization of the interior of the cell wall layers was not possible and the details of the different regions within the cell wall could not be clearly distinguished. There were no discernable changes seen in the cell wall layout between the treated and untreated images. Thus, X-ray CT was effective only in developing micron scale details of the biomass structure. However, it was ineffective for characterizing the cell wall structure at the nanoscale. Hence, it is clear that there is a need for a higher

resolution 3D technique for a more accurate characterization of the biomass cell wall architecture. As discussed earlier, TEM-CT is such a technique capable of high-resolution characterization.

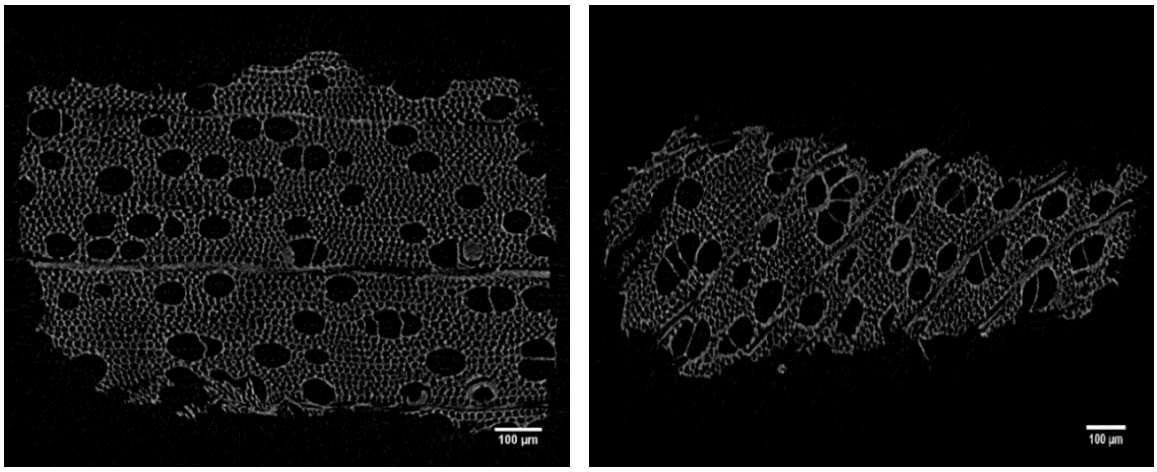

Figure 17. X-ray CT images of untreated (left) and treated (right) plant cell walls

4.2 TEM Computed Tomography

TEM-CT combines the principles of the conventional 2D TEM imaging as well as computed tomography. Even though this technique is more intrusive, and complex compared to X-ray CT, it is capable of visualizing the cell wall characteristics down to the nanoscale and give detailed information about the layout of the different layers and their structural evolution which is very essential for a fundamental understanding of the pretreatment process. TEM's can visualize up to a few Angstroms of length.

4.2.1 TEM-CT Sample Preparation

The sample preparation for TEM-CT is elaborate as it has to be ensured that there is no damage to the specimen during sample preparation or image acquisition. Since plant cell walls are soft materials, they first have to be embedded in a hard resin to preserve the structure while cutting a thin nanoscale slice of the material and imaging. Two techniques were chosen for the sample preparation process (Abad et al., 1988; Chundawat et al., 2011).

In the first technique, the procedure used for sample preparation and imaging was a slightly modified version of the procedure adopted by Chundawat *et. al*. and is described below (Chundawat et al., 2011).

- One set of samples were fixed twice for 6 min (2 min on, 2 min off, 2 min on) in 2.5% glutaraldehyde solution buffered in 0.1 M sodium cacodylate buffer under vacuum. The other set of samples were fixed with 1% $KMnO_4$ for 10 min.
- Dehydration was carried out in a graded ethanol series for 1 min each (15%, 30%, 60%, 90%, twice for 100% ethanol) for all samples.
- Samples were infiltrated with Epoxy resin in the microwave under vacuum and incubated overnight at room temperature with increasing concentrations of the resin (15%, 30%, 60%, 90%, thrice for 100% resin, diluted in ethanol).
- Samples were then be embedded in fresh resin and polymerized in an oven at 40 °C for 1 day and 60 °C for two days.
- The samples were sectioned to 150 nm with a Diatome diamond knife on a Leica UC6 ultramicrotome (Leica, Wetzlar, Germany) and collected on 200 mesh Formvar grids.
- Grids containing samples fixed with glutaraldehyde were post-stained for 6 min with 2% aqueous uranyl acetate and 1% $KMnO_4$ for 10 min to selectively stain for lignin and dried.
- The TEM grid was mounted on a single-tilt Fischione tomography holder (Fischione Instrument, Export, PA).
- The images were taken with a 4k-by-4k Gatan UltraScan CCD camera (Gatan, Pleasanton, CA) on a FEI Tecnai F30 300 kV FEG TEM (FEI, Hilsboro, OR).
- The tomogram tilt series was recorded by tilting the specimen stage -69 to 69 degrees with 1.5-degree interval at 20,000X nominal magnification using a serial EM.
- Tomograms were reconstructed using an R-weighted back projection within the IMOD software package.

An alternative sample preparation procedure was tried using the quetol resin by the method prescribed by A.R Abad *et. al*. and is described below (Abad et al., 1988).

- Samples were fixed with 1% $KMnO_4$ for 15 min followed by rinsing with distilled water thrice for 10 minutes under vacuum.

- The fixed samples were dehydrated in 75% quetol 651 for an hour followed by dehydration with 100% quetol 651 solution twice for an hour each under vacuum.
- Subsequently they were infiltrated with the quetol resin for an hour twice under vacuum and polymerized at 74°C for 8 hours in an oven.
- The samples were sectioned to 150 nm with a Diatome diamond knife on a Leica UC6 ultramicrotome (Leica, Wetzlar, Germany) and collected on 200 mesh Formvar grids.

4.2.2 TEM-CT image acquisition and reconstruction

Once the TEM grid was stained and dried, it was ready to be imaged. Appropriate imaging conditions such as the operating voltage, imaging mode and beam conditions were chosen depending on the nature of the sample and the type of information to be extracted. The consequent image acquisition and reconstruction steps are as follows:

i. Tilt series acquisition and alignment

The TEM-CT grid containing the stained sample was inserted into the specimen holder and a tilt series was acquired. The specimen holder was tilted either along a single or a dual axis and images at regular tilt intervals, typically 1-2° (Saghi and Midgley, 2012) are acquired. Unlike X-ray CT where the entire sample was scanned using X-ray and the back projections are captured, the TEM- CT the tilt series does not cover the entire 360 degrees. Only a part of the sample was tilted, and the corresponding projections are obtained.

ii. Tilt series alignment

Colloid gold particles were used as fiducial markers which aid in aligning the tilt series acquired. Digital imaging software packages such as IMOD and AMIRA use these markers to solve for tilt angles, shifts, rotations and size changes and align the tilt series (Kremer et al., 1996).

iii. 3D reconstruction

The 3D reconstruction was accomplished digitally with the help of software packages such as IMOD or Amira. The reconstruction was usually carried out in 2D by back-projecting within a slice perpendicular to the tilt axis and then building the 3D model slice by slice (Saghi and Midgley, 2012). Software packages such as IMOD or AMIRA include a variety of options for viewing, segmenting, and quantifying the reconstructed volumes.

There are several variations to the TEM-CT sample preparation and image acquisition steps that are intended to better preserve the structural features and enhance the imaging capabilities. The sample preparation or image acquisition steps can either be carried out at room temperatures or at much lower temperatures in a cryo-chamber. Low temperature and high-pressure techniques such as freeze substitution and high pressure freezing can also be employed (Murray, 2008). The method chosen for sample preparation and imaging depends on the nature of the specimen to be imaged, the level of preservation required and the type of information that is to be obtained from imaging.

4.2.3 TEM-CT Image Processing

Images obtained from TEM-CT can contain artifacts that arise from the sample preparation process or imaging conditions and they can interfere with the interpretation and analysis of the images. Hence, these images are processed in order to reduce or eliminate these artifacts. Before delving into developing effective image processing strategies, it is important to understand some of the basic concepts of digital images (Sluder and Wolf, 2013). A 2D digital image is made up of numerous smaller square units of same size which are known as pixels (Toriwaki, 2009). For a 3D image, the smallest unit is a cube and is known as a voxel. Each voxel is assigned a certain grayscale value which corresponds to the light intensity at that voxel. The images obtained from TEM-CT are usually 8-bit images and the grayscale values at any voxel range between 0 and 255. A plot of the frequency of the occurrence of grayscale values with respect to the intensity is called a histogram (Das, 2015). Figure 18 shows the TEM image and the corresponding histogram for a biomass sample. The outline of the cell wall region, layout of the different cell wall layers and the cell lumen are visible in the figure. The reconstructed 3D image stack was processed to reduce artifacts and obtain a binary image that was used for further analysis. Software packages such as ImageJ, MATLAB, IMOD or Amira can be used for image processing. The choice of image processing techniques depends on the image quality. For the TEM-CT images, contrast enhancement, anisotropic diffusion, despeckling and binarization techniques were used which are described in the further sections.

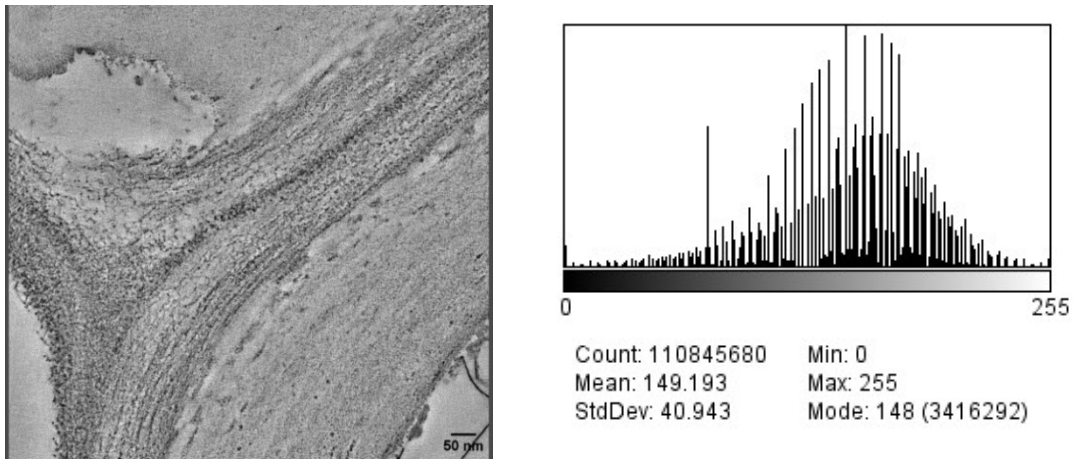

Figure 18. TEM image slice of an untreated Arabidopsis cell wall and its corresponding histogram before processing (Lawrence Berkeley National Laboratory, CA)

4.2.3.1 Contrast enhancement

Usually, images from X-Ray CT or TEM-CT have low contrast despite staining during the specimen preparation stage. Hence, most often there is a need for contrast enhancement. One of the methods used for contrast enhancement is histogram equalization. Here, the contrast was enhanced by altering the histogram of the image so that it gets a desired shape (Celik, 2012; Ibrahim and Kong, 2007). For most TEM images an increase of 2-5% in contrast is sufficient in further processing of the images as seen in Figure 19.

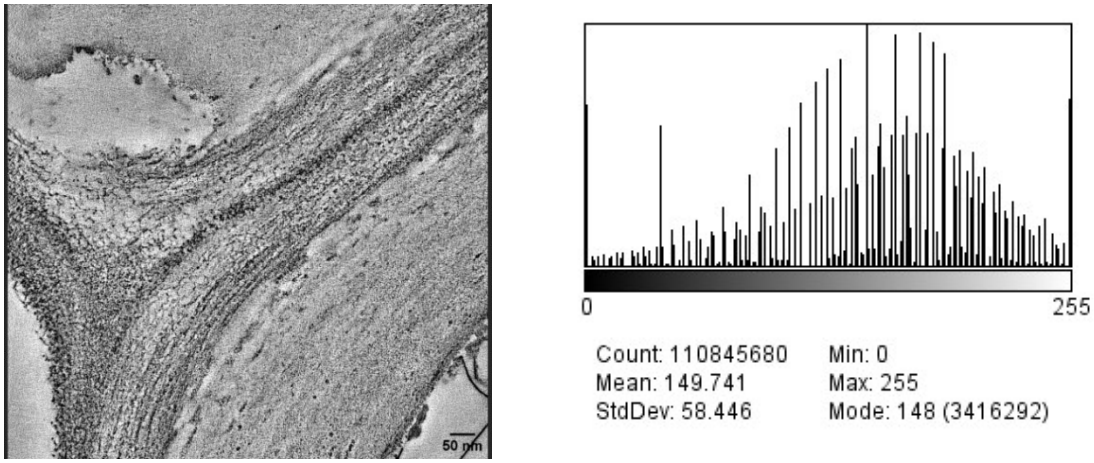

Figure 19. TEM image slice of an untreated Arabidopsis cell wall and its corresponding histogram after contrast enhancement

4.2.3.2 Anisotropic diffusion

The next step of image processing is the removal of noise from images, which is most essential. Anisotropic diffusion is one such technique that reduces noise while preserving edges at the interface of the pore and cell wall boundaries. It was originally developed by Perona and Malik in 1990 and has been modified and adapted in the previous work of Defrenne (Defrenne, 2008; Perona and Malik, 1990). The same technique was used for the TEM-CT images.

The approach used is analogous to applying the anisotropic heat diffusion equation to image processing in order to determine the voxel intensity (Perona and Malik, 1990). The voxel intensity was determined by the following equation:

$$\frac{\partial I}{\partial t} = div(c(x,y,z,t)\nabla I = c(x,y,z,t)\Delta I + \nabla c.\nabla I \quad (2)$$

Where I is the pixel intensity, t is the iteration and c represents the diffusion coefficient. A modified form of the above equation was used similar to the previous work (Defrenne, 2008). The diffusion coefficient was computed as:

$$c = \exp\left[-\left(\frac{\|\nabla I\|}{K}\right)^4\right] \quad (3)$$

Where K is a constant user defined value which may be different for each image. The value of K may be different for different iterations as well. Similar to the previous work, the value of K was chosen as 60 for the first two iterations and 30 for the following iterations (Defrenne, 2008). Figure 20 shows the gray scale distribution after applying the anisotropic diffusion equation to the raw data. It is clear that as a result of this step, the grayscale distribution of the TEM-CT images has been reduced to essentially two normal distributions, one representing the pore phase and the other representing the solid cell wall phase.

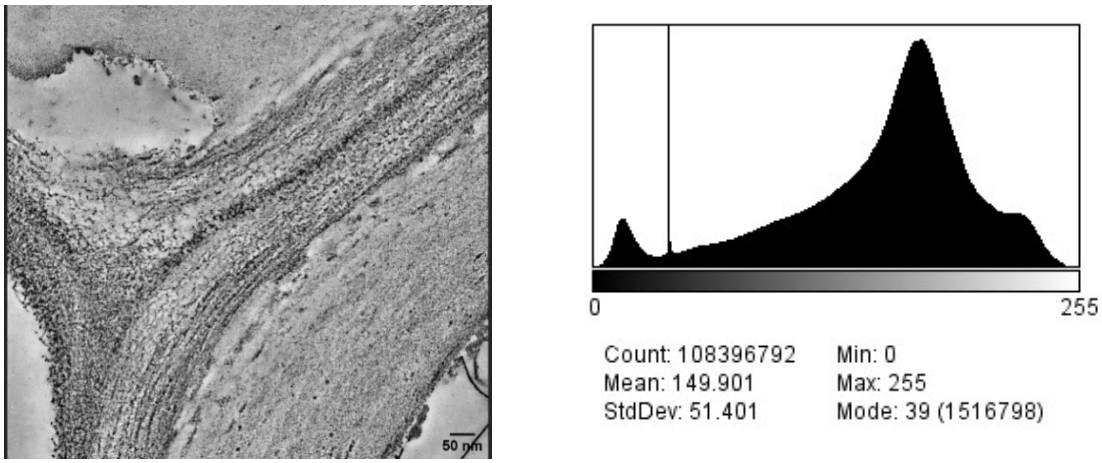

Figure 20. TEM image slice of an untreated Arabidopsis cell wall and its corresponding histogram after anisotropic diffusion

4.2.3.3 Despeckling and binarization

Despeckling is another noise reduction technique where the intensity of each pixel was replaced with the median value in its neighborhood, which comprises of the current pixel and the eight surrounding pixels (Zhang and Cheng, 2020). The next and final step of image processing is binarization. A binary image is preferred for further analysis and quantification. In a binary image, the grayscale intensity at any pixel can have only two values i.e., 0 or 1 (Toriwaki, 2009) which correspond to two distinct structural features or phases of the image. A binary image stack was obtained by choosing a threshold grayscale value based on its histogram (Defrenne, 2008; Toriwaki, 2009). All pixels below the threshold value belong to one phase and all pixels above the threshold value belong to another phase. In case of biomass samples, one phase is the pore or void space, and the other phase is the solid cell wall or cell wall fiber phase as seen in Figure 21. A threshold intensity value was chosen that retained most of the structural features. The threshold can either be chosen manually or by using standard options available in image analysis software packages. The method of minimum error thresholding was previously used for binarization of X-ray CT images where the point of intersection of the two bell curves in the histogram was chosen as the threshold. (Defrenne, 2008). Other options such as choosing the mean, median, etc., are available in software packages ImageJ which can be explored. In case of TEM-CT images, the threshold was chosen manually based on the image characteristics.

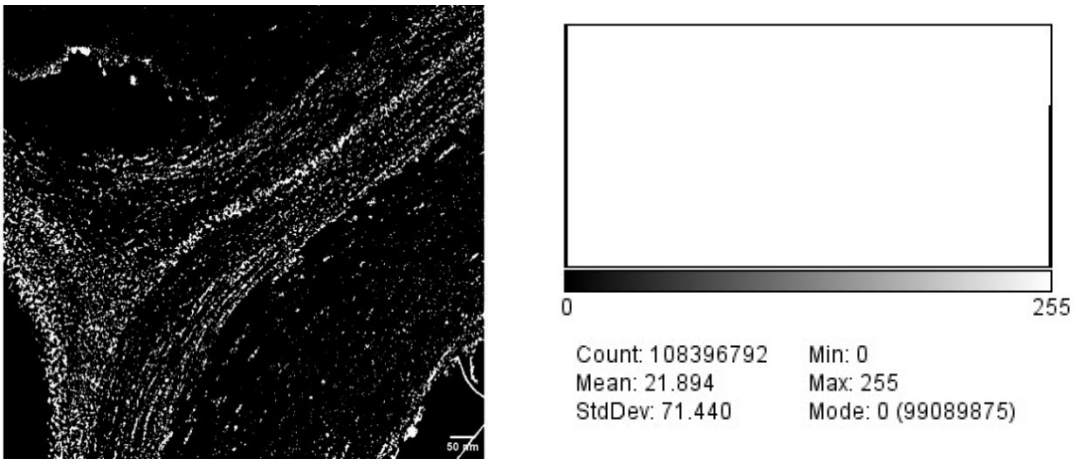

Figure 21. TEM image slice of an untreated Arabidopsis cell wall and its corresponding histogram after despeckling and binarization

It is important to recognize that image processing methods are heavily sample dependent. In the current work, both TEM-CT and Raman spectroscopy images are used. The nature of these images are different and hence appropriate image processing methods were employed depending on the noise level, contrast, and other details. For the Raman images, it may not be necessary to enhance the contrast or apply anisotropic diffusion filter depending on the image quality. In such cases, applying such techniques may result in loss of the structural details or creating new artifacts which were not present in the original image. The method of binarization also has to be chosen depending on the histogram. In cases where the histogram has a bimodal distribution, the minimum error threshold maybe most suitable. In other cases, the choice of the threshold has to be chosen in such a way so that it retains most structural features. In some cases, other image processing steps maybe required in addition to those mentioned above in order to get a usable image for structural and further analysis.

4.2.4 Visualization and characterization of Cell Wall Structure from TEM Images

In order to evaluate the 3D nanoscale structure of biomass and their evolution during pretreatment, untreated biomass samples and treated biomass samples of different species and different pretreatment conditions were studied. TEM images of both treated and untreated biomass samples were obtained in both 2D and 3D. These biomass species

include Aspen (hardwood) Arabidopsis (grass) and corn stover (agricultural residue). The 2D images of acid treated Aspen were obtained at the U of M Characterization Facilities. The 3D images of untreated Arabidopsis, ammonium oxalate Arabidopsis, sodium hydroxide treated Arabidopsis and ammonia fiber expansion (AFEX) treated corn stover were also obtained. The untreated Arabidopsis samples were prepared by different TEM-CT sample preparation techniques such as room temperature sample preparation and high pressure freezing. The biomass species and the treatment conditions were selected mostly based on what was available from our collaborators. TEM-CT images of Arabidopsis sample were obtained from Dr. Manfred Auer's group at Lawrence Berkeley National Laboratory (LBNL), CA. TEM-CT images of AFEX pretreated corn stover sample were obtained from Dr. Bryan Donohoe at National Renewable energy Laboratory (NREL), CO. Even though the TEM CT images were 3D images, only 2D images of a single slices are shown in Figures 22 through 24 for convenience.

It is evident from the TEM images of different treated and untreated biomass samples shown in Figures 22 through 25 that their nanoscale cell wall architecture was revealed. For the 3D TEM-CT images, selected slices of treated and untreated specimens which show the cell wall nanoscale ultrastructure are seen in Figures 22 through 24. As seen in these images, the cell wall structure undergoes changes layer by layer due to pretreatment. Certain cell wall components degrade as a result of pretreatment which opens up the pore spaces and enhances the accessibility to cellulose microfibrils. Figures 22 and 23 show 2D slices from 3D TEM-CT images of untreated, ammonium oxalate treated, and sodium hydroxide treated cell walls. Figure 24 shows an AFEX treated corn stover cell wall where the secondary wall has expanded and undergone degradation. Figure 25 shows conventional 2D TEM images of acid treated Aspen which reveal the nanoscale architecture. The different cell wall regions were clearly visible and marked. Among the treated image slices, it can be seen that sodium hydroxide pretreatment was more severe than ammonium oxalate pretreatment. In case of ammonium oxalate treated sample, the primary walls and middle lamella were disrupted, and the corresponding pores opened up. In case of the sodium hydroxide treated sample, it appears that most of the secondary wall was dissolved. In addition, the primary wall and middle lamella were significantly

disrupted. In case of the AFEX treated cell wall, expansion and dissolution of cell wall components further opened up pore spaces in the secondary wall and relocated the existing cell wall fibers. These results are corroborated in the further sections where the structural characteristics such as porosity and pore size distribution are determined.

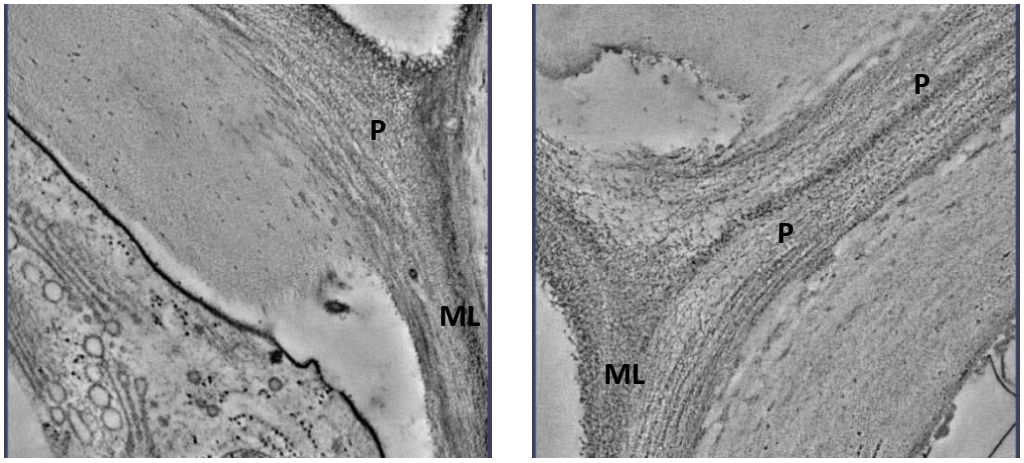

Figure 22. TEM image slices of untreated Arabidopsis sample prepared by high pressure freezing (left) and at room temperature (right). P - primary wall and ML - middle lamella (Image source: Lawrence Berkeley National Laboratory, CA)

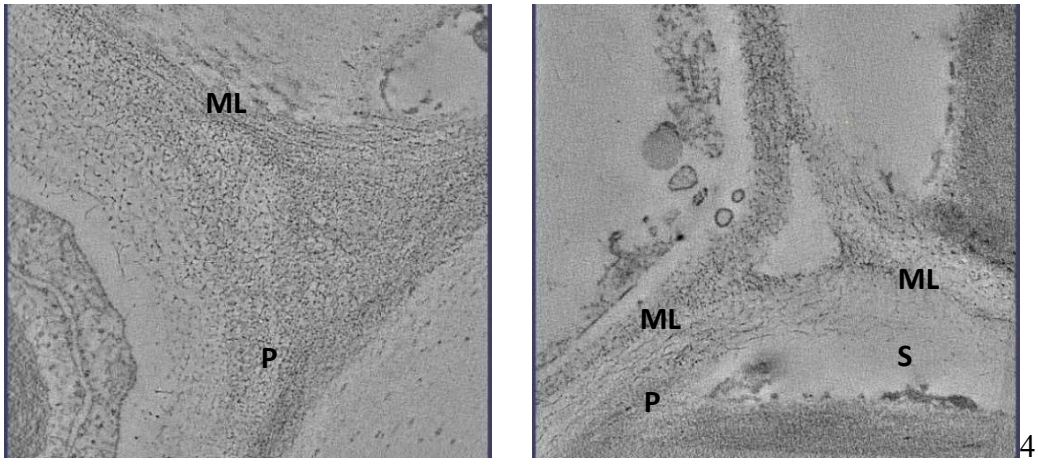

4

Figure 23. TEM image slices of ammonium oxalate treated (left) and sodium NaOH treated (right) Arabidopsis. P - primary wall, ML - middle lamella, S - secondary wall (Image source: Lawrence Berkeley National Laboratory, CA)

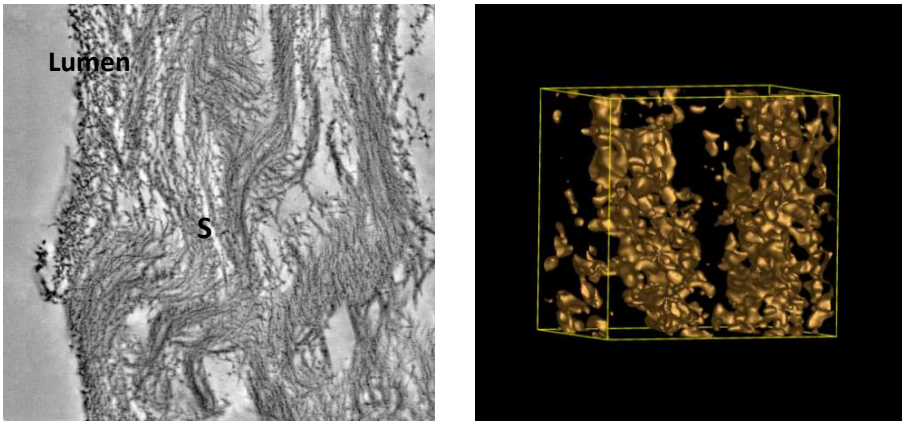

Figure 24. TEM image slices of AFEX pretreated corn stover (left) and its 3D reconstruction (right). S indicates secondary wall (Image source: National Renewable Energy Laboratory, CO)

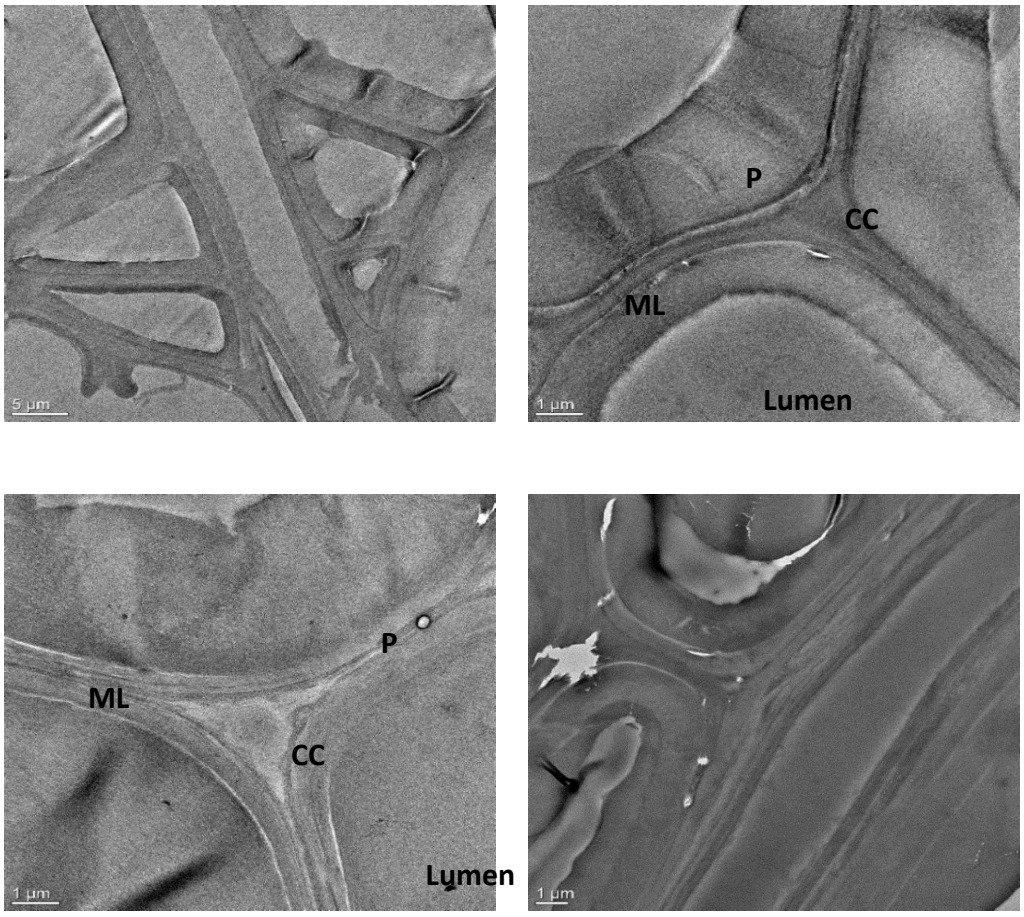

Figure 25. 2D TEM images of acid treated aspen. P- Primary wall, ML – middle lamella, CC – cell corner. (Image source: Characterization Facility, University of Minnesota)

4.2.5. Determination of 3D Structural Characteristics of untreated and treated biomass using TEM CT

Plant cell walls are porous materials with a complex network of biopolymers and the cells have intricate structures with varying amounts of these components depending on the plant species. The cell walls contain microfibrils which are arranged at varying orientations at the nanoscale as well as other crystalline and amorphous biopolymers. Recent findings indicate that the pore space in the plant cell wall is altered during pretreatment which facilitates further conversion processes (Chundawat et al., 2011). Hence, it is important to analyze the pore characteristics such as porosity, specific pore-cell wall interfacial area and 3D pore size distribution. Once the processed 3D TEM-CT images were obtained, they were used to determine these structural characteristics. In the processed binary images of plant cell walls, there are two distinct phases present – pore/voids and cell wall fibers. Using these binary image stacks, the porosity, specific surface area and 3D pore size distribution of treated and untreated plant cell walls were determined and compared. Different sets of untreated and treated images obtained were used for 3D structure characterization. The untreated image sets included Arabidopsis samples which were prepared at room temperature and by high pressure freezing (Sarkar et al., 2014). The treated samples included AFEX treated corn stover and ammonium oxalate treated Arabidopsis. Details of the structural characterization of the treated and untreated biomass samples are presented in further sections.

4.2.5.1 Porosity and specific surface area

The porosity and specific surface area can be computed by knowing how many voxels belong to the pore and fiber phases. The porosity of the sample is the ratio of the pore volume to the total volume of the sample, and is given by:

$$\varepsilon = \frac{\boldsymbol{number\ of\ pore\ voxels}}{\boldsymbol{total\ number\ of\ voxels}} \qquad (4)$$

The specific surface area or the interfacial area was computed using the method adopted by Goel and Defrenne (Defrenne, 2008; Goel, 2003). The total interfacial area, S_t was

determined by counting the number of voxels that correspond to the pore-fiber interface in the total sample volume including pores and solid phase and then multiplying that by the unit area of a square voxel. The specific surface area or the interfacial area per unit mass, S_W (m^2/g) and specific area per unit volume of the solid phase, S_v (m^2/m^3) are given by:

$$S_W = \frac{S_t}{(1-\varepsilon)\rho_f} \quad (5)$$

$$S_V = \frac{S_t}{1-\varepsilon} \quad (6)$$

Where S_t is the total interfacial area in a given sample volume, ε is the porosity and ρ_f is the cell wall density. Under normal conditions, the fiber (cell wall) density ρ_f was assumed to be 1.55 g/cm^3 (Stone et al., 1966). The porosity and specific surface area of different regions of the cell wall for untreated and treated specimen were reported in Figures 26 and 27 and Table 2.

It must be noted that, from our prior experience, the typical variations in measurement of structural characteristics in biomaterials were determined to be about ±1% to14% (Defrenne et al., 2017). Since we did not have access to a large number of TEM CT images under various treatments, it is reasonable to assume an average variability of ~±7% in such measurements. From the above results, it was evident both the porosity and specific surface area changed upon treatment due to dissolution of cell wall components Firstly, in both the untreated and treated images it was observed that the porosity and specific surface area of the primary wall was greater than the middle lamella indicating a more open or less dense structure in the primary wall. It was observed earlier that when the structure is more porous, there are a greater number of pore-cell wall interfaces thus leading to a higher interfacial area (Aaltosalmi et al., 2004; Defrenne et al., 2019, 2017). A higher porosity and interfacial area in the primary wall indicated higher dissolution during pretreatment as compared to the middle lamella. In case of the untreated samples, it was evident that the TEM-CT sample preparation methods had a significant effect on the measurement of structural characteristics. In case of room temperature sample preparation, the cell wall fibers were more prone to shrinking or swelling during dehydration, infiltration and microtoming steps. However, when the sample preparation was carried out by high

pressure freezing, the structure was better preserved. Secondly, both porosity and specific surface area increased as a result of pretreatment. This was attributed to dissolution of lignin and hemicellulose, thereby making the cell wall and cellulose chains more accessible. However, it was seen that the specific surface area of one of the samples prepared by high pressure freezing is still greater than the treated samples which could be attributed to the sample preparation methods used.

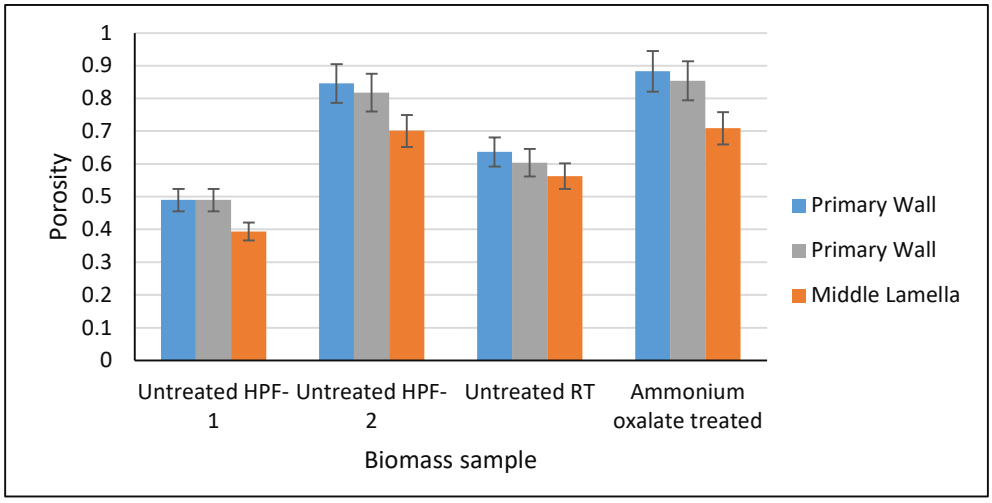

Figure 26. Porosity of different cell wall regions for treated and untreated Arabidopsis samples

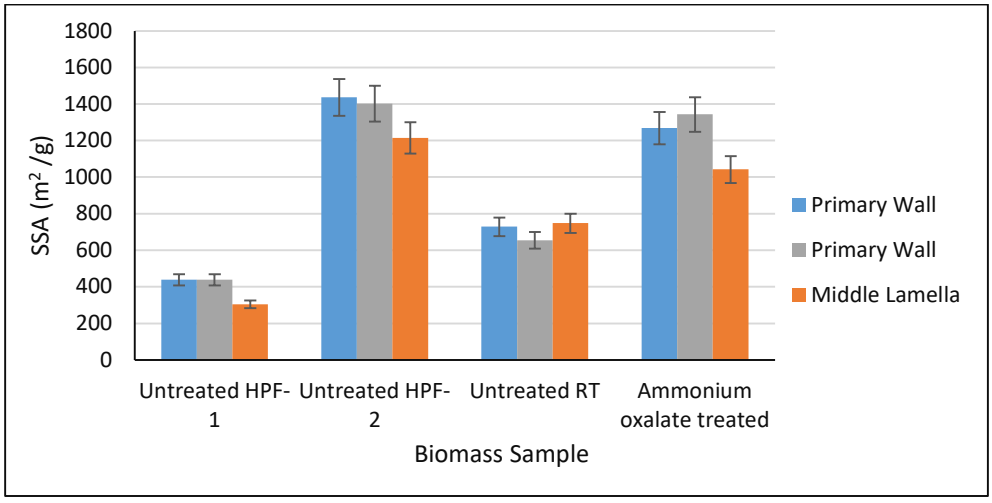

Figure 27. Specific surface area of different cell wall regions for different biomass samples

Sample	Region	Porosity	Specific surface area (m^2/m^3)	Specific surface area (m^2/g)
Untreated Arabidopsis (Room temperature prep)	Primary Wall	0.637	4.10E+08	728.69
	Primary Wall	0.604	4.02E+08	654.94
	CML	0.563	5.07E+08	748.51
Untreated Arabidopsis-1 (High Pressure Frozen)	Primary Wall	0.49	3.47E+08	438.96
	CML	0.394	2.86E+08	304.48
Untreated Arabidopsis-2 (High Pressure Frozen)	Primary Wall	0.846	3.43E+08	1437.00
	Primary Wall	0.818	3.95E+08	1401.84
	CML	0.701	5.62E+08	1215.17
Ammonium oxalate treated Arabidopsis	Primary Wall	0.883	2.30E+08	1268.27
	Primary Wall	0.854	3.04E+08	1343.35
	CML	0.709	4.70E+08	1042.01
AFEX treated Corn	S2	0.521	2.85E+08	383.86

Table 2. Porosity and specific surface area results for treated and untreated biomass samples

4.2.5.2 3D pore size distribution

In addition to porosity and specific surface area, the size distribution of the pores is also an important structural characteristic of porous materials. Although 2D pore size distribution in any given plane reveals useful information, they have certain limitations. Using the concept of hydraulic diameter, pore spaces in 2D can be represented by an equivalent diameter of a circle (Goel et al., 2001). In the case of long narrow pores, such a simplification can often result in misrepresentation of the actual 3D structure (Defrenne et al., 2017). Hence there is a clear need for 3D representation of the actual pore size distribution in porous materials. While techniques such as mercury intrusion porosimetry and nitrogen adsorption are available for this purpose, they are invasive and have inherent limitations. Hence, a sphere growing algorithm as described in the previous work was used to effectively determine the 3D pore size distribution of the cell walls (Defrenne, 2008; Defrenne et al., 2017). This approach involved growing spheres starting from the smallest diameter and incrementing the diameter till it reached the largest diameter that can be fit

into a given 3D pore space as shown in Figure 28. Hence, the largest sphere that can be fit at every pore voxel, without overlapping any fiber voxel determined the pore diameter at that location. The total amount of pore space corresponding to each sphere (pore) diameter was measured, thus giving the 3D pore size distribution of the cell wall.

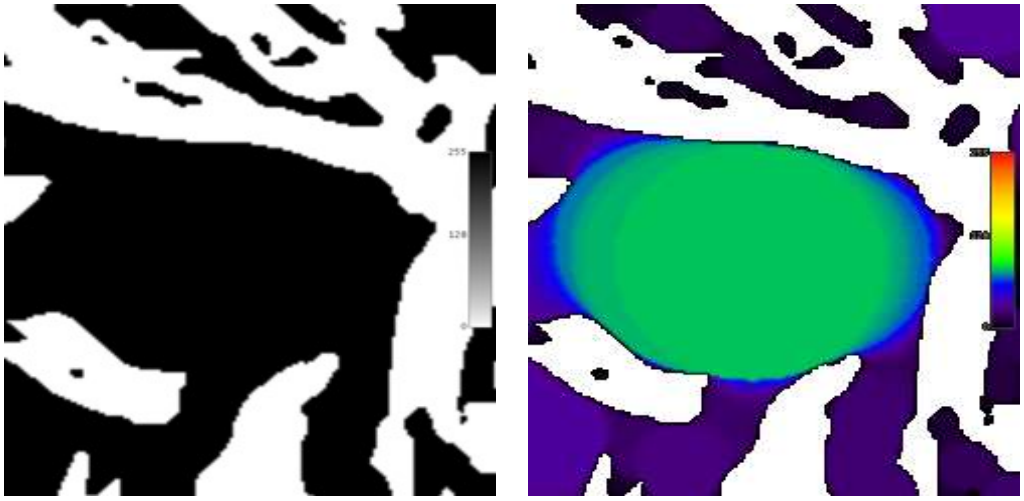

Figure 28. Sphere growing algorithm fitting the sphere with the largest possible diameter at a given pore space (Defrenne et al., 2017)

The pore size distributions and mean pore sizes for different regions of treated and untreated samples are shown in Table 3 and Figures 29 through 33, respectively. Upon a closer look at these figures and tables, a number of inferences were made with respect to the pore size distributions. Firstly, it was seen that the primary walls exhibited a slightly broader pore size distributions compared to the middle lamella for both treated and untreated samples. Additionally, the primary wall had bigger pores than the middle lamella in both treated and untreated samples. As seen in Figures 29 through 31, the primary lamella had a greater number of pores whose sizes were between 5-15 nm while a higher fraction of the pores in the middle lamella were less than 5 nm in size. The mean pore sizes were also slightly higher for the primary wall except for the untreated sample prepared by high pressure freezing as seen in Table 3 and Figures 29 through 31. Similar to the observed increases in porosity, this again can be attributed to the fact that the components of the primary wall were dissolved to a greater extent compared to the middle lamella. Also, the material from the primary wall could be expected to be dissolved prior to the middle

lamella. Secondly, in case of the untreated samples the method of sample preparation significantly affected pore size distribution measurements. The pore size distributions for the samples prepared at room temperature were quite different from that prepared by the high-pressure freezing technique as seen in Figure 32. The mean pore sizes for the samples prepared at room temperature were lower than those samples prepared by high pressure freezing. In addition, the pore size distribution was wider for the sample prepared at room temperature. It could be inferred that room temperature sample preparation techniques caused more shrinkage and swelling and could be more intrusive to the sample as compared to high pressure freezing.

Lastly, pretreatment process significantly altered the 3D pore size distribution of the cell wall as seen in Figures 32 and 33. It was observed that mean pore sizes of the primary and middle lamella of the treated walls was greater than that of untreated cell walls. The pore size distribution of the treated samples revealed the presence of a greater fraction of pores in the range of 5-15 nm while the untreated samples mainly contained pores which were less than 5 nm. This confirmed that during the biomass pretreatment process, due to the dissolution and redistribution of the cell wall lignocellulose components, the 3D pore space was modified which altered the pore size distribution. The standard deviation values of the 3D pore size distributions indicated a wider pore size distribution for the treated samples as compared to the untreated cell walls which suggested the creation of new pore spaces within the cell wall matrix. Again, this could be attributed to heterogeneous degradation of cell wall components. Similar observations have been made in previous literature. Ishizawa et. al, reported that pretreated corn stover samples showed a higher pore volume, especially in the pore sizes ranging greater than 3 nm as compared to untreated samples (Ishizawa et al., 2007). It has been reported that as material is removed from the cell wall, pores are created (Kerr and Goring, 1975; Stone and Scallan, 1965) . Stone et. al, reported that the median pore size increased up to 4 nm during delignification (Stone and Scallan, 1965). Kerr and Goring reported that the median pore width of white birch increased from 0.92 nm to 1.69 nm due to alkali pretreatment (Kerr and Goring, 1975). Herbaut et. al, studied the effect of dilute acid, hot water and ionic liquid pretreatments on Wheat straw, Poplar and Miscanthus and found an increase in the proportion of pores of

10-15 nm and more (Herbaut et al., 2018). Thus, it was seen that the method of sample preparation, nature and severity of the biomass pretreatment process, significantly affected the structural characteristics and hence contributed to their structural evolution as the pretreatment process progressed. Since the number of TEM-CT images analyzed here are quite small, it will be worth conducting further research on more biomass samples and varied pretreatment approaches.

Sample	**Region**	**Mean**	**SD**
Untreated Arabidopsis (Room temperature prepped)	Primary Wall	5.689	2.385
	Primary Wall	5.81	2.604
	CML	4.339	1.905
Untreated Arabidopsis-1 (High Pressure Frozen)	Primary Wall	6.095	3.144
	CML	6.661	3.555
Untreated Arabidopsis-2 (High Pressure Frozen)	Primary Wall	6.431	2.444
	Primary Wall	5.781	2.192
	CML	3.977	1.496
Ammonium oxalate treated Arabidopsis	Primary Wall	9.964	4.013
	Primary Wall	7.816	3.135
	CML	5.204	2.23
AFEX treated Corn Stover	S2	8.787	0.059

Table 3. 3D pore size distribution of treated and untreated cell walls

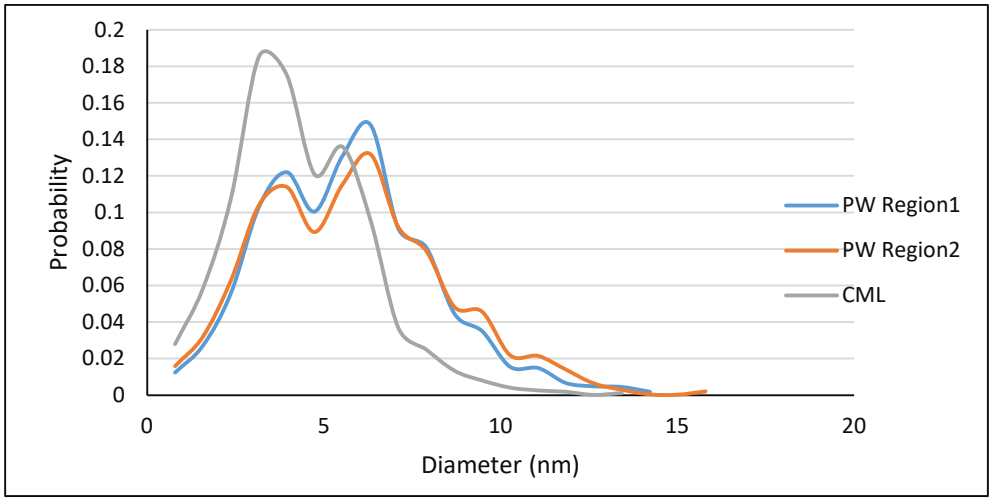

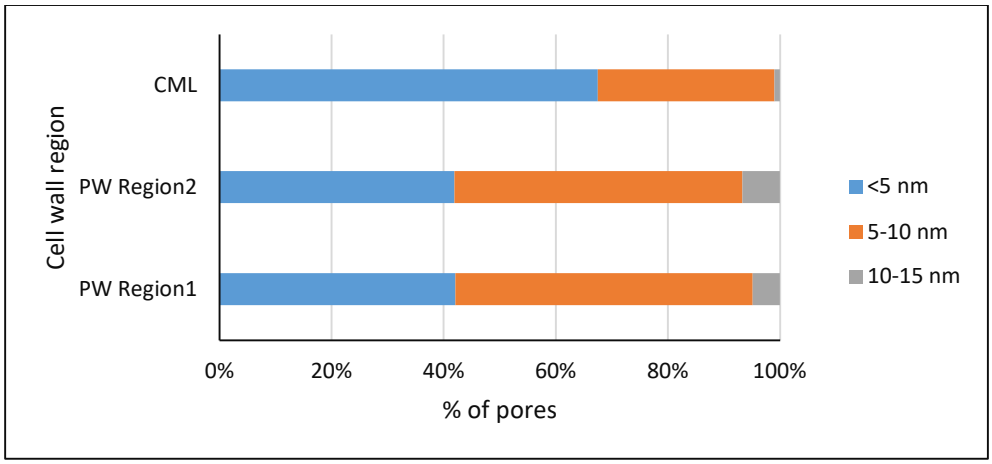

Figure 29. Comparison of 3D pore size distribution of different regions of primary wall (PW) and middle lamella (CML) in untreated Arabidopsis prepped at room temperature

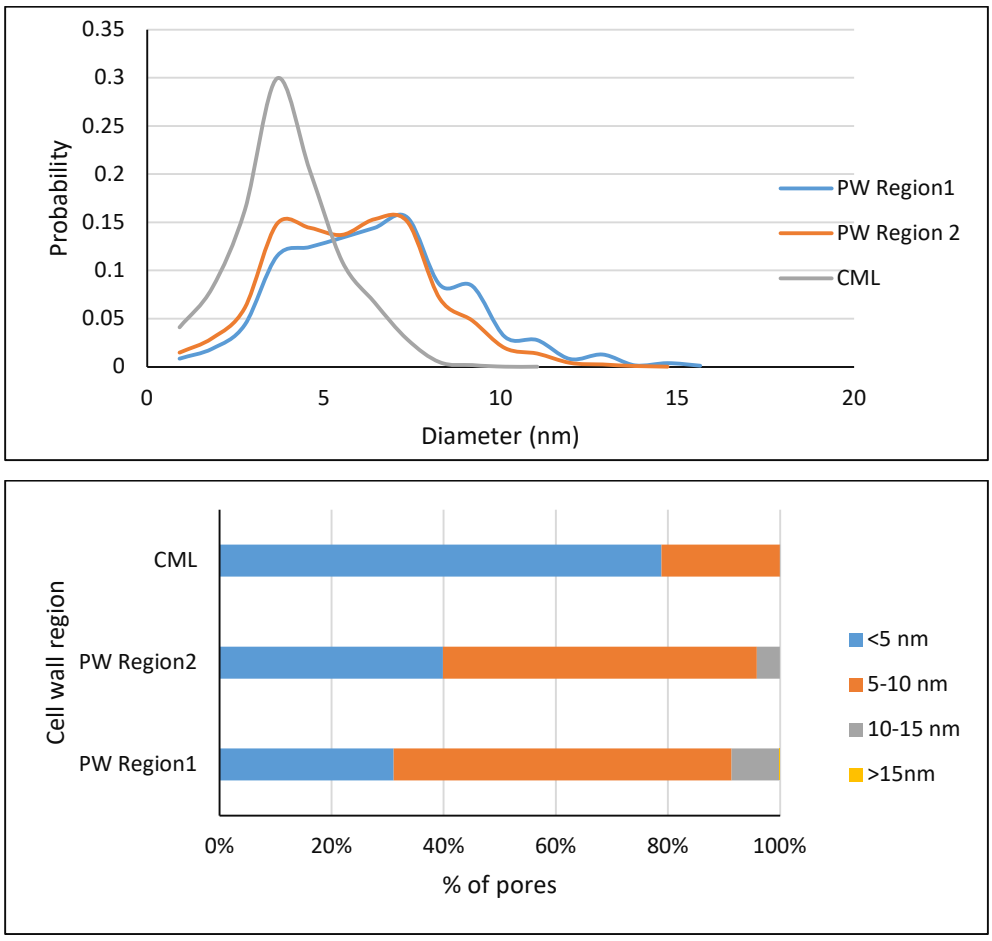

Figure 30. Comparison of 3D pore size distribution in different regions of primary wall and middle lamella in untreated Arabidopsis prepped by high pressure freezing

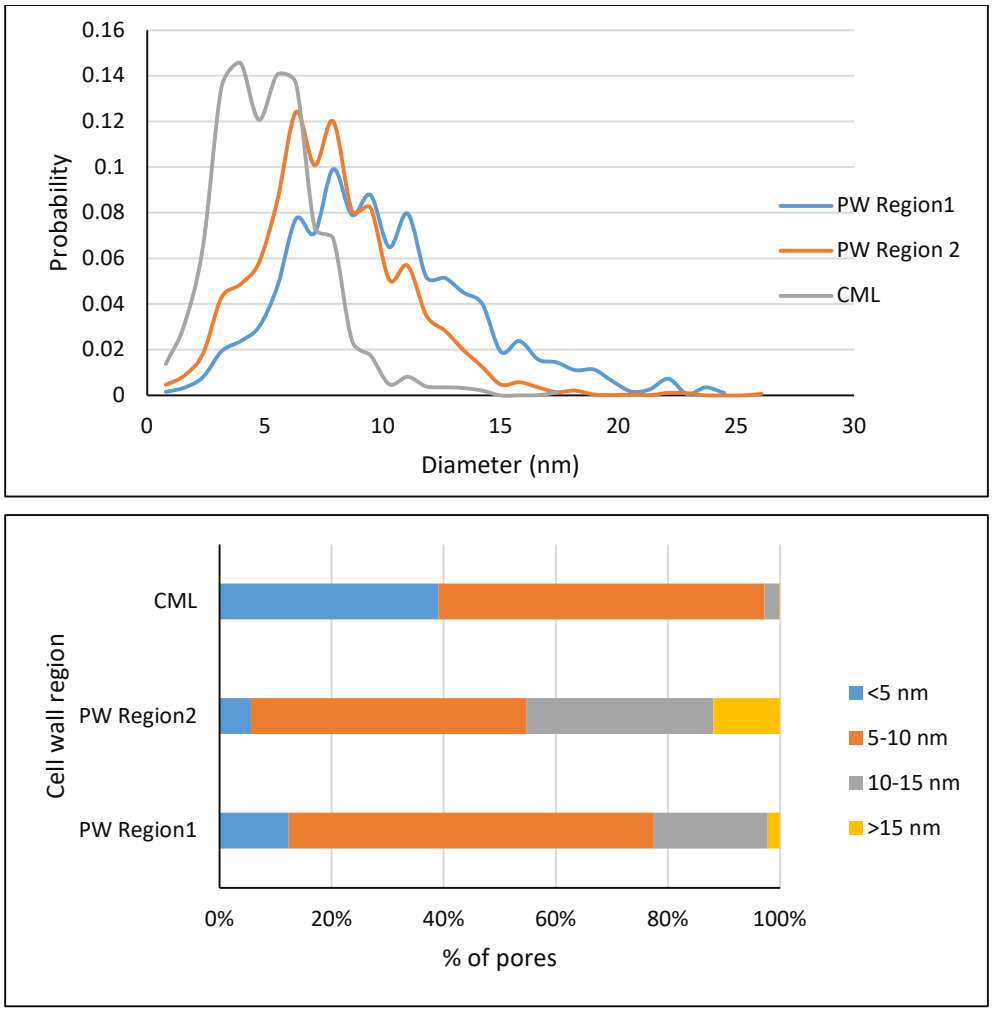

Figure 31. Comparison of 3D pore size distribution in different regions of the primary wall and middle lamella in Arabidopsis cell wall treated with ammonium oxalate

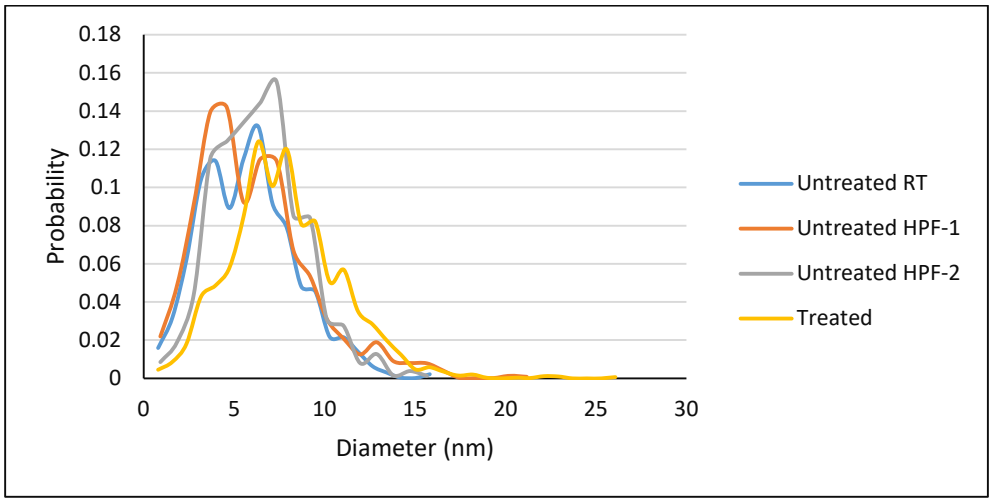

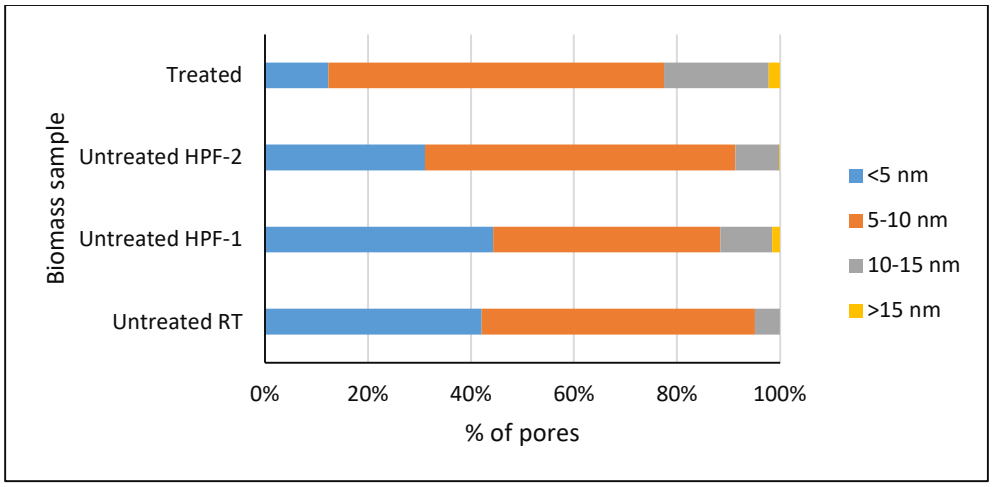

Figure 32. Comparison of 3D pore size distribution of primary wall in treated (ammonium oxalate) and untreated Arabidopsis

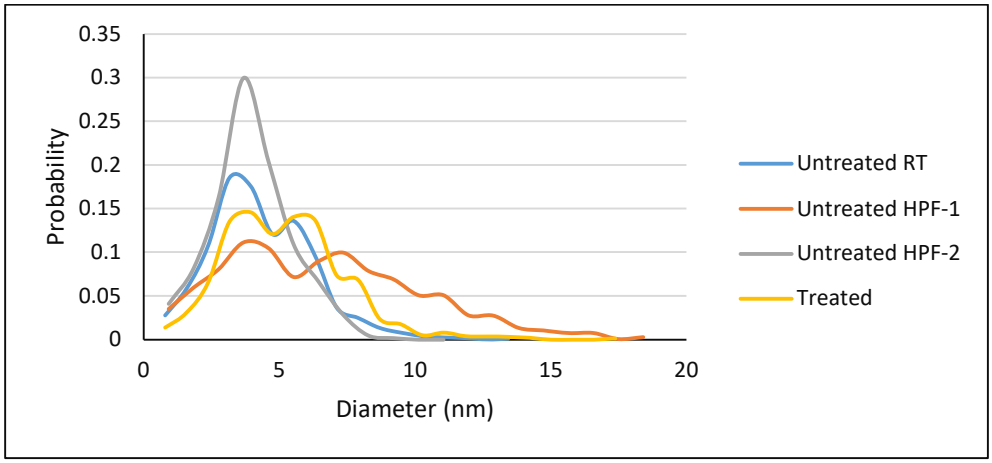

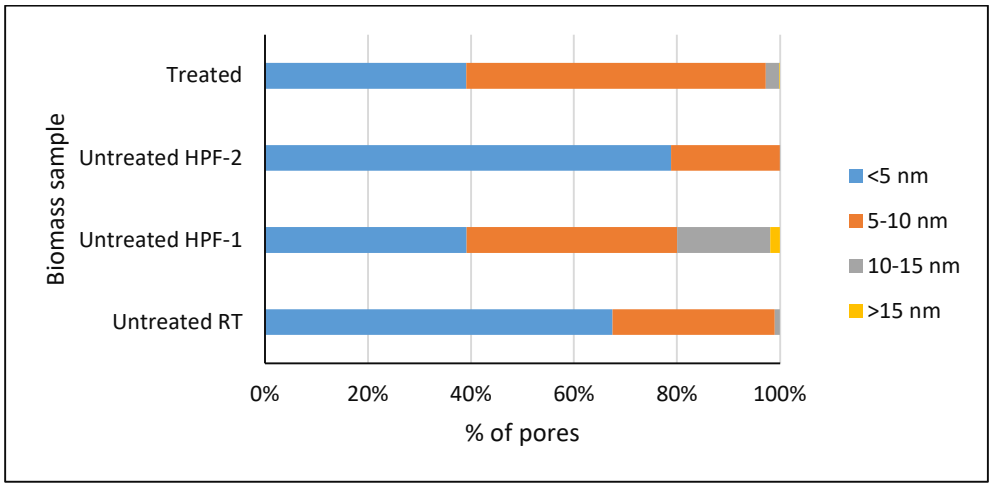

Figure 33. Comparison of 3D pore size distribution in the middle lamella of treated (ammonium oxalate) and untreated Arabidopsis

5. CHARACTERIZATION OF PLANT BIOMASS FROM RAMAN SPECTROSCOPY

As noted in the previous sections, it has been reported that the topochemical composition of plant cell walls were altered during the pretreatment process (Chundawat et al., 2011; Mosier et al., 2005; Zhao et al., 2014). It is necessary to quantify these topochemical changes and correlate them to the cell wall structure to gain a complete understanding of the biomass pretreatment process. Raman spectroscopy has proven to be an effective tool to characterize the bulk and spatial compositional changes in plant biomass and, hence, has been widely used. (Gierlinger and Schwanninger, 2006; Horvath et al., 2012; Ma et al., 2014; Zhao et al., 2014). The structural changes seen by TEM-CT during pretreatment can be correlated with the topochemical changes measured by Raman spectroscopy as seen in further sections. Raman images were obtained by creating Raman spectral intensity maps which are a function of component concentration (Gierlinger and Schwanninger, 2006; Horvath et al., 2012). It must be noted that TEM-CT is a 3D technique capable of providing structural information in three dimensions while Raman spectroscopy provides chemical component information in two dimensions. Hence, a stack of 2D Raman images from various sections from a given sample can be combined to create a 3D image stack. This approach was used to create the 3D images of untreated and treated biomass cell walls and these were used for further characterization. The bulk concentration profiles, spatial distribution of cell wall components and fraction of lignin bonds that completely dissolved were determined from the 3D stack of Raman images thus created.

5.1 Acquisition of Raman Spectra and Creation of Images

The Raman spectra and images based on the Raman intensity were obtained from our collaborators, Dr. Feng Xu's group at Beijing Forestry University and Dr. Ramarao's group from SUNY-ESF. The procedure followed for sample preparation and Raman spectroscopy were as cited in Ma et al (Ma et al., 2014). Biomass samples of different species, namely Aspen, Acer (Sugar Maple) and Poplar, were subjected to different pretreatments including hot water and alkali pretreatments for specific periods of time. All

the untreated and treated samples were cooled and thoroughly washed with deionized water (Ji et al., 2014). They were then cut transversely on a sliding microtome into 5 μm-thick sections and placed on glass slides with a coverslip of 0.17mm for Raman spectroscopy (Ma et al., 2014; Zhou et al., 2014). The Confocal Raman Microscope (CRM) used a laser excitation wavelength of 532nm, and an exposure time of 1s. The step size for collection of Raman spectra was 0.6 μm. Data was processed using LabSpec5 software which was paired with a microscope. Spectral intensity from the wavenumbers between 1550 and 1650 cm^{-1} correspond to lignin while the wavenumbers between 2850 and 2950 cm^{-1} correspond to polysaccharides (Gierlinger and Schwanninger, 2006; Ji et al., 2014). The wavenumbers chosen for lignin determination represent the aryl ring symmetric stretching, C=C stretching of the coniferyl alcohol and C=O stretching of the coniferyl aldehyde groups; together they include a majority of the lignin content (Gierlinger and Schwanninger, 2006; Ji et al., 2014). The Raman intensity is a function of the relative concentration of the cell wall components. Using the Raman data intensity in this range, an intensity map of lignin and carbohydrates in the cell wall was created and this corresponds to the topochemical distribution of cell wall components.

5.2 Topochemical Distribution of Plant Cell Walls

The topochemical distribution in the cell walls were obtained for both untreated and treated biomass samples based on the distribution of cell wall components in different regions. The color intensity corresponds to the relative concentration of the cell wall components. Both lignin and polysaccharide distribution were obtained in separate images by integrating over the corresponding ranges of wavenumbers. Figures 34 through 37 correspond to Raman images showing topochemical composition of Aspen, Poplar and Acer plant cell walls subjected to alkali and hot water pretreatment methods taken at different time intervals.

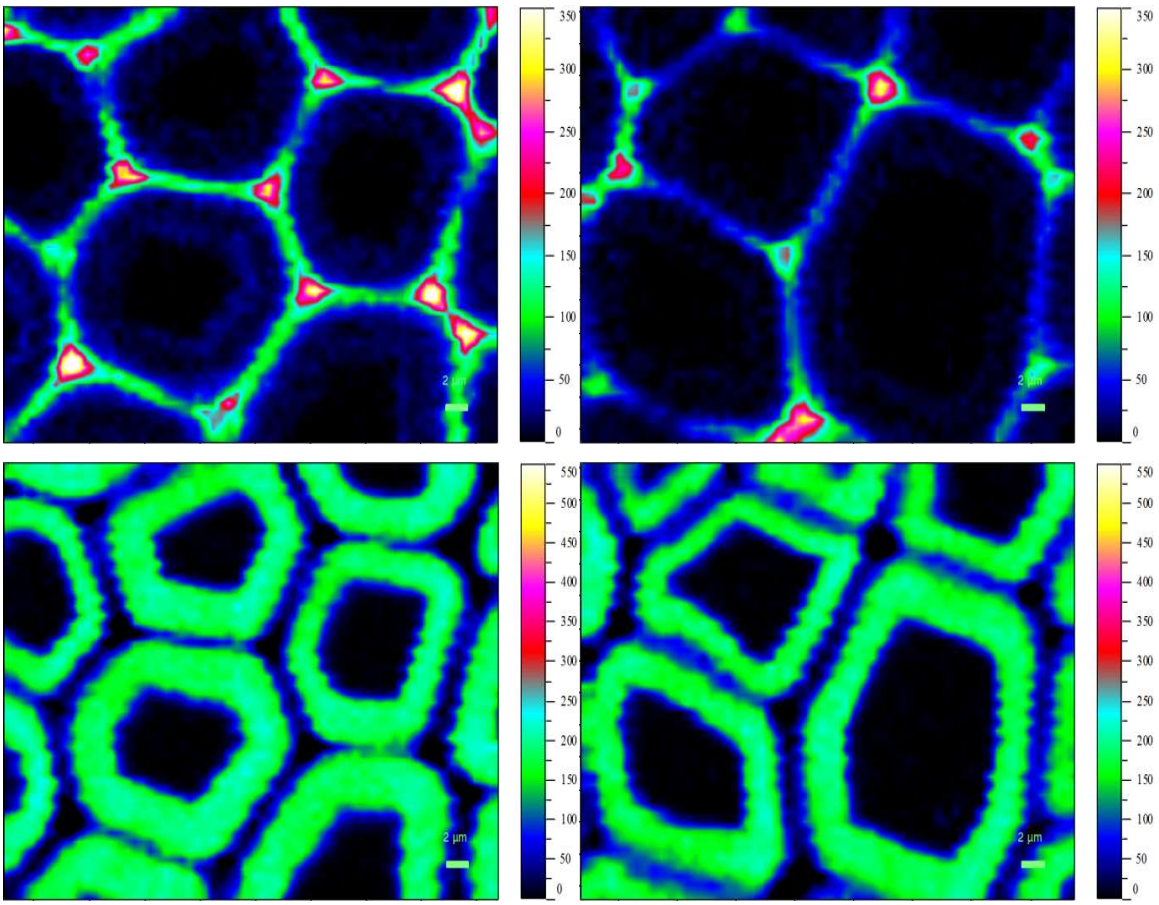

Figure 34. Raman images showing lignin distribution for untreated (top left), and alkali pretreated (top right) aspen and polysaccharide distribution for untreated (bottom left) and alkali pretreated (bottom right) aspen (Beijing Forestry University, China)

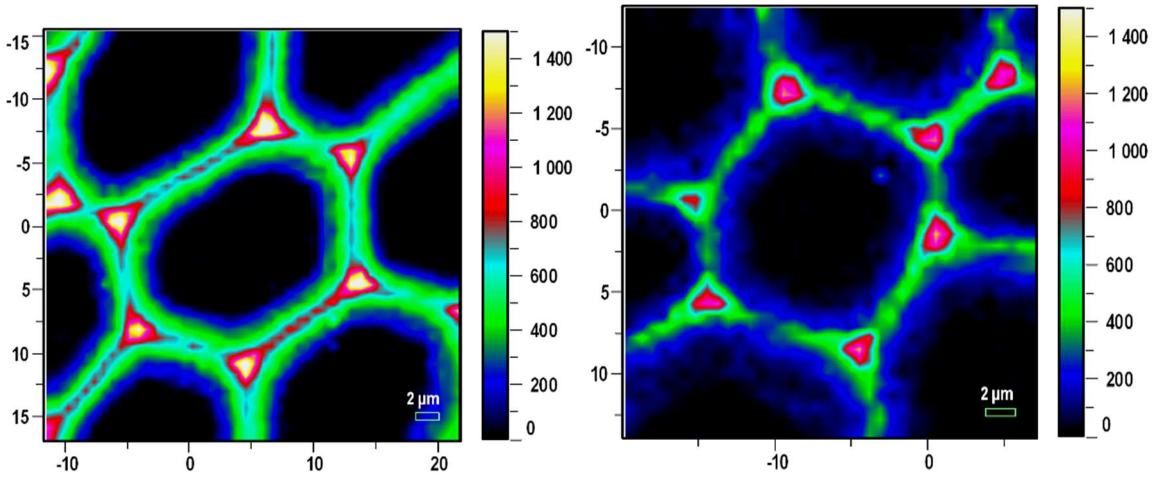

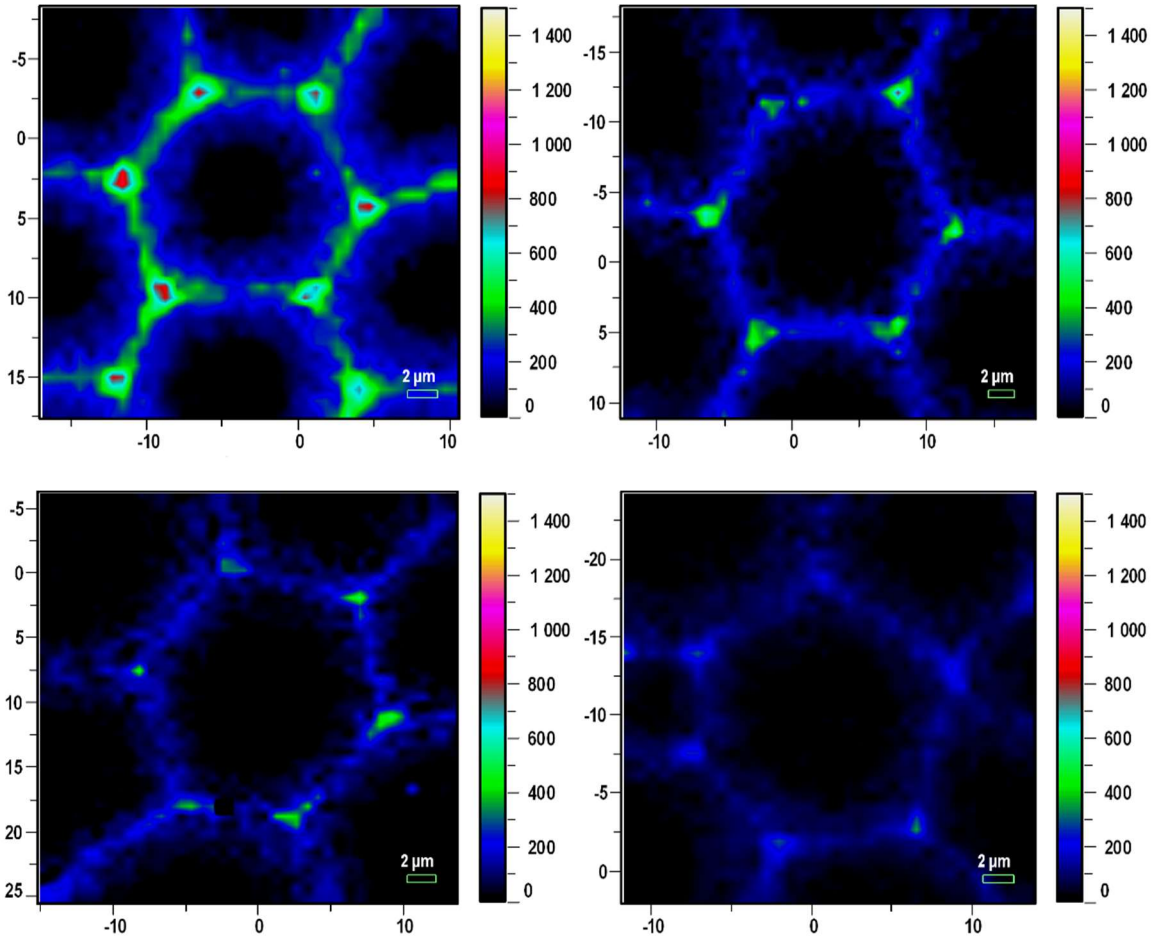

Figure 35. Raman images showing lignin distribution of alkali pretreated Poplar at 0 (top left), 10 (top right), 30 (middle left), 60 (middle right), 90 (top left) and 180 min (bottom right) during the pretreatment process

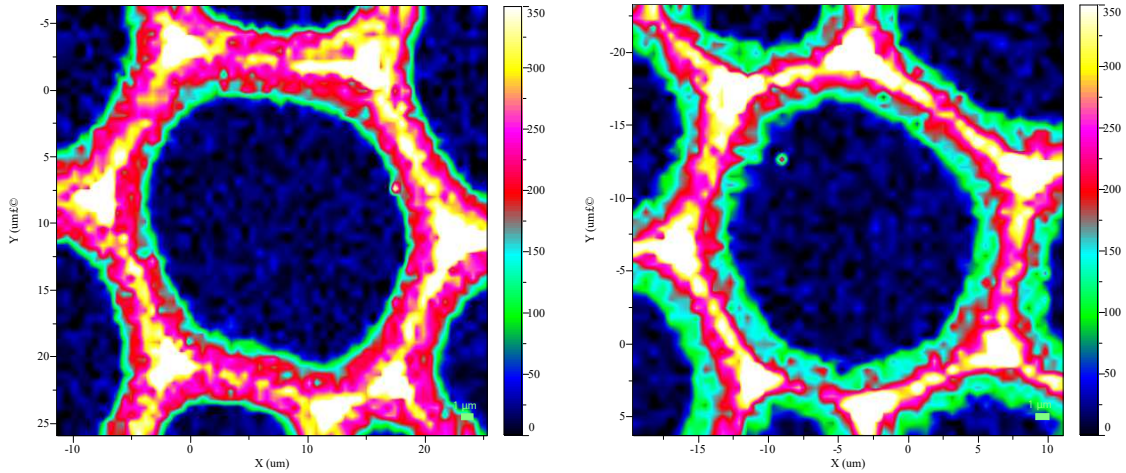

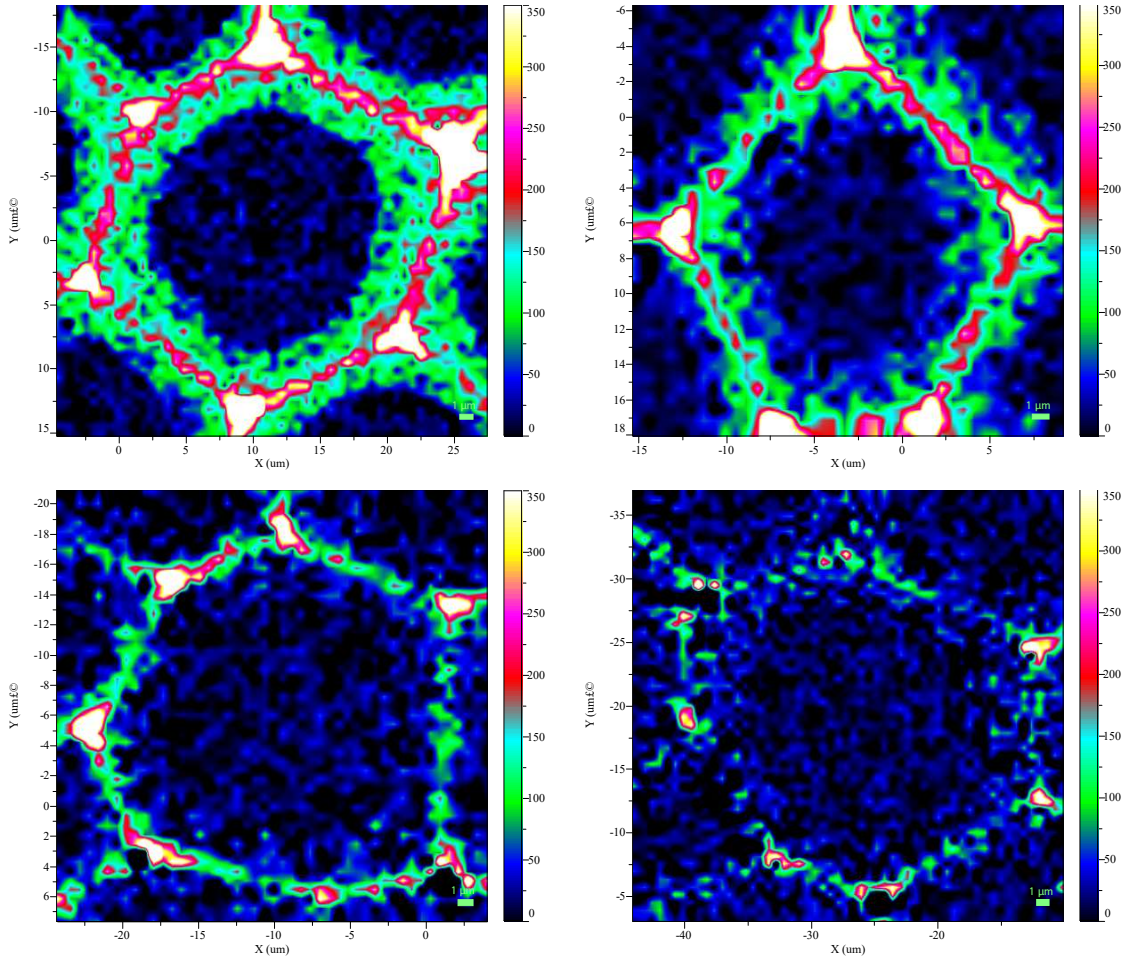

Figure 36. Raman images showing lignin distribution of hot water pretreated Acer (Sugar Maple) at 0 (top left), 5 (top right), 10 (middle left), 20 (middle right), 30 (bottom left) and 40 min (bottom right) during the pretreatment process

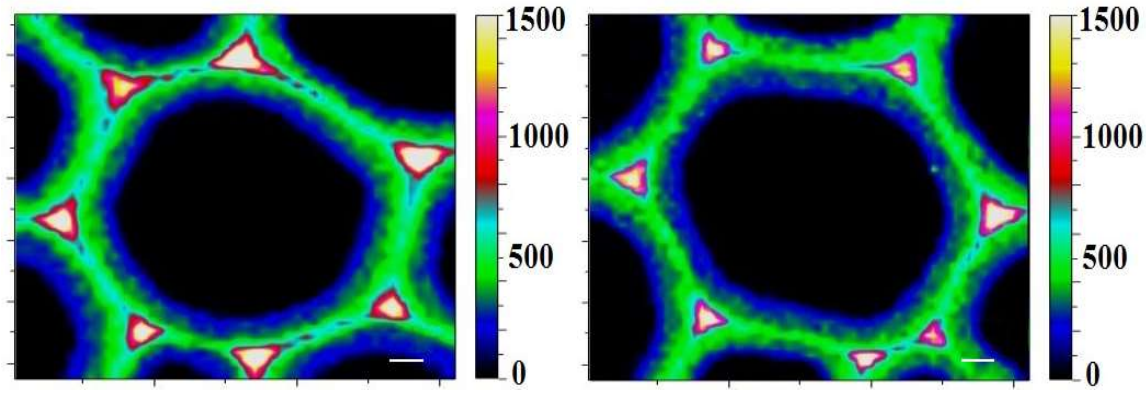

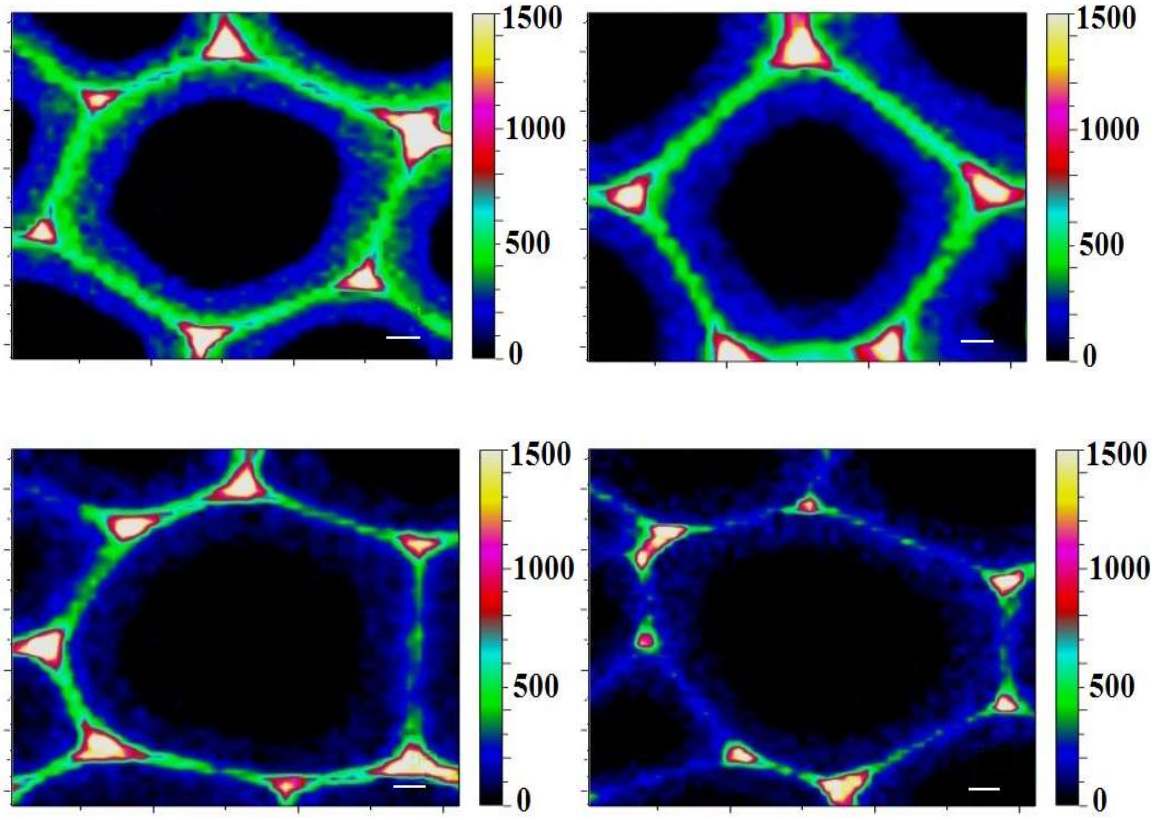

Figure 37. Raman images showing lignin distribution of hot water pretreated Poplar at 0 (top left), 5 (top right), 10 (middle left), 20 (middle right), 30 (bottom left) and 40 min (bottom right) during the pretreatment process

As seen from the above images, the changes in color intensity revealed that the relative composition of the cell wall components in different regions changed over the course of pretreatment. It must be noted that even though some of the images showed almost complete dissolution of one of the components, since there are other cell wall components still present, it does not necessarily mean that cell wall at that location is completely dissolved, and an additional pore space has been created. The dissolution started at the cell wall layers closer to the lumen, which then exposed the inner layers of cell wall to the reagent. Depending on the type of pretreatment, different regions of the cell wall reacted at different rates and the distribution of cell wall components changed as seen in Figure 34 through Figure 37 (Ji et al., 2014; Ma et al., 2014). Two sets of Raman images from the above set of experiments - alkali treated Poplar and hot water treated Acer - were chosen for further analysis (Figures 35 and 36). Raman intensity maps that correspond to

different times during the course of pretreatment were studied in particular for the current work. The relative changes in bulk concentration of lignin during pretreatment were obtained from the intensities of the Raman images and was used for further modelling. In order to ensure the validity of the lignin concentration profiles obtained from Raman spectroscopy, it may be necessary to compare them and corroborate them with conventional wet chemical analysis techniques. There are some inherent differences between Raman spectroscopy and wet chemical analysis techniques. Firstly, Raman spectroscopy provides the topochemical composition at a micron scale while wet analysis techniques provide bulk composition. Secondly, in this work, Raman spectroscopy was done using thin sections of the biomass sample of the order of 6 μm while wet techniques use powders (Li et al., 2016). Hence, the two results need to be correlated in order to analyze the overall lignin dissolution and removal. A linear correlation between the lignin content and Raman intensity as per Beer-Lambert's law has been reported in the literature using Poplar biomass species subjected to sodium chlorite and acetic acid treatment (Zhang, 2021). Assuming that such a linear correlation exists for the Raman images considered in the current work, the bulk lignin concentration profile and dissolution could be extrapolated from the Raman intensity ratios. However, it is important to note here that the validity of the Raman intensity to lignin concentration relationship needs to be verified using varying biomass species and pretreatment process conditions. In the current work, in addition to using Raman images for topochemical data, using the above correlation, they were also used to determine the fraction of lignin bonds that completely dissolved during the course of pretreatment. In the transport and reaction model developed and described in the subsequent sections the topochemical distribution of lignocellulose components in untreated biomass were used as initial conditions to predict the changes in topochemical distribution as the pretreatment process progressed.

As seen from the above time series topochemical images, the relative changes in cell wall spatial composition are evident. A preferential delignification was observed during pretreatment. For the untreated samples, the highest lignin concentrations were seen in the middle lamella and cell corners and the lowest lignin concentrations were seen in the secondary wall (Ji et al., 2014). Upon pretreatment, lignin was first removed from the

secondary cell walls and subsequently from the middle lamella and cell corners (Ji et al., 2014; Ma et al., 2014). This was observed during both alkali pretreatment and hot water pretreatment methods. In case of alkali pretreatment, it was observed that during the initial stages, there was a preferential delignification in the secondary wall, but for the overall process, the total amount of delignification was higher in the middle lamella than in the secondary wall, as seen in Figure 38 (Ji et al., 2014). In case of hot water pretreatment, even though the amount of lignin present in the S2 layer was lower, the extent of delignification or percent dissolution in the S2 layer was higher than that of the middle lamella, while hemicellulose dissolution followed the opposite trend as seen in Figure 39 (Ma et al., 2014). The structural details from the electron tomography could be correlated with the topochemical distribution from Raman to yield a complete understanding of the physiochemical evolution. Zhang et al., have used principal component analysis and cluster analysis methods to identify Raman spectra corresponding to different cell wall regions (Zhang et al., 2015). This revealed tremendous information about how individual cell wall layers respond to pretreatment techniques. Specific peaks were chosen from baseline corrected Raman data for PCA which reduced the variation present in the huge Raman spectral data set (Zhang et al., 2015). Additionally. a cluster analysis was further performed to systematically assign different groups that correspond to different cell wall regions based on the similarities in the PCA scores (Zhang et al., 2015).

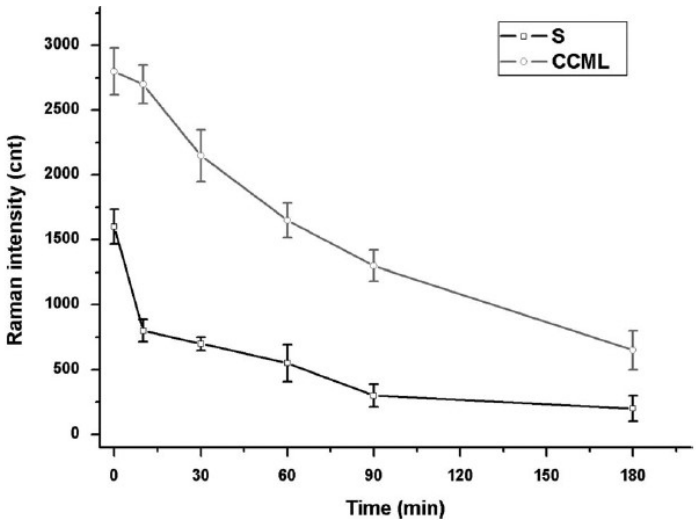

Figure 38. Variation Raman intensity of lignin bands during alkali pretreatment in different cell wall regions, which corresponds to rate of delignification (Ji et al., 2014)

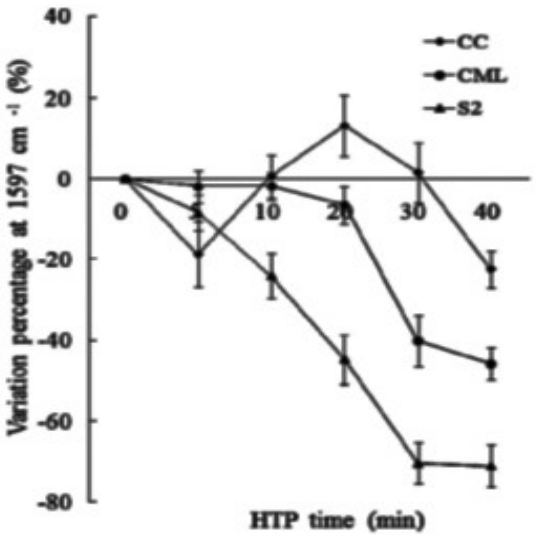

Figure 39. Variation of percentage of Raman intensity of lignin in different cell wall regions during hot water pretreatment, which corresponds to rate of delignification (Ma et al., 2014)

5.3 Structural Characterization from Raman Images

The topochemical distribution obtained from Raman images reveal important characteristics about the structural evolution and dissolution of cell wall components. Some of the methods used in the processing and analysis of TEM-CT can be applied here for this purpose. However, the TEM-CT images are already in 3D as they are acquired from a tilt series while Raman images are in 2D. Hence, a stack of 2D Raman images from various sections from a given sample can be combined to create a 3D image stack. This approach was used to create the 3D images of untreated and treated biomass cell walls and these were used for further characterization. These image stacks can then be processed and binarized similar to the TEM CT images. It is important to preserve the structural features during image processing. The threshold for binarization was chosen manually depending on the image characteristics to preserve maximum structural features and avoid misclassification of pore and fiber voxels.

It must be noted that the approaches used previously for TEM-CT images to determine structural characteristics such as porosity, specific surface area and pore size

distributions cannot be applied to Raman image stacks. This is because the Raman images indicate dissolution of only one of the cell wall components at a time while the distribution of the other cell wall components at the same time are unknown. Hence, it is not possible to determine how much of the cell wall space has degraded causing changes in the pore structure. However, the porosity algorithm can be applied to Raman images to indicate the fraction of completely dissolved or reacted lignin bonds. As seen from Tables 4 and 5 as well as Figure 40, it is evident that the fraction of lignin bonds that completely dissolved increased over time during the course of pretreatment. It was seen from Figure 40 that alkali pretreatment resulted in a greater fraction of lignin bonds that dissolved over a longer time period as compared to hot water pretreatment. Additionally, it was observed in the case of alkali pretreatment that the bulk of the lignin bonds completely dissolved in the first 60 minutes; beyond which, only a small fraction of the bonds completely dissolved or reacted. In case of hot water pretreatment, initially, the fraction of lignin that completely dissolved was small until about 20 min after which it increased. It must be noted that Figure 40 shows only a relative comparison of the lignin bonds that completely dissolved. The actual fraction of lignin bonds that completely reacted have to be obtained from other analytical techniques. Thus, even though detailed porosity and pore size measurements cannot be made with Raman images, unlike the TEM-CT images, it still provides valuable information about the topochemistry of the cell walls. They can always be correlated with data from TEM-CT, HPLC and other analytical techniques to provide a deeper insight into the fundamental structure property relationships of plant cell walls.

Time (min)	Fraction of lignin completely dissolved
0	0
10	0.416
30	0.495
60	0.870
90	0.929
180	0.992

Table 4. Fraction of lignin bonds completely degraded in Poplar due to alkali pretreatment

Time (min)	Fraction of lignin completely dissolved
0	0
20	0.336
30	0.675
40	0.877

Table 5. Fraction of lignin bonds completely degraded in Acer due to hot water pretreatment

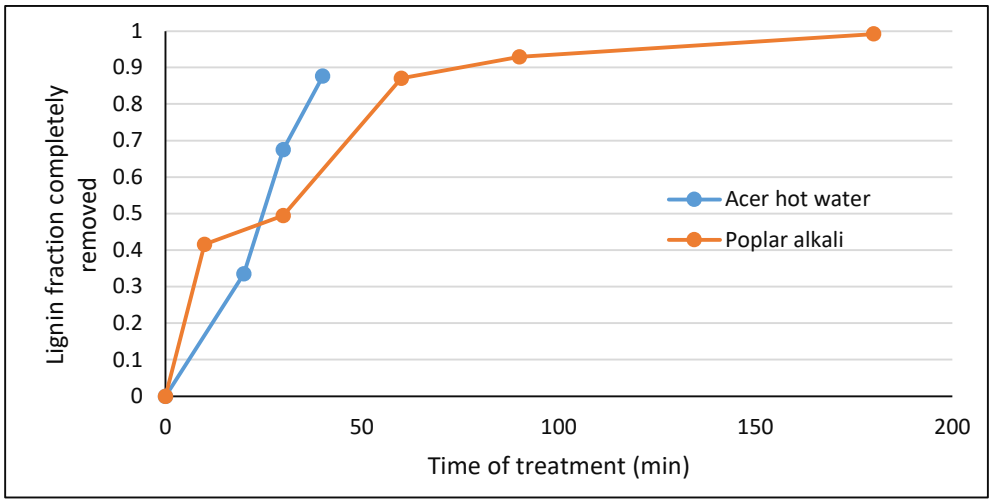

Figure 40. Fraction of lignin bonds completely degraded in plant cell wall samples during different types of pretreatment

6. TRANSPORT-REACTION MODEL FOR BIOMASS PRETREATMENT

The ultimate goal of this study was to understand the transport and reactive behavior of plant cell wall components simultaneously. This is extremely vital in determining the method and conditions of pretreatment and understand how the structure and property of the cell walls changed after reaction. Biomass pretreatment and conversion processes normally use a chemical or biochemical reactive agent, most often in aqueous media (Mosier et al., 2005). The reagents can be just water at higher temperatures, acid, alkali, enzymes or other chemical and biological agents (Chundawat et al., 2011; Esteghlalian et al., 1997; Keshwani and Cheng, 2010; Mosier et al., 2005). Biomass was first reduced to smaller chips or finer particles and then covered in the reacting medium. Different ratios of biomass and reacting medium, also known as solid-liquid ratios were used depending on the treatment and process conditions (Montané et al., 1998). Once the biomass was soaked in the reacting medium, the diffusion of the chemical reagent molecules, also referred to as tracers or walkers here, take place in the pore spaces which include the intercellular regions (i.e., lumen) and pore spaces in the interior of the cell wall. The diffusion process can be described by the molecules following a random path within the open areas of the biomass (Kansal and Torquato, 2002; Riley et al., 1995a; Siegel and Langert, 1986). It is plausible that when the cell walls are soaked in reactive media especially at higher temperature, the cell walls themselves can be conductive and allow the diffusive transport of the tracers (Donohoe et al., 2009b). The studies of Wang et al, showed that the rate of capture of ligands by a stationary species depends on the surface diffusion coefficients (Wang et al., 1992). It is necessary then to consider the simultaneous diffusive transport of the tracers both through the pore spaces as well as the solid cell wall regions of the biomass to fully describe the transport processes. During the simultaneous transport, appropriate considerations have to be incorporated for the differences in diffusivities and the corresponding random nature of the movement of the molecules and step lengths in the pores and cell wall regions of the biomass.

The underlying diffusion-reaction mechanisms that influence the pretreatment of biomass samples is similar to a porous catalyst pellet system through which reactant

molecules diffuse and react simultaneously. Such systems have been widely studied and modelled using analytical or numerical methods in several previous works (Bidabehere and Sedran, 2001; Kočí et al., 2010; Pereira et al., 2014; Reyes and Iglesia, 1991; Szukiewicz, 2000). The reactant undergoing diffusion through the catalyst pellet follows a tortuous path due to the presence of internal voids (Bird et al., 2007). The morphology of the catalyst pellet influences the rate at which the molecules traverse through the structure (Zalc et al., 2004). The local diffusivity values vary depending on the phase through which the reactant species is traversing (Riley et al., 1995b, 1995a). However, an effective diffusivity can be determined for the system which includes the contribution from all phases of the system and has been used in previous literature for modelling diffusion-reaction processes in porous materials (Bidabehere and Sedran, 2001; Riley et al., 1995a; Zalc et al., 2003). Diffusion can occur via bulk diffusion or Knudsen diffusion mechanisms or a combination of both depending on whether the molecular movement is controlled by molecule-molecule interactions or molecule-wall interactions respectively, which is dictated by the distance between collisions (Zalc et al., 2004). Accurate measurements of the effective diffusivity values of porous materials are very difficult and hence empirical or numerical methods are used. A widely used approach to determine the effective diffusivity is by using Maxwell's equation (Maxwell, 1954). The effective diffusivity can also be determined from the displacement-time data obtained from numerical methods using Einstein's equation (Einstein, 1956). The principles of bulk or molecular diffusion are valid for microporous systems and Fick's law can be applied to explain the transport process in porous materials (Bidabehere and Sedran, 2001; Bird et al., 2007; Kansal and Torquato, 2002; Riley et al., 1995a). The transport-reaction process can either be diffusion controlled or reaction controlled depending on the Thiele modulus which represents the relative influence of both diffusion and chemical reaction (Bird et al., 2007; Thiele, 1939).

In the previous work, a hybrid random walk model based on kinetic theory and stochastic principles was developed for gaseous diffusion in porous networks considering both the pore and fiber space transport (Defrenne, 2008; Defrenne et al., 2019, 2017; Goel, 2003). This approach has been extended to study the effect of combined diffusion-reaction processes taking place during the pretreatment process in three-dimensional space inside

the plant cell wall systems. In the earlier pure diffusion model, kinetic theory was used since it was a gaseous diffusion process. However, it is not applicable to the current work as we are interested in considering liquid phase diffusion. During the pretreatment process, once the wood chips were soaked in the reagent solution, the reactant molecules or tracers began to diffuse first from the bulk liquid into the lumen and then from the lumen into the interior of the cell wall. Similarly, depending on the type of biomass species, penetration of the liquid into larger areas such as vessel elements are also possible. The bulk penetration of the liquid into the lumen can be considered as a pressure driven flow and is accomplished relatively easily. As this is a case of simultaneous pore-fiber diffusion and reaction, there is a need to consider if the reagent molecules react or continue the diffusion path when they encounter a pore-cell wall interface in the biomass structure based on the reaction probability and diffusivity of the cell wall. The diffusion-reaction process was carried out for the intended residence time. The concentration changes in every voxel of the system and the path of the tracers were tracked throughout the process. Using the above approach, both the spatial and bulk concentration profiles of the cell wall components and tracers as well as the potential structural changes in the cell wall during the pretreatment process were determined. A transport coefficient K_T was computed based on the survival time of the tracers was reported, as was done in some of the earlier literature (Zheng and Chiew, 1989). An effective rate constant K_{eff} was also determined for the biomass dissolution process that is based on both simultaneous diffusion and reaction similar to some of the earlier work (Keshwani and Cheng, 2010; Montané et al., 1994). By comparing the results from the simulation with the experimental data, an appropriate effective rate constant K_{eff} for a given biomass species and pretreatment condition were determined. The effect of varying diffusion and reaction parameters on the overall pretreatment process was then analyzed. This provided additional insights and helped in developing a better understanding of the conditions required for efficient biomass conversion. As reported earlier, Raman intensity maps of cell wall components, specifically lignin, obtained from Dr. Feng Xu's group and Dr. Ramarao's group were used as initial conditions for the transport reaction simulations (Ji et al., 2014; Ma et al., 2014). Details of the model are described in the following sections.

6.1 Development of the Transport-Reaction Model

A transport-reaction model was developed in order to better understand and predict the kinetic and transport behavior of the biomass system during the pretreatment process. This model involved a stochastic dynamic approach that kept track of the change in spatial concentration of lignin and any potential changes in the biomass structure simultaneously. The Raman spectral intensity data was correlated to the relative concentration of the cell wall components and was used to provide the initial structure and spatial concentration profile. During the pretreatment, one or more of the cell wall components degraded upon reacting with the tracers and this change in concentration was determined as a function of position and time. The biomass sample was considered similar to a catalyst pellet system. The structure was made up of several smaller units known as representative elemental volumes (REVs) that truly represent the structure of the system. In the current scenario, the REV was considered as the biomass volume represented by a single fiber cell with its associated lumen, cell corners and adjacent biomass cells in all three dimensions. The whole biomass sample can be considered as repeating units of such REVs throughout the volume. For modeling purposes, the smallest unit was considered as the three-dimensional cubic voxel that is specified by its x, y, and z coordinates within the sample volume. The concentrations and structural characteristics within a given voxel were assumed to be uniform while the characteristics of each voxel can vary throughout the biomass sample. The changes in lignocellulose compositions for every spatial voxel were tracked during pretreatment to provide the spatial distribution and the topochemical evolution. Similarly, the concentrations of individual voxels can be summed up over the entire volume of the image to determine the bulk concentration of the lignocellulose component at any given time over the course of pretreatment. The topological distribution of structural characteristics as a function of biomass pretreatment can also be determined. The Raman image stack used was initially binarized and hence each voxel either corresponded to the pore or cell wall phase within the biomass. As revealed from Raman intensity maps, and discussed earlier, the chemical composition was different for different regions of the cell wall (i.e., primary wall, secondary wall, middle lamella, cell corner). As noted previously, every voxel in the cell wall was assigned a certain initial concentration of lignin, cellulose

and hemicellulose based on the Raman intensity which changed over time as reaction proceeds.

Biomass is a two-phase system consisting of pore or void spaces and cell wall fibers that are composed of the major cell wall components, namely, cellulose, hemicellulose, and lignin. The biomass particles were soaked in the reacting medium which contains the reagent used for pretreatment, which could be an acid, alkali, hot water, or any other chemical reagent based on the type of pretreatment. The reagent molecules are referred to here as tracers. The current model as described cannot be used to model biological methods such as enzymatic pretreatments as the kinetics involved for such a process is significantly different from pure chemical reactions and substrate-enzyme and other interactions need to be considered. Specifically, modeling and characterizing lignin dissolution during biomass pretreatment was the primary objective in the current work. However, a similar approach could be extended to other biomass components, namely, cellulose and hemicellulose dissolution considering their respective local reaction kinetics. At the start of the reaction, a large number of particles of the tracer or pretreatment reagent such as acid, hot water, alkali etc., which is representative of its concentration were present in the system. The tracers diffused and penetrated through the wood chips in due time. The transport process alone was an unsteady state diffusion process in three dimensions and described by Fick's second law for each dimension as,

$$\frac{\partial C}{\partial t} = \frac{\partial}{\partial x}\left(D\frac{\partial C}{\partial x}\right) \tag{7}$$

where C (x, t) is the concentration of the reactant (kg moles/m^3), t is the time (s), and D is the diffusivity (m^2/s). The analytical solution to the above diffusion for a given boundary and initial conditions could be given by an exponential concentration profile as follows:

$$C(x,t) = \frac{n}{\sqrt{4\pi Dt}} exp\left(\frac{-x^2}{4Dt}\right) \tag{8}$$

The analytical solution described in equation (8) is valid for a simple homogenous system. In the case of biomass samples, the system is quite complex and heterogenous and arriving at the analytical solution is a tedious process. However, there have been several

previous attempts to model transport phenomena analytically in such complex porous systems (Kočí et al., 2010; Siyakatshana et al., 2005; Tomadakis and Rupani, 2007). Considering the complexities involved in using analytical methods, several numerical or stochastic methods have also been used to describe transport and reaction phenomena in heterogenous porous systems (Kansal and Torquato, 2002; Liu and Mostaghimi, 2018; Riley et al., 1995b; Siyakatshana et al., 2005). Kansal et. al, and Torquato et. al modeled the transport and reaction in a heterogeneous medium containing catalyst pellets using a stochastic dynamic approach (Kansal and Torquato, 2002; Torquato, 1991). In their system, surface reaction and absorption at the catalyst surface as the walkers diffused through the medium was modeled and the corresponding mass balance equation at the interface was given by,

$$\boldsymbol{D\frac{\partial C}{\partial n} + KC = 0} \tag{9}$$

where K is the surface reaction/absorption rate constant (m/s), n is the unit outward normal from the pore space and C is the concentration of the diffusing/reacting species (Kansal and Torquato, 2002; Torquato, 1991). The above equation assumes equilibrium at the interface and hence the net diffusion flux of the reagent is equal to the rate of reaction at the interface. Here, diffusion inside the catalyst pellet is not considered. If K has a value of 0, the system is a perfect reflector and when K has a value of ∞, the system is a perfect absorber. For all other values of K, both absorption and reflection at the surface occur depending on the relative values of K and D. In our case in addition to potential surface reaction, the transport and reaction internal to the biomass cell wall need to be considered as well.

In the previous work of Goel, Defrenne and Zhandkin, the principles of a hybrid random walk and kinetic theory of gases was used to model the simultaneous diffusion through the pores and fibers in paper samples (Defrenne, 2008; Defrenne et al., 2019; Goel, 2003). In the current model, in addition to the simultaneous diffusion through the pore and cell wall phases, an additional reaction component has to be considered at the cell wall interface and in the interior of the cell wall. The random movement of the tracers as they diffuse and react through the pore or cell wall phases of the biomass system were

considered. Similar to the earlier work, the step length of the random walkers, λ (m), was chosen randomly by pooling from an exponential distribution whose mean is equal to the mean step length $\bar{\lambda}$ of the tracer molecules and is given by, (Defrenne, 2008; Defrenne et al., 2019):

$$\boldsymbol{f(\lambda) = \frac{1}{\bar{\lambda}} exp(\frac{-\lambda}{\bar{\lambda}})} \quad (10)$$

where λ is chosen from the following logarithmic distribution.

$$\boldsymbol{\lambda = -\bar{\lambda}\, ln(\xi)} \quad (11)$$

ξ is chosen from the uniform distribution $U_{(0,1)}$ (Defrenne, 2008). In the current model, $\bar{\lambda}$ was chosen to be of the order of the voxel dimensions.

The ensemble average of the mean square displacement of the tracers during random walk in 1D scales linearly with time according to Einstein's equation, as,

$$\boldsymbol{\langle x^2 \rangle = \frac{\int_{-\infty}^{\infty} x^2 f(x,t) dx}{\int_{-\infty}^{\infty} f(x,t) dx} = 2Dt} \quad (12)$$

where x is the displacement, t is the time and D is the diffusion coefficient of the medium (Einstein, 1956). Unlike the previous case, where the diffusion coefficient was computed using kinetic theory of gases, appropriate values of diffusivity that are closer to liquid diffusion were used. The above-mentioned Einstein's equation when extended to three dimensions gives,

$$\boldsymbol{\langle R^2 \rangle = 6 D_{eff} t} \quad (13)$$

In this case, D_{eff} refers to the effective diffusivity of the medium, as the medium comprises of both pore and cell wall phases. The slope from a plot of the ensemble average of the mean square displacement $\langle R^2 \rangle$ in three dimensions versus time t, was used to calculate the effective diffusivity (D_{eff}). In the case of a pure diffusion process, this slope is constant giving a constant value of effective diffusivity for the process as long as a sufficient number of tracers were used for the simulation (Defrenne, 2008). But in the case of a diffusion reaction process, this slope is not constant throughout, as the tracers ceased to exist after reaction and the total number of tracers available for diffusion or reaction decreases with time as seen in the later sections. Hence, a separate simulation was run for pure liquid diffusion without reaction for the same system under consideration to determine the

effective diffusivity of the medium. However, during the transport-reaction simulations, local values of diffusivity in the pore and cell walls respectively were used for most computations as seen later in this section.

The above model when used for simulating a true random walk following every step of each tracer took a fairly large amount of time for computation. In order to cut down on computation time and make the model more effective, the first passage time (FPT) principle was used, as in the previous work, to track the path of the particle in the pore phase when it is far away from the interface (Defrenne, 2008; Siegel and Langert, 1986). When the tracer in the pore phase was at a distance greater than five times the mean step length $5\bar{\lambda}$ (as described in equation 10) from the fiber/cell wall interface, the method of first passage time was employed (Defrenne et al., 2019; Siegel and Langert, 1986). According to this method, when the tracer was away from the interface, a much bigger step size was chosen which is equivalent to the size of several smaller steps. Similar to the sphere growing method, a map of the largest sphere that can be fit at a certain voxel was calculated and the FPT step size is the radius of the largest sphere at that spatial location (Defrenne 2008). The average time during the FPT is given by,

$$\boldsymbol{t = \frac{R^2}{D_O}} \tag{14}$$

Where R is the step length and D_O is the diffusivity of the pore space. It must be noted that the first passage time method was applicable only in the case of pure diffusion when the tracers are present in the pore phase. It was not extended to the cell wall where both diffusion and reaction occur simultaneously. A true random walk following the individual steps of each tracer molecule was used for the movement of tracers within the cell wall. Figure 41 shows a schematic of the diffusion process in the cell lumen/pore space where the tracer position was determined by either first passage time or true random walk depending on its vicinity to the cell wall interface.

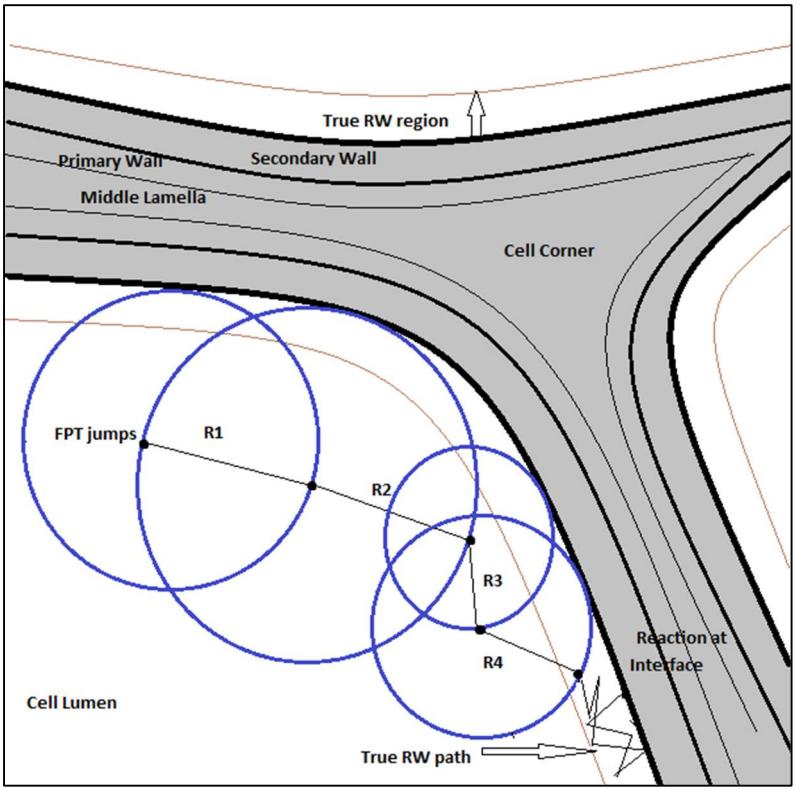

Figure 41. Schematic of the diffusion-reaction process during pretreatment of plant biomass

After navigating the pore space via a random path, when the tracers reached the pore-cell wall interface, two possibilities for its path forward were considered.

i. The tracers reacted with cell wall components at the interface and are consumed, thereby ending the random walk.
ii. The tracers diffused into the fiber space and continued their path forward. The step length for such a molecule was altered depending on the ratio of diffusivity between the pore and fiber spaces.

From the previous work of Torquato and others, it has been found that when the tracers reached the interface, they reacted with the components of the cell wall using a reaction probability which depends on both the diffusion and reaction characteristics of the system (Kansal and Torquato, 2002; Riley et al., 1995b; Siyakatshana et al., 2005). Quantitatively, the reaction probability, P_K, is dependent on the Thiele modulus of the system. In a diffusion-reaction system, Thiele modulus, ϕ, as given in equation 15 is the ratio of the reaction behavior to diffusion behavior of the system. It has been reported in earlier work

that the dissolution of lignin in biomass is a pseudo first order reaction dependent on lignin concentration (Keshwani and Cheng, 2010; Kim and Holtzapple, 2006; Montané et al., 1994; Sierra-Ramírez et al., 2011). Assuming the reagent tracers are present in abundance, the reaction kinetics can be defined by a pseudo first order reaction where the rate of reaction is solely dependent on the lignin concentration. For such a pseudo first order reaction, the Thiele modulus is defined as,

$$\boldsymbol{\phi} = \sqrt{\boldsymbol{k'_L R^2}/\boldsymbol{D}} \tag{15}$$

where k'_L is the local reaction rate constant (s^{-1}) and R (m) is the characteristic length that is representative of the structure. In the case of our biomass system using 3D images, the voxel size was used as the appropriate characteristic length. Assuming equimolar pseudo first order reaction between the diffusing reagent and lignocellulose component (i.e., lignin), the rate of change in lignin concentration in a given elemental voxel can be given by,

$$\boldsymbol{r} = -\boldsymbol{dC}/\boldsymbol{dt} = -\boldsymbol{dC_L}/\boldsymbol{dt} = -\boldsymbol{k'_L C_L} \tag{16}$$

where C_L is the concentration of the lignin in that voxel at time t and k'_L is the local rate constant. Assuming that there is no accumulation of the diffusing tracers within the elemental volume, the steady state diffusion reaction equation for an elemental volume in 1D is given by,

$$\boldsymbol{D}\frac{\boldsymbol{\partial^2 C}}{\boldsymbol{\partial x^2}} + \boldsymbol{r} = \boldsymbol{0} \tag{17}$$

The above equation can easily be expressed in a dimensionless form in terms of the Thiele modulus representing the ratio of reaction to diffusion rate as described in equation 15. Using a stochastic dynamic approach and running random walk simulations in solving similar diffusion and reaction problems in systems containing catalyst particles, a reaction probability, P_K, has been used to define the probability of reaction of the diffusing walkers as follows (Kansal and Torquato, 2002; Riley et al., 1995b; Siyakatshana et al., 2005):

$$\boldsymbol{P_K} = \frac{\boldsymbol{1}}{\boldsymbol{1 + \phi^2}} \tag{18}$$

The relationship between reaction probability, diffusivity and reactivity is given by equation 18. At any instance, as the tracers diffused and approached a voxel in the cell wall, the reaction probability will decide the path of tracer going forward. The diffusivity and reactivity of the cell wall where lignocellulose reactions take place was used to calculate P_K. Following the earlier work on simultaneous diffusion, the diffusivity of the cell wall was determined from the ratio of intrinsic diffusivities of cell wall and pores as,

$$\boldsymbol{D^* = D_F / D_O} \tag{19}$$

Where D_F (m^2/s) is the diffusivity of the cell wall, D_O (m^2/s) is the diffusivity in the pore space and D* is the ratio of diffusivities. The Thiele modulus and reaction probability in the cell wall are given by (Kansal and Torquato, 2002; Riley et al., 1995a),

$$\boldsymbol{\phi_F = \sqrt{k'_L R^2 / D_F}} \tag{20}$$

$$\boldsymbol{P_{KF} = \frac{1}{1 + \phi_F^{\,2}}} \tag{21}$$

Appropriate values of open space or pore space diffusivity were considered based on liquid phase diffusion. Each time a tracer reached a pore-cell wall interface, a random number between 0 and 1 was chosen and compared to the reaction probability. Reaction occurs only when the random number chosen was lesser than the calculated reaction probability. As noted earlier, the changes in lignin concentration in a given elemental voxel volume when reaction occurs, assuming a pseudo first order reaction kinetics, is given by,

$$\boldsymbol{dC_L / dt = -k'_L C_L} \tag{22}$$

where C_L is the concentration of the lignin in that voxel, k'_L is the local reaction rate constant (s^{-1}) and t is the time. As diffusion and reaction takes place, a finite difference approximation can be used for equation 22 and the concentration of lignin after a specific time interval Δt, is given by,

$$\boldsymbol{C_{L,t+\Delta t} = C_{L,t} - [k'_L C_L]_t * \Delta t} \tag{23}$$

The initial concentration of lignin at time t=0 ($C_{L,t=0}$) in each voxel was known from the Raman spectral intensity data for a given untreated biomass species. The reaction time Δt was calculated from the step length of the current step as,

$$\Delta t = {\lambda^2}/{6D} \quad (24)$$

The appropriate diffusivity, D, was used for the above calculation depending on whether the tracer reached the interface by travelling through the pore or fiber spaces. If reaction occurred, then the tracer was consumed and ceased to exist.

If the random number was greater than reaction probability, P_{KF}, the tracers did not react with the cell wall components at that location and hence diffused further into the cell wall, continuing the random walk process. The new coordinates of the molecule in the cell wall/fiber phase are given by,

$$x2 = xi + \sqrt{D^*}(x1 - xi) \quad (25)$$

where x1 is coordinate where it would have landed in the absence of an interface and xi is the interface co-ordinate (Defrenne et al., 2019). The y and z coordinates were computed similarly. When the tracers were in the fiber phase, appropriate changes were made to the step length and diffusivity. The step length in the above case was shorter than it would be in the absence of an interface (Defrenne, 2008). A similar approach was adopted in the works of Riley et. al while modelling diffusion-reaction processes in immobilized cell systems (Riley et al., 1995a, 1995b). The step length in the fiber phase is given by,

$$\lambda_F = \lambda D^* \quad (26)$$

The above-mentioned routine was repeated for each step of the tracer in the fiber phase after deciding on reaction or diffusion. If there was no reaction, then diffusion process is continued, and the tracer proceeds on its path forward in the fiber phase. In the case the tracer proceeded through the entire dimension of the cell wall and approached the fiber-pore interface at the other end, then, similar to the earlier case, there are again two possibilities for its path forward. The tracer could again react with the cell wall components with the same reaction probability as mentioned above or diffuse into the pore phase. Similar to the case where the tracer reached the fiber interface from traversing from the pore space, a random number was chosen between 0 and 1 and is compared to P_{KF} to decide the possibility of reaction. In the event a reaction does not occur, the tracer enters the pore, and the step length was modified accordingly considering the differences in diffusivity between the two phases. The new coordinate is given by,

$$x2 = xi + {1}/{\sqrt{D*}}(x1 - xi) \quad (27)$$

where x1 is co-ordinate where it would have landed in the absence of an interface and xi is the interface co-ordinate (Defrenne et al., 2019). The y and z coordinates were computed similarly. The simulation was carried out for a certain reaction time as specified by the experimental conditions.

The changes in concentration of lignin in each voxel due to pretreatment were recorded throughout the course of the diffusion-reaction process. Using this information, both the spatial concentration and bulk concentration changes were tracked during the course of the reaction and the results at a given reaction time was compared to the experimental concentration profiles obtained from the Raman images. Based on the bulk concentration versus time results, the bulk dissolution rate of lignin for a specific pretreatment method and species of biomass was determined. Then assuming a pseudo-first order kinetics for the overall dissolution rate of biomass components as described in equation 22, an effective rate constant, K_{eff} (s^{-1}), for the biomass pretreatment was determined from the slope of the reaction rate versus concentration data,

$$K_{eff} = -\frac{dC_L/dt}{C_L} \quad (28)$$

As per equation 28, the effective rate constant K_{eff} is function of bulk lignin concentration C_L at that time t. However, as discussed later in the results and reported in the literature, the effective rate constant may be a constant or a function of time (Chiang et al., 1990; Keshwani and Cheng, 2010; Montané et al., 1998). Our modeling results showed, under higher diffusivity conditions, the effective rate constant was found to be time dependent as described by some previous works (Dang and Nguyen, 2006; Keshwani and Cheng, 2010; Kopelman, 1988; Montané et al., 1994). However, at lower diffusivities, K_{eff} was found to be independent of time. The effective rate constant for both the cases were obtained by curve fitting the results obtained from simulation as discussed in detail in the later sections. An overall transport coefficient K_T (s^{-1}) was also established based on the mean (ensemble average) survival time of the tracers $< t_S >$as (Zheng and Chiew, 1989),

$$K_T = 1/\langle t_S \rangle \quad (29)$$

Two cases of pretreatment were studied in the current work – alkali pretreatment in Poplar and hot water pretreatment in Acer and compared to the experimental data. The bulk and spatial concentration profiles, reaction rates and transport coefficient and effective reaction rate constant were obtained for all cases. All concentration values reported for both tracer and lignocellulose component were normalized with respect to the initial concentration. Appropriate values of the diffusion and reaction parameters were determined so that they were in agreement with the experimental data. The effect of several parameters such as structure, diffusivity and reactivity were then studied to better understand their effect on the biomass pretreatment process. Thus, using such a comprehensive approach it was possible to determine the transport and reaction conditions which would result in efficient conversion of the biomass species. In addition, valuable structure property relationships for different types of biomass species and pretreatments were also predicted.

6.2 Evaluation of the Model for an Ideal System

It is necessary to evaluate the validity of the transport-reaction model using an ideal system before it can be applied to an actual biomass sample. A similar approach was successfully used earlier in the development of the simultaneous dual phase diffusion model (Defrenne, 2008; Defrenne et al., 2019). The ideal system considered here is a uniform isotropic structure consisting of a bed of spheres of equal radii spaced at regular intervals (also known as Maxwell spheres) as shown in Figure 42 (Defrenne, 2008). The spheres are grey and the black space in between the spheres represent the pores. By altering the sphere radii and the distance between them it is possible to obtain structures of wide-ranging porosity. The transport reaction model was first validated using a similar system. In the current work, in order to minimize the computational time, a representative elemental volume of such a system consisting of a single sphere and surrounding empty pore space having the same sphere diameter and porosity instead of a bed of spheres was considered. This system was consistent with the bed of spheres used earlier and provided similar results. The single sphere system is similar to the case of a catalyst pellet system where the reactant molecules undergo simultaneous diffusion and reaction as shown in Figure 43.

The model was evaluated under varying Thiele moduli and ratio of intrinsic diffusivities and, hence, reaction probability values. Additionally, the effect of structure was studied by varying the sphere diameter or porosity. Thus, such an approach not only validated the model but allowed for general conclusions to be drawn about how the transport characteristics varied with the Thiele modulus, concentration of reagents used and structure. After validation of the transport reaction model with the bed of sphere samples, they were then evaluated for the Raman images.

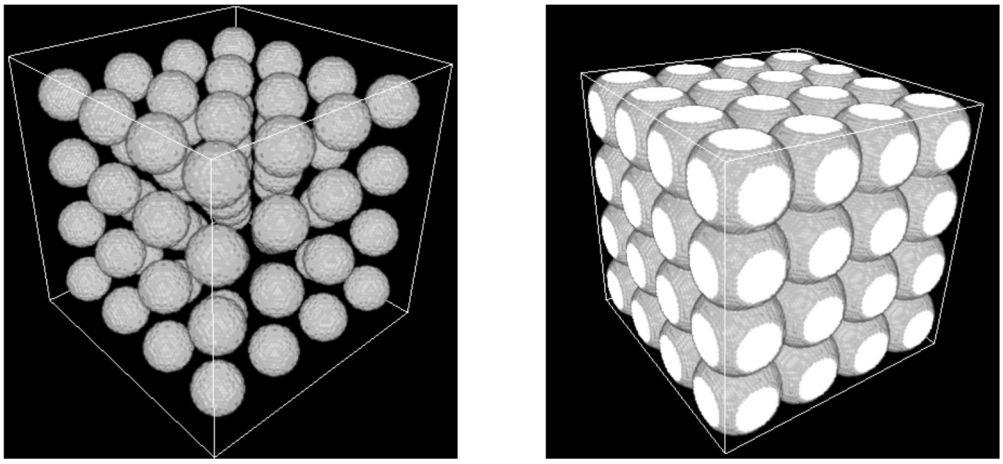

Figure 42. A typical bed of sphere sample used for evaluation of the simultaneous diffusion model (Defrenne, 2008)

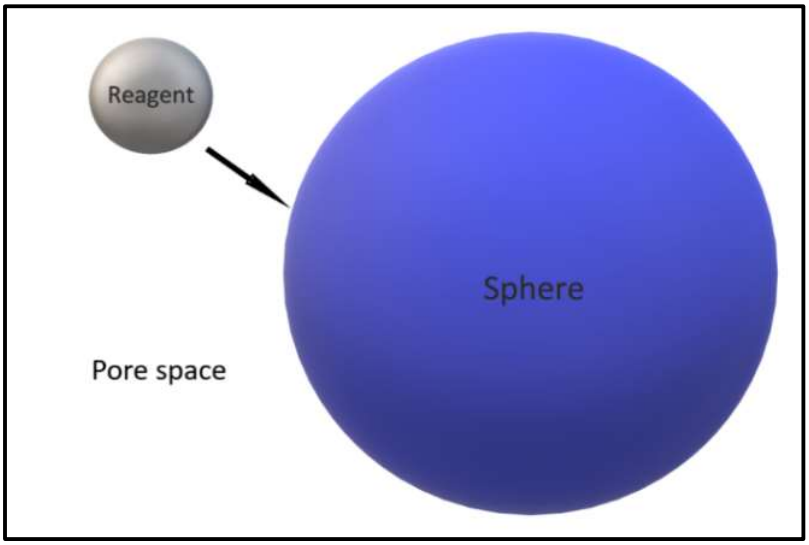

Figure 43. Single sphere and surrounding pore space representing diffusion and reaction in catalyst pellet used to evaluate the transport reaction model

The transport reaction simulations were run using a fixed number of total reagent tracers used for pretreatment for a given total reaction time. As discussed earlier, the reagent particles which diffuse through the structure are referred to as tracers. The total number of tracers used is analogous to its concentration. The time chosen in the simulation corresponds to the duration of the reaction or the residence time. Several parameters were varied for each run and the results were analyzed. Firstly, the effect of structure was studied by varying the sphere diameter and thereby the solidity. Next, the effect of reaction and diffusion on the process were studied by varying the local rate constant and diffusivity of the structure respectively to obtain a wide range of Thiele moduli. The effective diffusivity of the structure was varied by varying the ratio of intrinsic diffusivities since the actual diffusivity of the sphere was not known. The ratio of the diffusivities D* was varied between 0.005 and 0.8 to obtain a sphere diffusivity between 3.9E+05 and 6.24E+05 $\mu m^2/s$. The diffusivity values were reported in $\mu m^2/s$ since a micron scale structure was considered. The effective diffusivities were determined for each condition from a distance versus displacement squared plot obtained from a pure diffusion simulation as previously described (Defrenne, 2008; Defrenne et al., 2019). However, for analyzing the results, the diffusivity and Thiele modulus of the sphere phase was used since the effective diffusivity varied across different solidities for the same pore diffusivity and D*. The local rate constant was varied between 1.86E+05 and 1.86E+08 s^{-1} and the Thiele modulus of the sphere phase varied between 0.0015 and 233.61. Lastly, the effect of the number of tracers used at the start of the simulation was studied. The changes in concentration of the tracers and the sphere, instantaneous reaction rate of the sphere, effective rate constant and transport coefficient of the tracers were reported for all cases. The behavior of these parameters were analyzed for each condition to determine optimum conditions for efficient conversion. Such studies revealed useful insights into the fundamental nature of transport and reaction in ideal porous structures which was then applied to biomass samples.

6.2.1 Impact on tracer consumption

The effect of different parameters such as the structure, diffusivity, reactivity, and the number of tracers used at the start on the concentration and consumption of the tracers

were studied. Although, the number of tracers did not have a direct effect on the reaction as seen in equation 22, they still had an indirect effect on the overall process. The depth of penetration of the tracer in the sphere phase and the rate of consumption of tracers indirectly affect the dissolution of the reactant in the sphere phase. Hence, the effect of different structural and transport parameters on the concentration and transport of tracers were studied. The tracer concentration reported was normalized with respect to the number of tracers present at the start of the reaction.

6.2.1.1 Effect of structure

In order to study the effect of structure on transport-reaction characteristics of the ideal system, the structure was varied by varying the sphere diameter and thereby the solidity of the overall structure. Three different solidities were chosen and the concentration profile of the tracers and the corresponding transport coefficient, K_T, were determined. The total number of tracers corresponding to the initial concentration of the diffusive reactant was kept constant and the simulation was carried out until all the tracers were exhausted. The concentration profiles and K_T values were reported for different solidities over a range of Thiele moduli obtained by varying both the reaction rate constant and ratio diffusivities as seen in Figures 45 through 47 and Tables 6a and 6b. It is interesting to note from Figure 44 that for a given total time and Thiele moduli, as the solidity of the structure increased, the concentration of tracers decreased, indicating relatively higher levels of consumption of tracers. With increasing solidity, the sphere occupied a greater fraction of the sample volume and the tracers came in contact with the sphere more often resulting in greater consumption. The rate of consumption of the tracers was higher at a higher solidity. In each case, when a sufficient number of the tracers have reacted, the rate of consumption of the tracers slowed down. Table 6a and 6b and Figures 45 and 46 showed the effect of structure on K_T at different Thiele moduli. It is evident that at a given Thiele moduli, increasing the solidity increased K_T indicating faster consumption of tracers. This is consistent with the concentration profiles shown in Figure 45. Interestingly, at a given solidity, increasing Thiele moduli had limited effect on the transport coefficient as seen in Figures 45 and 46 and Tables 6a and 6b.

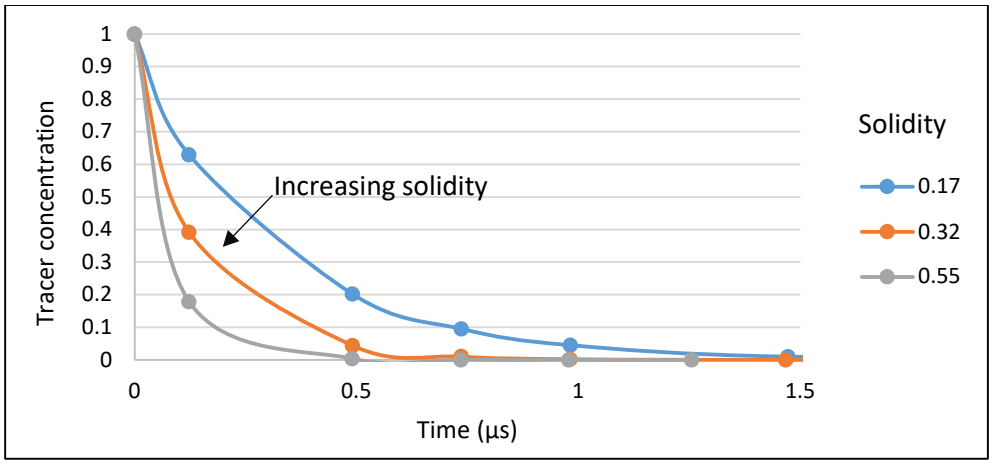

Figure 44. Effect of solidity on the tracer concentration profile (φ^2 233.61)

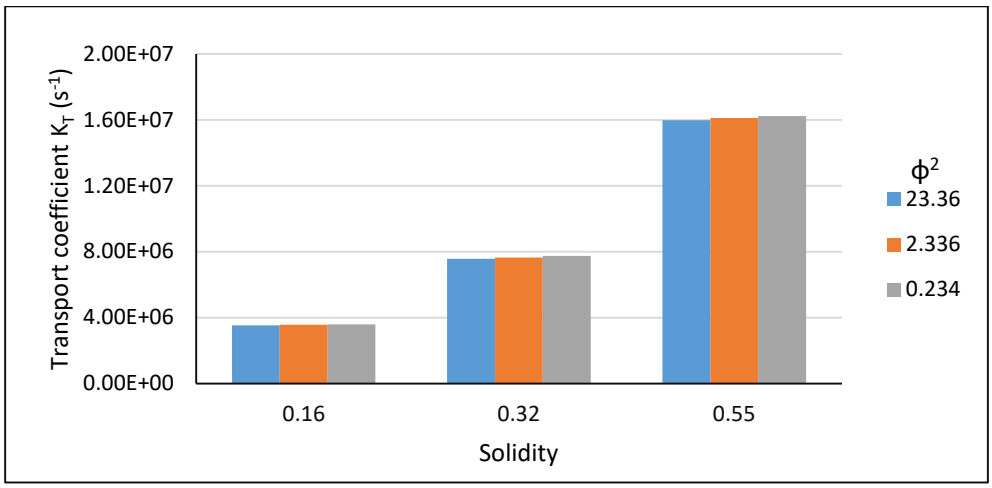

Figure 45. Effect of solidity on the transport coefficient at different φ^2 (k' 1.86E+07)

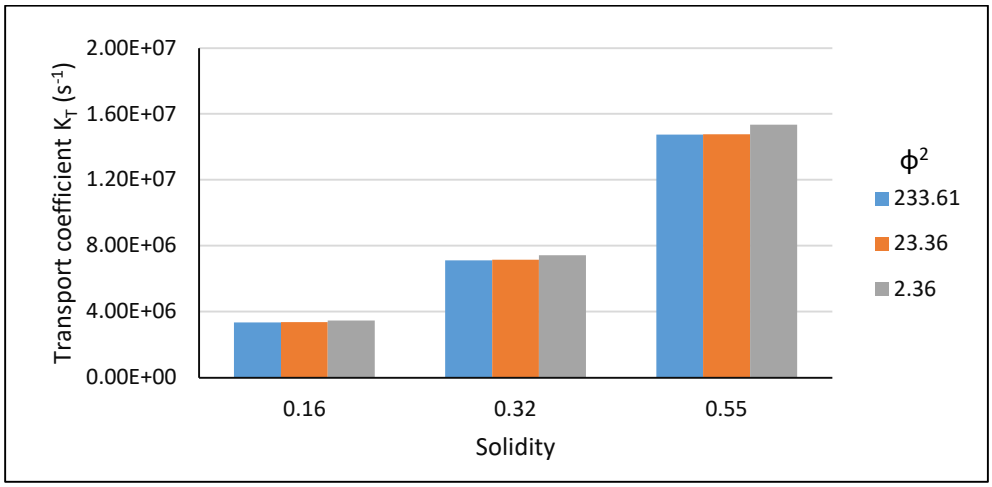

Figure 46. Effect of solidity on the transport coefficient at different φ^2 (k' 1.86E+08)

φ^2	K_T (s^{-1})		
	Solidity 0.16	Solidity 0.32	Solidity 0.56
23.36	3.518E+06	7.563E+06	1.597E+07
5.84	3.532E+06	7.615E+06	1.599E+07
2.34	3.563E+06	7.639E+06	1.612E+07
1.46	3.566E+06	7.661E+06	1.600E+07
0.58	3.581E+06	7.684E+06	1.624E+07
0.23	3.580E+06	7.749E+06	1.624E+07
0.15	3.578E+06	7.701E+06	1.637E+07

Table 6a. Variation of transport coefficient with solidity at different φ^2 (k' -1.86E+07)

φ^2	K_T (s^{-1})		
	Solidity 0.16	Solidity 0.32	Solidity 0.56
233.61	3.334E+06	7.111E+06	1.474E+07
58.40	3.336E+06	7.145E+06	1.477E+07
23.36	3.364E+06	7.149E+06	1.476E+07
14.60	3.372E+06	7.168E+06	1.485E+07
5.84	3.400E+06	7.260E+06	1.500E+07
2.34	3.462E+06	7.418E+06	1.535E+07
1.46	3.482E+06	7.461E+06	1.557E+07

Table 6b. Variation of transport coefficient with solidity at different φ^2 (k' - 1.86E+08)

6.2.1.2 Effect of Thiele modulus

The Thiele modulus is a very important parameter which influences the conversion process enormously. It is affected by changes in the intrinsic diffusivities of the sphere D_F as well as the rate constant k' as is evident from equation 15. In order to study the effect of Thiele modulus, both the sphere diffusivity and reactivity were varied, and the corresponding results were analyzed. It was seen that with increasing diffusivity, the Thiele modulus decreased, and the reaction probability P_K increased. Also, increasing k' at a given diffusivity, increased the Thiele modulus and decreased the reaction probability correspondingly. Thus, a wide range of Thiele modulus values were obtained over which the results were compared. The variation of Thiele modulus with diffusivity at different reaction rate constants is shown in Figure 47 over the entire range for which all of the transport reaction simulations were carried out.

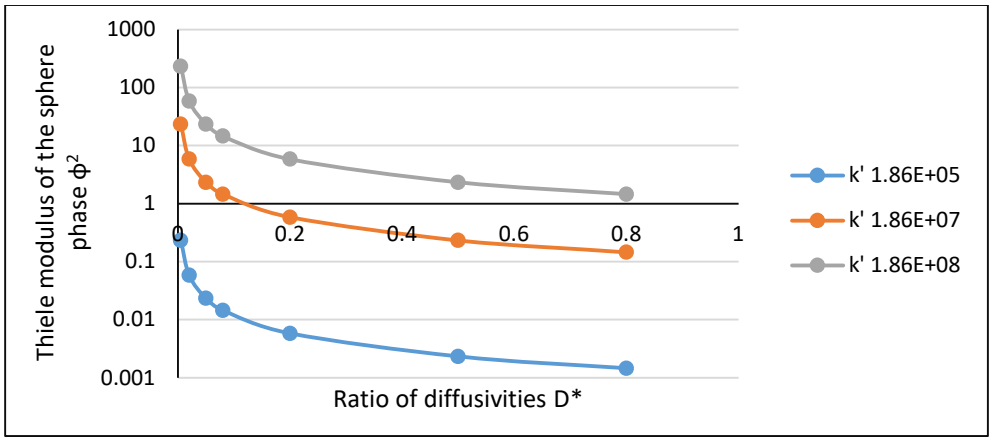

Figure 47. Variation of Thiele modulus (φ^2) squared with D* and k'

At first the diffusivity of sphere was varied while keeping the rate constant unchanged. As shown in Figure 48 and Table 7, at a constant k', increasing the diffusivity or decreasing Thiele moduli increased the transport coefficient K_T. As the spheres became more diffusive, the tracers traversed further into the sphere making more contact with sphere particles. Decreasing the Thiele moduli also increased the reaction probability P_K leading to faster consumption of the tracers, thereby decreasing their survival time and increasing K_T. Thus, it was seen that diffusion enhanced the tracer consumption rate. However, it must be noted that for a low k', (1.86E+05 s^{-1}), the variation in K_T with diffusivity was minimal and increasing the diffusivity beyond a certain threshold decreased the transport coefficient. It is interesting to note that despite the high P_K in this case, the tracers travelled further into the sphere which increased their survival time leading to a decreased K_T. Thus, the survival of tracers was dependent on both diffusion and reaction.

k' - 1.86E+05		k' - 1.86E+07		k' - 1.86E+08	
φ^2	K_T (s^{-1})	φ^2	K_T (s^{-1})	φ^2	K_T (s^{-1})
0.234	3.601E+06	23.36	3.518E+06	233.61	3.334E+06
0.058	3.608E+06	5.84	3.532E+06	58.40	3.336E+06
0.023	3.612E+06	2.34	3.563E+06	23.36	3.364E+06
0.015	3.600E+06	1.46	3.566E+06	14.60	3.372E+06
0.006	3.597E+06	0.58	3.581E+06	5.84	3.400E+06
0.002	3.590E+06	0.23	3.580E+06	2.34	3.462E+06
0.001	3.595E+06	0.15	3.578E+06	1.46	3.482E+06

Table 7. Effect of diffusivity on the transport coefficient

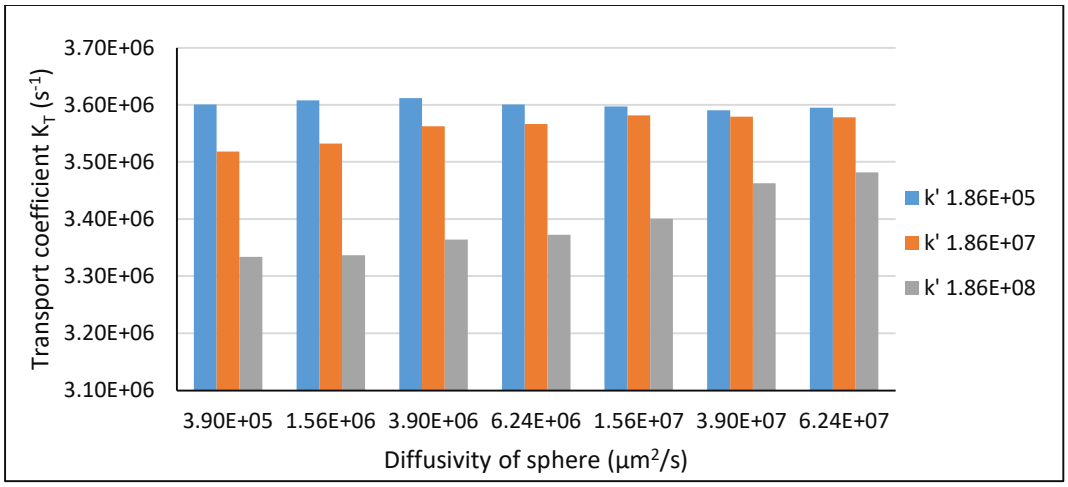

Figure 48. Effect of diffusivity on the transport coefficient

The Thiele Modulus can also be varied by varying the reaction rate constant k'. At a given diffusivity, increasing k' increased the Thiele modulus and thereby decreasing the reaction probability. Although the increased k' led to a greater amount of reaction within the sphere, it resulted in longer tracer survival times and lower transport coefficients. Although, it may seem from equation that the rate constant does not influence tracer concentration directly, it indeed had an indirect effect due to the pseudo first order kinetics of the process. Additionally, it must be noted that although a decreased k' would increase K_T, lower values of k' would reduce the rate of reaction in the spheres greatly. This aspect is studied in detail in the upcoming sections. It must be noted that local rate constant and ratio of diffusivities are used instead of Thiele modulus in Figure 49 to avoid ambiguity.

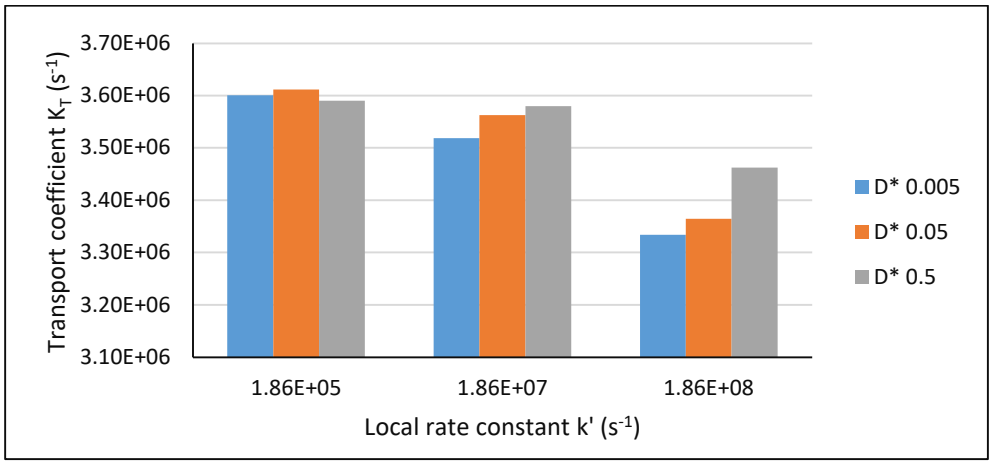

Figure 49. Effect of local rate constant on the transport coefficient

It was seen from Figures 48 and 49 as well as Table 7 that increasing the diffusivity and decreasing the rate constant facilitated faster consumption of tracers as indicated by the increased transport coefficient values. However, it should be noted that the k' used for the calculation of Thiele modulus of the sphere phase corresponds to the desired component in the sphere and not the tracers. Hence, an increased K_T does not automatically result in greater dissolution of the desired component within the sphere. This aspect will be studied in greater detail in the upcoming sections. Another interesting feature to be noted is that different values of k' and D* that yield the same Thiele modulus in the sphere phase, resulted in different transport characteristics as indicated by K_T values in Table 8. This was explained by the fact that even though the Thiele modulus in the sphere phase is the same, the effective diffusivity and effective Thiele modulus of the structure are different as seen in Table 8. A higher transport coefficient was observed for a lower effective Thiele modulus. This is attributed to the fact that a lower effective Thiele modulus resulted in a higher reaction probability due to which the mean the survival time of the tracers decreased leading to a higher transport coefficient. However, it must be noted that even though lower Thiele moduli (lower diffusivity and lower rate constant) yielded a higher transport co-efficient, it did not guarantee a greater dissolution rate of the desired component in the sphere as will be seen in the upcoming sections.

D*	k' (s^{-1})	φ^2	D_{eff}	φ^2	K_T (s^{-1})
0.005	1.86E+05	0.23	6.10E+07	0.001	3.60E+06
0.5	1.86E+07	0.23	7.00E+07	0.130	3.58E+06
0.05	1.86E+07	2.34	6.16E+07	0.148	3.56E+06
0.5	1.86E+08	2.34	7.00E+07	1.301	3.46E+06
0.005	1.86E+07	23.36	6.10E+07	0.149	3.52E+06
0.05	1.86E+08	23.36	6.16E+07	1.480	3.36E+06

Table 8. Variation of transport coefficient with φ^2

6.2.1.3 Effect of number of tracers

The total number of tracers used in the transport reaction simulation is analogous to its concentration. The reaction follows pseudo first order kinetics which means one of

the reactants was available in abundance compared to the other. In this case, the mobile tracers (reagent) that diffuse through the porous structure were available in abundance while the concentration of the stationary sphere components (i.e., lignocellulose component) was limited. Although it may seem that the tracer concentration did not affect the reaction rate as per equation 22, it still had an indirect effect on the reaction. It was seen in the previous section as well that the rate of tracer consumption and K_T are sensitive to changes in k'. The rate at which the tracers are consumed dictate the residence of the reaction, thereby influencing the rate of reaction. As seen from Figure 50, an increase in the initial number of tracers allowed for more tracers to diffuse through structure and traverse further into the sphere before being depleted. Consequently, the concentration of the tracers available for consumption was greater at any given time as seen in Figure 50. As a result, the mean survival time generally decreased, and K_T increased as seen in Figure 51. The concentration of tracers in this case is measured in terms of the total number of tracers used per total number of voxels in the volume. The concentration cannot be normalized with respect to the initial number of tracers as they kept varying. Thus, from Figures 51 and 52 it is clear that a sufficient number of tracers were required at the start of the reaction to ensure a constant supply of tracers through the intended residence time. Having too few tracers would result in them being consumed early on in the reaction and would not allow the reaction to run for the intended reaction time.

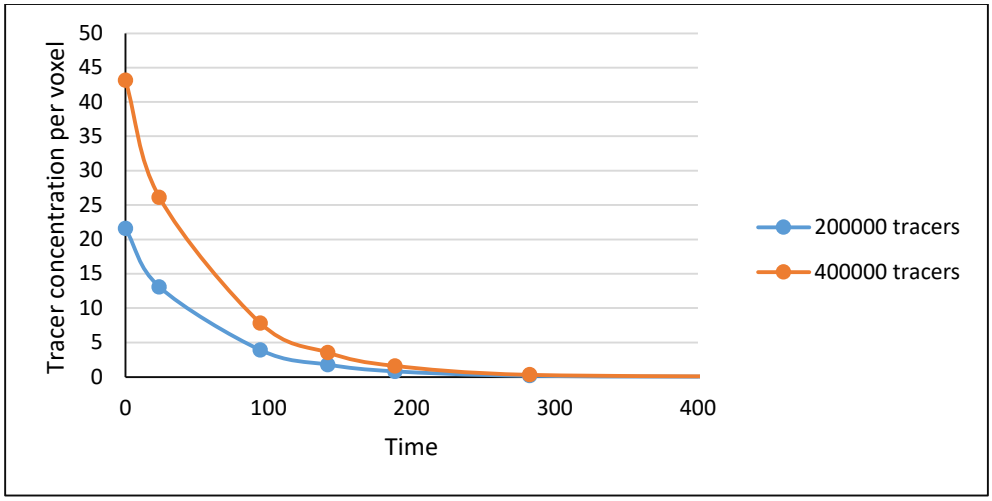

Figure 50. Variation of tracer concentration profile with initial number of tracers

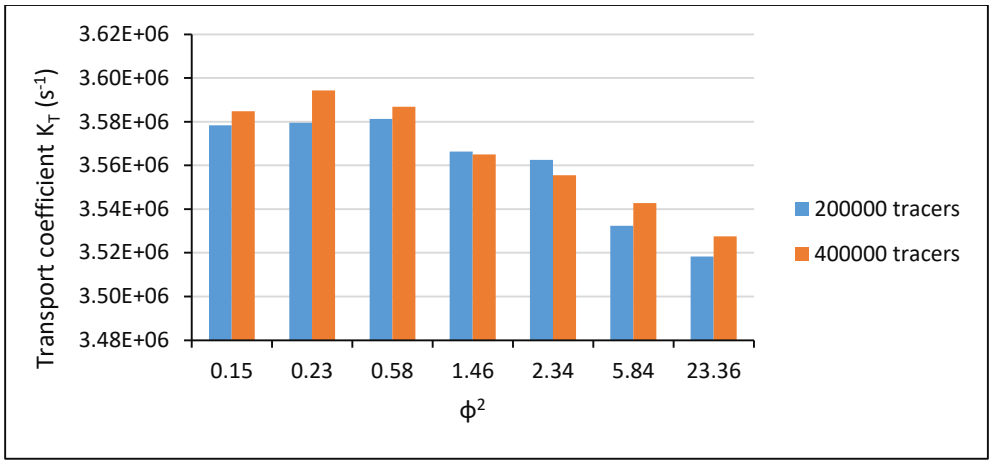

Figure 51. Variation of transport coefficient with initial number of tracers for different φ^2

6.2.2 Impact on the reaction within the sphere

The ultimate goal of the transport reaction model is to study the dissolution of the stationary reactant within the sphere (i.e., biomass component) and obtain its concentration profile which is affected by both transport and reaction properties of the system. The concentration profiles as well as the corresponding instantaneous reaction rates were determined using the current approach. An effective rate constant K_{eff} was determined from the instantaneous reaction rate, which accounted for both the transport and reaction phenomena in the system. Unlike a typical first order reaction, it was found that K_{eff} was time dependent throughout the range of Thiele moduli for which the simulation was carried out. Such a time dependent rate constant has been predicted in previous literature (Dang and Nguyen, 2006; Keshwani and Cheng, 2010). The effect of structure, number of tracers and Thiele modulus on the stationary species concentration in the sphere was studied. As mentioned earlier, the Thiele modulus was affected by both the reaction rate constant as well as the intrinsic diffusivity. The effect of both these parameters was explored. The variation of concentration within different layers of the sphere was also analyzed to study the combined effect of diffusion and reaction. The effect of each of these parameters was elucidated by comparing the bulk concentration profiles and the corresponding instantaneous reaction rates. For convenience, the bulk concentrations were normalized with respect to the initial bulk concentration of the stationary species. As mentioned earlier, the Thiele modulus of the sphere was used for comparison to maintain consistency. The

effect of structural and transport properties on the reaction kinetics were studied which helped in determining effective conversion processes for that reactant.

6.2.1.1 Effect of structure

The effect of the structure was studied by varying the solidity as seen in the earlier section. For a given Thiele modulus and number of tracers, increasing the solidity increased the availability of the reactant leading to a higher dissolution. This allowed for tracers to encounter sphere particles and pore-sphere interfaces more often, increasing the instantaneous rate of reaction dC/dt as seen in Figures 52 and 53. As the instantaneous reaction rate had a negative value, (-dC/dt) was used in the plots. It was observed that although a higher concentration of the sphere reacted at a higher solidity, the relative concentration of the remaining sphere particles was higher for higher solidities since a higher initial concentration of the reactant was available in the spheres. The radial concentration profile of the spheres at different time points, starting from the center until the radius of the sphere R was plotted in Figure 54. The radial concentration profile revealed that a greater fraction of the sphere reacted at lower solidity than at higher solidity as seen in the bulk concentration profiles. It was also observed that the rate of reaction decreased more rapidly at higher solidities indicating greater dissolution in the sphere. Consequently, the effective rate constant increased with increase in solidity. It was seen earlier in Figures 44 and Tables 6a and 6b that an increase in solidity led to an increase in the transport coefficient and faster depletion of the tracers.

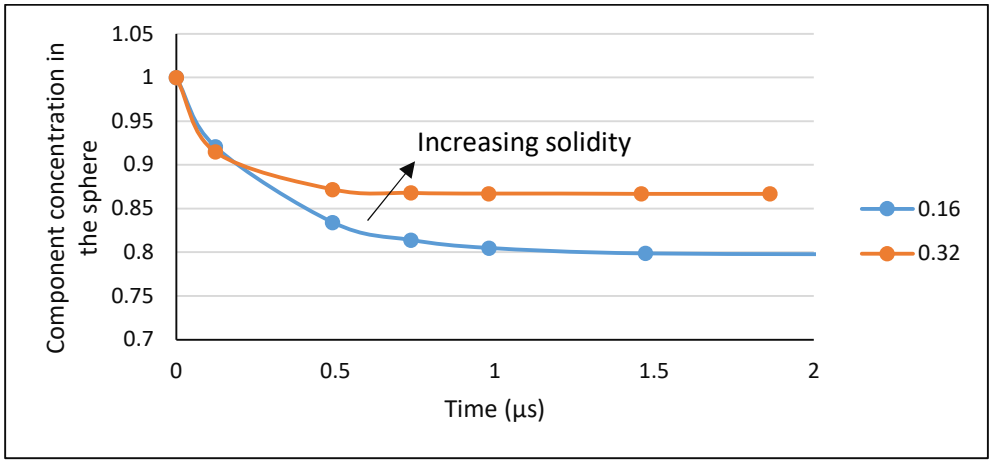

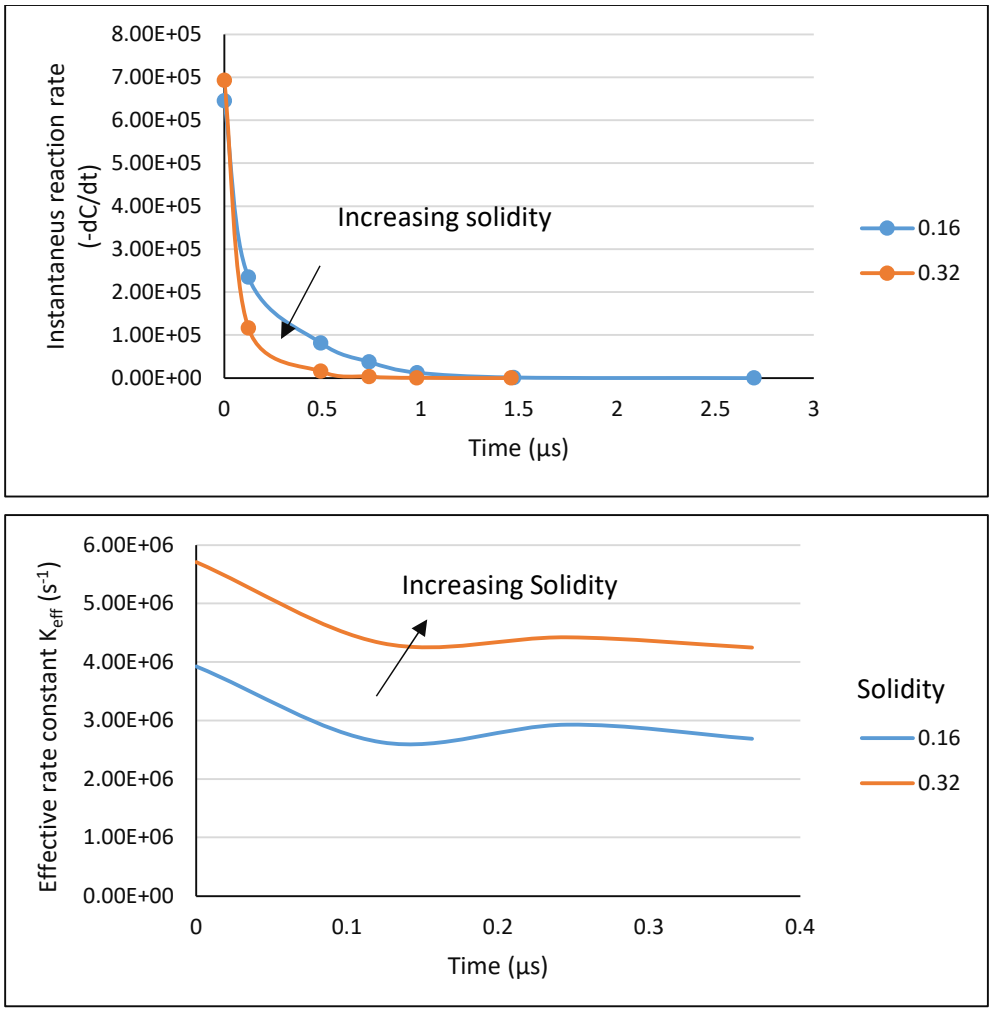

Figure 52. Effect of solidity on the bulk concentration profile of sphere, instantaneous reaction rate and effective rate constant (φ^2 0.233)

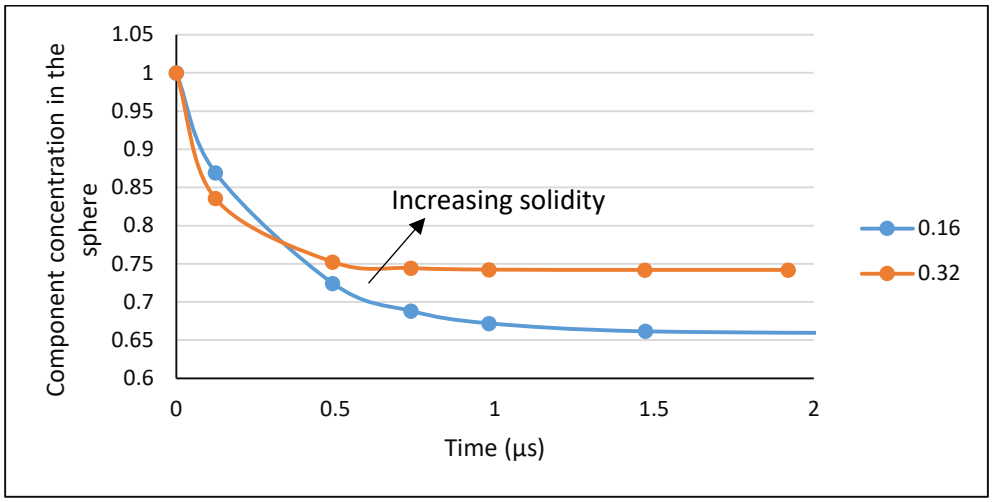

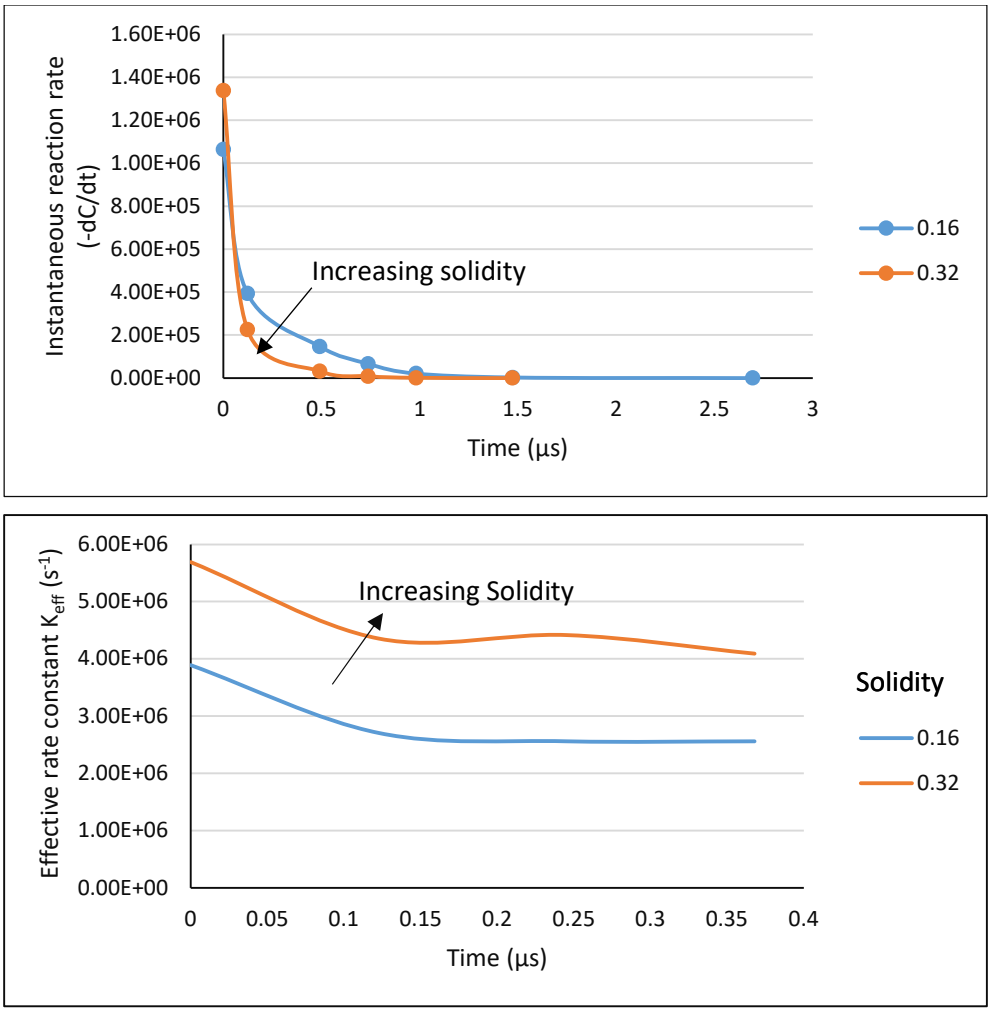

Figure 53. Effect of solidity on the bulk concentration profile of sphere, instantaneous reaction rate and effective rate constant (φ^2 2.34)

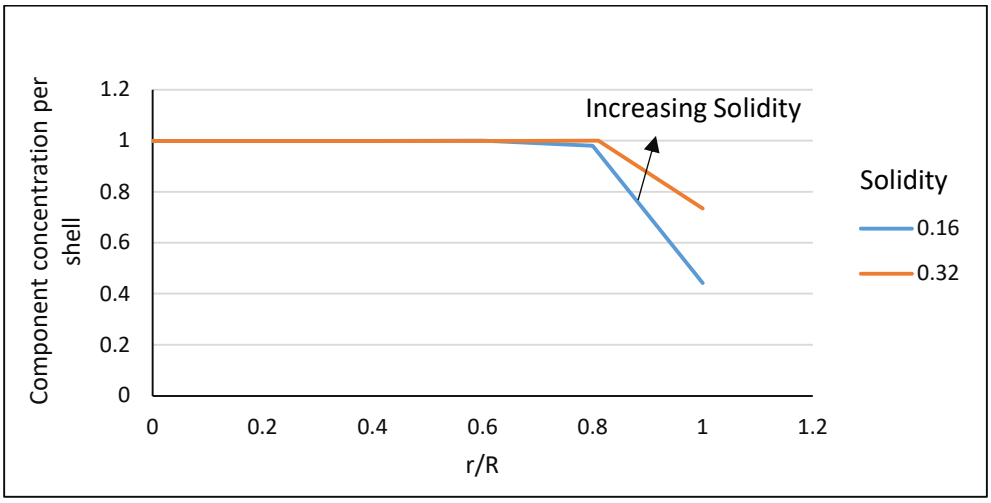

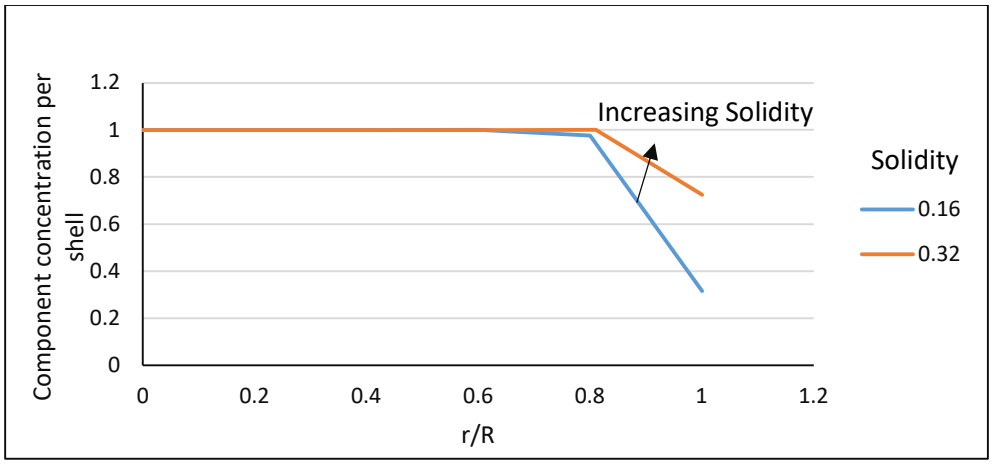

Figure 54. Effect of structure on the radial concentration profiles of the sphere at times t1 (top) and t2 (bottom) (t2>t1 and φ^2 2.34)

6.2.1.3 Effect of Thiele Modulus

The effect of Thiele modulus on the transport-reaction process is multifold and has to be understood in great detail in order to determine conducive reaction conditions. The Thiele modulus can be changed by changing either the reaction rate constant k' or the ratio of diffusivity D* as shown in Figure 47 and either of these phenomena affect the reaction differently depending on whether it is a diffusion or reaction dominant process. The Thiele modulus was first varied by changing only the intrinsic diffusivity of the sphere while keeping the reaction rate constant unchanged. Since a direct measure of the diffusivity of the sphere is unavailable, the ratio of intrinsic diffusivities D* are varied between 0.005 and 0.8 to obtain a wide range of Thiele moduli. As the diffusivity of the spheres increased, the tracers penetrated further into the sphere and increasingly came in contact with unreacted regions thus increasing the possibility for additional reaction. The higher reaction probability led to greater reaction as well as faster tracer consumption. The increase in transport coefficient with increase in diffusivity as seen earlier in Figure 48 and Table 7 also confirmed this observation. Hence, the increase in diffusivity led to greater dissolution within the sphere as seen from the bulk concentration profiles in 56 and 57. Consequently, the instantaneous rate of reaction and the effective rate constant also increased as seen in Figures 55 and 56. It was observed that the changes in concentration and the corresponding reaction rates with increasing diffusivity were higher at lower

diffusivities or higher Thiele moduli range. Additionally, greater differences in concentration occurred at higher k' as seen in Figures 55 and 56.

The radial concentration profiles of the sphere were also determined at different times during the reaction as shown in Figure 57. It can be seen that higher the diffusivity or lower the Thiele moduli, greater the dissolution occurring per shell. With increase in diffusivity, the reaction proceeded to the inner layers of the sphere along with surface reaction. Thus, it can be inferred that diffusion enhanced the reaction within the sphere as was seen with the case of tracer consumption rate. Hence, it is important to maintain the reaction conditions such that the solid phase was more diffusive. Alternatively using tracers or reactants that can disrupt the sphere phase can also be used to increase the diffusivity of the system.

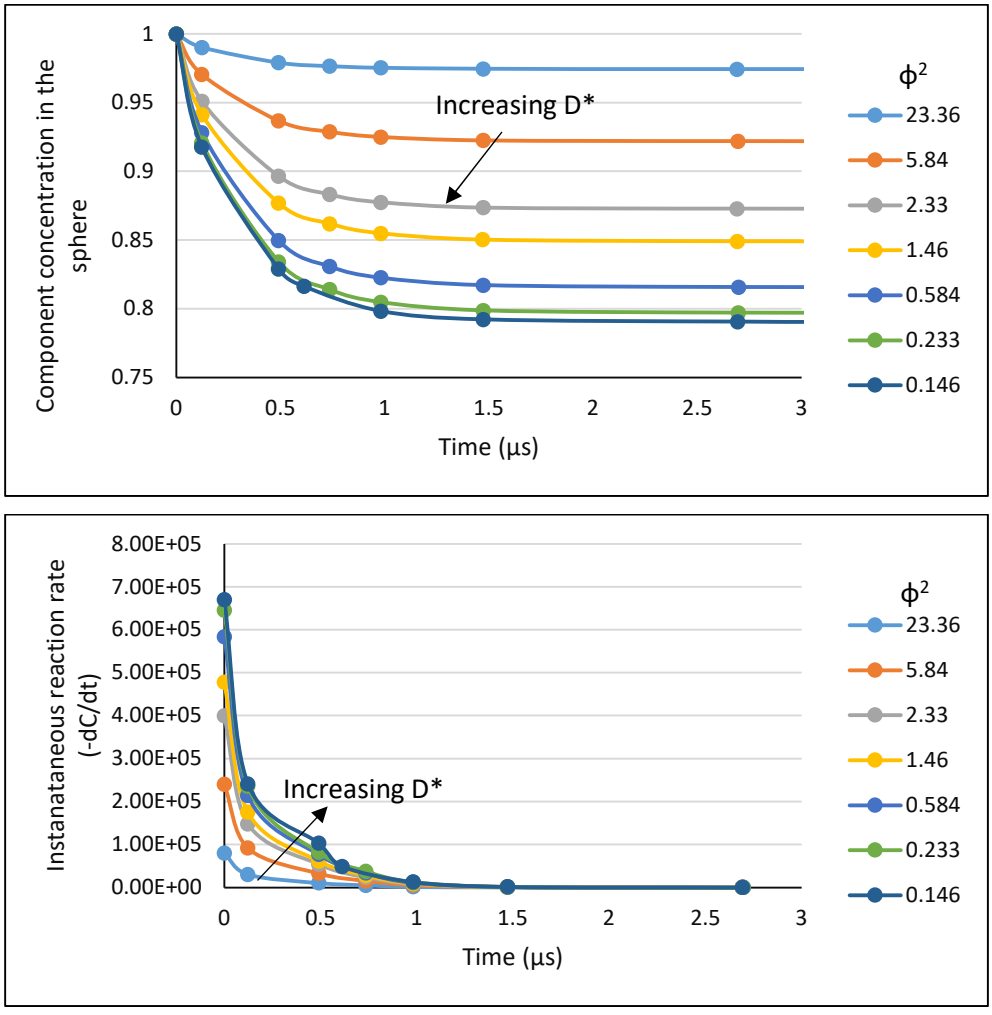

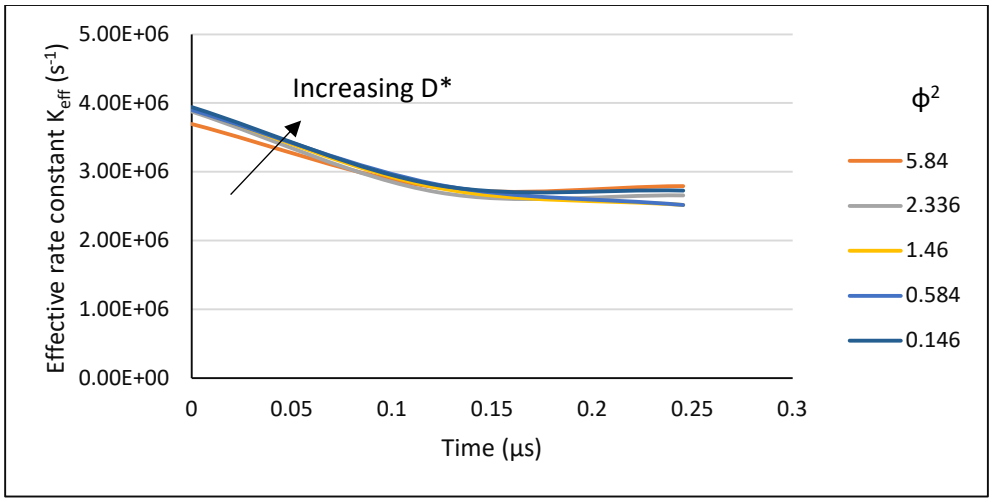

Figure 55. Effect of diffusivity on the bulk concentration profile of sphere, instantaneous reaction rate and effective rate constant (k' 1.86E+07 s^{-1})

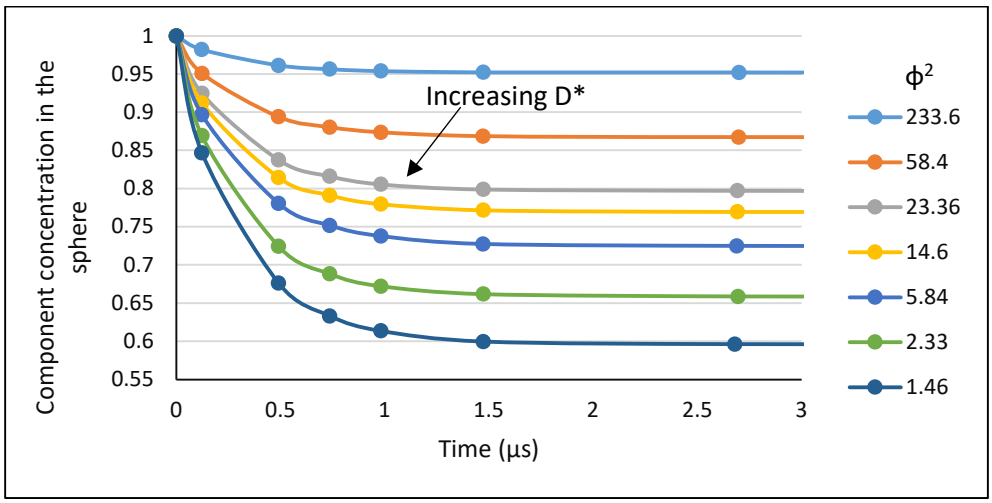

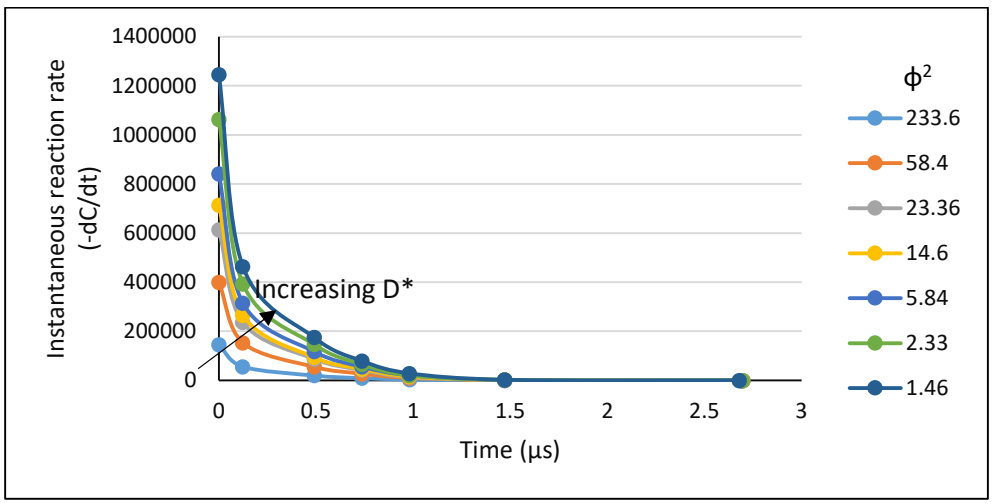

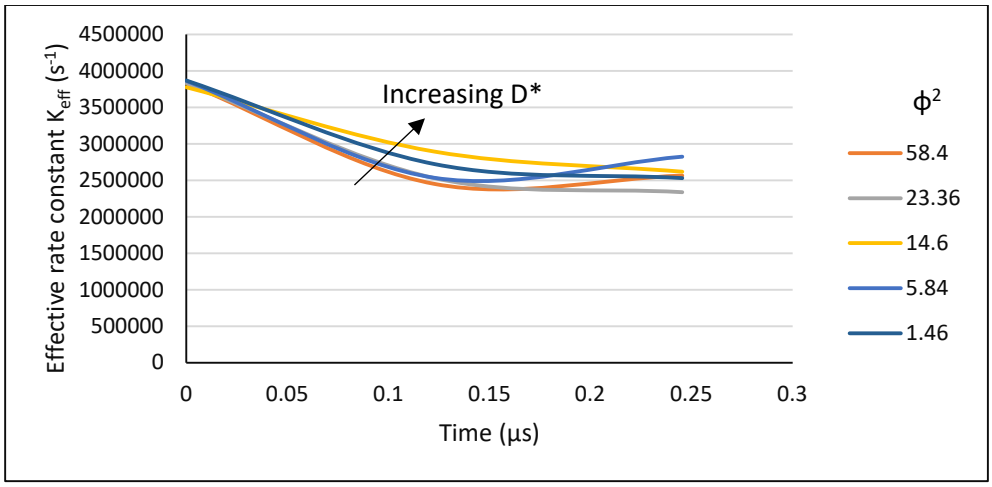

Figure 56. Effect of diffusivity on the bulk concentration profile of sphere, instantaneous reaction rate and effective rate constant (k' 1.86E+08 s^{-1})

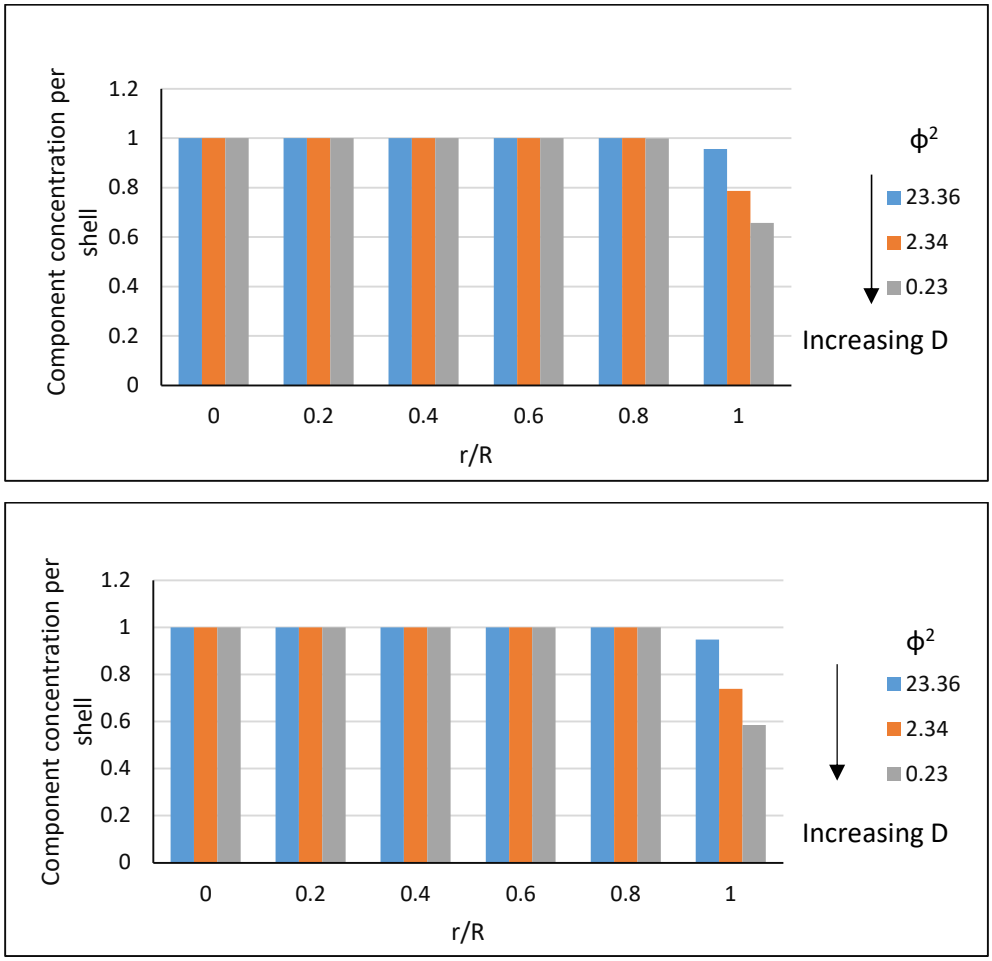

Figure 57. Effect of diffusivity on the radial concentration profiles of the sphere at times t1 (top) and t2 (bottom) (t2>t1 and k' 1.86E+07 s^{-1})

The Thiele modulus was then varied by changing the reaction rate constant while keeping the diffusivity constant. The effect of changing the reaction rate constant is more complex due to the pseudo first order kinetics of the reaction. Equation 22 showed that increasing k' enhanced the reaction rate significantly. This means that although the probability of reaction is lower for every encounter of the tracer with the sphere, a higher concentration of the reactant underwent reaction with every encounter that led to a reaction. Thus, increasing the local rate constant resulted in greater dissolution within the sphere as seen in the bulk concentration profiles in Figures 58 through 60. Consequently, the instantaneous rate of reaction and the effective rate constant also increased with increase in k'. This fact is also reiterated by the radial concentration profiles at different times during the reaction as seen in Figure 61. It can be seen that with increase in k', reaction occurred not only at the surface of the sphere but also begins to proceed to the inner layers of the sphere in due time. This was explained by the fact that at a higher k', the reactant in the outer layers of the sphere reacted faster creating more open spaces and allowing the tracer particles to penetrate further into the sphere over time. It was observed earlier in Figure 50 that increasing the local rate constant decreased the transport coefficient. However, that did not hinder the reaction within the sphere as seen in Figures 59 through 61. Hence depending on the diffusivity and reactivity of the system, either an increase or decrease in K_T can be beneficial for the process. Thus, the transport coefficient alone is not sufficient to determine the behavior of the process.

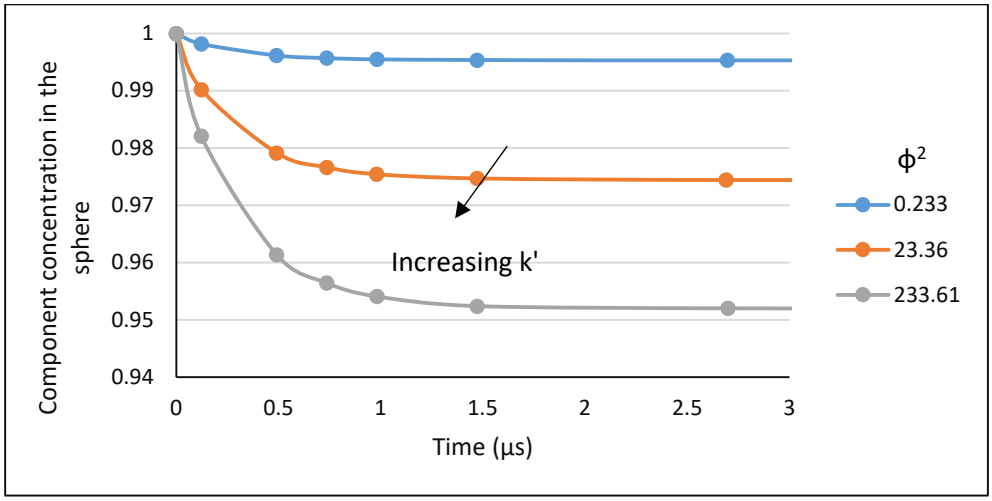

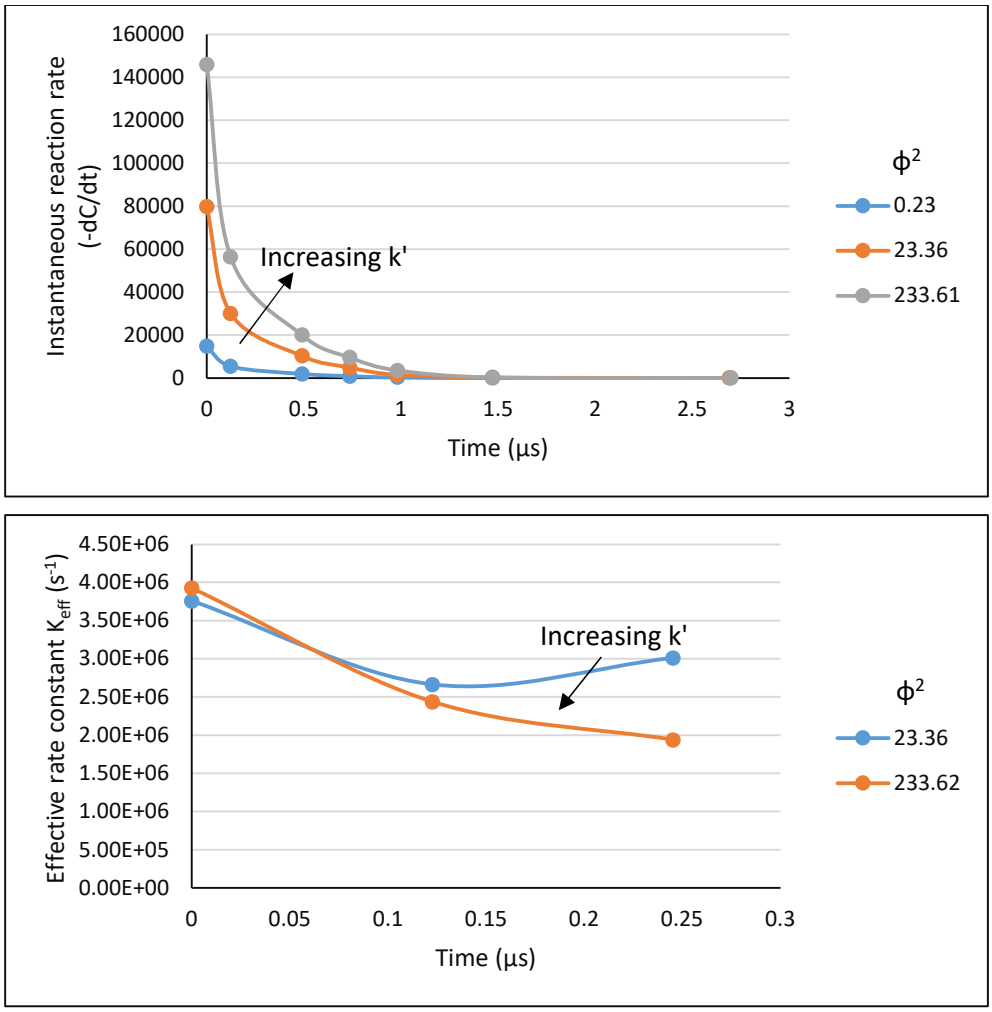

Figure 58. Effect of local rate constant on the bulk concentration profile of the sphere, instantaneous reaction rate and effective rate constant (D* 0.005)

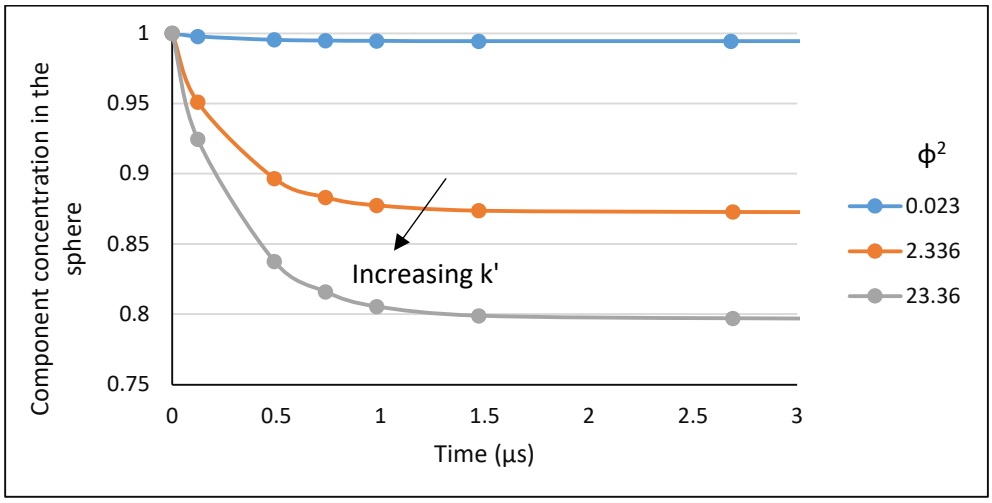

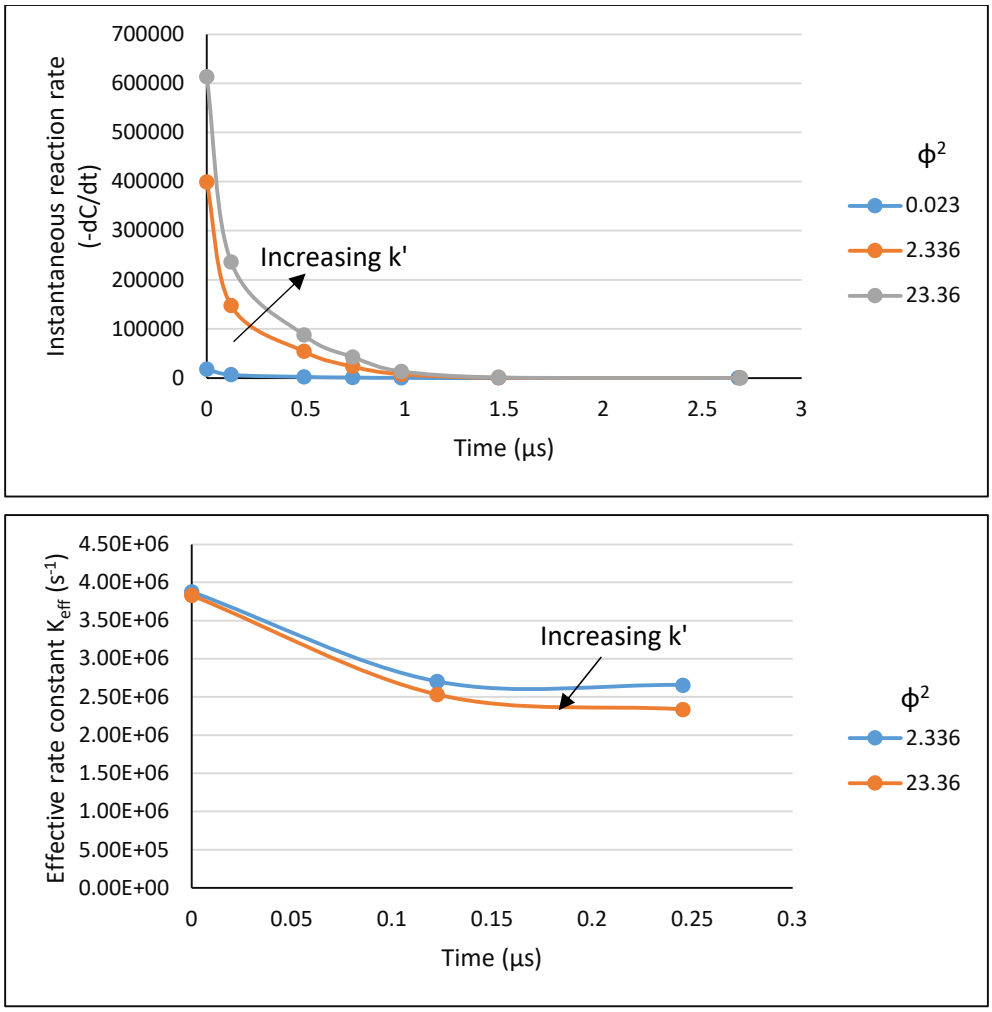

Figure 59. Effect of local rate constant on the bulk concentration profile of the sphere, instantaneous reaction rate and effective rate constant (D* 0.05)

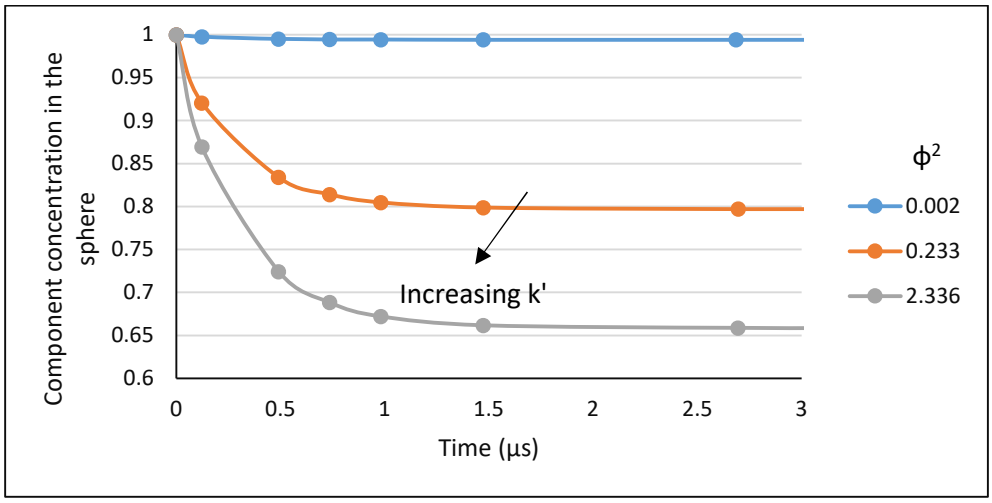

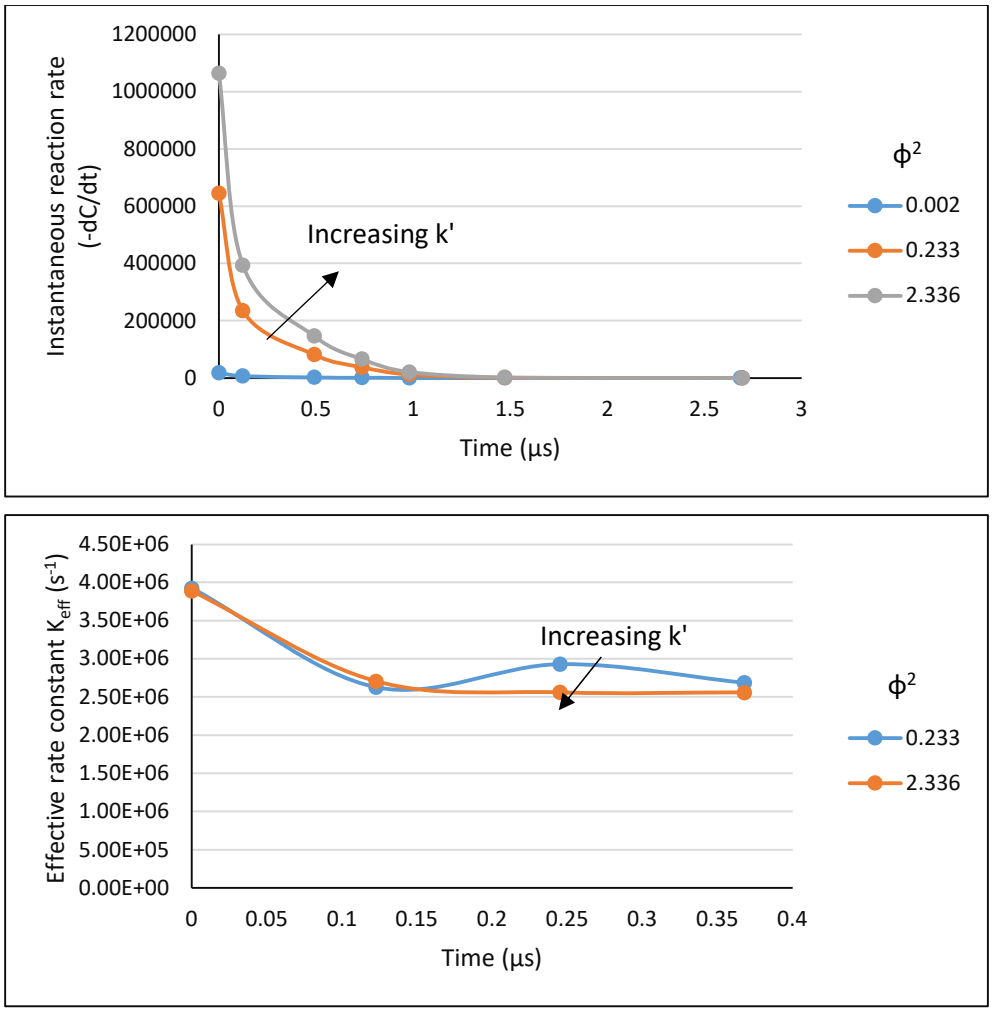

Figure 60. Effect of local rate constant on the bulk concentration profile of the sphere, instantaneous reaction rate and effective rate constant (D* 0.5)

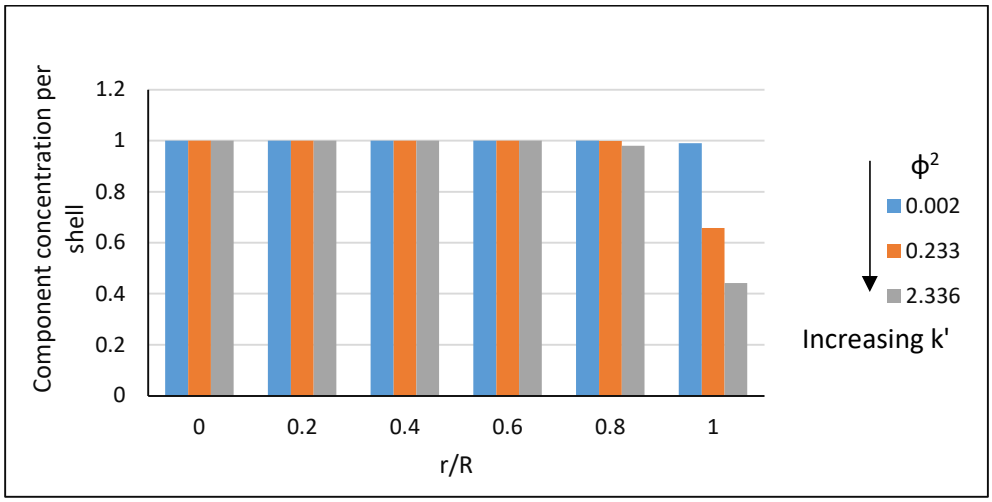

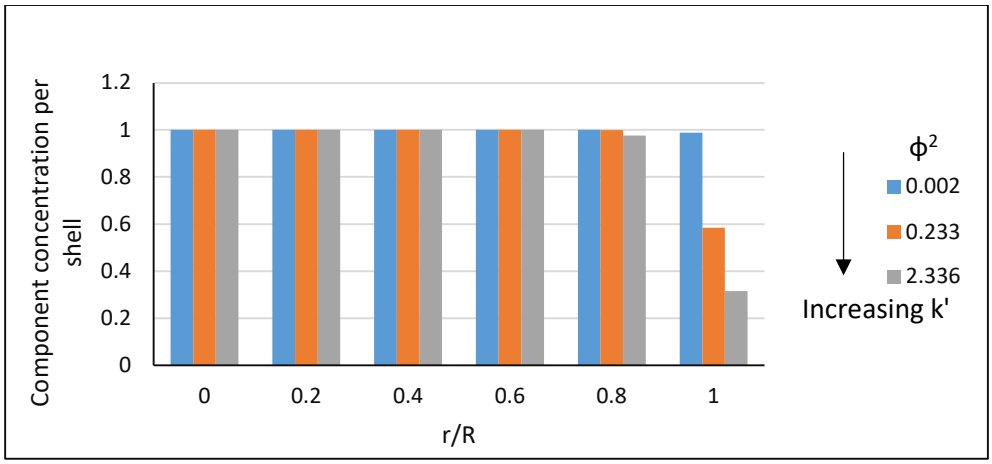

Figure 61. Effect of k' on the radial concentration profile of the sphere at time t1 (top) and t2 (bottom) (t2 > t1 and D* 0.5)

It is now clear that at the same Thiele modulus of the sphere, different k' and D' yielded different effective Thiele moduli which resulted in different transport coefficient as seen in Table 8. The same observation holds true for the concentration of the component in the sphere as seen in Figures 62 and 63. Consequently, the instantaneous reaction rates and the effective rate constants were also different. A higher effective diffusivity and a higher rate constant provided greater dissolution within the sphere. It must be noted that although a higher K_T was observed at lower D_{eff} and k' as seen in Table 8, greater reaction of the desired component in the sphere was observed at higher D_{eff} and k'.

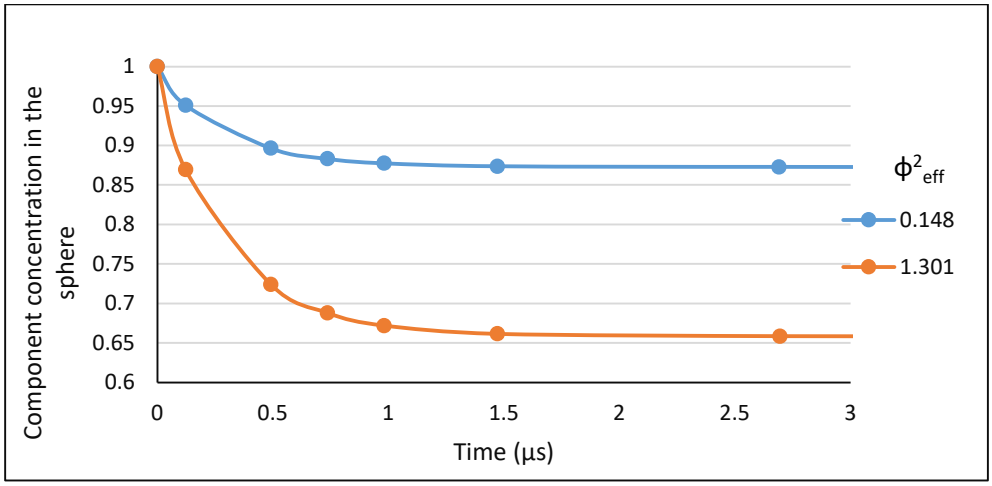

Figure 62. Concentration profile of the sphere and the corresponding instantaneous reaction rate rates for the same φ^2 (2.33) but different k' and D_{eff}

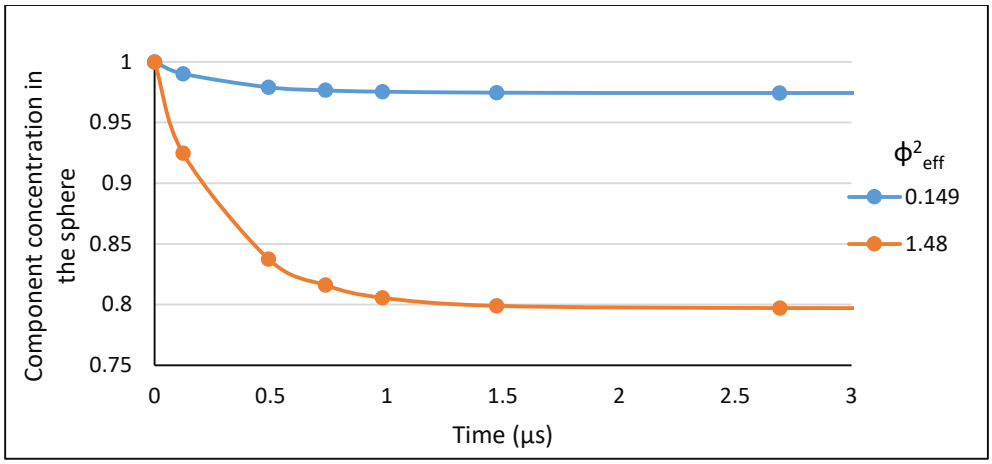

Figure 63. Concentration profile of the sphere and the corresponding instantaneous reaction rate rates for the same φ^2 (23.36) but different k' and D_{eff}

6.2.1.3 Effect of number of tracers

The current transport-reaction model assumes pseudo first order kinetics where the tracers were available in abundance compared to the concentration of the component in the sphere. Although the rate equation (equation 22) did not show a direct dependence on the tracer concentration, they indirectly affected the concentration profiles of the spheres and the corresponding reaction rates. If the number of tracers is low, they exhausted quickly, and the reaction ended earlier than desired leading to the failure of the model in predicting the concentration changes. Hence the number of tracers chosen for the simulation is an important parameter. It was seen in Figure 50 that greater the number of tracers at the start, a larger number of tracers were available for reaction at any given time. Thus, a higher degree of dissolution was observed within the sphere as seen in Figures 64 and 65. This fact is reiterated from the radial concentration profiles shown in Figure 66. With the availability of a higher number of tracers, they were able to penetrate further into the sphere leading to more reaction. Once the tracers were exhausted, there were no further changes in concentration of the sphere. As seen in Figures 64 and 65, the concentration curve flattened out and reached a minimum value. It must be noted that this is solely a result of exhausting the tracers and not due to complete depletion the stationary species in the sphere. Hence, it is important to choose a sufficient number of tracers so that enough tracers were available throughout and the reaction did not stop before the intended residence time.

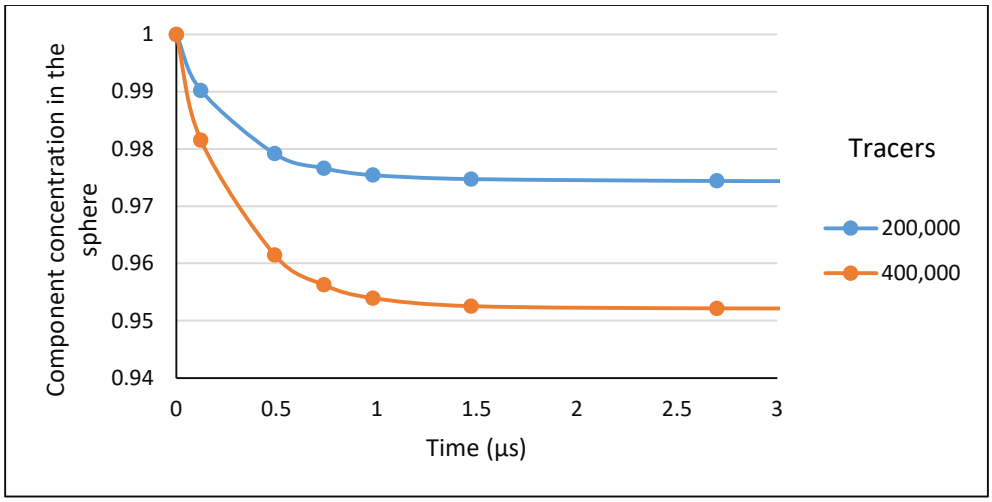

Figure 64. Effect of number of tracers on the sphere concentration (φ^2 233.36)

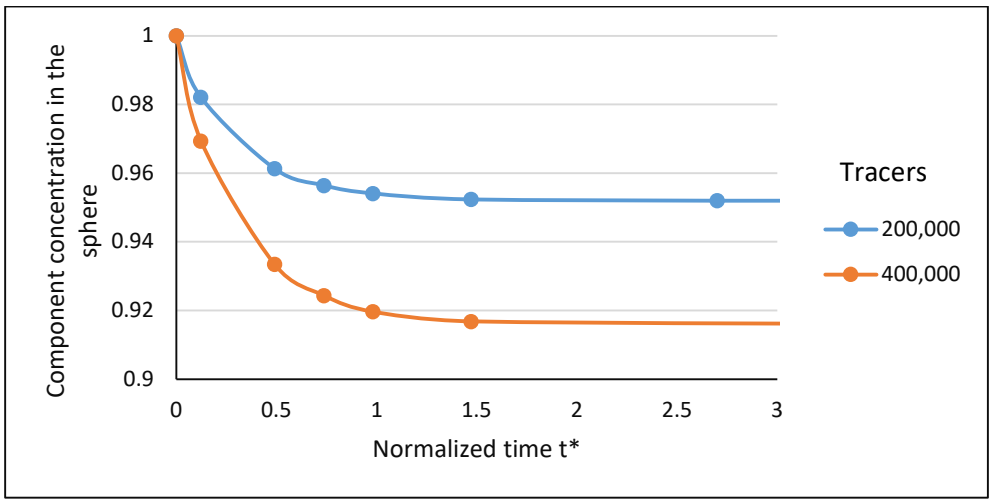

Figure 65. Effect of number of tracers on the sphere concentration (φ^2 23.36)

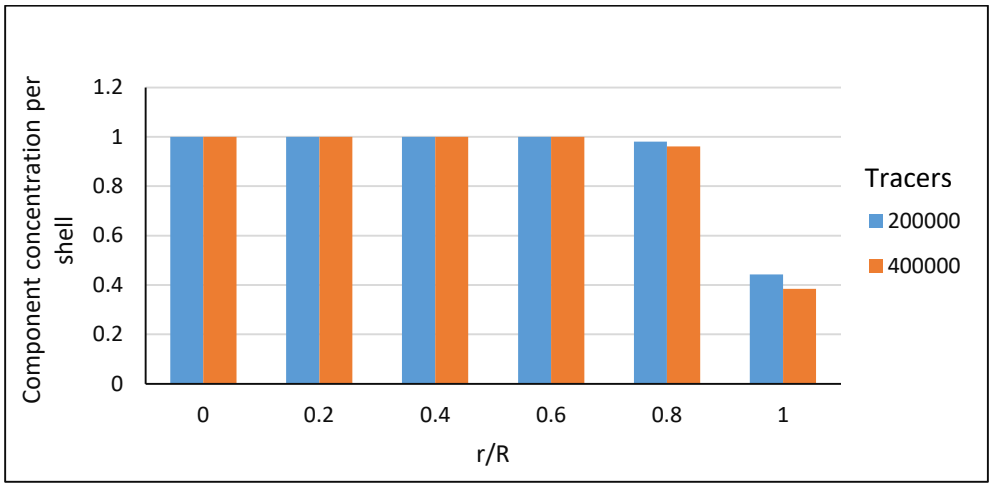

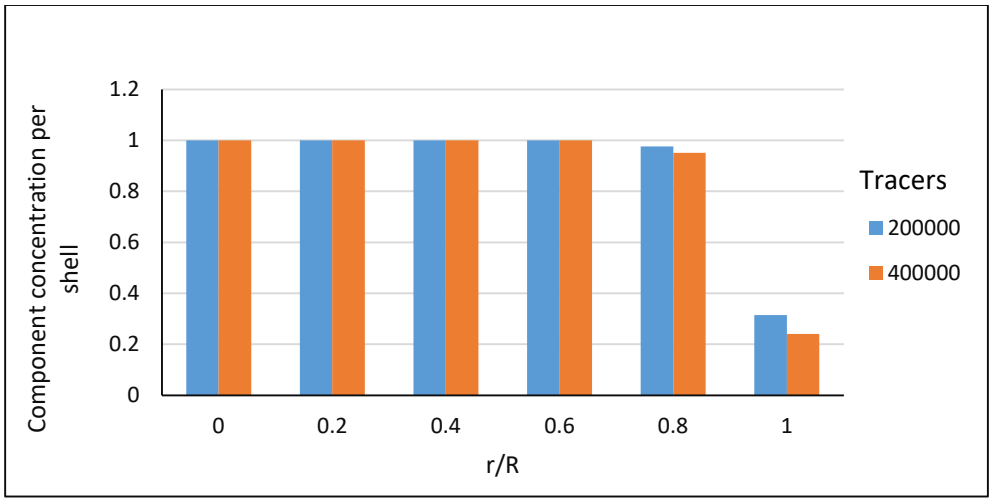

Figure 66. Effect of number of tracers on the radial concentration profile of the sphere at times t1 and t2 (t2>t1 and φ^2 2.34)

The above evaluations performed for both the tracer transport and the changes in sphere concentration proved that the process followed pseudo first order kinetics. The effect of diffusive transport of the tracers, reactivity of the spheres and the structure on the overall process were extensively studied. The Thiele modulus which is inclusive of both the diffusive and reactive nature of the process is the biggest factor that affects the transport-reaction process. As seen from multiple simulations, a diffusion enhanced reaction process provided the best results in terms of conversion. A higher diffusivity and a higher local reaction rate constant yielded greater dissolution. However, it must be noted that the effect of increasing diffusivity was lower at a higher diffusivity range. As a result, drastically improving the diffusivity of the sphere or the stationary phase may only increase the rate of reaction minimally while requiring a higher cost and energy. Additionally, increasing the local reaction rate constant beyond a certain threshold without increasing the diffusivity may reduce the reaction probability to an extent where potential benefits of increased reaction rate constant may not be fully realized. Considering the above factors, the optimum parameters for effective conversion can be chosen.

Several studies have described the transport and reaction behavior of heterogeneous or catalytic systems in terms of the Thiele modulus (Bidabehere and Sedran, 2001; Kansal and Torquato, 2002; Keshwani and Cheng, 2010; Riley et al., 1995a, 1995b; Siyakatshana

et al., 2005; Szukiewicz, 2000). However, an effective value of the diffusivity was used in many cases (Bidabehere and Sedran, 2001; Siyakatshana et al., 2005; Szukiewicz, 2000). The current work uses local diffusivities of the pore and fiber phases for the transport-reaction simulations similar to some of the previous work (Defrenne et al., 2019; Riley et al., 1995a, 1995b). Additionally, the model estimates an effective overall rate constant K_{eff} which accounts for transport as well as reaction and better describes the behavior of the system similar to some of the previous work (Dang and Nguyen, 2006; Keshwani and Cheng, 2010; Montané et al., 1994). The model provided consistent results for different structures over a wide range of values of Thiele moduli. Hence, it can now be applied to evaluate the changes in topochemistry during the biomass pretreatment processes using Raman image stacks and compare it with the experimental values.

7. APPLICATION OF THE TRANSPORT-REACTION MODEL TO BIOMASS PRETREATMENT

The transport reaction model was first evaluated in an ideal system of periodic array of spheres and found to be valid under different conditions, as discussed in the previous chapter. In this chapter, the model was applied to Raman images of untreated plant cell walls to predict the pretreatment kinetics and transport. Several kinetic models have been developed to explain the biomass pretreatment processes in some of the earlier work (Faravelli et al., 2010; Greenwood et al., 2013; Grénman et al., 2011; Keshwani and Cheng, 2010; Kim and Holtzapple, 2006; Kim and Lee, 2006; Mittal et al., 2009; Morinelly et al., 2009; Sierra-Ramírez et al., 2011; Zhao et al., 2014). Here, in order to apply the transport and reaction model to the pretreatment process, 3D stacks of Raman images were created from the conventional 2D CLSRM images and used as mentioned in the earlier sections. Two sets of Raman images showing the initial (untreated) lignin topochemical distribution within the cell wall that correspond to different species and pretreatment methods were used to evaluate the lignin dissolution using the transport reaction model. They included alkali treated Poplar and hot water treated Acer shown earlier in Figures 35 and 36 (Ji et al., 2014). The effect of diffusivity and reactivity on the pretreatment process was studied by varying the Thiele modulus. The effective diffusivity of the dual phase system including the pores and the cell walls was determined separately from pure liquid diffusion simulations. The diffusivity and reactivity parameters for efficient conversion of biomass were predicted through the model. For all simulations, the number of tracers used at the start was 1 million to ensure a continuous availability of tracers throughout the reaction time and accomplish sufficient dissolution. This was also verified through the mean square displacement curves. The simulations where the tracers were exhausted before the intended residence time was completed were discarded. The results from the model were compared with the experimental results.

Experimentally, the topochemical concentration profiles of the cell walls were obtained from the Raman intensity or the color intensity values from the Raman images. The Raman intensity data over the appropriate wavelength region was proportional to the concentration

of lignin using appropriate calibrations. The normalized Raman intensity ratios are directly used in the model as an indicator of lignin dissolution. As mentioned earlier, the Raman intensity ratio can be correlated to the actual lignin concentration obtained from other wet techniques. In the work of Zhang, a linear correlation was be developed between the Raman intensity ratio and lignin concentration (Zhang, 2021). Such a relationship could also be developed for the type of biomass species and pretreatment conditions used in the current work using the appropriate experimental data and the lignin concentration. However, this is recommended as a part of future work. The current model predicts the relative changes in these intensities as an indicator of the extent of topochemical change due to pretreatment. Although the current model predicts lignin dissolution, it can also be extended to the cellulose and hemicellulose dissolution, considering the appropriate experimental data and reaction kinetics. This is also suggested as part of future work. The results from the transport reaction model applied for two different cases considered are presented and evaluated.

7.1 Poplar alkali pretreatment

Alkaline pretreatment methods such as treatment with NaOH, lime and KOH have been explored for biomass (Chang and Holtzapple, 2000; Keshwani and Cheng, 2010; McIntosh and Vancov, 2011; Mosier et al., 2005; Sierra-Ramírez et al., 2011). It primarily causes disruption of the lignin structure by breakage of ester linkages between lignin and hemicelluloses through saponification (McIntosh and Vancov, 2011; Sun and Cheng, 2002). They also target the removal of acetyl and uronic acid substitutions from hemicellulose and enhance the accessibility of hemicellulose and cellulose to enzymes and other reactants (Mosier et al., 2005). Alkali pretreatment methods generally require lower temperature, pressure and residence times compared to other techniques (McIntosh and Vancov, 2011). The amount of lignin removed depends on the pretreatment conditions such as time and temperature and the lignin content in the biomass feedstock (Chang and Holtzapple, 2000; McIntosh and Vancov, 2011). Hence it is necessary to determine optimum pretreatment conditions. Alkali pretreatment was carried out by Ji et. al, and the corresponding topochemical concentration profiles and associated images were obtained at

different pretreatment intervals using Raman spectroscopy. Blocks of Poplar samples were presoaked in 15 ml of 2% NaOH and heated in an oven for 20 min to reach a desired temperature of 121 °C, at which pretreatment was performed for different residence times (Ji et al., 2014). Raman spectra were acquired at 10, 30, 60, 90 and 180 min. The Raman intensity maps for lignin distribution were created at different time intervals using the spectra as shown in Figure 35.

The experimental topochemical concentration profile of the cell wall was obtained from the Raman images where the intensity of each voxel in the images is proportional to the concentration (Ji et al., 2014). The intensity of each voxel varied between 0 and 255 corresponding to minimum and maximum concentrations in the sample. The intensity of each voxel in the image was divided by 255 and then summed up to obtain a normalized bulk lignin concentration profile as a function of pretreatment time, as shown in Figure 67. The corresponding instantaneous reaction rate as a function of pretreatment time is shown in Figure 68. As seen from Figures 67 and 68, under these conditions, the bulk concentration of lignin decreased rapidly for the first 600 seconds reaching almost half of the initial concentration. Then over the next 3000 seconds, the remaining lignin was removed. However, as the reaction proceeded further, the rate of lignin dissolution decreased. This continued until most of the lignin reacted at about 5400 seconds, following which the rate of dissolution slowed down until almost all of the lignin was dissolved from the cell wall. This observation agreed with the work of Ji. Et al, which stated that, initially, a preferential delignification occurred in the secondary wall. When the residence time was over 3600 seconds, the reagent penetrated further into the cell wall causing dissolution in the middle lamella (Ji et al., 2014). Additionally, as seen in Figure 68, the rate of reaction also varied with time as per a pseudo first order reaction. The experimental concentration profile obtained from Raman spectroscopy could be correlated to that obtained from wet analytical techniques as mentioned earlier (Zhang, 2021). It is possible that a greater dissolution was observed in our case since thin slices of the wood chips were used for pretreatment and Raman imaging.

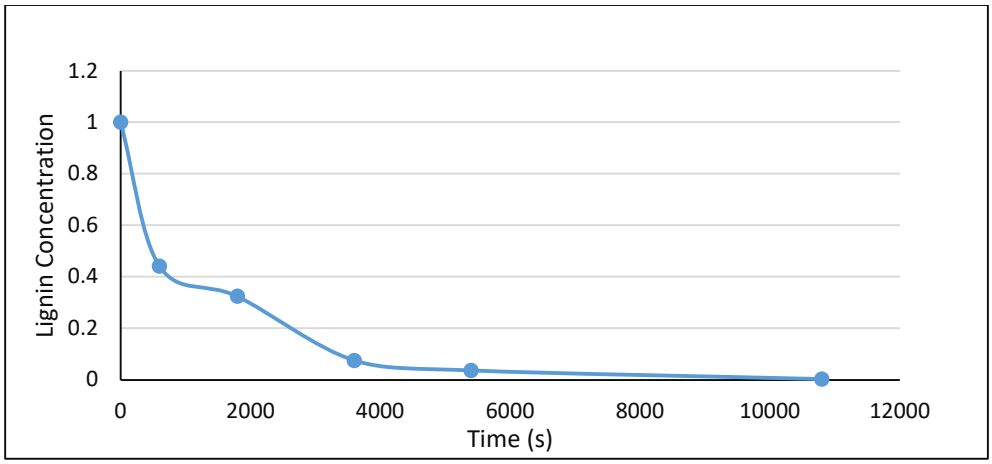

Figure 67. Relative bulk concentration profile of lignin during Poplar alkali pretreatment from experimental data (Ji et al., 2014)

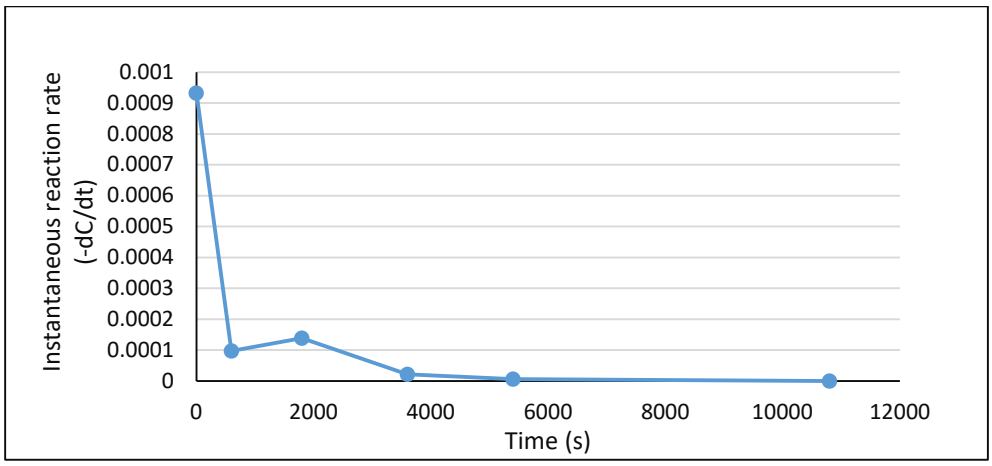

Figure 68. Instantaneous reaction rate of lignin during Poplar alkali pretreatment from experimental data

7.1.1 Model simulations using Raman images for Poplar

The transport reaction model developed here was applied to the Raman image of the untreated polar alkali sample which served as the initial condition for the simulations. Several simulations with different parameters were run for the entire course of the reaction and the results were analyzed. For all simulations, the number of tracers used at the start was 1 million. By comparison with the experimental data, the appropriate effective diffusivity and reaction rate constant were determined for a given biomass pretreatment process. The effect of varying the diffusion and reaction parameters of the system over a

wide range of Thiele moduli on the biomass dissolution kinetics were studied. The rate equation and conditions that matched with the experiment were determined. In the earlier work on pure gaseous diffusion, the diffusivity in the pore phase was precisely determined by kinetic theory (Defrenne et al., 2019). However, in the current liquid diffusion-reaction system, appropriate liquid diffusivity values were chosen to model the pore space diffusion. Similarly, the cell wall diffusivities were varied using the ratio of intrinsic diffusivities D* similar to the previous work (Defrenne et al., 2019).

In order to maintain uniformity of the results and include all features of the system, the values of effective diffusivity, D_{eff} and effective Thiele modulus, φ^2_{eff} were used to describe the diffusion characteristics for the system. The values of pore diffusivity Do were varied between 0.01 and 0.1 $\mu m^2/s$ (or 10^{-14} to 10^{-13} m^2/s). The ratio of diffusivity D* was varied between 0.2 and 0.8 to obtain cell wall diffusivities between 0.002 and 0.08 $\mu m^2/s$. The effective diffusivity thus obtained for the biomass structure from the simulations varied between 0.007 and 0.082 $\mu m^2/s$. The diffusivity values were reported in $\mu m^2/s$ since other measurements associated with the Raman images are of the order of μm. In addition, the local reaction rate constant was varied between 0.01 and 1 s^{-1}. Thus, the effect of diffusion and reaction parameters on the pretreatment kinetics using the transport-reaction model was evaluated over a wide range of φ^2_{eff}, namely, between 0.517 to 51.675. The Thiele modulus is inversely proportional to diffusivity and linearly proportional to local rate constant. The variation of the effective Thiele modulus over the entire range of D_{eff} and k' considered are shown in Figures 69 and 70, respectively. It was seen from Figure 69 that at any value of k', initially the Thiele modulus decreased significantly with the increase in the effective diffusivity. In this case, D_{eff} refers to the effective diffusivity of the structure and not the cell wall diffusivity alone, as used in the previous simulations for the sphere system. However, as D_{eff} increased gradually, the rate of decrease of φ^2_{eff} slowed down and beyond a certain diffusivity, the decrease in Thiele modulus was minimal. It was evident from Figure 70 that the effective Thiele modulus increased linearly with the local reaction rate for any given diffusivity for the range in which the model was evaluated. The concentration profile and reaction rate varied with change in effective diffusivity and local rate constant in a similar manner as φ^2_{eff}, as will be seen in later sections.

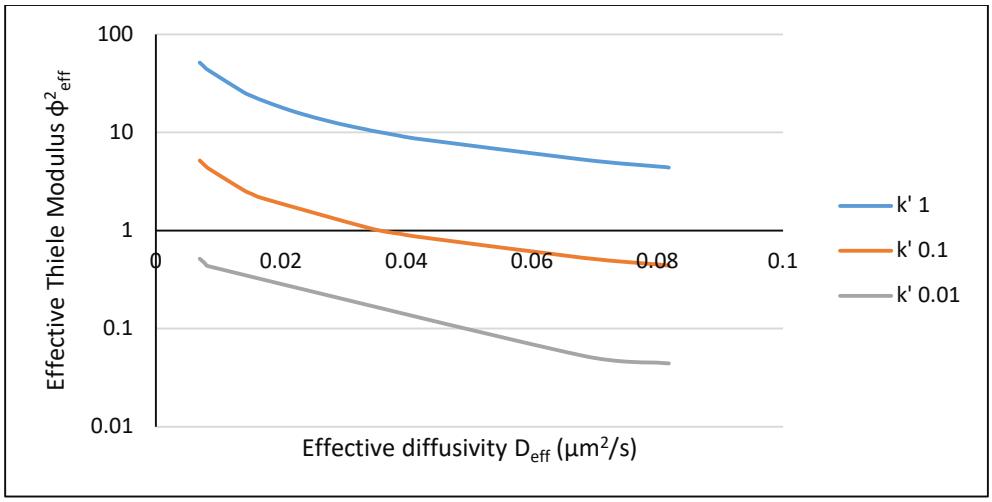

Figure 69. Variation of effective Thiele modulus with effective diffusivity

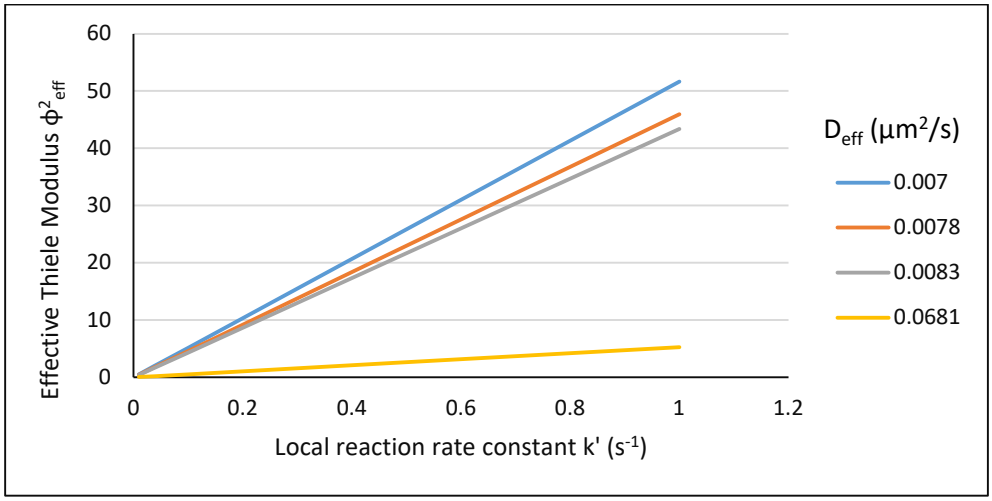

Figure 70. Variation of effective Thiele modulus with local reaction rate constant

7.1.2 Effect of diffusivity

Similar to the ideal system of periodic sphere structures, the effect of diffusivity on the pretreatment process was studied using the Raman images. The effective diffusivity was varied so as to obtain a wide range of effective Thiele moduli values. The effective diffusivity was used here as it encompassed the characteristics of both the pore and cell wall and was determined from the slope of displacement versus time curves that were obtained by carrying out pure liquid diffusion simulations. It was evident from Figure 69 that the effective diffusivity and Thiele modulus do not have a linear relationship. Lower

values of effective diffusivity affect the Thiele modulus more significantly than at higher values. A similar behavior was observed with lignin concentration changes. The concentration profiles as a function of time at two different values of local rate constants are shown in Figure 71 and 72. Figure 72a and 72b show the variation in concentration profiles at two different ranges of Thiele moduli. At the higher Thiele moduli range, an increase in the effective diffusivity (decrease in Thiele modulus) resulted in an increased lignin dissolution as seen in Figure 72a. This corresponds to small changes in diffusivity leading to larger changes in Thiele moduli as seen in Figure 70, and hence higher lignin dissolution as seen in Figure 72a. Hence, the concentration profiles were further apart. However, at the lower Thiele moduli range (higher diffusivities), any further in increase in effective diffusivity of the structure did not significantly contribute to additional lignin dissolution as seen in Figure 72b. Here, the Thiele modulus decreased by small amounts even though the effective diffusivity was increased, and the amount of lignin reacted did not vary greatly. Thus, the concentration profiles were extremely close to each other or almost overlapped. Hence, the diffusion enhanced reaction more significantly at higher Thiele moduli ranges. Similarly, the influence of diffusivity was more pronounced at higher local reaction rate constants as seen from Figure 72. The concentration profiles as well as the plots that will follow in further sections used φ^2_{eff} as a uniform parameter to track the changes since it included both the diffusive and reactive characteristics of both the pore and cell wall.

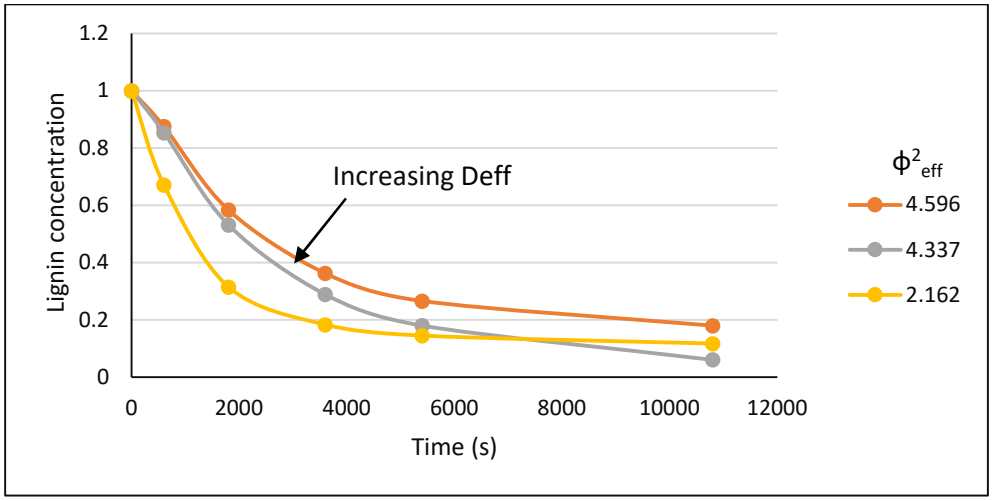

Figure 71. Effect of diffusivity on lignin concentration profile (k' 0.1 s^{-1})

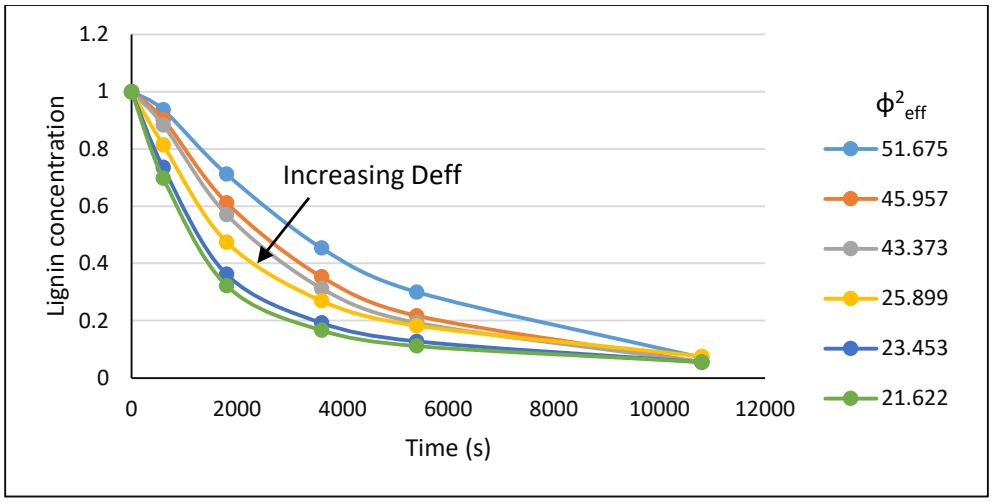

Figure 72a. Effect of diffusivity on the lignin concentration profile at higher φ^2_{eff} (k' $1s^{-1}$)

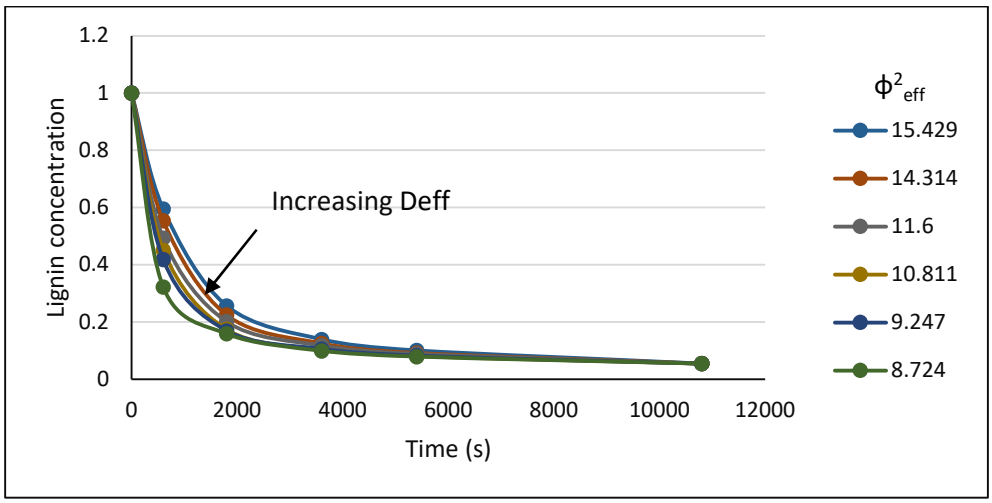

Figure 72b. Effect of diffusivity on the lignin concentration profile at lower φ^2_{eff} (k' $1s^{-1}$)

Additional observations on the effect of diffusivity were made by studying the concentration versus effective Thiele modulus plots at different time periods as shown in Figures 73 and 74. The corresponding spatial concentration distribution maps obtained at different time periods for different Thiele modulus values are shown in Figures 75 through 77. These figures reiterate the earlier observation that there was a greater impact of diffusivity on the concentration profiles at higher Thiele moduli than at lower Thiele moduli. It was evident that most of the concentration changes occurred during the initial part of the reaction in most cases due to greater and easier availability of lignin. As time proceeded and the lignin reacted, the tracers needed to penetrate further into the cell wall

to access the lignin molecules leading to smaller changes in concentration. However, at higher values of the local rate constant, it was observed that at higher Thiele moduli (lower effective diffusivities), only a small amount of the lignin reacted close to the start of the reaction after which greater changes in the concentration were observed.

The changes in lignin dissolution were better visualized through the concentration maps shown in Figures 75 through 77. It is also interesting to note that at lower diffusivities, the predicted topochemical distribution from the simulation showed a gradual dissolution in the cell wall close to the lumen which then progressed to the interior regions as seen in Figure 75. Comparing this to Figure 76, where a higher diffusivity was used at the same reaction time (i.e., 600s or 1800s), there was greater penetration of the tracers into the interior regions of the cell wall resulting in faster dissolution of lignin. This phenomenon is due to the fact that at higher Thiele moduli, or lower diffusivity the tracer particles took a longer time to penetrate through the cell wall and access the lignin molecules. In addition, the reaction probability is low leading to a slow reaction and minimal concentration changes at the beginning. However, as the process continued, a larger number of the tracers penetrated through the cell wall and encountered more lignin molecules leading to greater reaction as seen from the concentration profiles in Figures 73 and 74.

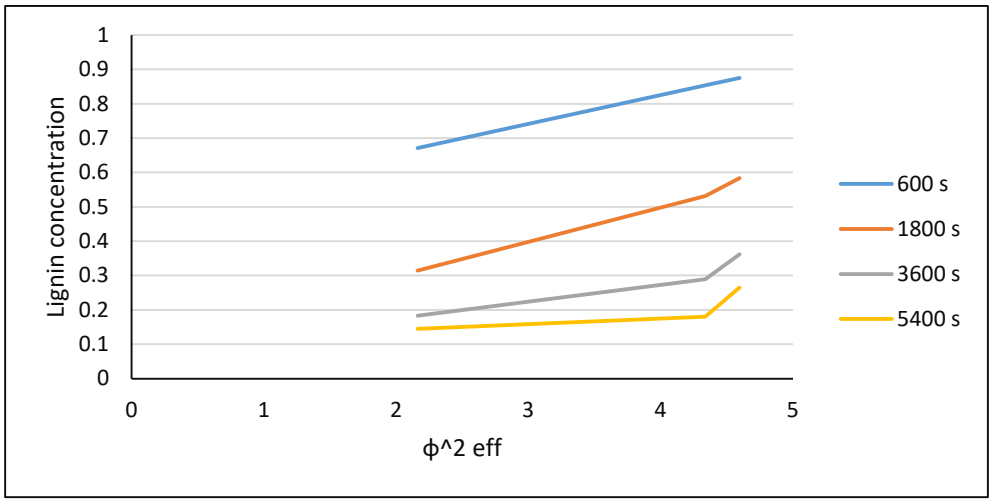

Figure 73. Variation of lignin concentration with diffusivity at different times during the pretreatment process (k' 0.1 s^{-1})

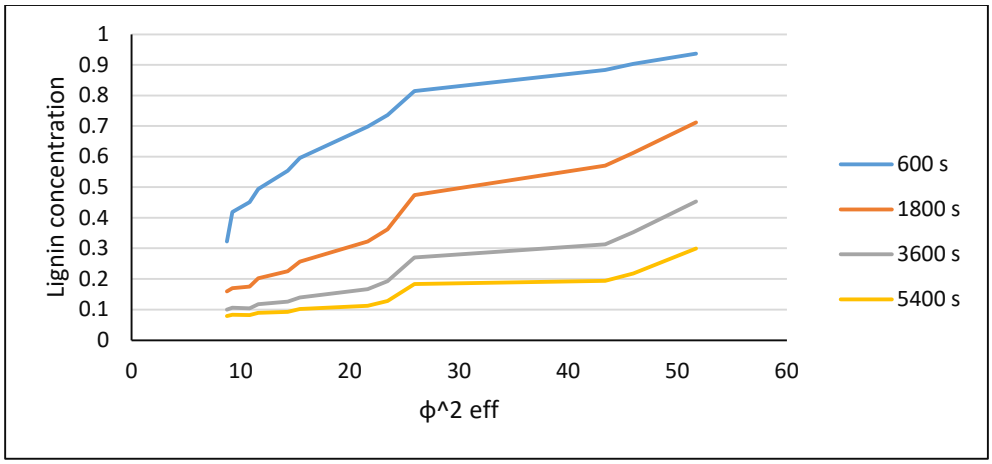

Figure 74. Variation of lignin concentration with diffusivity at different times during the pretreatment process (k' $1s^{-1}$)

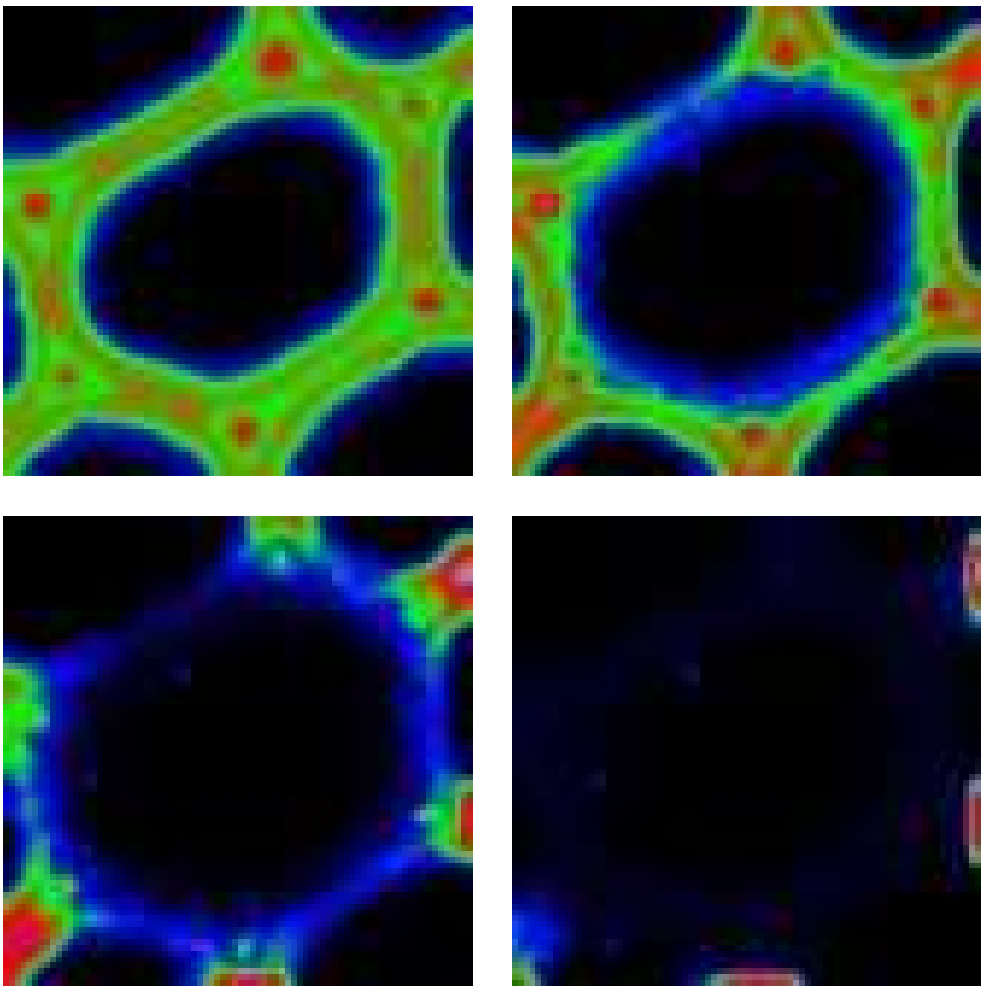

Figure 75. Spatial concentration map of lignin during Poplar alkali pretreatment at 0s (top left), 600s (top right), 1800s (bottom left) and 3600s (bottom right) (φ^2_{eff} 45.957)

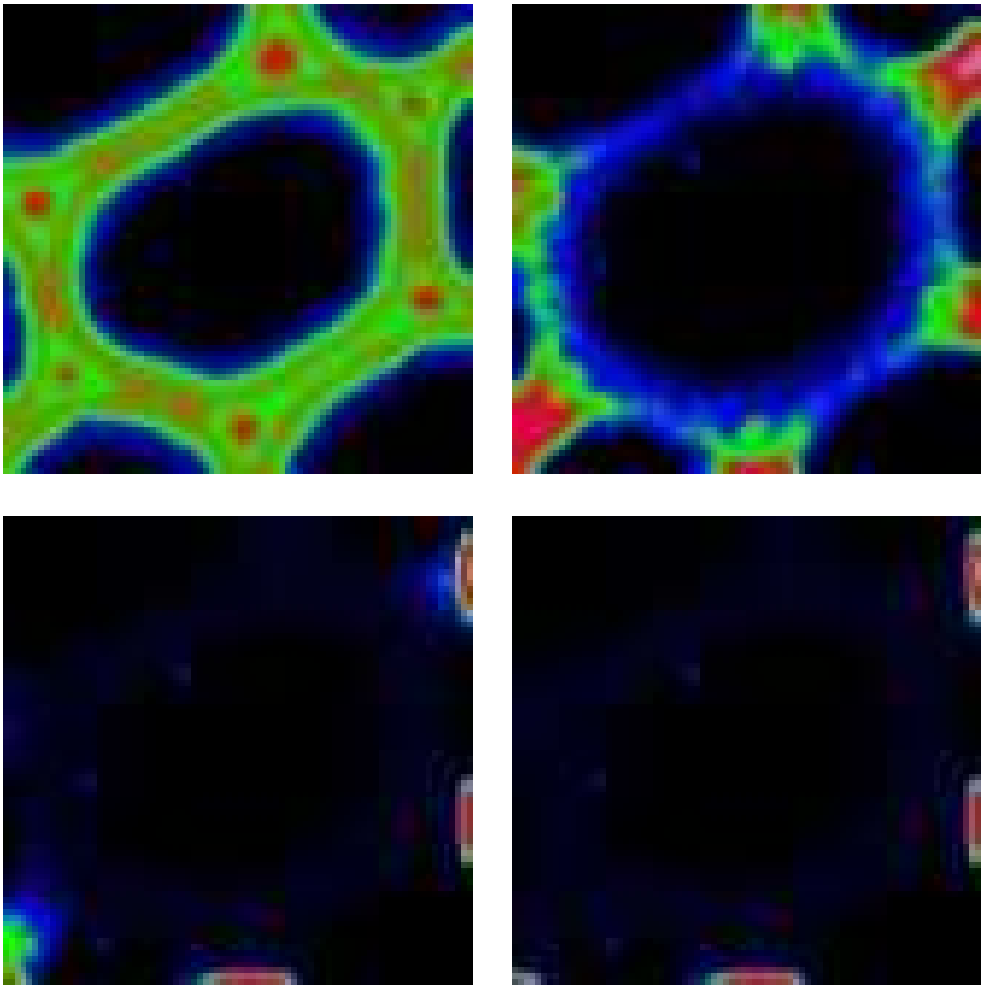

Figure 76. Spatial concentration map of lignin during Poplar alkali pretreatment at 0s (top left), 600s (top right), 1800s (bottom left) and 3600s (bottom right) (φ^2_{eff} of 21.622)

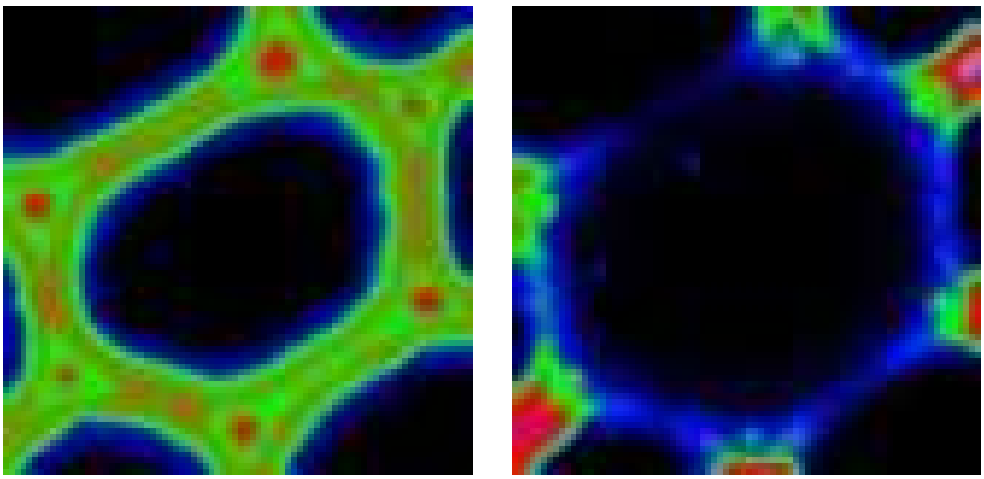

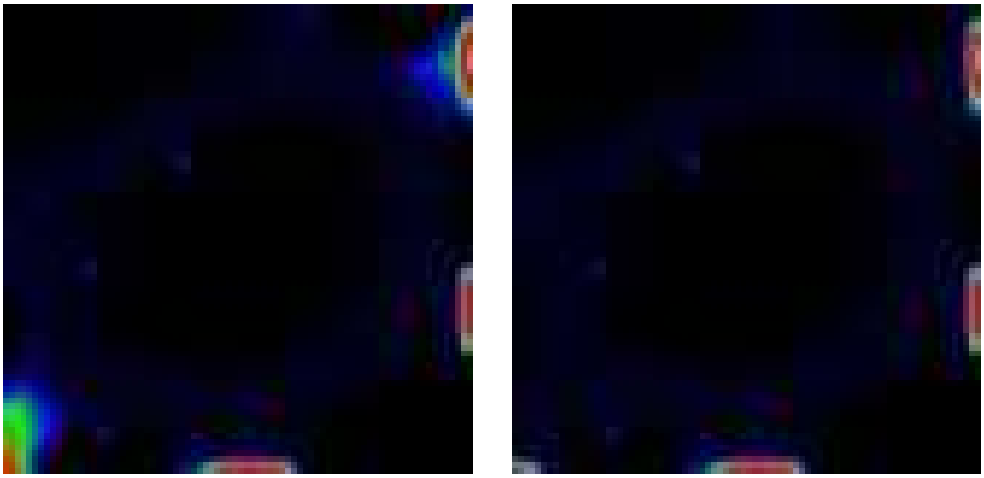

Figure 77. Spatial concentration map of lignin during Poplar alkali pretreatment at 0s (top left), 600s (top right), 1800s (bottom left) and 3600s (bottom right) (φ^2_{eff} 11.6)

The effect of diffusivity on the instantaneous reaction rate -dC/dt at different k' values are shown in Figures 78 and 79. As the reaction rate has a negative value, (-dC/dt) was used in the plots. At the beginning, the reaction rate was high in most cases due to abundant availability of lignin. As the reaction proceeded, more lignin was consumed, and the reaction rate decreased until almost all of the lignin was consumed. The variation of reaction rate with diffusivity was in accordance with the variation of concentration profile trends. The variation in reaction rates with time was greater during the beginning of the reaction due to a higher lignin concentration available for reaction. As the reaction proceeded and more of the lignin was consumed, the reaction rate decreased more gradually, especially at high diffusivities. Additionally, the reaction rate decreased faster with time at lower φ^2_{eff} or higher D_{eff} indicating greater reaction. It was seen that at low D_{eff} or high φ^2_{eff}, there was an initial delay in the lignin dissolution as indicated by a low reaction rate. The spatial concentration maps also showed this feature (Figures 75 through 77). At higher φ^2_{eff}, due the combination of low D_{eff} and low P_K, the tracers required a longer time to penetrate into the cell wall and react with the lignin molecules. This was also associated with an increase in reaction rate during the initial stages of reaction at higher φ^2_{eff}, resulting from a lag in the reaction as seen in Figure 78 and 79. With time, a larger number of tracers penetrated the cell wall and reacted leading to faster reaction in the later stages. At lower φ^2_{eff}, the tracers penetrated further into the cell wall faster and reacted more uniformly with lignin leading to a gradual decrease in the reaction rate.

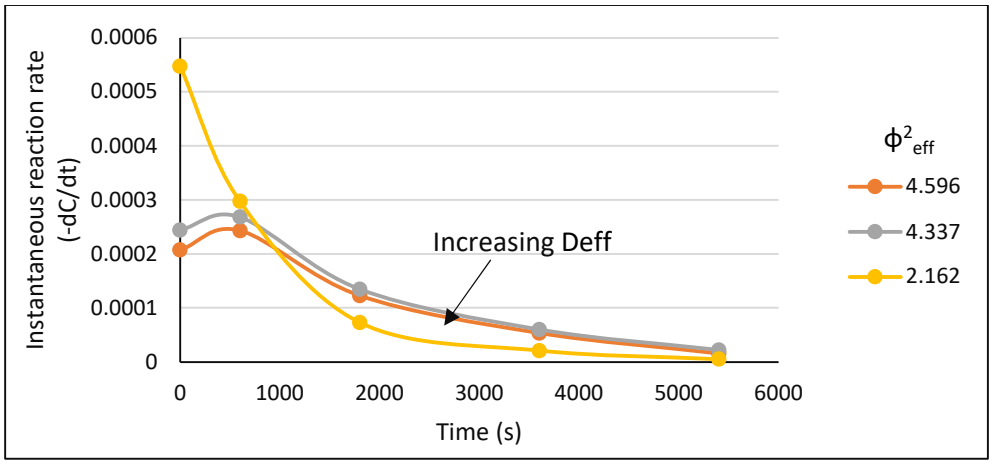

Figure 78. Effect of diffusivity on the instantaneous reaction rate (k' 0.1 s^{-1})

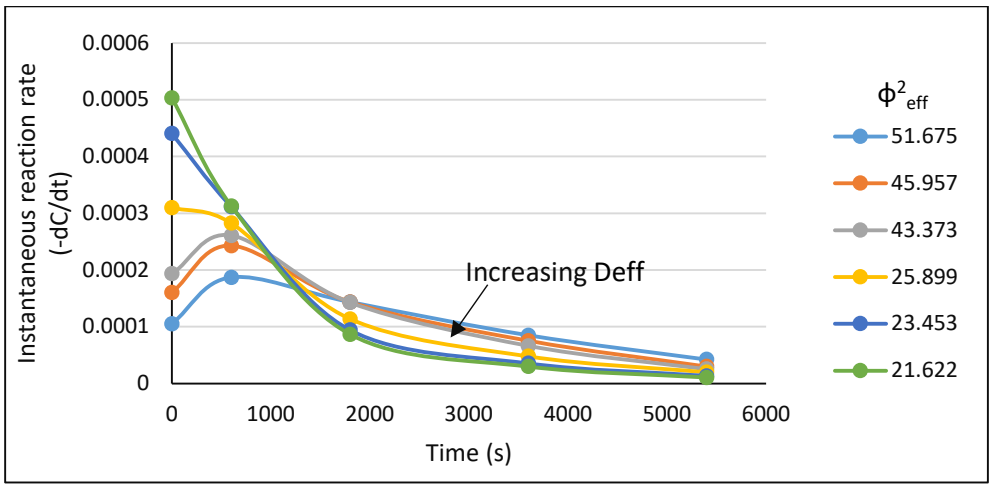

Figure 79a. Effect of diffusivity on the instantaneous reaction rates at higher φ^2_{eff} (k' 1s^{-1})

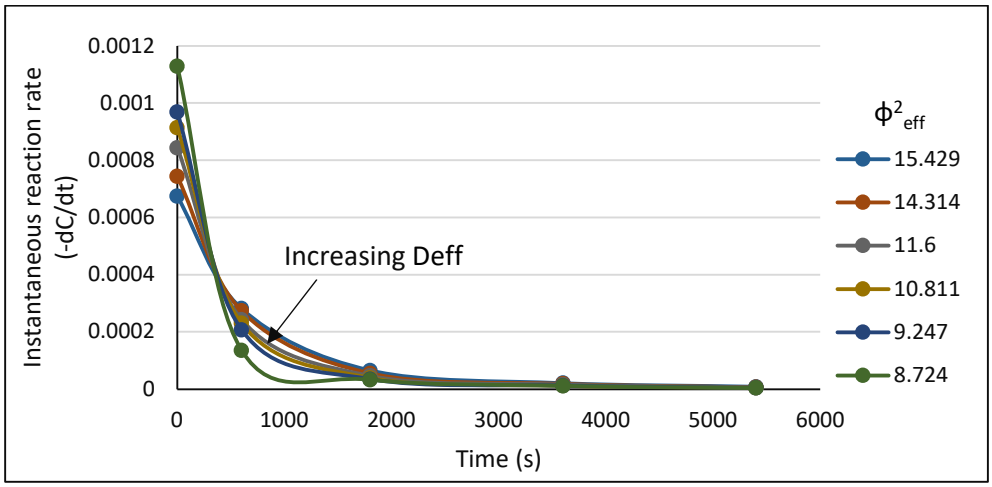

Figure 79b. Effect of diffusivity on the instantaneous reaction rates at lower φ^2_{eff} (k' 1s^{-1})

One of the important parameters in process design and development is to derive an expression for the effective bulk lignin dissolution rate constant. Based on the predicted lignin concentration profiles, an effective rate constant for the bulk lignin dissolution, K_{eff} (s^{-1}), that accounted for both transport and reaction was determined at any time t similar to what was determined in the ideal system of spheres as,

$$dC_L/dt = -K_{eff}C_L \quad (30)$$

If K_{eff} is a constant and independent of time it is obtained from the following equation,

$$C_L = C_{LO}\, exp(-K_{eff}t) \quad (31)$$

The behavior of K_{eff} at lower diffusivity or higher Thiele moduli was found to be different from that at higher diffusivities or lower Thiele moduli at any given k'. At lower diffusivity or higher Thiele modulii, the bulk concentration profile of lignin at any time was given by equation 31 where C_{LO} was the initial concentration of lignin. Using the above equation, a curve fit was performed on the concentration results obtained from simulation to predict K_{eff}. The effective rate constant thus predicted was independent of time as expected for first order reaction. This is attributed to the fact that a higher Thiele modulus resulted in a lower reaction probability and hence the tracers required a longer time to diffuse through the cell wall and react with lignin. The time required for transport of the tracers was greater than the time required for reaction. The K_{eff} values for different φ^2_{eff} were reported in Table 9. From the table, it is evident that K_{eff} increased with increase in diffusivity or decrease in Thiele modulus in the range of Thiele moduli considered for simulations, indicating greater dissolution of lignin at higher diffusivities. The rate of lignin dissolution in this regime is limited by the diffusion of the tracers due to the higher Thiele modulus of the system.

φ^2_{eff}	k'	K_{eff}
4.337	0.1	0.00033
4.596	0.1	0.00026
21.622	1	0.00056
23.453	1	0.00049
25.899	1	0.00036
43.373	1	0.00030
45.957	1	0.00028
51.675	1	0.00021

Table 9. Effective rate constant for bulk dissolution of lignin for higher φ^2_{eff}

With the increase in diffusivity or decrease in Thiele modulus at any given k', the tracers diffused faster into the cell wall leading to greater lignin dissolution. Consequently, as seen earlier, a faster reaction rate was observed which decreased gradually over time. The time required for transport of the tracers was comparable to the time required for reaction. In this regime, the effective rate constant obtained using the approach used earlier, was found to vary with time. The rate of lignin dissolution in this regime was limited by surface reaction due to the lower Thiele modulus of the system This time dependent nature of the effective overall rate constant was also observed experimentally and has been reported in previous literature (Dang and Nguyen, 2006; Keshwani and Cheng, 2010; Kopelman, 1988; Montané et al., 1994). This is quite intriguing to observe a time dependent effective rate constant under some conditions of diffusivity and reactivity and not at other conditions.

The variation of the time dependent effective rate constant for different Thiele moduli is shown in Figures 80. It was observed that the behavior of K_{eff} with diffusivity was analogous to the behavior observed with the rate of reaction. The effective rate constant decreased rapidly at the beginning due to greater lignin consumption leading to faster reaction and then decreased more gradually with time due to slower reaction. Similar to the reaction rate, greater the diffusivity, higher the effective rate constant due to greater lignin dissolution. At higher diffusivities, the effective rate constant was found to be a function of time. The data from the simulation for K_{eff} versus time was curve fitted for the various conditions and the best fit was given by the following power law relation,

$$\boldsymbol{K_{eff} = K_o t^{-n}} \qquad (32)$$

Where t is the time, and K_O and n are constants that are dependent on the effective Thiele modulus, biomass species and pretreatment process. The values of parameters K_O and n for different φ^2_{eff} that were obtained by curve fitting are mentioned in Table 10. A similar relationship has been reported in earlier literature and the authors have attributed this behavior to the transport characteristics and differences in kinetic behavior of the various lignocellulose components and their monomeric species. (Dang and Nguyen, 2006; Keshwani and Cheng, 2010). Using the above relationship, and pseudo first order kinetic principles, the lignin concentration at any time can be given by,

$$C_L = C_{LO} exp\left(-K_O \frac{t^{1-n}}{1-n}\right) \quad (33)$$

Using this expression, it is possible to predict the bulk lignin concentration profile as a function of time and compare it to the experimental data. As shown in Figure 81, the bulk concentration profiles obtained from the model were in close agreement with that from the empirical relation described in equation 33 that used for curve fitting. for a given Thiele modulus.

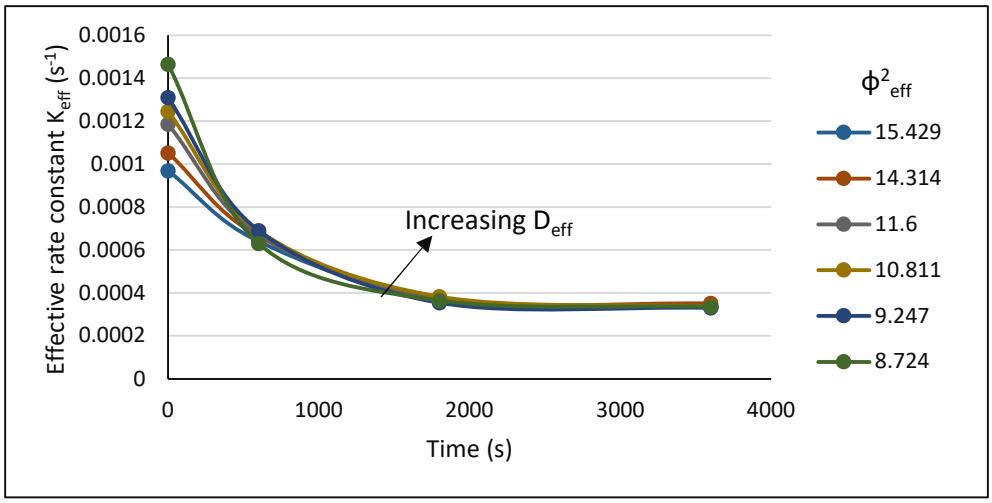

Figure 80. Variation of effective rate constant with time at high diffusivities (k' $1s^{-1}$)

φ^2_{eff}	k'	Ko	n
2.162	0.1	0.0035	0.2729
8.724	1	0.0078	0.3954
9.247	1	0.0143	0.4757
10.811	1	0.0116	0.4429
11.600	1	0.0109	0.4378
14.314	1	0.0090	0.4104
15.429	1	0.0083	0.4029

Table 10. Estimated model parameters Ko and n used for determination of K_{eff}

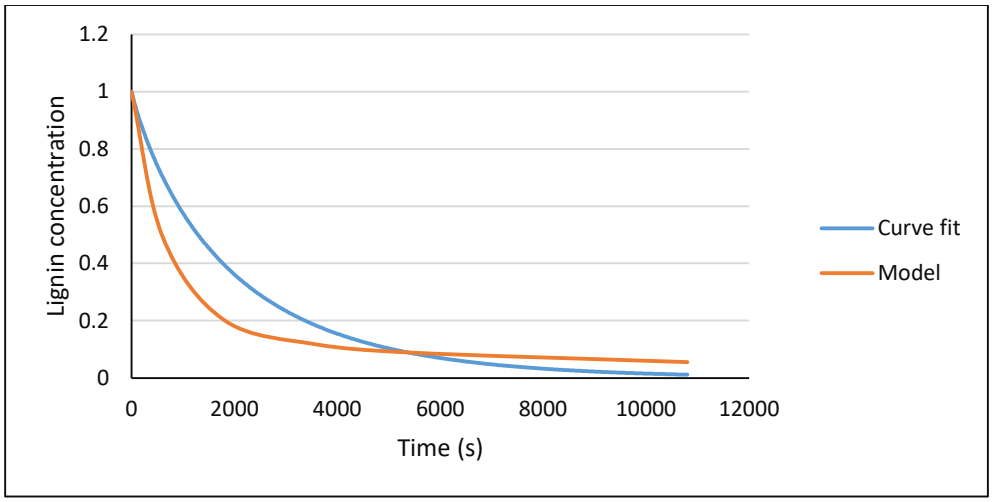

Figure 81. Comparison of concentration profiles from the model and curve fit (φ^2_{eff} 11.6)

Another important parameter that was determined from the simulation was the transport coefficient of the tracers K_T, which is based on the mean survival time of the tracers as given by equation 29. It gives an insight into the effect of transport of tracers on the pretreatment process. Since the process follows pseudo first order kinetics, the tracers have an indirect but significant impact on the lignin dissolution characteristics. The transport coefficient is an indicator of how far the tracers penetrated through the cell wall and how fast they were consumed by reaction with the cell wall lignin. Figures 82 and 83 show the variation of K_T over a wide range of diffusivities. It was seen that changing the diffusivity of the pore space and cell wall affected K_T differently. Increasing the pore space diffusivity allowed the tracers to reach the cell wall faster and access the lignin molecules. As a result, the tracers reacted faster with the lignin molecules, thereby decreasing their survival time, and increasing the transport coefficient. However, this does not necessarily mean that the lignin dissolution increased. Although, the tracers reached the cell wall interface earlier, the penetration of the tracers into the cell wall and further reaction depend on the diffusivity of the cell wall. The decreased survival time of tracers at higher pore diffusivities also indicate that it is necessary to have a sufficient number of tracers to begin with so that there are a considerable number of tracers available through the entire course of the reaction.

Figures 82 and 83 also showed that that at any given pore diffusivity, increasing the cell wall diffusivity allowed the tracers to penetrate further into the cell wall before reacting leading to an increased survival time and a decreased transport coefficient. Although the transport coefficient decreased, it was revealed from previous sections that lignin dissolution increased with the cell walls being more diffusive. However, it is important that even if the cell wall diffusivity was enhanced, the diffusivity of the pore space should be high enough to ensure that the tracers come in contact with the cell wall early on and diffuse without creating a lag in the onset of lignin dissolution as seen earlier in Figure 79a. Additionally, greater changes in the transport coefficient was observed at lower diffusivities of both pore space and cell wall than at higher diffusivities analogous to changes observed in the other reaction characteristics as previously discussed. Thus, depending on the pore and cell wall diffusivities of the system, either an increase or decrease in the transport coefficient leads to a greater lignin dissolution. The transport coefficient is an indicator of the rate of consumption of tracers, and it alone is not sufficient to determine the extent of lignin dissolution.

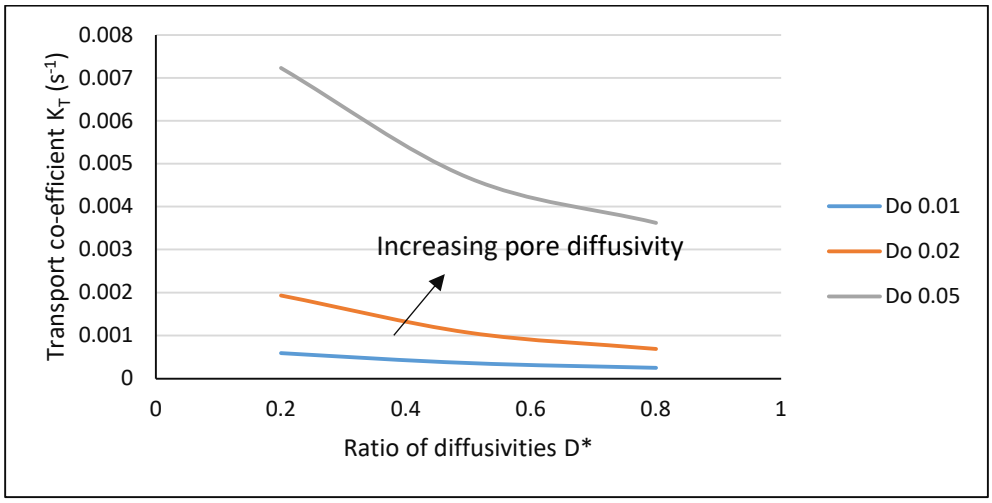

Figure 82. Effect of diffusivity on the transport coefficient K_T (k' $0.1s^{-1}$)

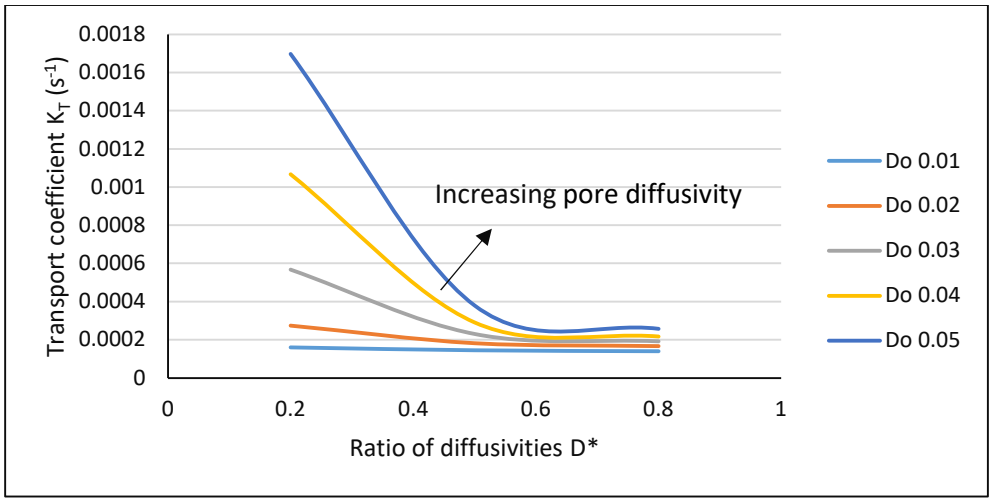

Figure 83. Effect of diffusivity on the transport coefficient K_T (k' $1s^{-1}$)

The displacement-time curves of the tracers obtained from the diffusion-reaction simulation reveal several characteristics about the transport of tracers and their impact on the pretreatment process similar to the transport coefficient. It is an indicator of how far the tracers were able to diffuse through system before they were consumed by reaction. In case of pure diffusion processes, the mean square displacement is linearly proportional to the time and was used to estimate the effective diffusivity as mentioned earlier. However, in case of a diffusion-reaction process, the mean square displacement follows a linear relationship with time in the earlier stages and then remained constant over time in the later stages. This is because the tracers were consumed for reaction and their count decreased over time leading to almost a constant mean square displacement over time. A similar behavior was observed in the literature with "biased" random walk and here the "bias" can be related to the reaction that is taking place. The displacement of the tracers was greater at higher diffusivities or lower φ^2_{eff} as seen from Figures 84 and 85. This is a result of the tracers diffusing further into the system before consumption which facilitated a greater access to the lignin content in the cell wall, leading to greater dissolution. The concentration profiles in Figures 71 and 72 and the reaction rate plots in Figures 78 and 79 also corroborated this observation. The increase in the mean square displacement with increased diffusivities resulted in longer survival times and lower transport coefficient as observed in Figures 83 and 84. The impact of diffusivity on the displacement of tracers was greater at lower diffusivities than at higher diffusivities as observed with other reaction

characteristics. The transport coefficient and the displacement time curves of the tracers clearly explained the impact of tracer transport and consumption on the overall process.

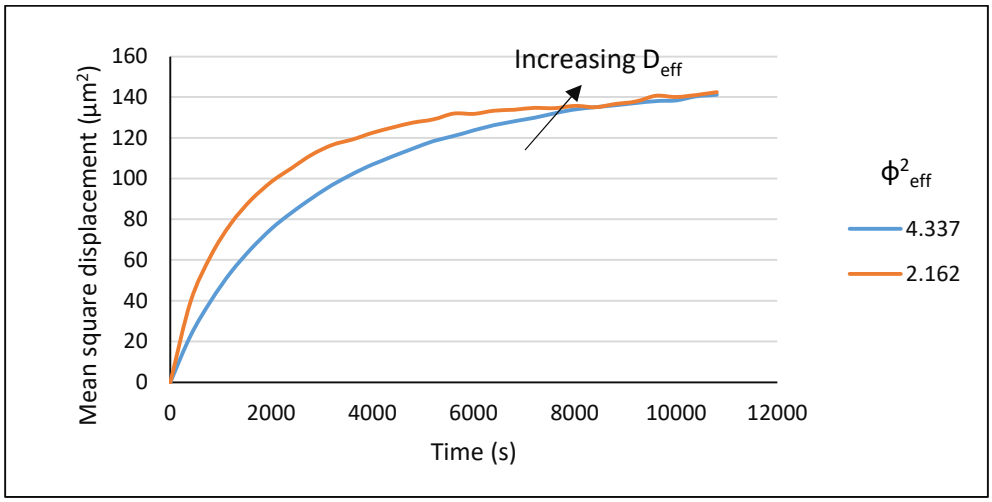

Figure 84. Effect of diffusivity on the mean sq. displacement for different φ^2_{eff} (k' 0.1 s^{-1})

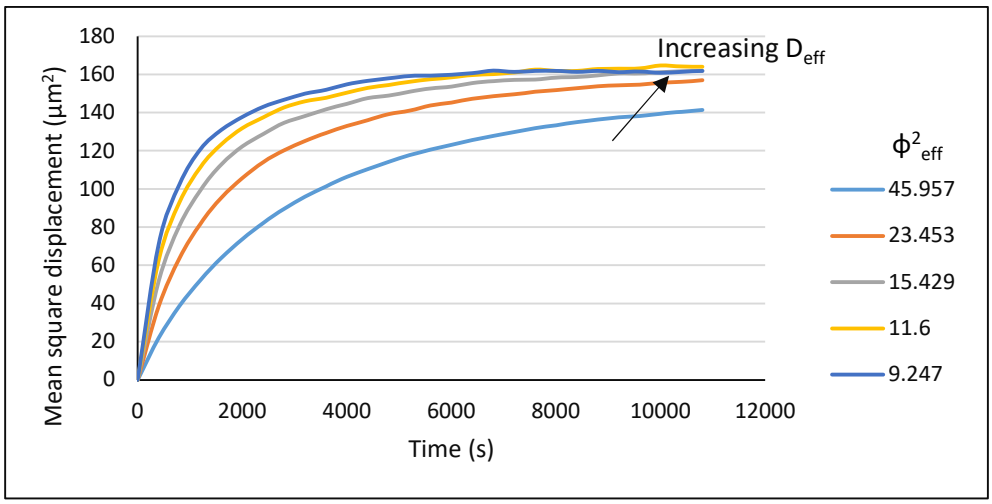

Figure 85. Effect of diffusivity on the mean sq. displacement for different φ^2_{eff} (k' 1 s^{-1})

From the analysis of the different parameters, it was clear that higher values of effective diffusivities yielded better results. The reaction was faster, and a higher dissolution of lignin was observed. In addition, higher diffusivities also enabled better transport of the tracers by allowing them to diffuse faster and further into the system allowing greater access to the lignin content. Thus, it is clear that diffusion enhanced reaction. In addition, the transport coefficient K_T is analogous to the rate of tracer

consumption by the cell wall lignin. Modifying the reaction conditions such as increasing the temperature or opening up the cell walls by other thermomechanical or thermochemical pretreatments to increase diffusivity and access to the interior regions of the cell wall can facilitate better reaction. This was more effective at lower diffusivities. At very high diffusivities, enhancing the diffusivity further results in minimal increase in lignin dissolution. Such a process could require very high energy and costs and may not be optimal. This observation is very important in deciding the reaction conditions and the extent to which the transport characteristics need to be improved for more efficient conversion.

7.1.3 Effect of local reaction rate constant

The local reaction rate constant k' is purely dependent on the kinetic behavior of the reactants involved (i.e., alkali and lignin) and does not account for any transport related behavior. It is different from the effective rate constant K_{eff} determined from the simulation. In order to understand the effect of purely the reaction between the tracers and lignin on the overall system, the effect of varying k' was analyzed similar to the bed of sphere cases. Since there is no reaction occurring in the pore phase, the effect of k' is seen only in the cell wall. The results were interpreted in terms of the effective Thiele modulus instead of k' to maintain uniformity. It was seen earlier from equation 15 that an increase in k' led to an increase in Thiele modulus and a decrease in reaction probability. The effect of local rate constant on the lignin concentration profile is shown in Figure 86. Higher k' or higher φ^2_{eff} values led to higher lignin dissolution. This was also reflected in the spatial concentration maps at different times in Figure 87 and 88. Although, the reaction probability reduced with increase in k', a greater amount of lignin was dissolved with each encounter that led to a reaction. It was also observed that the impact of increasing k' was greater at lower effective diffusivities than at higher effective diffusivities since the Thiele modulus changed more drastically at lower effective diffusivities than at higher effective diffusivities.

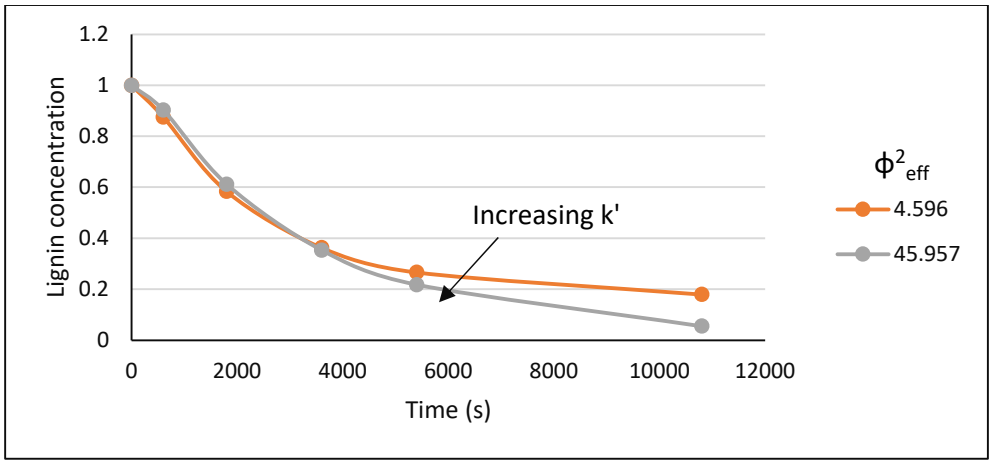

Figure 86a. Effect of local rate constant on the lignin concentration profile (D_{eff} 0.00783 $\mu m^2/s$)

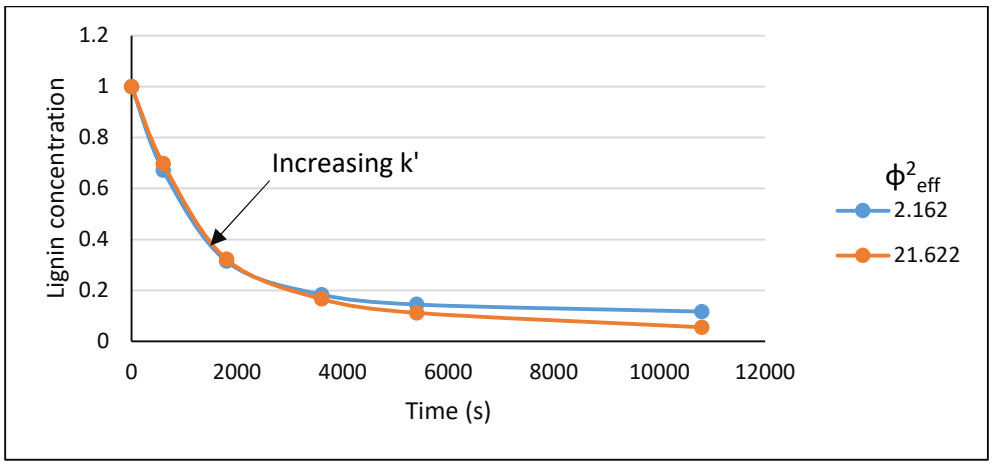

Figure 86b. Effect of local rate constant on the lignin concentration profile (D_{eff} 0.1665 $\mu m^2/s$)

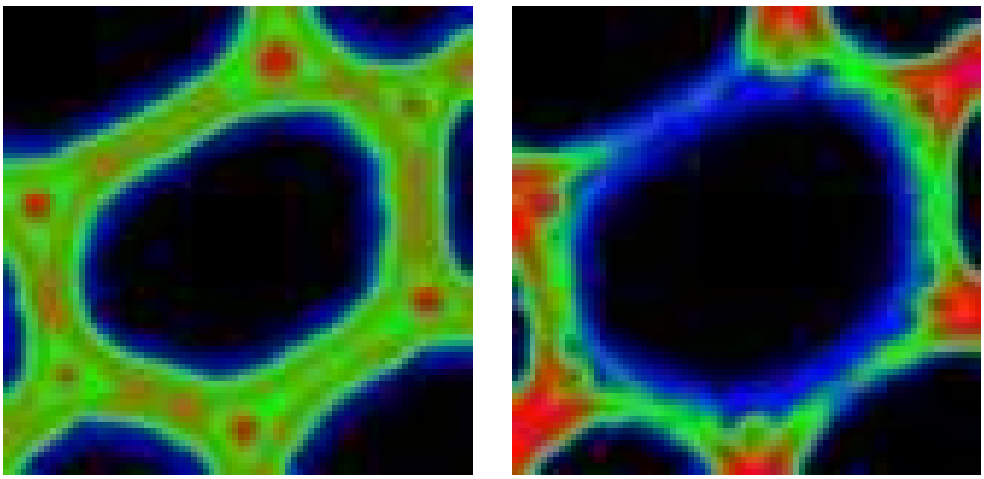

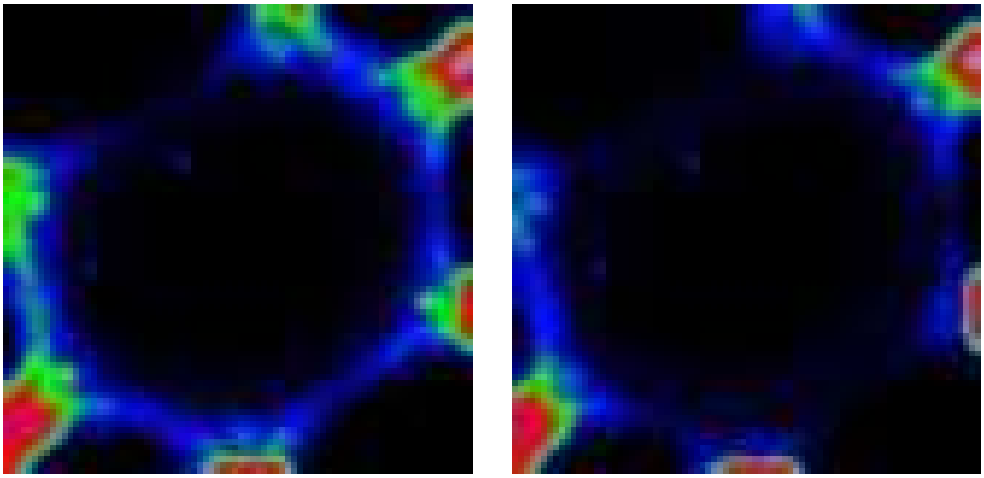

Figure 87. Spatial concentration map of lignin during Poplar alkali pretreatment at 0s (top left), 600s (top right), 1800s (bottom left) and 3600s (bottom right) (φ^2_{eff} 2.162)

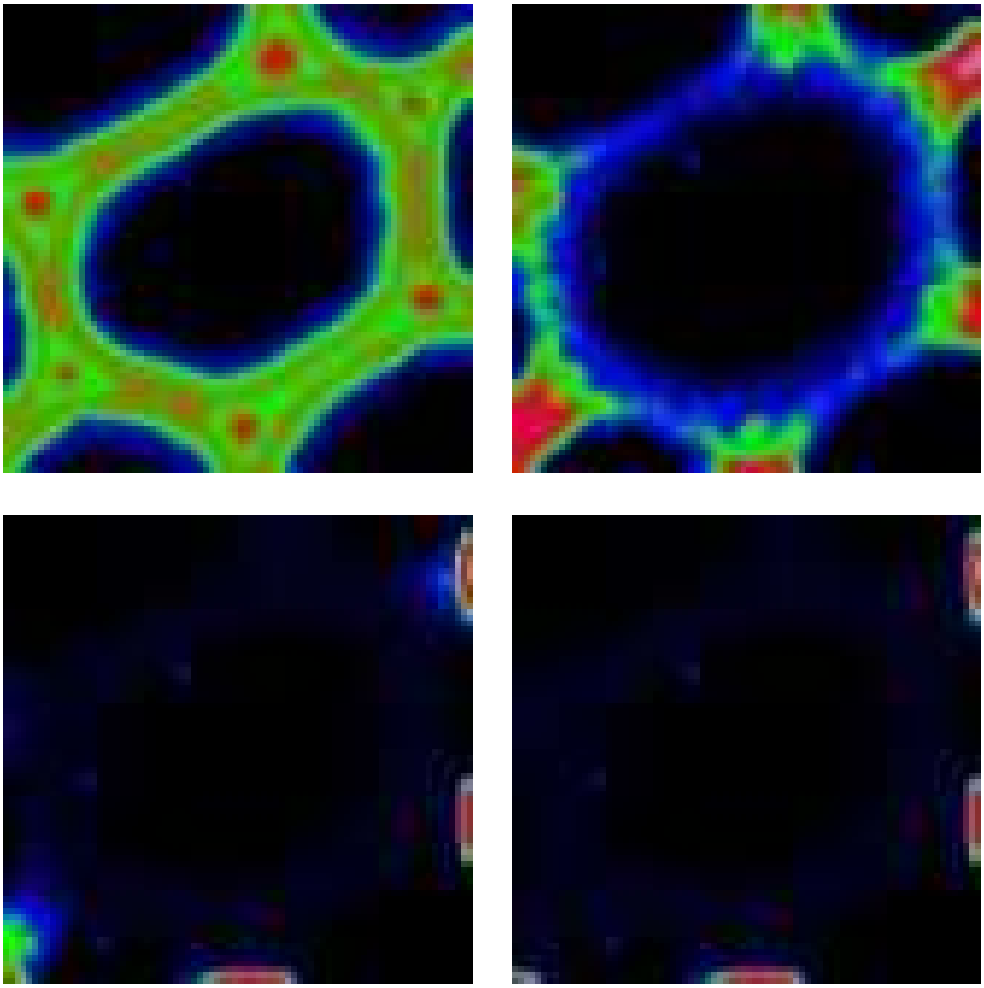

Figure 88. Spatial concentration map of lignin during Poplar alkali pretreatment at 0s (top left), 600s (top right), 1800s (bottom left) and 3600s (bottom right) (φ^2_{eff} 21.622)

The variation of the instantaneous rate of reaction with k' is shown in Figure 89. The rate of reaction increased with increase in k' due to greater dissolution. The impact of k' was greater at lower D_{eff} values than at higher D_{eff} values. An initial lag in the onset of lignin dissolution was observed at lower effective diffusivities and correspondingly a longer time was taken to reach the reaction sites. The initial lag in lignin dissolution at lower diffusivities was more pronounced at higher k' values than at lower k' values. This can be explained by the fact that low k' values resulted in a high reaction probability and the process is dominated by a fast reaction as compared to diffusion. However, at higher k' values, the combination of low diffusivity and reaction probability leads to slower diffusion and reaction leading to a bigger lag in lignin dissolution at the beginning.

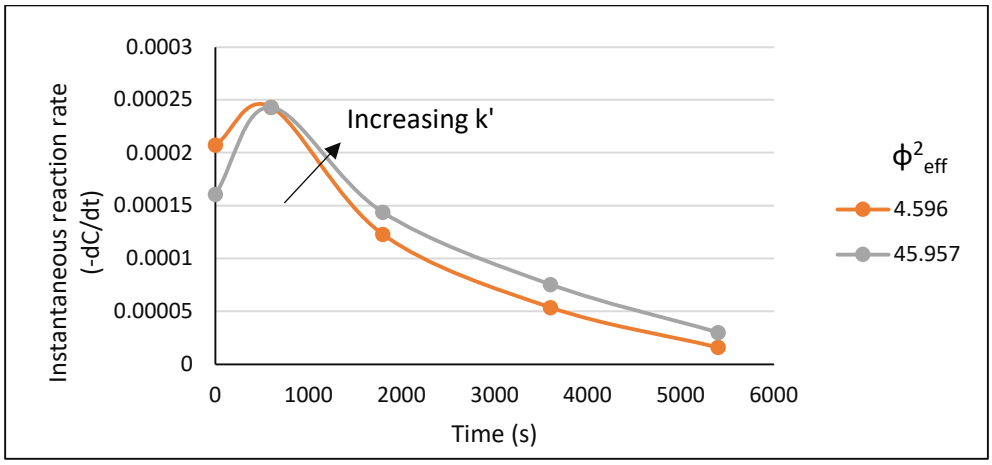

Figure 89a. Effect of local rate constant on the instantaneous reaction rate(D_{eff} 0.008 $\mu m^2/s$)

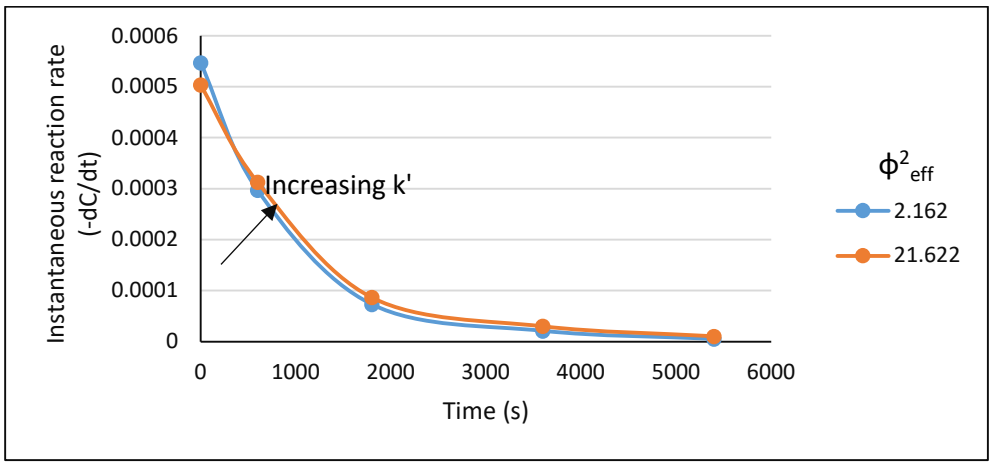

Figure89b. Effect of local rate constant on the instantaneous reaction rate(D_{eff} 0.167 $\mu m^2/s$)

As mentioned earlier, the effective rate constant K_{eff} was found to be time independent at lower diffusivities and a function of time at higher diffusivities. The variation of the effective rate constant with k' at higher diffusivities where K_{eff} is time dependent is shown in Figures 90a and b. In this regime, increasing the local rate constant resulted in a slight decrease in the K_{eff} which was attributed to a lower reaction probability. The effect of local rate constant on K_{eff} was studied in both these regimes separately. The variation of the effective rate constant with k' at lower diffusivities where K_{eff} is independent of time is shown in Table 11. Increasing the local rate constant increased the effective rate constant initially but beyond a particular k', the effective rate constant decreased. This is due to very low reaction probability at high k' values.

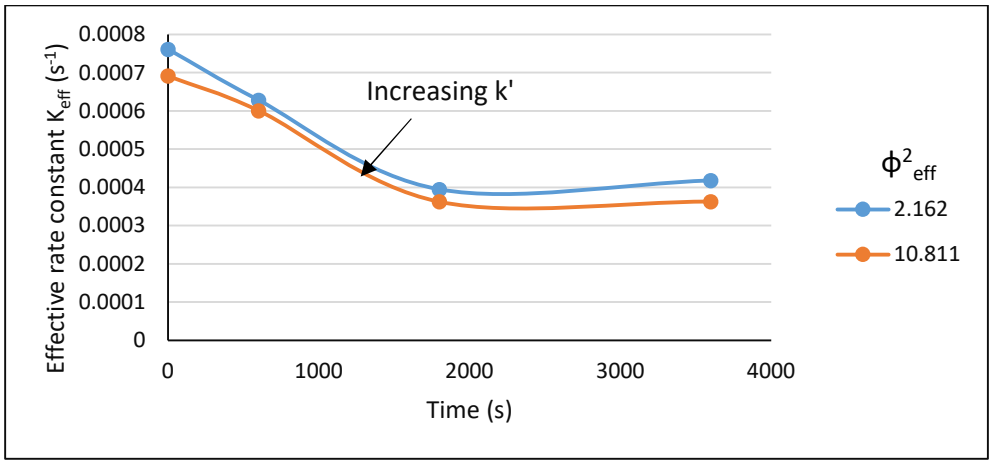

Figure 90a. Effect of local rate constant on the effective rate constant (D_{eff} 0.0167 $\mu m^2/s$)

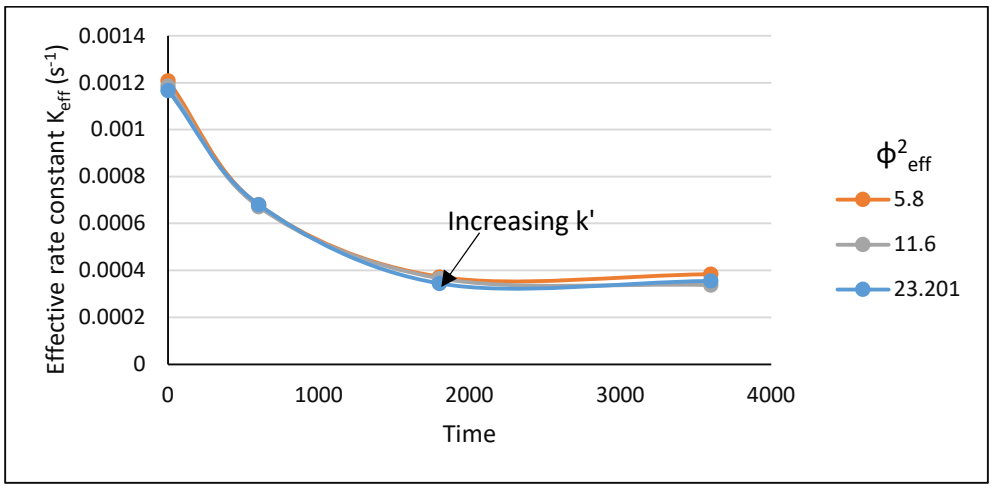

Figure 90b. Effect of local rate constant on the effective rate constant (D_{eff} 0.031 $\mu m^2/s$)

D_{eff}	φ^2_{eff}	k'	K_{eff}
0.007833	4.596	0.1	0.00026
	22.979	0.5	0.0003
	45.957	1	0.00028
0.01665	21.622	1	0.00056
	43.243	2	0.0003

Table 11. Variation of effective rate constant with local rate constant at low D_{eff}

The local reaction rate also has an effect on the tracer consumption rate. In order to understand this aspect, the variation of survival time and transport coefficient K_T with the local reaction rate k' was studied. Increasing the local rate constant led to a decrease in the reaction probability. Hence, the possibility of reaction occurring every time the tracer encountered the lignin in the cell is lower. As a result, the tracers are consumed at a slower rate leading to an increase in their mean survival time and a decrease in the transport coefficient. The effect of local rate constant on the transport coefficient at different effective diffusivities is shown in Figure 91. The effect of k' on the transport coefficient is greater at lower diffusivities than at higher diffusivities due to greater variability of reaction probability at lower diffusivities. As mentioned earlier, it is important to recognize that the transport coefficient is a measure of the tracer consumption rate and how far the tracers were able to penetrate into the cell wall. It alone is not an indicator of the extent of lignin dissolution in the plant cell wall.

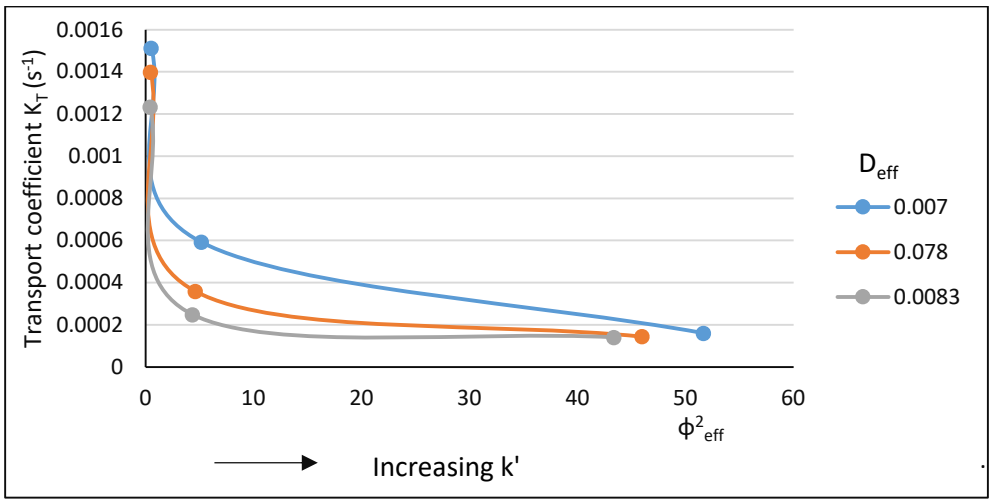

Figure 91. Effect of local rate constant on the transport coefficient

The effect of local rate constant on the displacement of the tracers was also studied. The mean square displacement versus time plots is shown in Figure 92a and 92b. With an increase in the local rate constant, the reaction probability decreased, and the tracers traversed further into the cell wall providing increased access to lignin which led to a higher dissolution rate as seen in the previous sections. Additionally, the impact of the local rate constant on the mean square displacement of the tracers were greater at lower effective diffusivities than at higher effective diffusivities as seen with other reaction characteristics.

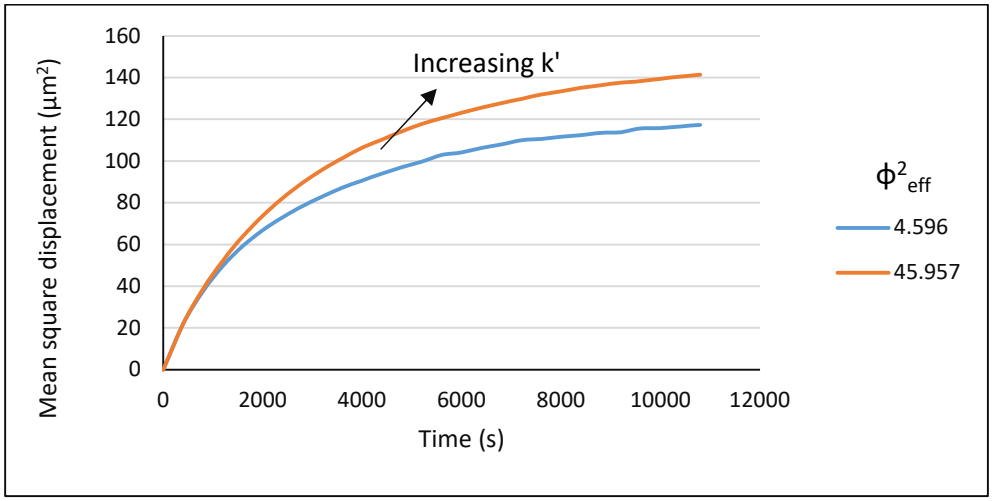

Figure 92a. Effect of local rate constant on the mean sq. displacement for different φ^2_{eff} (D_{eff} 0.00783 $\mu m^2/s$)

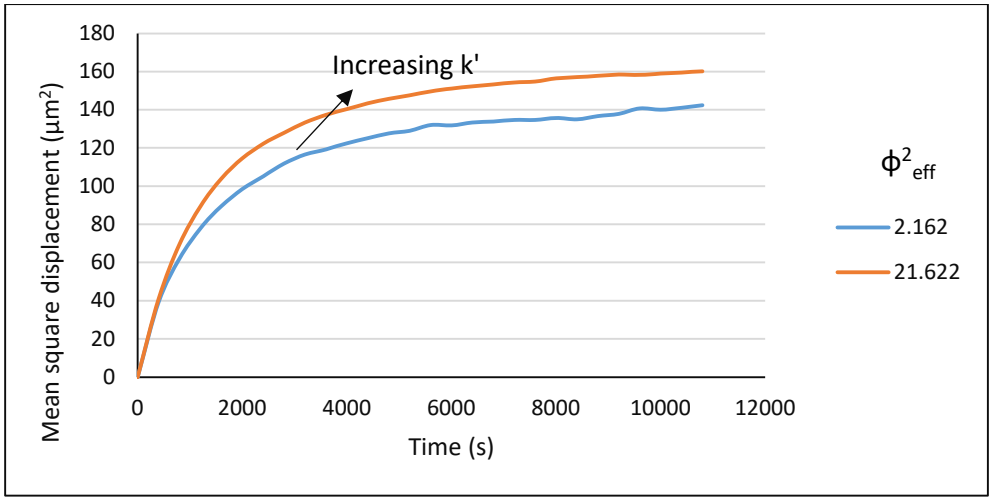

Figure 92b. Effect of local rate constant on the mean sq. displacement for different φ^2_{eff} (D_{eff} 0.1665 $\mu m^2/s$)

Thus, based on the analysis of the results from a wide range of simulations it can be concluded that modifying the pretreatment conditions by increasing the pH, temperature etc., which led to an increase in the reaction rate constant is beneficial for the overall process. Increasing the k' led to greater lignin dissolution. Even though the reaction probability decreased with increase in k', a higher concentration of lignin dissolved for every encounter between the tracer and lignin molecule that resulted in a reaction. It must also be noted that increasing the k' is very efficient until a certain threshold after which there are minimal changes due to greater impact of diffusion and reduced reaction probability. Increasing the k' beyond this point may be not optimal due to the energy and cost involved compared to the effect it would have on lignin dissolution.

7.1.4 Effect of the numbers of tracers

The number of tracers used for the simulation is representative of the concentration of the reagent used for pretreatment. The pretreatment order is a pseudo first order reaction where the reagent concentration is very large compared to the lignin. Hence, it is very important to represent this condition by choosing a large number of tracers compared to the initial lignin concentration in the cell wall. If the number of tracers is too low, then they are exhausted earlier than the desired time of reaction and no lignin dissolution occurs thereafter. In the pure diffusion case, choosing too few tracers resulted in a skewed mean square displacement curve (Defrenne, 2008). A similar observation was made in the diffusion reaction case. At conditions of low local rate constant or high effective diffusivities, the reaction probability is very high causing the tracers to be consumed faster than the rate of lignin dissolution. In such a situation, the tracers are exhausted before the intended time of reaction and the mean square displacement- time plots are skewed. In Figure 93, when the local rate constant was low ($\varphi^2_{eff} - 0.517$) or the diffusivity was high ($\varphi^2_{eff} - 4.49$) the tracers were exhausted earlier resulting in skewed curves. However, at the intermediate values of Thiele moduli, the number of tracers were sufficient not to be prematurely exhausted showing the appropriate displacement square versus time behavior. During the simulation and analysis, care was taken to make sure that we do not observe any anomalous behavior with respect to the tracer displacement.

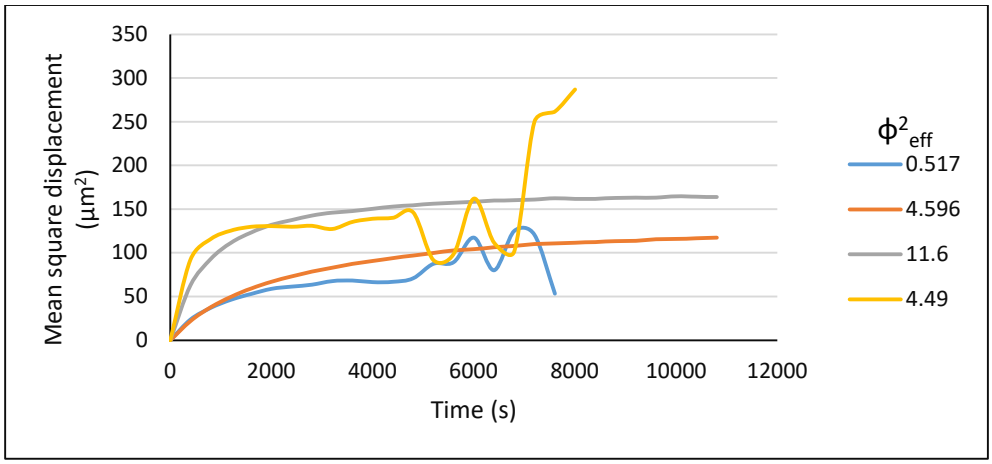

Figure 93. Mean sq. displacement-time curves for different φ^2_{eff}

7.1.5 Comparison with experimental data

The objective of the transport-reaction model was to simulate the pretreatment process successfully. One way of verifying this objective was to compare the results from the simulation with the experimental results obtained from the Raman images. For the case of alkali pretreatment of Poplar, model simulations were run using appropriate diffusivity and reaction rate constants and compared with experimental data. It was found that the appropriate effective Thiele modulus that matched with the experimental data was 11.6 (D_{eff} – 0.031μm^2/s and k' 1s^{-1}). The concentration profiles obtained from the simulation and experiment at this condition are shown in Figure 94. It is clear from the Figure 94 that the simulation results were in close agreement with the experiment. As discussed earlier, the effective rate constant for bulk dissolution of lignin was found to be a function of time in this case and the following relationship was obtained.

$$K_{eff} = 0.0109t^{-0.4378} \quad (34)$$

A time dependent rate constant and a power law relationship between rate constant and time for heterogeneous reactions such as biomass pretreatment and pulping has been reported previously (Dang and Nguyen, 2006; Keshwani and Cheng, 2010; Kopelman, 1988; Montané et al., 1994). Thus, the model showed that Poplar alkali pretreatment is a pseudo first order reaction and the rate expression for lignin dissolution is given by,

$$dC_L/dt = -0.0109t^{-0.4378}C_L \quad (35)$$

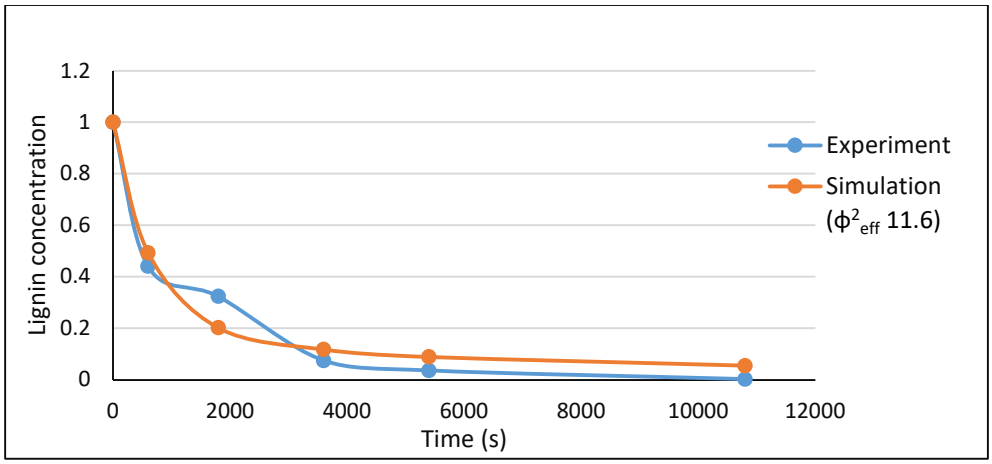

Figure 94. Comparison of bulk lignin concentration profiles from experiment and simulation for Poplar alkali pretreatment

7.2 Acer hot water pretreatment

Hydrothermal methods for pretreatment of biomass using saturated steam or hot water have been extensively used to weaken the lignocellulosic structure, increase the reactivity and enhance the accessibility to enzymes (Montané et al., 1998). Such pretreatments are typically carried out at high temperatures and short residence times to increase hemicellulose solubilization and prevent degradation of the solubilized oligomers (Converse et al., 1989). In addition, higher pressures are used to maintain the water in a liquid state at elevated temperatures (Mosier et al., 2005). Hot water pretreatment results in more than 90% solubilization of hemicellulose, 35-60% dissolution of lignin, 4-22% dissolution of cellulose and overall, 40-60% dissolution of biomass (Mok and Antal, 1992; Mosier et al., 2005). The amount of hemicellulose recovered was shown to be impeded by higher lignin dissolution (Mok and Antal, 1992).

The pretreatment process was carried out in a M&K digester using 500 g of Acer saccharum chips. DI water was then added to maintain a liquid to solid ratio of 4:1. The temperature was maintained at 160°C with a heating time of 30 min (Duarte et al., 2011). Raman spectra were acquired at 5, 10, 20, 30 and 40 min. The Raman intensity maps for lignin distribution were obtained experimentally at different time intervals using the spectra as shown in Figure 36. The concentration profile and instantaneous reaction rate of lignin

are shown in Figures 95 and 96. The concentration changes are initially smaller indicating a lower rate of dissolution until about 5 min. However, a higher lignin dissolution rate was observed in the later stages. The experimental concentration profile obtained from Raman spectroscopy could be correlated to that obtained from wet analytical techniques as mentioned earlier (Zhang, 2021). It is possible that greater dissolution was observed in our case since thin slices of wood chips were used for pretreatment and Raman imaging. It is also possible that the pretreatment was carried out in more severe conditions than reported in previous literature leading to a higher degree of dissolution as seen in Figure 95.

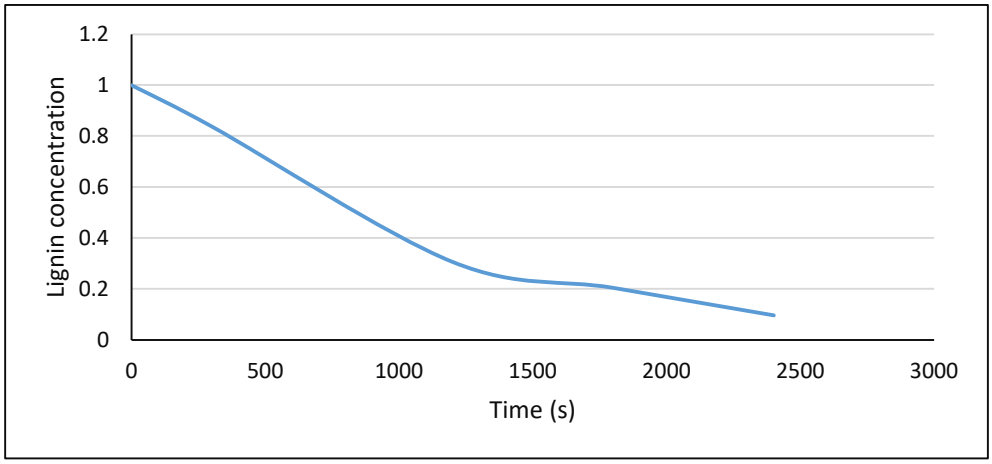

Figure 95. Relative bulk concentration profile of lignin during Acer hot water pretreatment from experimental data

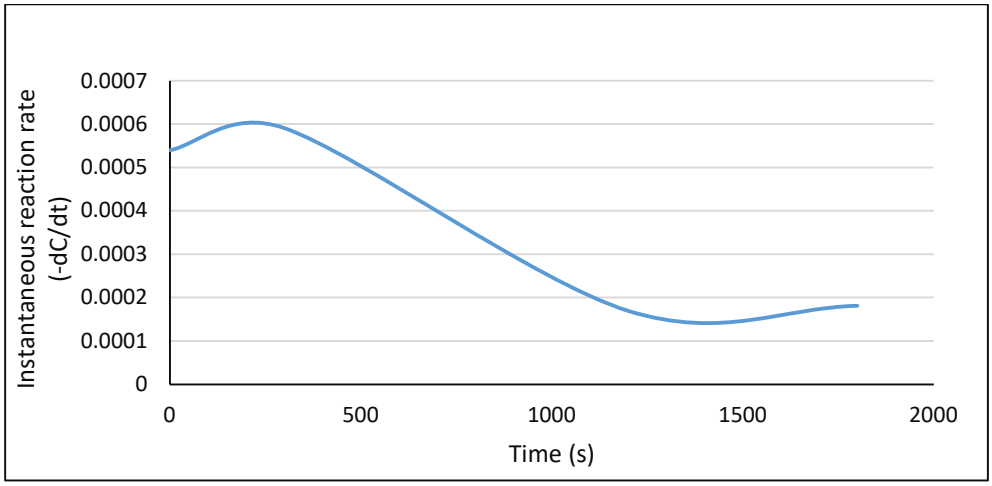

Figure 96. Instantaneous reaction rate of lignin during Acer hot water pretreatment from experimental data

7.2.1 Model simulations using Raman images of Acer (Sugar Maple)

Similar to the Poplar biomass and alkali pretreatment, the transport-reaction model developed here was applied to the Raman image for the untreated Acer biomass sample which served as the initial condition for the simulations. Several simulations with different diffusion and reaction parameters were run for the entire course of the reaction and the results were analyzed. For all simulations, the number of tracers used at the start was 1 million. The objective of these simulations is to study the effect of transport and reaction parameters in Acer biomass under varying conditions to better understand the hot water pretreatment process. Thus, the effect of diffusion and reaction parameters on the pretreatment kinetics using the transport-reaction model was evaluated over a wide range of φ^2_{eff} namely between 8.298 and 121.55. The effective diffusivity and local rate constant were varied to obtain a wide range of Thiele moduli. The pore diffusivity Do was varied between 0.03 and 0.06 $\mu m^2/s$ and ratio of diffusivity D* between 0.2 and 0.8 to obtain a range of effective diffusivity D_{eff} between 0.022 and 0.052 $\mu m^2/s$. The local rate constant was varied between 1 and 10 s^{-1}. The variation of Thiele modulus over the entire range of effective diffusivity and local rate constant considered for evaluating the model are shown in Figure 97. The model simulations were also compared with experimental data and an effective bulk lignin dissolution rate constant K_{eff} was determined for the Acer biomass subjected to hot water pretreatment.

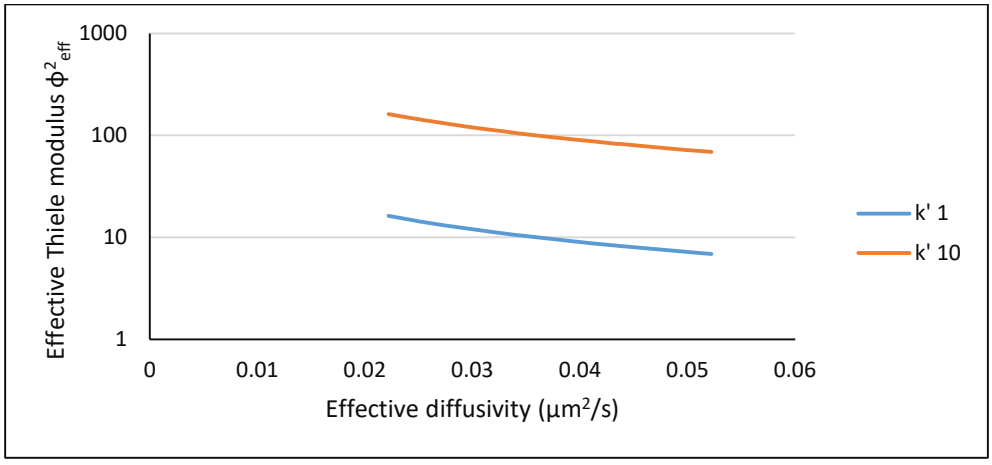

Figure 97. Variation of effective Thiele modulus with effective diffusivity and local rate constant

7.2.2 Effect of diffusivity

The effective diffusivity of the system was obtained from the slope of the mean square displacement versus time curve of a pure diffusion simulations using the Acer biomass image. The effective diffusivity was varied to obtain a wide range of effective Thiele moduli for which simulations were carried out. The variation of bulk lignin concentration profiles with time and the lignin topochemical distribution maps for different Thiele modulus values are shown in Figures 98 through 101. The lignin dissolution was slow during the start of the reaction and later increased over time. At lower range of effective diffusivities or higher range of effective Thiele moduli, increasing the effective diffusivity of the structure increased the lignin dissolution significantly leading to higher concentration changes at any given local rate constant (Figures 98 and 99). However, at the high range of diffusivities or lower range of Thiele moduli (Figure 99 bottom), increasing effective diffusivity of the structure did not significantly improve the lignin dissolution. The spatial concentration maps in Figures 100 and 101 revealed that a slow a gradual dissolution in the cell wall begins close to the lumen which then progresses to the interior regions. The lignin dissolution was minimal and limited to the region close to the lumen at the beginning for all diffusivity ranges as seen in Figures 98 and 99 and the spatial concentration maps in Figure 100 and 101.

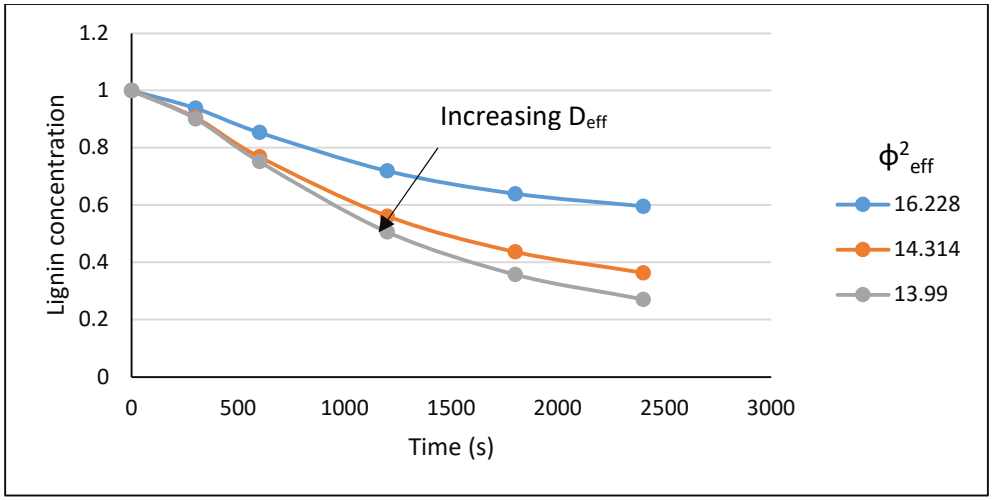

Figure 98. Effect of diffusivity on the lignin concentration profile (k' 1 s^{-1})

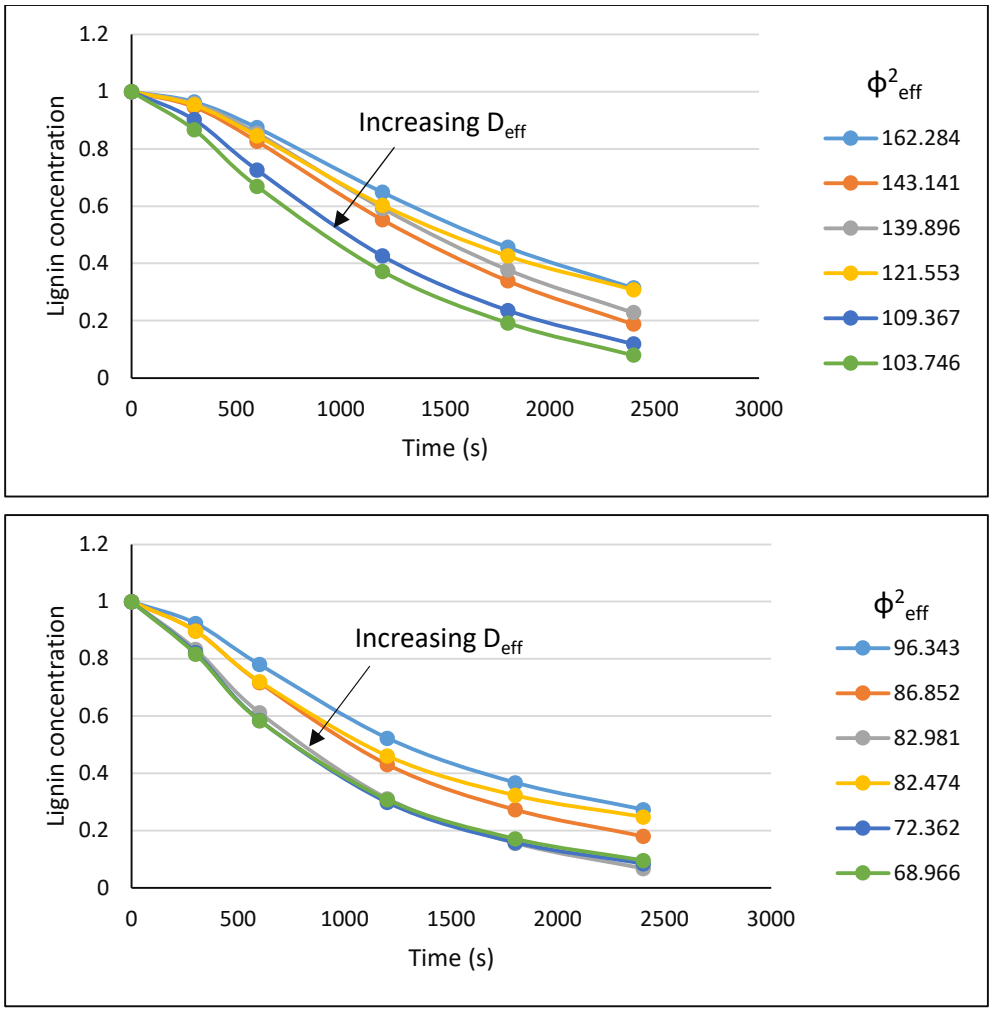

Figure 99. Effect of diffusivity on the lignin concentration profile at higher (top) and lower φ^2_{eff} (bottom) (k' 1 s^{-1})

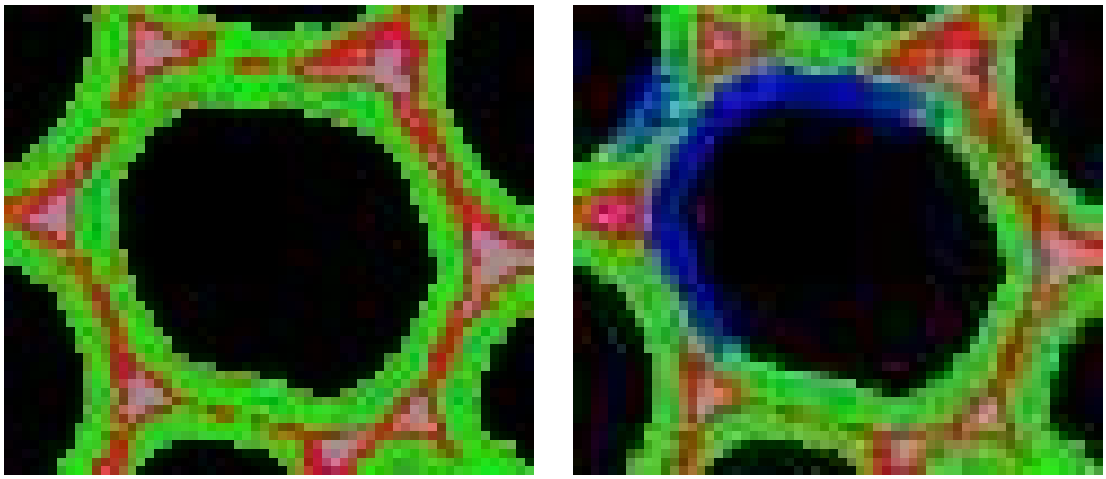

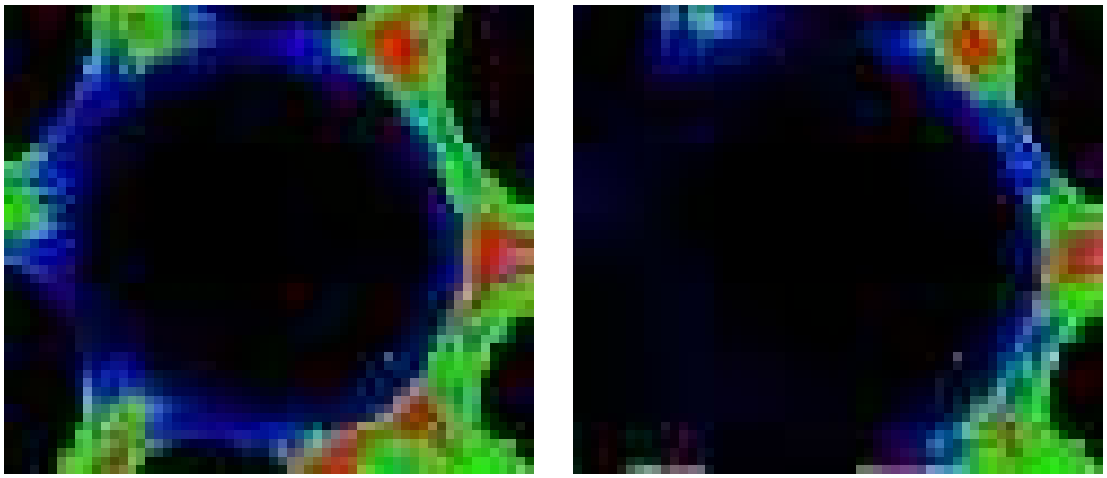

Figure 100. Spatial concentration map of lignin during Acer hot water pretreatment at 0s (top left), 300s (top right), 1200s (bottom left) and 2400s (bottom right) (φ^2_{eff} 141.14)

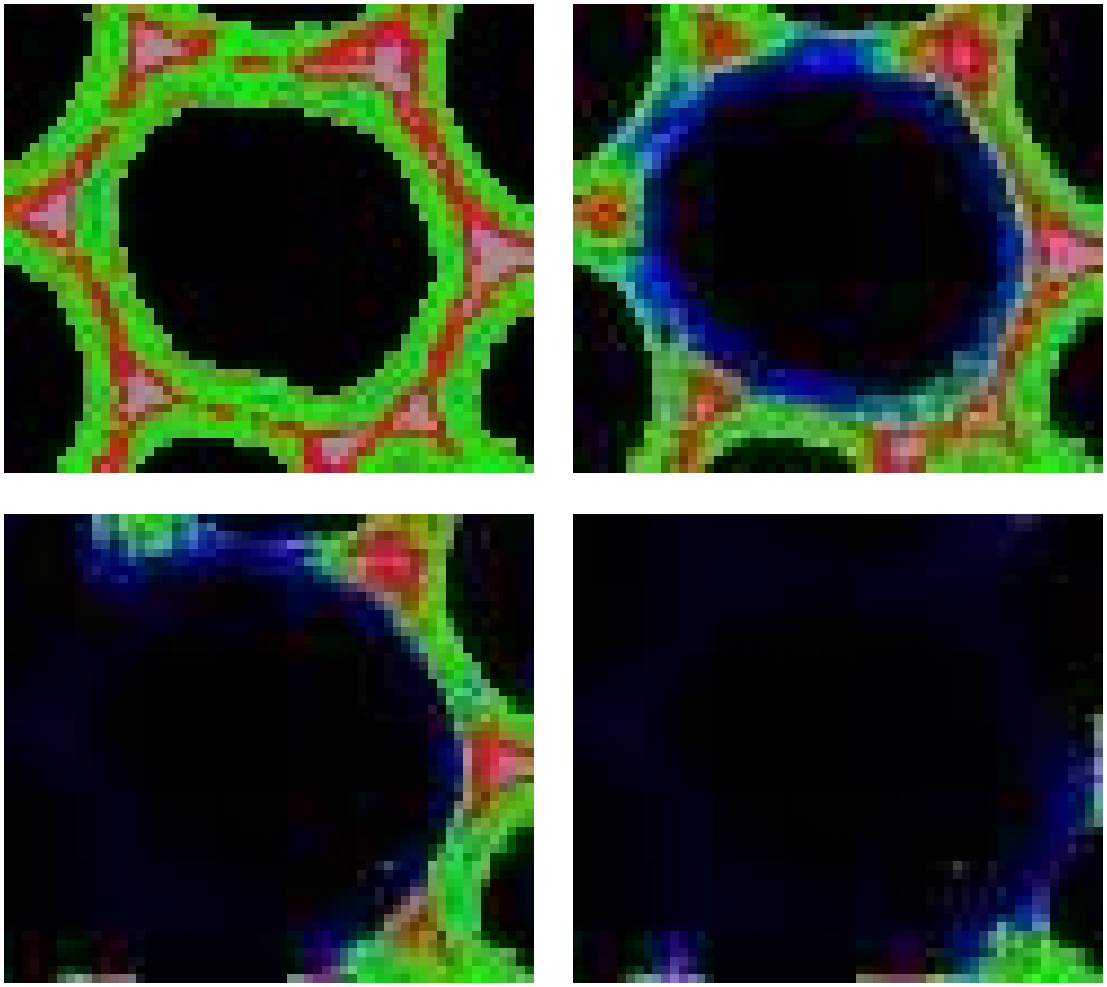

Figure 101. Spatial concentration map of lignin during Acer hot water pretreatment at 0s (top left), 300s (top right), 1200s (bottom left) and 2400s (bottom right) (φ^2_{eff} 72.36)

The effect of diffusion of the instantaneous rate of reaction followed the same trend as the concentration profiles and the results are shown in Figures 102 and 103. An initial delay in the onset of lignin dissolution was observed over the entire range of Thiele moduli considered. A similar trend was observed during alkali pretreatment of Poplar but only at lower diffusivities or higher Thiele moduli as seen in Figures 78 and 79. This is attributed to the higher range of Thiele modulus or lower range of reaction probability considered during hot water pretreatment. This resulted in slower diffusion of reagent molecules into the cell wall causing a delay in the onset of lignin dissolution. Additionally, in the case of Acer plant cell walls, as indicated by analysis of Raman images, the fraction of pore spaces (exterior to the cell wall region) in the total sample volume was greater than that in the Poplar samples. Hence, a longer time was required for the tracers to reach the interface and penetrate the cell wall to access the lignin. Thus, in this case, the pretreatment conditions should ensure higher diffusivity to overcome the initial delay caused in the transport of tracers. Similar to the concentration profile, the instantaneous rate of reaction increased with increase in effective diffusivity at higher Thiele moduli. At lower Thiele moduli, the effect of diffusion on the instantaneous reaction rate was minimal. At very high diffusivities, the process was diffusion dependent and increasing the diffusivity further increased the instantaneous rate of reaction.

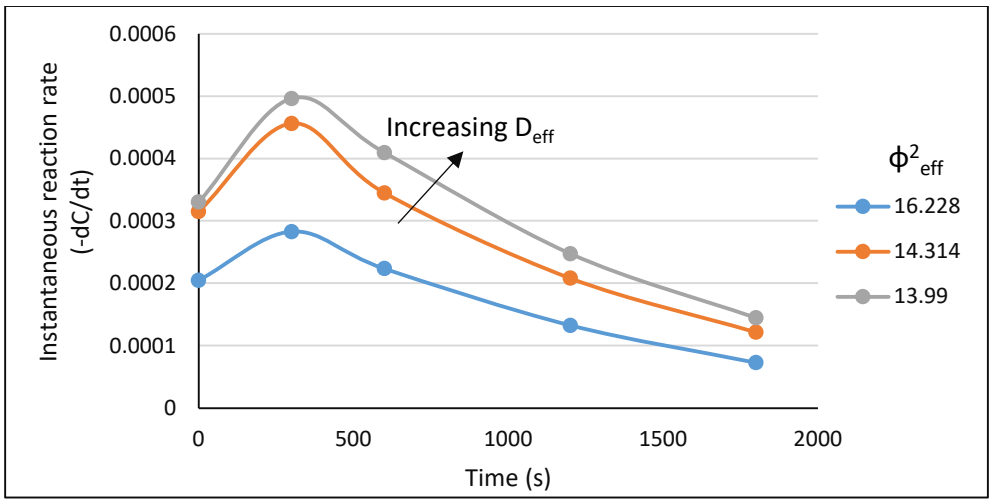

Figure 102. Effect of diffusivity on the instantaneous reaction rate (k' 1 s^{-1})

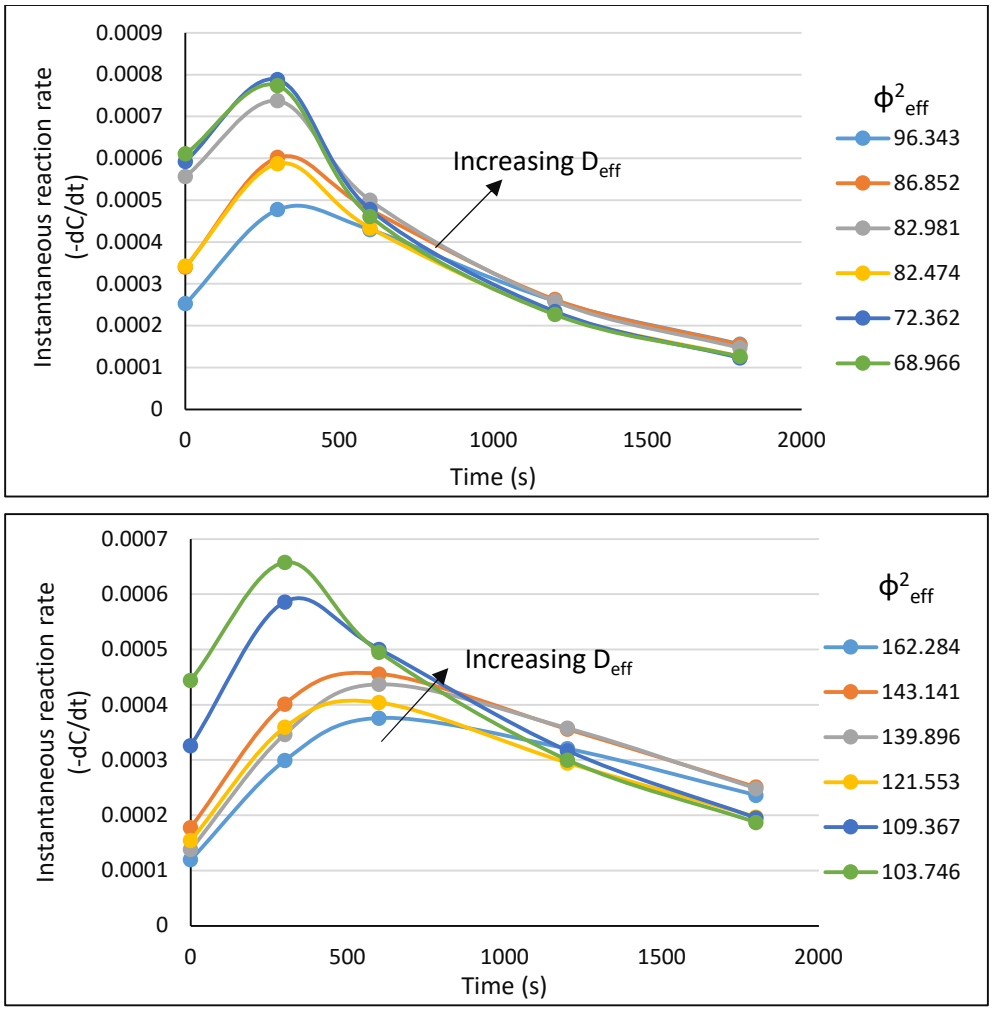

Figure 103. Effect of diffusivity on the instantaneous reaction rate at higher (top) and lower φ^2_{eff} (bottom) (k' 10 s^{-1})

An effective rate constant K_{eff} for different Thiele moduli was predicted from curve fitting the concentration profile obtained from the simulation and reported in Table 12. Unlike the alkali pretreatment methods, the effective rate constant was found to be independent of time for the entire range of diffusivities indicating that the process is reaction controlled throughout this range. This could be attributed to the differences in the cell structure, porosity, and lignin content. Additionally, the range of the local rate constant considered in this case is higher resulting in higher effective Thiele moduli and lower reaction probability. Thus, the time required for transport of the tracers was much greater than the time required for reaction. Hence K_{eff} is independent of time in the range of Thiele moduli considered.

k' 1		k' 10	
φ^2_{eff}	K_{eff}	φ^2_{eff}	K_{eff}
16.228	0.00024	162.284	0.0004
14.314	0.00045	143.141	0.00054
13.990	0.00054	139.896	0.00048
12.155	0.00022	121.553	0.00044
10.937	0.0004	109.367	0.00071
10.375	0.00044	103.746	0.00081
9.634	0.0002	96.343	0.00052
8.685	0.00049	86.852	0.00066
8.298	0.0006	82.981	0.00092
8.247	0.00018	82.474	0.00059
7.236	0.00041	72.362	0.00094
6.897	0.00071	68.966	0.00093

Table 12. Effective rate constant for bulk dissolution of lignin for different φ^2_{eff}

In order to study the effect of diffusion on transport characteristics of the tracer molecules, the transport coefficient was determined from the simulation based on survival time of the tracers. This provided an understanding of the rate of tracer consumption and the accessibility to the cell wall lignin. As seen earlier, K_T is affected differently by the changes in pore space diffusivity and cell wall diffusivity. Increasing the pore space diffusivity, allowed the tracers to approach the cell wall faster and react with the lignin molecules, thereby reducing their survival time and enhancing the transport coefficient as seen in Figures 104 and 105. However, at very low pore diffusivities, even though the tracers took a longer time to reach the cell wall, due to high reaction probability, the tracers were consumed faster decreasing their survival time and increasing the transport coefficient. The pore space diffusivity had a greater effect on the transport coefficient at lower k' values. At any given pore diffusivity, increasing the ratio of intrinsic diffusivities or cell wall diffusivities, allowed the tracers to penetrate further into the cell wall, thereby increasing their survival time and decreasing the transport coefficient. However, at high k' values, this trend is not followed strictly although the variation in K_T is minimal. It must be noted that in cases where the transport coefficient was high, the tracers were consumed rapidly. Hence it is very important to have a large number of tracers at the beginning of the simulation to ensure a continuous supply of tracers throughout the intended reaction time.

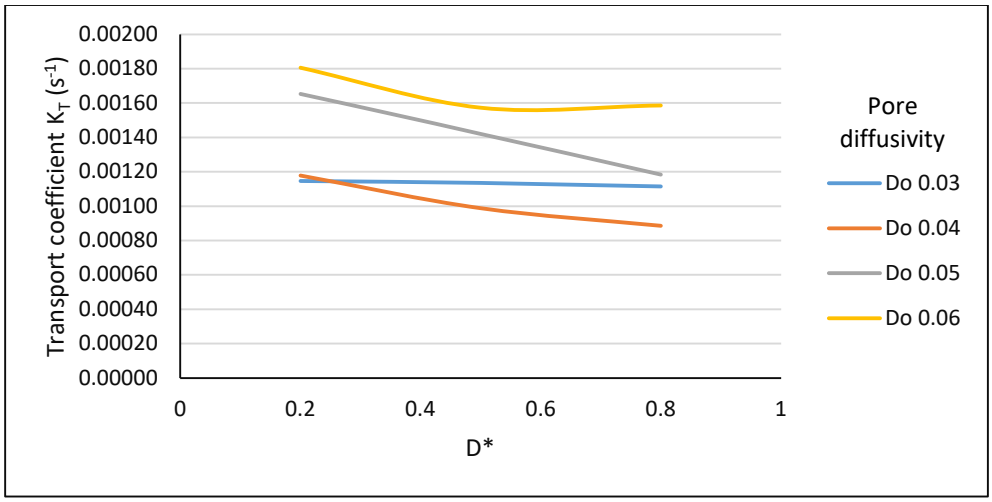

Figure 104. Effect of diffusivity on the transport coefficient (k' $1s^{-1}$)

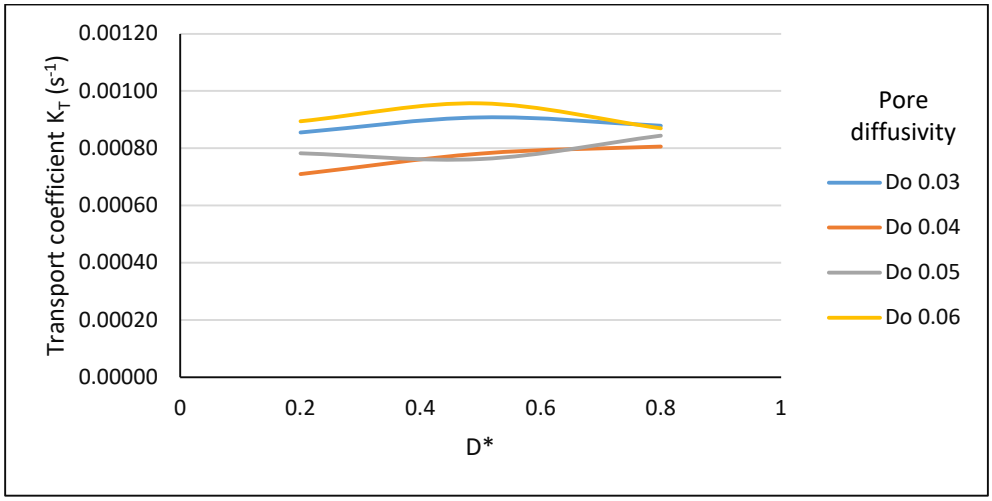

Figure 105. Effect of diffusivity on the transport coefficient (k' $10s^{-1}$)

The displacement time curves obtained from the simulation are shown in Figures 106 and 107. They determine the extent to which the tracers traversed through the cell wall and accessed the lignin molecules. In general, an increase in the effective diffusivity of the system allowed the tracers to move further into the cell wall increasing their displacement and allowing greater access to lignin and eventually resulting in a higher dissolution rate. The concentration profiles in Figures 98 and 99 also reiterate this observation except at very high diffusivities where the tracers may not be able to penetrate too far into the cell wall due to faster consumption. An enhanced effective diffusivity could be achieved by increasing either the pore space diffusivity or the cell walls diffusivity or both.

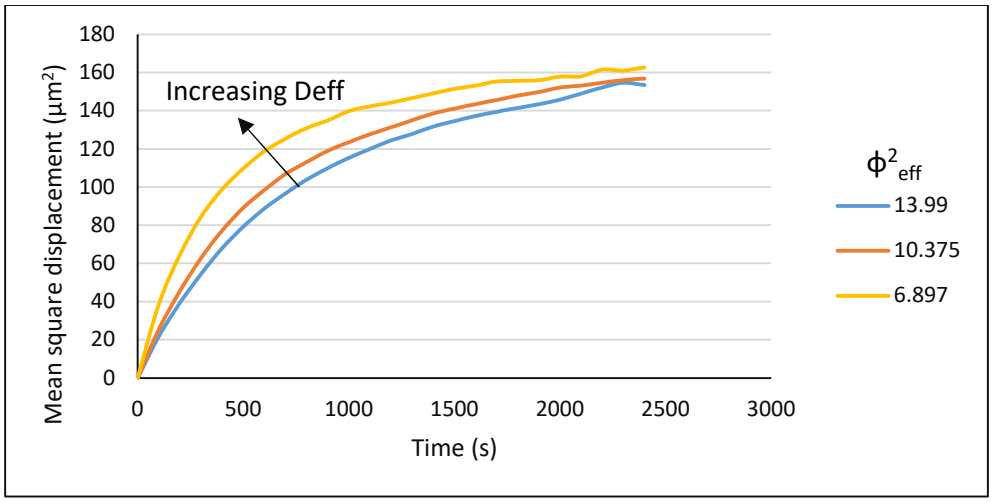

Figure 106. Effect of diffusivity on the mean sq. displacement for different φ^2_{eff} (k'1s^{-1})

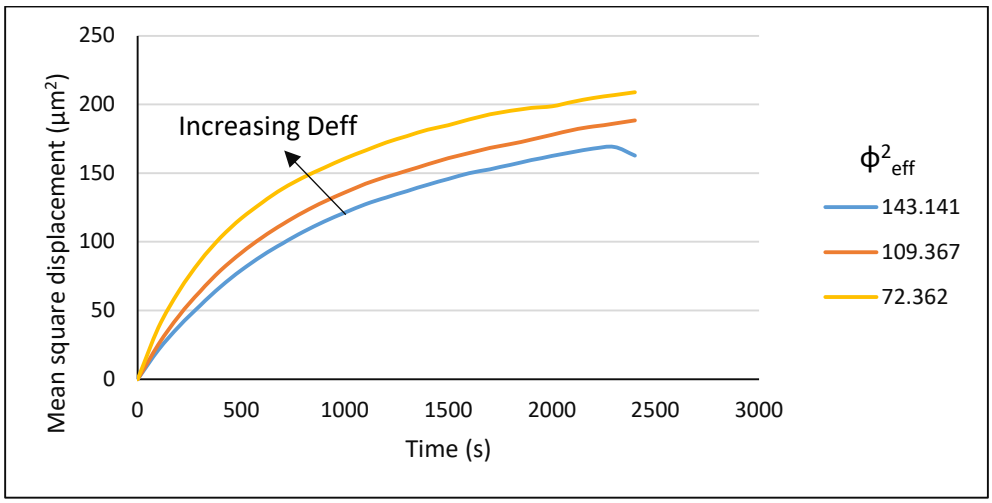

Figure 107. Effect of diffusivity on the mean sq. displacement for different φ^2_{eff} (k'10s^{-1})

7.2.3 Effect of local rate constant

The local reaction rate constant k' for lignin dissolution is purely dependent on reaction kinetics and is different from the effective rate constant determined from the simulation. As seen earlier, the effective Thiele modulus increased linearly with the local rate constant. The effect of local rate constant on the concentration profiles, instantaneous reaction rate, effective rate constant and tracer consumption were studied. The concentration profiles and the lignin distribution maps at different Thiele moduli are shown in Figure 108 through 111. As the local rate constant increased, the lignin dissolution also

increased leading to greater concentration changes as seen earlier in the alkali pretreatment of Poplar. Even though the reaction probability was reduced with an increase in the local rate constant, the amount of lignin dissolved for every tracer-lignin encounter that resulted in a reaction was greater thus explaining the improved dissolution rates. The initial lag in the lignin dissolution process was greater at higher k' and lower effective diffusivities due to slower transport of tracers to the cell wall and reduced reaction probability.

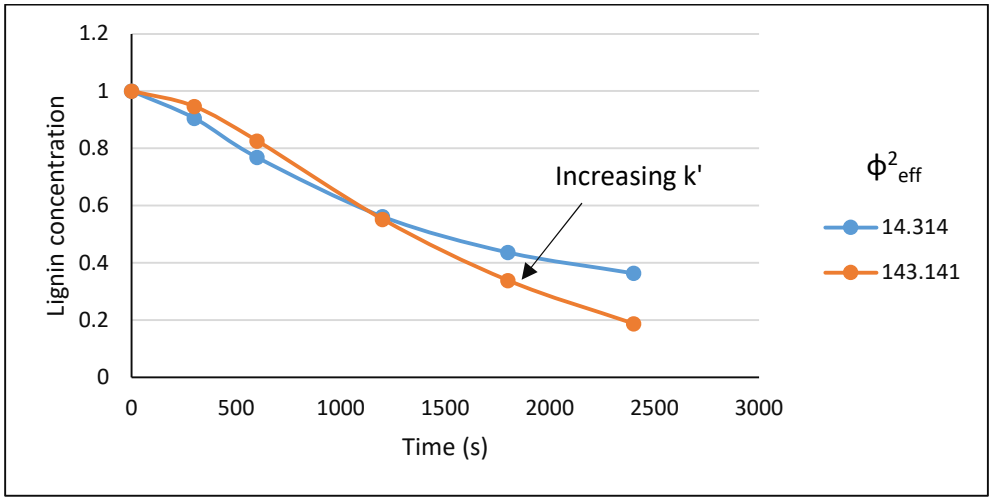

Figure 108. Effect of local rate constant on the lignin concentration profile (D_{eff} 0.025 $\mu m^2/s$)

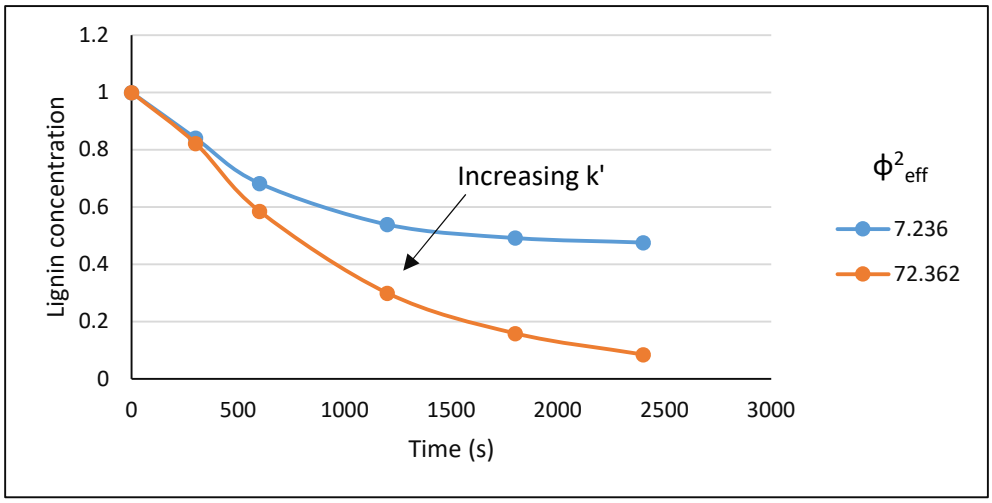

Figure 109. Effect of local rate constant on the lignin concentration profile (D_{eff} 0.05 $\mu m^2/s$)

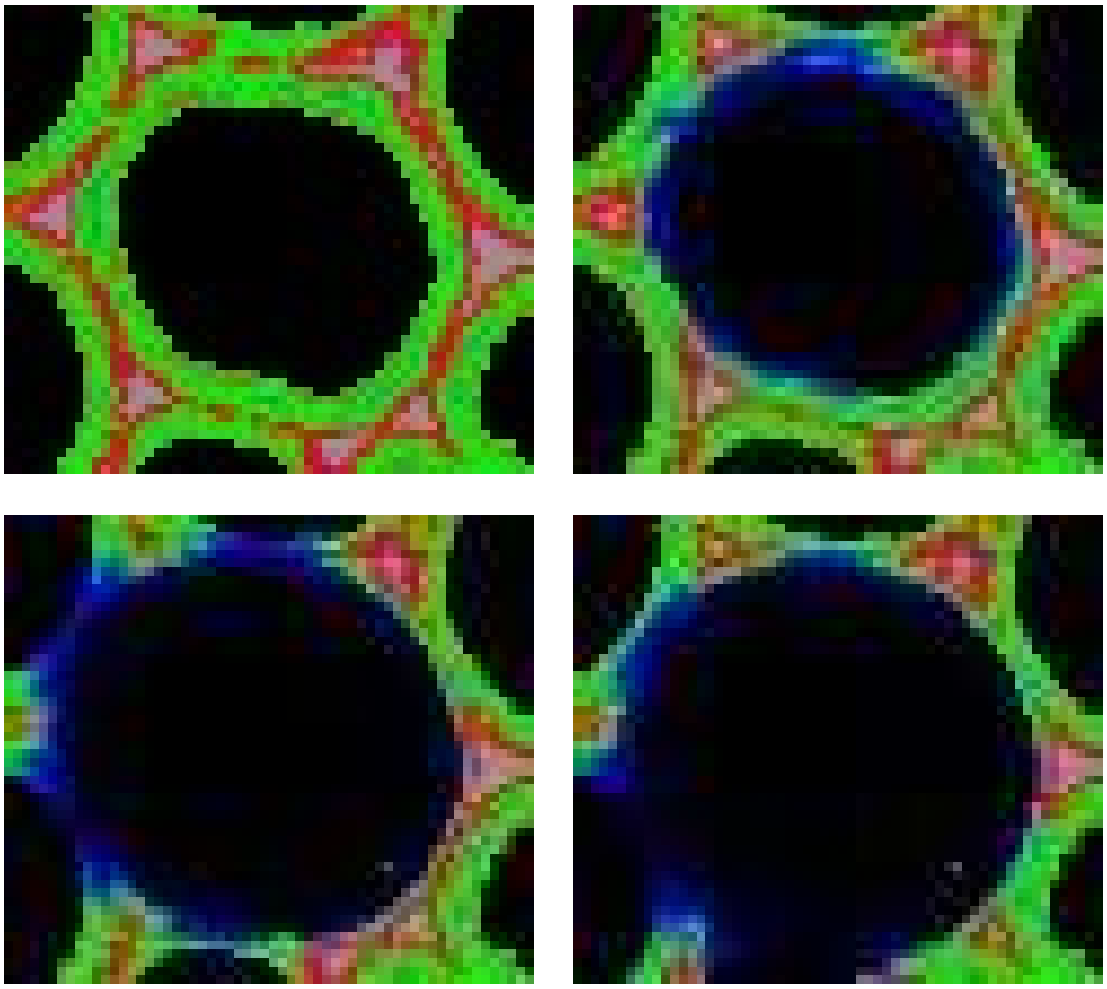

Figure 110. Spatial concentration map of lignin during Acer hot water pretreatment at 0s (top left), 300s (top right), 1200s (bottom left) and 2400s (bottom right) for φ^2_{eff} of 7.236

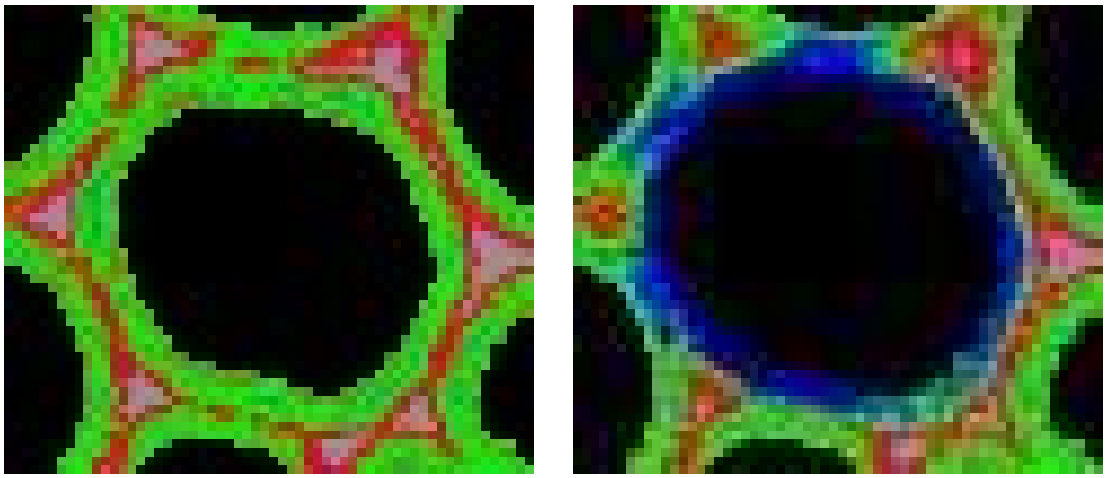

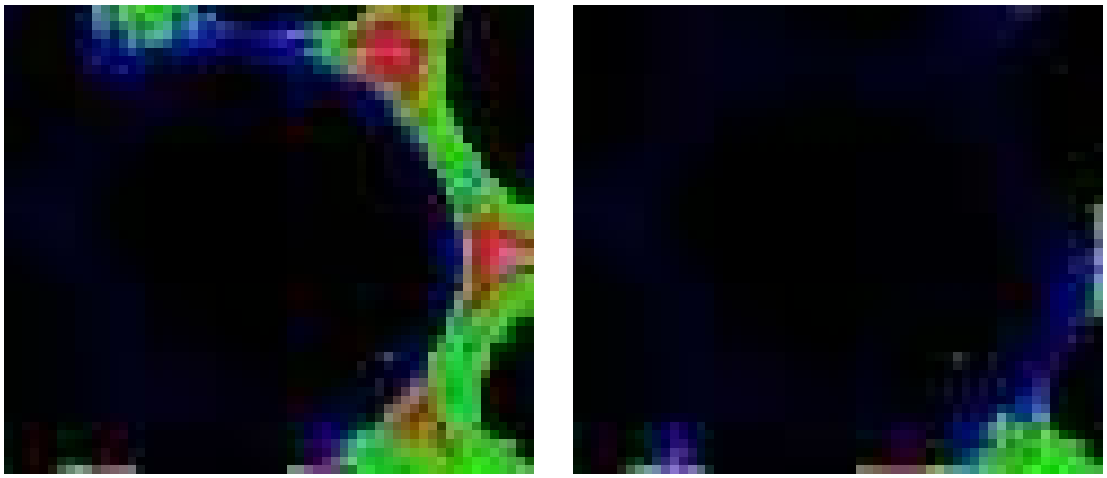

Figure 111. Spatial concentration map of lignin during Acer hot water pretreatment at 0s (top left), 300s (top right), 1200s (bottom left) and 2400s (bottom right) for φ^2_{eff} of 72.36

The effect of local rate constant on the instantaneous reaction rate is shown in Figures 112 and 113. Generally, the rate of reaction increases with the increase in the local rate constant. However, at lower effective diffusivities, the lag in the onset of lignin dissolution resulted in lower reaction rates even at higher k' values. Once a sufficient number of tracers have penetrated through the cell wall, the rate of reaction increased with increase in k' values. The overall rate constant K_{eff} was time independent for the range of local rate constant values considered for simulation indicating that the process was reaction dependent. Comparing the effective rate constants from Table 12, a higher K_{eff} was observed for higher k' in general, indicating greater lignin dissolution.

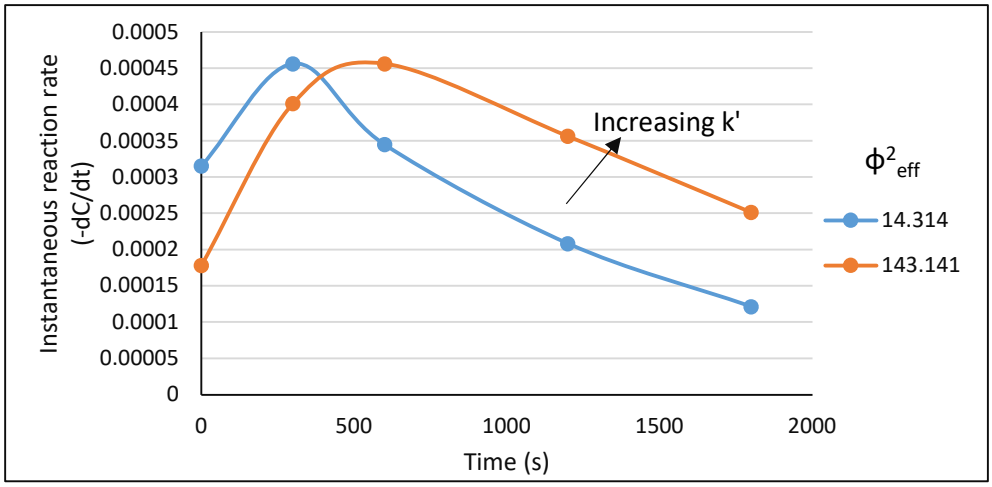

Figure 112. Effect of local rate constant on the reaction rate (D_{eff} 0.025 $\mu m^2/s$)

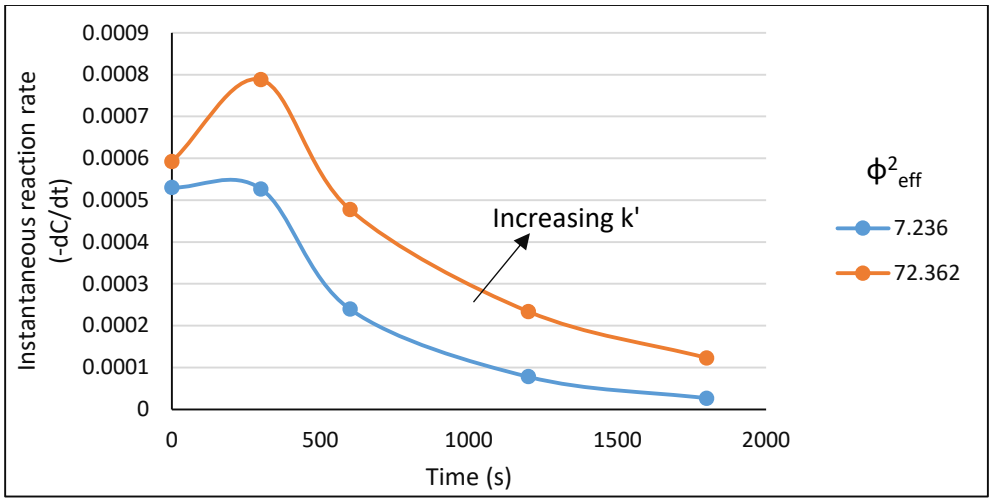

Figure 113. Effect of local rate constant on the reaction rate (D_{eff} 0.05 $\mu m^2/s$)

In order to the study the effect of local reaction rate on the tracer consumption and survival time, the transport coefficient and the displacement time curves were studied. The transport coefficient for different Thiele moduli were compared in Table 13. Increasing the local rate constant decreased the reaction probability which allowed the tracers to traverse further into the system, increasing their survival time and decreasing the transport coefficient. Additionally, the displacement of the tracers was greater as seen from Figures 114 and 115. It must be noted that a sufficiently large number of tracers have to be present at the start to avoid the tracers from exhausting before the intended residence time, which is more likely in cases of low local rate constant or high diffusivity. A skewed displacement time curve would be obtained in such cases.

k'	D_{eff}	φ^2_{eff}	K_T
1	0.025	14.31	1.14E-03
10		143.14	9.08E-04
1	0.033	10.94	9.89E-04
10		109.37	7.82E-04
1	0.041	8.69	1.42E-03
10		86.85	7.62E-04
1	0.050	7.24	1.57E-03
10		72.36	9.57E-04

Table 13. Variation of transport coefficient with the local rate constant

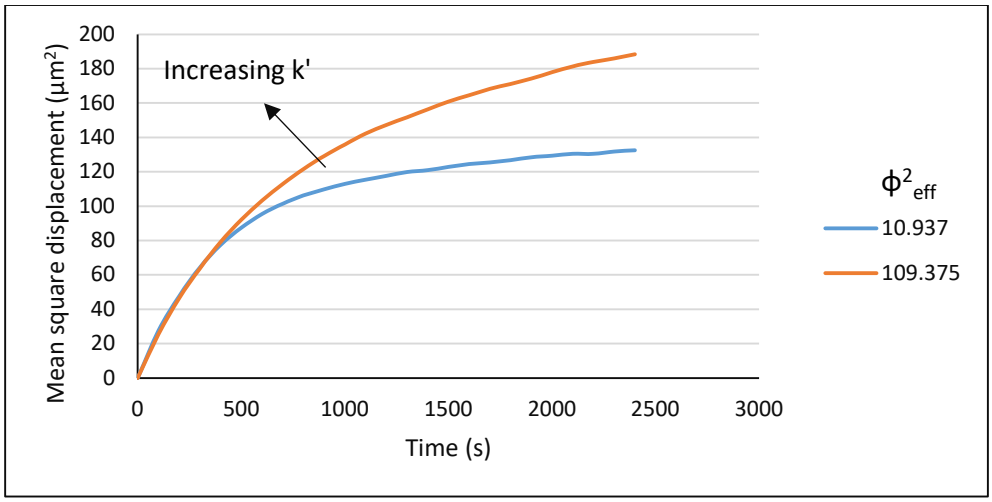

Figure 114. Effect of local rate constant on the mean sq. displacement for different φ^2_{eff} (D_{eff} 0.033 $\mu m^2/s$)

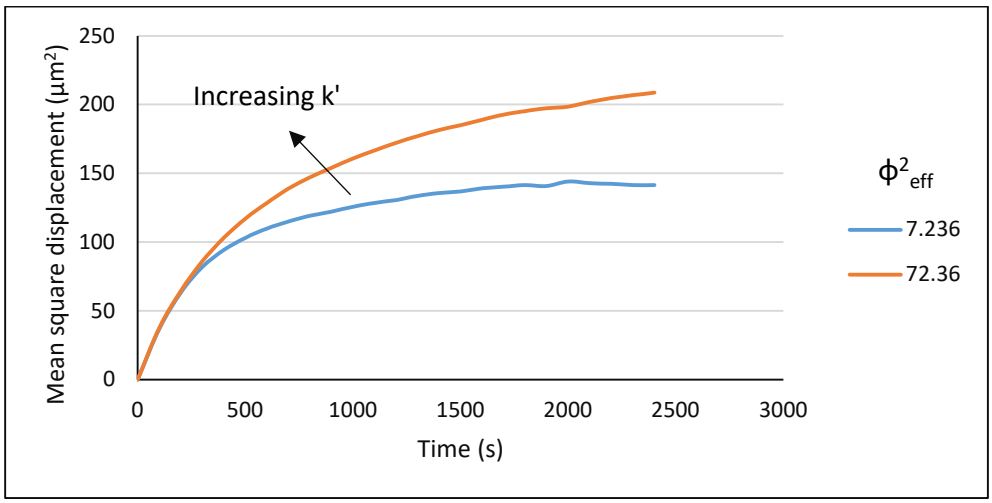

Figure 115. Effect of local rate constant on the mean sq. displacement for different φ^2_{eff} (D_{eff} 0.05 $\mu m^2/s$)

7.2.4 Comparison with experimental data

As seen earlier, the objective of the transport-reaction model was to simulate the pretreatment process successfully. One way of verifying this objective is to compare with experimental results obtained from Raman images. For the Acer biomass sample subjected to hot water pretreatment, model simulations were run using appropriate diffusivity and reaction rate constants and compared with experimental data. It was found that the

appropriate effective Thiele modulus for Acer subjected to hot water pretreatment was 72.362 (D_{eff} – 0.05 $\mu m^2/s$, k' – 10 s^{-1}). The concentration profiles obtained from the simulation and experiment at this condition are shown in Figure 116. As is clear from the Figure 116 that the simulation results were in close agreement with the experiment. The effective rate constant for bulk lignin dissolution (K_{eff}) was also determined from a curve fit of the data from simulation. Unlike the Poplar alkali pretreatment, the effective rate constant for the Acer hot water pretreatment was found to be constant and independent of time, which was typical for a first order reaction. The value of K_{eff} was determined to be 0,00094 s^{-1} from curve fitting. Thus, the rate expression for the Acer hot water pretreatment process was given by,

$$\frac{dC_L}{dt} = -0.00094C_L \tag{36}$$

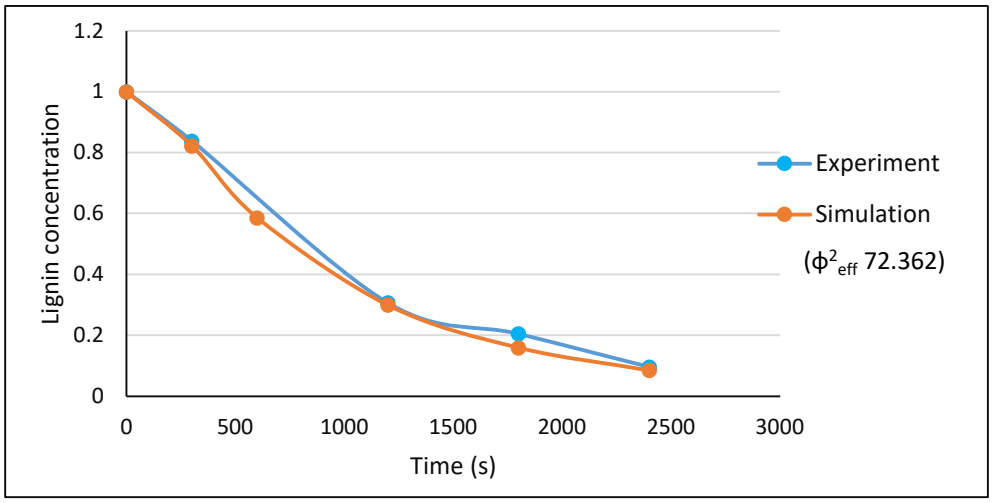

Figure 116. Comparison of bulk lignin concentration profiles from experiment and simulation for Acer hot water pretreatment

7.3 Comparison between Poplar alkali pretreatment and Acer hot water pretreatment

The results obtained from the simulation for alkali pretreatment of Poplar and hot water pretreatment of Acer are significantly different due to the nature and pretreatment of biomass. In both cases, the lignin intensity obtained from Raman imaging which is

proportional to actual lignin concentration is considered. As described earlier, the correlation between the experimentally obtained Raman intensity and the actual lignin concentration obtained from wet techniques have been reported (Zhang, 2021). Comparing the Thiele modulus between the two cases, the hot water pretreatment required a higher φ^2_{eff} of 72.36 as compared to the alkali pretreatment which required a φ^2_{eff} of 11.6. Both the effective diffusivity and local rate constant were also higher for the hot water pretreatment case. Acer has a lower total lignin content than Poplar (S. Chen et al., 2016; Duarte et al., 2011; Ma et al., 2014). In case of the Acer plant cell walls, as indicated by analysis of Raman images, the fraction of pore spaces (exterior to the cell wall region) in the total sample volume was greater in Acer biomass sample than that in the Poplar sample. Additionally, hot water pretreatment causes differential swelling in the cell wall which leads to easier diffusion of the hot water molecules into the cell wall (S. Chen et al., 2016). Hence the diffusivity of the cell wall during hot water pretreatment of Acer was greater than the diffusivity of the cell wall of Poplar during alkali pretreatment. It is interesting to note that during alkali pretreatment of Poplar, the lignin dissolution process is more rapid during the beginning of the reaction while there is a delay in the onset of lignin dissolution during hot water pretreatment of Acer leading to different kinetic and transport characteristics as seen by the effective rate constant values. Although the hot water pretreatment required a higher k' than the alkali pretreatment, it had a lower overall reactivity for lignin dissolution as indicated by a higher Thiele modulus and lower reaction probability. Thus, an initial lag in lignin dissolution and slow onset of reaction was observed for all diffusivity ranges. It has been reported in previous literature that hot water pretreatment cleaves hemiacetal linkages and uronic acid substitutions and releases organic acids which facilitates further breaking of ether linkages resulting in lignin dissolution (Mosier et al., 2005). It has also been reported lignin re-localization and globule formation occurs during hot water pretreatment (Donohoe et al., 2011). Once the initial lag is overcome, the higher diffusivity and higher local rate constants in hot water pretreatment of Acer resulted in faster overall dissolution during hot water pretreatment. The effective rate constant obtained for the alkali pretreatment of Poplar was a function of time while it was independent of time for the hot water pretreatment of Acer.

Comparing the results between the two pretreatment methods, it is evident that alkali pretreatment required a longer residence time but resulted in almost complete delignification at a lower diffusivity and local rate constant as seen by both the experimental and simulation results (Ji et al., 2014). On the other hand, even though the hot water pretreatment was carried out for a shorter time and probably at more severe conditions than reported in previous literature, the extent of lignin dissolution was lower than of alkali pretreatment. This could be attributed to lower reactivity of the system for lignin dissolution. As mentioned earlier, breakage of acetyl linkages and release of organic acids occur during hot water pretreatment which facilitate breakage of lignin (Mosier et al., 2005). Additionally, lignin re-localization also occurs during hot water pretreatment (Donohoe et al., 2011). It is also important to note that alkali pretreatments mainly focus on removal of lignin while hot water pretreatments focus on hemicellulose solubilization which explains the higher and more rapid delignification during alkali pretreatment as compared to hot water pretreatment (Mosier et al., 2005). If the model were extended to simulate the carbohydrate dissolution, it is likely that we will observe the earlier dissolution of carbohydrates in the case of hot water pretreatment. Thus, it can be concluded the nature of biomass and pretreatment affect the structure and topochemistry of the cell walls.

8. CONCLUSIONS AND FUTURE WORK

Porous materials such as wood, paper etc. have a complex 3D internal structure consisting of pore and fiber networks which influences their material properties as well as their manufacturing processes. Characterization of the structure of biomass and understanding its influence on the physical and chemical properties as well as their role during conversion processes is the key to achieve their efficient conversion. In this regard, the current work is aimed at 3D characterization of the cell wall architecture followed by a transport-reaction model to predict the changes in the lignin concentration during pretreatment of biomass.

In order to fully understand the ultrastructure of plant biomass and its influence on material properties, it is necessary to visualize and characterize the cell wall architecture in three dimensions (3D). Computed tomography using X-rays, SEM or TEM enabled 3D visualization of the cell wall structure in a non-intrusive manner. In the previous work, X-ray computed tomography was used to visualize and characterize the structural and transport properties of paper structures (Defrenne, 2008; Defrenne et al., 2019; Goel, 2003). Although X-ray CT was able to visualize the cell wall structure at a micron scale, it was not sufficient to visualize the internal nanoscale ultrastructure of the different cell wall layers and study their structural evolution during the pretreatment. Hence, TEM-CT was used for this purpose as it provided a higher resolution at the nanoscale. Images of untreated and ammonium oxalate treated Arabidopsis samples were obtained from Lawrence Berkeley National Laboratory, CA while corn stover samples treated by ammonia fiber expansion method were obtained from the National Renewable Energy Laboratory, CO. The untreated Arabidopsis samples were either prepped at room temperature or by high pressure freezing prior to imaging. The TEM-CT images were first processed to remove noise and other artifacts while preserving edges using the anisotropic diffusion technique followed by binarization to obtain a grayscale image that clearly distinguished between the pore and cell wall spaces. Using the TEM-CT images, structural characteristics such as porosity, pore-cell wall interfacial surface area and the pore size distribution for different parts of the cell wall were obtained. It was observed that the primary wall was more porous

and had a greater surface area compared to the middle lamella for both treated and untreated samples. They also had a broader pore size distribution compared to the middle lamella. This suggested that the primary wall is more accessible and amenable to dissolution of cell wall components compared to the middle lamella. The porosity and surface area of the treated samples were greater than that of the untreated samples due to dissolution of cell wall components. The treated samples had a wider pore size distribution and a higher mean pore size compared to the untreated samples. It appears that some of the pretreatments were able to open up the pores in the cell wall whose diameter was greater than 5-10 nm thus enabling their accessibility and reactivity. Among the untreated samples, it was observed that the method of sample preparation prior to imaging had an effect on the structural properties. The samples prepared at room temperature showed a higher porosity and broader pore size distribution as compared to the samples prepared by high pressure freezing. This indicated that room temperature prepping of the sample was more intrusive and caused greater shrinkage and swelling of the cell walls.

The structural characteristics of biomass from 3D images obtained by TEM-CT, were correlated with the topochemical distribution obtained from Raman spectroscopy to provide a complete understanding of the pretreatment process. In this regard, a transport-reaction model was developed based on stochastic and kinetic principles to predict the bulk and spatial changes in lignin concentration during pretreatment. This model was an extension of the previous work on simultaneous diffusion in porous structure (Defrenne, 2008; Defrenne et al., 2019; Goel, 2003). The current model included a hybrid random walk approach for diffusion of the reagent particles used for pretreatment combined with pseudo first order kinetics for lignin dissolution to track the cell wall dissolution for pretreatment. According to the pseudo first order kinetics, the reagent used for pretreatment is available in abundance and the lignin concentration alone controls the rate of reaction. A transport coefficient K_T based on the survival time of the tracers till they reacted was reported. Additionally, based on bulk lignin dissolution, an effective rate constant K_{eff} for the overall process that accounts for both transport and reaction was determined. It was observed that K_{eff} was either time dependent or time independent depending on the diffusive and reactive conditions within the system and the biomass species.

The transport-reaction model was first verified using an ideal system consisting of a periodic array of spheres. The model system was represented by a single sphere surrounded by a pore space similar to a catalyst pellet system in order to test the validity of the model. In addition to the diffusing reagent, the sphere was assumed to contain known initial concentration and distribution of reactive species (i.e., lignin in biomass cell wall). The simulations were carried out for a wide range of diffusive and reactive parameters and the results were compared.

The effect of 3D structure, Thiele modulus (which included both diffusive and reactive behavior) and the number of tracers used for the simulation on both the tracer consumption and concentration as well as the topochemical distribution of the stationary species in the sphere were evaluated. Increasing the solidity of the structure increased the transport coefficient and rate of consumption of tracers. The rate of reaction within the sphere and K_{eff} also increased. However, at a higher solidity, the amount of reactant available within the sphere was greater and hence the relative amount of the component that reacted was lower at a higher solidity. In order to study the effect of Thiele modulus, both the diffusivity and local rate constant of the system was varied separately, and the results were compared. Increasing the diffusivity allowed further penetration of tracers within the system and resulted in an increased transport coefficient. A greater dissolution of the reactant was observed due to increased accessibility to the reactant within the sphere. Consequently, a higher reaction rate and K_{eff} were observed. This proved that diffusion enhanced reaction. However, the effect of increasing diffusivity was greater at lower diffusivities than at higher diffusivities. This is due to the fact that lower diffusivities caused greater changes in the Thiele modulus than higher diffusivities. Increasing the local rate constant k' decreased the reaction probability and hence, the transport coefficient decreased. However, a greater dissolution of the reactant was observed since a greater concentration of the reactant was dissolved for every tracer-sphere encounter that led to reaction based on the reaction kinetics. Consequently, the rate of reaction and K_{eff} also increased with an increase in k'. It must be noted that the transport coefficient is only a measure of the tracer consumption rate and cannot alone determine the reaction

characteristics within the sphere. Lastly, the effect of the number of tracers which is proportional to the concentration of the diffusing reagent species was analyzed. Although the tracer concentration did not have a direct impact on the reaction within the sphere, it influenced the residence time. Choosing too few tracers at the start resulted in the tracers being consumed quickly during reaction and they could be exhausted before the intended residence time. Hence, it is necessary to have sufficient number of tracers present at the start of the reaction to ensure a continuous supply of tracers throughout the reaction. Thus, upon evaluating the transport reaction model, it was clear a higher diffusivity and reactivity yielded the best result in terms of conversion of the reactant. However, it must be noted that increasing the diffusivity beyond a certain threshold resulted in minimal changes in the dissolution of the reactant within the sphere and this may not be a feasible choice given the energy and cost considerations involved.

Once the transport-reaction model was successfully evaluated for the ideal sphere system, they were then applied to biomass pretreatment using Raman images. The Raman images were obtained from Dr. Feng Xu's group at Beijing Forestry University, China and from Dr. Ramarao's group at SUNY-ESF. The Raman intensity in the range of wavenumbers between 1550 and 1650 cm^{-1} were representative of the lignin concentration (Gierlinger and Schwanninger, 2006; Ji et al., 2014). Although, Raman intensity ratios are considered which is proportional to the lignin concentration, they can be correlated to the bulk lignin concentration obtained from wet techniques. A linear correlation has been developed between the Raman intensity ratios and lignin concentration in the work of Zhang (Zhang, 2021). Assuming that this concept could be extended to the current work, the bulk lignin concentration could be extrapolated. Such a relationship could also be developed for the type of biomass species and pretreatment conditions used in the current work using the appropriate experimental data and the lignin concentration. However, this is not conducted in the current work and is suggested as a part of the future work. It must be noted that the Raman imaging and the corresponding lignin dissolution reported in the current work maybe greater than those commonly reported in the literature using wood chips under similar pretreatments. This is possibly because in the current work, thin slices of biomass were used for the study while other literature commonly used wood chips. This

might contribute to a relatively greater dissolution in thin slices as compared to larger wood chips. The model used a 3D image stack created from the processed 2D Raman images for untreated biomass samples. The Raman topochemical distribution of the untreated biomass samples were used as initial conditions in the model. Two sets of images that correspond to alkali pretreatment of Poplar and hot water pretreatment of Acer (maple) were analyzed over a wide range of Thiele moduli and compared to the results obtained from the experiment. The number of tracers chosen for each condition was sufficient enough to ensure a continuous supply of tracers throughout the intended residence time. The effect of diffusivity and local rate constant were studied for each condition. Comparing with the experimental data, an effective Thiele modulus of 11.6 (D_{eff} – 0.031$\mu m^2/s$ and k' $1s^{-1}$) was required for alkali pretreatment and an effective Thiele modulus of 72.362 (D_{eff} – 0.05 $\mu m^2/s$, k' – 10 s^{-1}) was required for hot water pretreatment. In both cases, the rate expressions describing the overall bulk lignin dissolution during biomass pretreatment were successfully determined. Similar to the sphere system, increasing the diffusivity enhanced reaction. The effect of diffusivity was greater at lower diffusivity than at higher diffusivities. Increasing the local rate constant also enhance reaction as seen in the case of spheres. The impact of increasing rate constant was greater at lower effective diffusivities than at higher effective diffusivities.

During the alkali pretreatment of Poplar, a lag in the onset of lignin dissolution was observed at lower diffusivities since the tracers required longer time to penetrate the cell wall and access the lignin. Additionally, K_{eff} was found to be independent of time indicating that the process was diffusion dependent. At higher diffusivities, there was no lag in the onset of lignin dissolution as the tracers were quickly able to penetrate the cell wall and react with lignin. It was observed that K_{eff} was time dependent at higher diffusivities and followed a power law relationship with time. This was similar to some of the previous literature (Dang and Nguyen, 2006; Keshwani and Cheng, 2010). At lower diffusivities, the effective rate constant was independent of time since the time required for transport of the tracers was much greater than the time required for reaction with lignin. Alternatively. K_{eff} was a function of time when the time required for transport of the tracers was comparable to the time required for reaction with the lignin molecules. The results

obtained from hot water pretreatment were different from that of alkali pretreatment. A slower reaction was observed initially in experimental hot water treatment of Acer. Experimentally, this was attributed to initial dissolution of low molecular weight sugars such as hemicellulose as well as breakage of acetyl linkages and release of organic acids which facilitated lignin dissolution and later lignin re-localization and globule formation during hot water pretreatment (Donohoe et al., 2011; Mosier et al., 2005). In the transport and reaction modeling here, the initial lag and slow onset of reaction is attributed to the higher Thiele moduli and correspondingly lower reaction probabilities. Once the initial lag was overcome, the higher diffusivity and higher local rate constants in hot water pretreatment of Acer resulted in faster overall dissolution during hot water pretreatment. A time independent K_{eff} was observed at all conditions for the hot water pretreatment indicating that the time required for transport of the reagent molecules was greater than the time required for reaction.

Comparing the two pretreatment cases, it was observed that alkali pretreatment required a longer residence time but resulted in greater and almost complete delignification at a lower diffusivity and local rate constant as seen by both the experimental and simulation results (Ji et al., 2014). The hot water pretreatment was carried out for a shorter time and probably at more severe conditions than reported in previous literature. The extent of lignin dissolution was lower than that seen in alkali pretreatment. The diffusivity of the cell wall during hot water pretreatment of Acer was greater than the diffusivity of the cell wall during alkali pretreatment of Poplar. This is attributed to the differential swelling in the cell wall. Additionally, Acer has a lower total lignin fraction than Poplar as reported in literature and from analysis of Raman images (S. Chen et al., 2016; Duarte et al., 2011; Ma et al., 2014). The hot water pretreatment required a higher k' than the alkali pretreatment but had a lower reactivity for lignin dissolution due to initial dissolution of acetyl groups, uronic substitutions and hemicellulose as well as lignin re-localization and globule formation during hot water pretreatment (Donohoe et al., 2011; Mosier et al., 2005). Thus, analyzing the results from the simulation it is clear that the alkali pretreatment of Poplar and hot water pretreatment of Acer yielded different results due to the differences in nature of biomass and type of pretreatment which leads to different kinetic and transport behavior

during the pretreatment process. It is also important to note that alkali pretreatments mainly focus on removal of lignin while hot water pretreatments focus on hemicellulose solubilization which explains the higher and more rapid delignification during alkali pretreatment as compared to hot water pretreatment (Mosier et al., 2005). If the model were extended to simulate the carbohydrate dissolution, it is likely that we will observe the earlier dissolution of carbohydrates. Thus, it can be concluded the nature of biomass and pretreatment affect the structure and topochemistry of the cell walls.

The transport reaction model successfully predicted the lignin concentration profiles during pretreatment and the corresponding diffusive and reactive parameters. The effective rate constant that accounted for both transport and reaction and the rate expressions were successfully determined. In addition, the effect of changing diffusivity and reactivity were understood using the model, which is key in deciding the conditions for pretreatment. Thus, additional fundamental insights into the pretreatment process were gained. This is beneficial in determining the optimum conditions for effective conversion of biomass. In the future, the model can also be extended to cellulose and hemicellulose dissolution with appropriate consideration of their corresponding local rection kinetics and initial topochemical distribution. Additionally, the model developed here is applicable to other types of biomass species and pretreatment processes considering the appropriate kinetics and this can be explored as a path forward. The existing transport reaction model could also be modified appropriately and extended to TEM-CT images at the nanoscale to interpret diffusion and reaction in different regions of the cell wall. The topochemical information for individual cell wall layers obtained from Raman images and principal component analysis and cluster analysis can be superimposed on the TEM-CT images to obtain the necessary initial topochemical distribution (Zhang et al., 2015). Such a model would provide immense information on the behavior of different cell wall layers during pretreatment and further enhance the understanding of the pretreatment process.

REFERENCES

Aaltosalmi, U., Kataja, M., Koponen, A., Timonen, J., Goel, A., Lee, G., Ramaswamy, S., 2004. Numerical analysis of fluid flow through fibrous porous materials. Journal of Pulp and Paper Science 30, 251–255.

Abad, A.R., Cease, K.R., Blanchette, R.A., 1988. A rapid technique using epoxy resin Quetol 651 to prepare woody plant tissues for ultrastructural study. Canadian Journal of Botany 66, 677–682. https://doi.org/10.1139/b88-097

Abdul Khalil, H.P.S., Bhat, A.H., Ireana Yusra, A.F., 2012. Green composites from sustainable cellulose nanofibrils: A review. Carbohydrate Polymers 87, 963–979. https://doi.org/10.1016/J.CARBPOL.2011.08.078

Anderson, C., Carroll, A., … L.A.-P., 2010, U., 2010. Real-time imaging of cellulose reorientation during cell wall expansion in Arabidopsis roots. Plant Physiology 152, 787–796.

Ayache, J., Beaunier, L., Boumendil, J., Ehret, G., Laub, D., 2010. Sample Preparation Handbook for Transmission Electron Microscopy, Sample Preparation Handbook for Transmission Electron Microscopy. https://doi.org/10.1007/978-1-4419-5975-1

Barakat, A., de Vries, H., Rouau, X., 2013. Dry fractionation process as an important step in current and future lignocellulose biorefineries: A review. Bioresource Technology. https://doi.org/10.1016/j.biortech.2013.01.169

Batonneau, Y., Laureyns, J., Merlin, J.C., Brémard, C., 2001. Self-modeling mixture analysis of Raman microspectrometric investigations of dust emitted by lead and zinc smelters, in: Analytica Chimica Acta. https://doi.org/10.1016/S0003-2670(01)00909-6

Beisl, S., Friedl, A., Miltner, A., 2017. Lignin from micro- To nanosize: Applications. International Journal of Molecular Sciences. https://doi.org/10.3390/ijms18112367

Bidabehere, C.M., Sedran, U., 2001. Simultaneous diffusion, adsorption, and reaction in fluid catalytic cracking catalysts. Industrial and Engineering Chemistry Research. https://doi.org/10.1021/ie990803z

Bird, B., Stewart, W., Lightfoot, E., 2007. Transport phenomena, Rev. 2nd ed. ed. New York : J. Wiley, New York.

Brinchi, L., Cotana, F., Fortunati, E., Kenny, J.M., 2013. Production of nanocrystalline cellulose from lignocellulosic biomass: Technology and applications. Carbohydrate Polymers. https://doi.org/10.1016/j.carbpol.2013.01.033

Brunow, G., Kilpeläinen, I., Sipilä, J., Syrjänen, K., Karhunen, P., Setälä, H., Rummakko, P., 1998. Oxidative Coupling of Phenols and the Biosynthesis of Lignin. ACS Symposium Series. https://doi.org/10.1021/bk-1998-0697.ch010

Cegelski, L., O'Connor, R.D., Stueber, D., Singh, M., Poliks, B., Schaefer, J., 2010. Plant cell-wall cross-links by REDOR NMR spectroscopy. Journal of the American Chemical Society 132. https://doi.org/10.1021/ja104827k

Celik, T., 2012. Two-dimensional histogram equalization and contrast enhancement. Pattern Recognition 45. https://doi.org/10.1016/j.patcog.2012.03.019

Chang, V.S., Holtzapple, M.T., 2000. Fundamental factors affecting biomass enzymatic reactivity, in: Applied Biochemistry and Biotechnology - Part A Enzyme Engineering and Biotechnology. https://doi.org/10.1385/abab:84-86:1-9:5

Chen, S., Zhang, X., Ling, Z., Ji, Z., Ramarao, B. V., Ramaswamy, S., Xu, F., 2016. Probing and visualizing the heterogeneity of fiber cell wall deconstruction in sugar maple (: Acer saccharum) during liquid hot water pretreatment. RSC Advances 6. https://doi.org/10.1039/c6ra18333f

Chen, X., Wang, W., Ciesielski, P., Trass, O., Park, S., Tao, L., Tucker, M.P., 2016. Improving Sugar Yields and Reducing Enzyme Loadings in the Deacetylation and Mechanical Refining (DMR) Process through Multistage Disk and Szego Refining and Corresponding Techno-Economic Analysis. ACS Sustainable Chemistry and Engineering 4. https://doi.org/10.1021/acssuschemeng.5b01242

Chiang, V.L., Yu, J., Eckert, R.C., 1990. Isothermal reaction kinetics of kraft delignification of douglas-fir. Journal of Wood Chemistry and Technology 10. https://doi.org/10.1080/02773819008050241

Chundawat, S.P.S., Donohoe, B.S., da Costa Sousa, L., Elder, T., Agarwal, U.P., Lu, F., Ralph, J., Himmel, M.E., Balan, V., Dale, B.E., 2011. Multi-scale visualization and characterization of lignocellulosic plant cell wall deconstruction during thermochemical pretreatment. Energy & Environmental Science 4, 973. https://doi.org/10.1039/c0ee00574f

Ciesielski, P.N., Crowley, M.F., Nimlos, M.R., Sanders, A.W., Wiggins, G.M., Robichaud, D., Donohoe, B.S., Foust, T.D., 2015. Biomass Particle Models with Realistic Morphology and Resolved Microstructure for Simulations of Intraparticle Transport Phenomena. Energy & Fuels 29, 242–254. https://doi.org/10.1021/ef502204v

Ciesielski, P.N., Matthews, J.F., Tucker, M.P., Beckham, G.T., Crowley, M.F., Himmel, M.E., Donohoe, B.S., 2013. 3D Electron Tomography of Pretreated Biomass Informs Atomic Modeling of Cellulose Microfibrils. ACS Nano 7, 8011–8019. https://doi.org/10.1021/nn4031542

Converse, A.O., Kwarteng, I.K., Grethlein, H.E., Ooshima, H., 1989. Kinetics of thermochemical pretreatment of lignocellulosic materials. Applied Biochemistry and Biotechnology 20–21. https://doi.org/10.1007/BF02936473

Dang, V., Nguyen, K.L., 2006. Characterisation of the heterogeneous alkaline pulping kinetics of hemp woody core. Bioresource Technology 97. https://doi.org/10.1016/j.biortech.2005.07.008

Das, A., 2015. Guide to signals and patterns in image processing : foundations, methods and applications. Cham : Springer, Cham.

Defrenne, Y., 2008. Three dimensional structural analysis of porous materials via micro-tomography image processing. University of Minnesota.

Defrenne, Y., Zhdankin, V., Ramanna, S., Ramaswamy, S., Ramarao, B.V., 2019. The dual phase moisture conductivity of fibrous materials using random walk techniques in X-

ray microcomputed tomographic structures. Chemical Engineering Science. https://doi.org/10.1016/j.ces.2018.09.055

Defrenne, Y., Zhdankin, V., Ramanna, S., Ramaswamy, S., Ramarao, B.V., 2017. Three-dimensional pore structure visualization and characterization of paper using X-ray computed tomography. Tappi Journal 16, 519–530.

Donohoe, B.S., Selig, M.J., Viamajala, S., Vinzant, T.B., Adney, W.S., Himmel, M.E., 2009a. Detecting cellulase penetration into corn stover cell walls by immuno-electron microscopy. Biotechnology and Bioengineering 103, 480–489. https://doi.org/10.1002/bit.22281

Donohoe, B.S., Selig, M.J., Viamajala, S., Vinzant, T.B., Adney, W.S., Himmel, M.E., 2009b. Detecting cellulase penetration into corn stover cell walls by immuno-electron microscopy. Biotechnology and Bioengineering 103, 480–489. https://doi.org/10.1002/bit.22281

Donohoe, B.S., Vinzant, T.B., Elander, R.T., Pallapolu, V.R., Lee, Y.Y., Garlock, R.J., Balan, V., Dale, B.E., Kim, Y., Mosier, N.S., Ladisch, M.R., Falls, M., Holtzapple, M.T., Sierra-Ramirez, R., Shi, J., Ebrik, M.A., Redmond, T., Yang, B., Wyman, C.E., Hames, B., Thomas, S., Warner, R.E., 2011. Surface and ultrastructural characterization of raw and pretreated switchgrass. Bioresource Technology 102, 11097–11104. https://doi.org/10.1016/j.biortech.2011.03.092

Duarte, G. V., Ramarao, B. V., Amidon, T.E., Ferreira, P.T., 2011. Effect of hot water extraction on hardwood kraft pulp fibers (Acer saccharum, sugar maple). Industrial and Engineering Chemistry Research 50. https://doi.org/10.1021/ie200639u

Duff, S.J.B., Murray, W.D., 1996. Bioconversion of forest products industry waste cellulosics to fuel ethanol: A review. Bioresource Technology 55, 1–33. https://doi.org/10.1016/0960-8524(95)00122-0

Dutta, S., De, S., Saha, B., Alam, M.I., 2012. Advances in conversion of hemicellulosic biomass to furfural and upgrading to biofuels. Catalysis Science and Technology. https://doi.org/10.1039/c2cy20235b

Einstein, A., 1956. Investigations on the theory of the Brownian movement. New York : Dover Publications, New York].

Energy Independence and Security Act of 2007 : A Summary of Major Provisions., 2007. . [publisher not identified], Place of publication not identified].

Esteghlalian, A., Hashimoto, A.G., Fenske, J.J., Penner, M.H., 1997. Modeling and optimization of the dilute-sulfuric-acid pretreatment of corn stover, poplar and switchgrass. Bioresource Technology 59, 129–136. https://doi.org/10.1016/S0960-8524(97)81606-9

Faravelli, T., Frassoldati, A., Migliavacca, G., Ranzi, E., 2010. Detailed kinetic modeling of the thermal degradation of lignins. Biomass and Bioenergy 34, 290–301. https://doi.org/10.1016/J.BIOMBIOE.2009.10.018

Ferhan, M., Yan, N., Sain, M., 2013. A New Method for Demethylation of Lignin from Woody Biomass using Biophysical Methods. J Chem Eng Process Technol. https://doi.org/10.4172/2157-7048.1000160

Fromm, J., 2013. Cellular Aspects of Wood Formation. Plant Cell Monographs. https://doi.org/10.1007/978-3-642-36491-4

Ghaffar, S.H., Fan, M., 2013. Structural analysis for lignin characteristics in biomass straw. Biomass and Bioenergy. https://doi.org/10.1016/j.biombioe.2013.07.015

Gierlinger, N., Burgert, I., 2006. Secondary cell wall polymers studied by confocal raman microscopy: Spatial distribution, orientation, and molecular deformation, in: New Zealand Journal of Forestry Science.

Gierlinger, N., Goswami, L., Schmidt, M., Burgert, I., Coutand, C., Rogge, T., Schwanninger, M., 2008. In Situ FT-IR Microscopic Study on Enzymatic Treatment of Poplar Wood Cross-Sections. Biomacromolecules 9, 2194–2201. https://doi.org/10.1021/bm800300b

Gierlinger, N., Keplinger, T., Harrington, M., 2012. Imaging of plant cell walls by confocal Raman microscopy. Nature Protocols 7, 1694–1708. https://doi.org/10.1038/nprot.2012.092

Gierlinger, N., Schwanninger, M., 2006. Chemical imaging of poplar wood cell walls by confocal Raman microscopy. Am Soc Plant Biol 140, 1246–1254.

Glauert, A., Lewis, P., 1998. Biological specimen preparation for transmission electron microscopy. Princeton, N.J. : Princeton University Press.

Goel, A., 2003. Numerical methods and image analysis to predict the transport properties of porous media. University of Minnesota.

Goel, A., Tzanakakis, M., Huang, S., Ramaswamy, S., Choi, D., Ramarao, B. V., 2001. Characterization of the three-dimensional structure of paper using x-ray microtomography. Tappi Journal.

Greenwood, A.A., Farrell, T.W., O'Hara, I.M., 2013. Understanding mild acid pretreatment of sugarcane bagasse through particle scale modeling. Biotechnology and Bioengineering 110. https://doi.org/10.1002/bit.24984

Grénman, H., Salmi, T., Murzin, D.Y., 2011. Solid-liquid reaction kinetics - Experimental aspects and model development. Reviews in Chemical Engineering 27. https://doi.org/10.1515/REVCE.2011.500

Herbaut, M., Zoghlami, A., Habrant, A., Falourd, X., Foucat, L., Chabbert, B., Paës, G., 2018. Multimodal analysis of pretreated biomass species highlights generic markers of lignocellulose recalcitrance. Biotechnology for Biofuels 11. https://doi.org/10.1186/s13068-018-1053-8

Horvath, L., Peszlen, I., Gierlinger, N., Peralta, P., Kelley, S., Csoka, L., 2012. Distribution of wood polymers within the cell wall of transgenic aspen imaged by Raman microscopy. Holzforschung 66, 717–725. https://doi.org/10.1515/hf-2011-0126

Hughes, L., Hawes, C., Monteith, S., Vaughan, S., 2014. Serial block face scanning electron microscopy-the future of cell ultrastructure imaging. Protoplasma. https://doi.org/10.1007/s00709-013-0580-1

Ibrahim, H., Kong, N.S.P., 2007. Brightness preserving dynamic histogram equalization for image contrast enhancement. IEEE Transactions on Consumer Electronics 53. https://doi.org/10.1109/TCE.2007.4429280

Ishizawa, C.I., Davis, M.F., Schell, D.F., Johnson, D.K., 2007. Porosity and its effect on the digestibility of dilute sulfuric acid pretreated corn stover. Journal of Agricultural and Food Chemistry 55. https://doi.org/10.1021/jf062131a

Ji, Z., Xu, F., Ma, J., 2014. Multi-Scale Visualization of Dynamic Changes in Poplar Cell Walls During Alkali Pretreatment Topochemistry of wood cell wall View project Isolation, characterization and modification of cellulose, hemicelluloses and lignin in lignocellulosic biomass View project Multi-Scale Visualization of Dynamic Changes in Poplar Cell Walls During Alkali Pretreatment. Microsc. Microanal 20, 566–576. https://doi.org/10.1017/S1431927614000063

John, M.J., Thomas, S., 2008. Biofibres and biocomposites. Carbohydrate Polymers 71, 343–364. https://doi.org/10.1016/J.CARBPOL.2007.05.040

Kacuráková, M., Capek, P., Sasinková, V., Wellner, N., Ebringerová, A., 2000. FT-IR study of plant cell wall model compounds: Pectic polysaccharides and hemicelluloses. Carbohydrate Polymers 43. https://doi.org/10.1016/S0144-8617(00)00151-X

Kansal, A.R., Torquato, S., 2002. Prediction of trapping rates in mixtures of partially absorbing spheres. Journal of Chemical Physics. https://doi.org/10.1063/1.1479718

Kerr, A.J., Goring, D.A.I., 1975. The Role of Hemicellulose in the Delignification of Wood. Canadian Journal of Chemistry 53. https://doi.org/10.1139/v75-134

Keshwani, D.R., Cheng, J.J., 2010. Modeling changes in biomass composition during microwave-based alkali pretreatment of switchgrass. Biotechnology and Bioengineering 105, 88–97. https://doi.org/10.1002/bit.22506

Kim, S., Holtzapple, M.T., 2006. Delignification kinetics of corn stover in lime pretreatment. Bioresource Technology. https://doi.org/10.1016/j.biortech.2005.04.002

Kim, T.H., Lee, Y.Y., 2006. Fractionation of corn stover by hot-water and aqueous ammonia treatment. Bioresource Technology. https://doi.org/10.1016/j.biortech.2005.02.040

Kočí, P., Novák, V., Štěpánek, F., Marek, M., Kubíček, M., 2010. Multi-scale modelling of reaction and transport in porous catalysts. Chemical Engineering Science. https://doi.org/10.1016/j.ces.2009.06.068

Kopelman, R., 1988. Fractal reaction kinetics. Science 241. https://doi.org/10.1126/science.241.4873.1620

Kremer, J.R., Mastronarde, D.N., McIntosh, J.R., 1996. Computer visualization of three-dimensional image data using IMOD. Journal of Structural Biology. https://doi.org/10.1006/jsbi.1996.0013

Larkin, P.J., 2017. Infrared and Raman Spectroscopy: Principles and Spectral Interpretation, Infrared and Raman Spectroscopy: Principles and Spectral Interpretation.

Li, H.Y., Chen, X., Wang, C.Z., Sun, S.N., Sun, R.C., 2016. Evaluation of the two-step treatment with ionic liquids and alkali for enhancing enzymatic hydrolysis of Eucalyptus: Chemical and anatomical changes. Biotechnology for Biofuels 9. https://doi.org/10.1186/s13068-016-0578-y

Liu, M., Mostaghimi, P., 2018. Numerical simulation of fluid-fluid-solid reactions in porous media. International Journal of Heat and Mass Transfer. https://doi.org/10.1016/j.ijheatmasstransfer.2017.11.141

Luo, H., Hu, J., Zhu, Y., Wu, J.-Y., Zhang, S., Fan, Y., Ye, G., 2013. Mechanically adaptive cellulose-poly(acrylic acid) polymeric composites in wet-dry cycles. Journal of Applied Polymer Science 127, 675–681. https://doi.org/10.1002/app.37851

Ma, J., Zhang, X., Zhou, X., Xu, F., 2014. Revealing the Changes in Topochemical Characteristics of Poplar Cell Wall During Hydrothermal Pretreatment Article in BioEnergy Research. https://doi.org/10.1007/s12155-014-9472-2

Maxwell, J.C., 1954. A treatise on electricity and magnetism. Journal of the Franklin Institute 258. https://doi.org/10.1016/0016-0032(54)90053-8

Mayo, S.C., Chen, F., Evans, R., 2010. Micron-scale 3D imaging of wood and plant microstructure using high-resolution X-ray phase-contrast microtomography. Journal of Structural Biology 171, 182–188. https://doi.org/10.1016/j.jsb.2010.04.001

McIntosh, S., Vancov, T., 2011. Optimisation of dilute alkaline pretreatment for enzymatic saccharification of wheat straw. Biomass and Bioenergy 35. https://doi.org/10.1016/j.biombioe.2011.04.018

Mittal, A., Chatterjee, S.G., Scott, G.M., Amidon, T.E., 2009. Modeling xylan solubilization during autohydrolysis of sugar maple and aspen wood chips: Reaction kinetics and mass transfer. Chemical Engineering Science 64. https://doi.org/10.1016/j.ces.2009.03.011

Mok, W.S.L., Antal, M.J., 1992. Uncatalyzed Solvolysis of Whole Biomass Hemicellulose by Hot Compressed Liquid Water. Industrial and Engineering Chemistry Research 31. https://doi.org/10.1021/ie00004a026

Montané, D., Farriol, X., Salvadó, J., Jollez, P., Chornet, E., 1998. Fractionation of wheat straw by steam-explosion pretreatment and alkali delignification. cellulose pulp and byproducts from hemicellulose and lignin. Journal of Wood Chemistry and Technology 18. https://doi.org/10.1080/02773819809349575

Montané, D., Salvadó, J., Farriol, X., Jollez, P., Chornet, E., 1994. Phenomenological kinetics of wood delignification: application of a time-dependent rate constant and a generalized severity parameter to pulping and correlation of pulp properties. Wood Science and Technology. https://doi.org/10.1007/BF00225458

Moon, R.J., Martini, A., Nairn, J., Simonsen, J., Youngblood, J., 2011. Cellulose nanomaterials review: Structure, properties and nanocomposites. Chemical Society Reviews. https://doi.org/10.1039/c0cs00108b

Moran-Mirabal, J.M., 2013. The study of cell wall structure and cellulose–cellulase interactions through fluorescence microscopy. Cellulose 20, 2291–2309. https://doi.org/10.1007/s10570-013-0010-8

Morinelly, J.E., Jensen, J.R., Browne, M., Co, T.B., Shonnard, D.R., 2009. Kinetic Characterization of Xylose Monomer and Oligomer Concentrations during Dilute Acid Pretreatment of Lignocellulosic Biomass from Forests and Switchgrass. Industrial & Engineering Chemistry Research 48, 9877–9884. https://doi.org/10.1021/ie900793p

Mosier, N., Wyman, C., Dale, B., Elander, R., Lee, Y.Y., Holtzapple, M., Ladisch, M., 2005. Features of promising technologies for pretreatment of lignocellulosic biomass. Bioresource Technology 96, 673–686. https://doi.org/10.1016/J.BIORTECH.2004.06.025

Murray, S., 2008. Chapter 1 High Pressure Freezing and Freeze Substitution of Schizosaccharomyces pombe and Saccharomyces cerevisiae for TEM. Methods in Cell Biology. https://doi.org/10.1016/S0091-679X(08)00401-9

O'Sullivan, A.C., 1997. Cellulose: The structure slowly unravels. Cellulose. https://doi.org/10.1023/A:1018431705579

Pauly, M., Keegstra, K., 2008. Cell-wall carbohydrates and their modification as a resource for biofuels. The Plant Journal 54, 559–568. https://doi.org/10.1111/j.1365-313X.2008.03463.x

Pereira, J.M.C., Navalho, J.E.P., Amador, A.C.G., Pereira, J.C.F., 2014. Multi-scale modeling of diffusion and reaction-diffusion phenomena in catalytic porous layers: Comparison with the 1D approach. Chemical Engineering Science 117. https://doi.org/10.1016/j.ces.2014.06.028

Perona, P., Malik, J., 1990. Scale- space and edge detection using anisotropic diffusion. Pattern Analysis and Machine Intelligence, IEEE Transactions on 12, 629–639. https://doi.org/10.1109/34.56205

Poletto, M., Ornaghi, H., Zattera, A., 2014. Native Cellulose: Structure, Characterization and Thermal Properties. Materials 7, 6105–6119. https://doi.org/10.3390/ma7096105

Reddy, N., Yang, Y., 2006. Properties of high-quality long natural cellulose fibers from rice straw. Journal of Agricultural and Food Chemistry 54. https://doi.org/10.1021/jf0617723

Reyes, S.C., Iglesia, E., 1991. Effective diffusivities in catalyst pellets: New model porous structures and transport simulation techniques. Journal of Catalysis 129.

Riemersma, J.C., 1968. Osmium tetroxide fixation of lipids for electron microscopy a possible reaction mechanism. Biochimica et Biophysica Acta (BBA)/Lipids and Lipid Metabolism. https://doi.org/10.1016/0005-2760(68)90118-5

Riley, M.R., Muzzio, F.J., Buettner, H.M., Reyes, S.C., 1995a. Diffusion in heterogeneous media: Application to immobilized cell systems. AIChE Journal 41, 691–700. https://doi.org/10.1002/aic.690410326

Riley, M.R., Muzzio, F.J., Buettner, H.M., Reyes, S.C., 1995b. The effect of structure on diffusion and reaction in immobilized cell systems. Chemical Engineering Science. https://doi.org/10.1016/0009-2509(95)00177-7

Rolland du Roscoat, S., Decain, M., Thibault, X., Geindreau, C., Bloch, J.-F., 2007. Estimation of microstructural properties from synchrotron X-ray microtomography and determination of the REV in paper materials. Acta Materialia 55, 2841–2850. https://doi.org/10.1016/j.actamat.2006.11.050

Rowell, R.M., 2012. Handbook of wood chemistry and wood composites, second edition, Handbook of Wood Chemistry and Wood Composites, Second Edition. https://doi.org/10.1201/b12487

Saghi, Z., Midgley, P.A., 2012. Electron Tomography in the (S) TEM: From Nanoscale Morphological Analysis to 3D Atomic Imaging. Annual Review Of Materials Research, Vol 42; Ann.Rev.Mater.Res. https://doi.org/10.1146/annurev-matsci-070511-155019

Sarkanen, K. V., Ludwig, C.H., 1971. Lignins: occurrence, formation, structure and reactions,. Wiley-Interscience.

Sarkar, P., Bosneaga, E., Yap, E.G., Das, J., Tsai, W.-T., Cabal, A., Neuhaus, E., Maji, D., Kumar, S., Joo, M., Yakovlev, S., Csencsits, R., Yu, Z., Bajaj, C., Downing, K.H., Auer, M., 2014. Electron Tomography of Cryo-Immobilized Plant Tissue: A Novel Approach to Studying 3D Macromolecular Architecture of Mature Plant Cell Walls In Situ. PLoS ONE 9, e106928. https://doi.org/10.1371/journal.pone.0106928

Shmulsky, R., Jones, P.D., 2011. Forest Products and Wood Science An Introduction: Sixth Edition, Forest Products and Wood Science An Introduction: Sixth Edition. https://doi.org/10.1002/9780470960035

Siegel, R.A., Langert, R., 1986. A new Monte Carlo approach to diffusion in constricted porous geometries. Journal of colloid and interface science 109, 426–440. https://doi.org/10.1016/0021-9797(86)90320-6

Sierra-Ramírez, R., Garcia, L.A., Holtzapple, M.T., 2011. Selectivity and delignification kinetics for oxidative short-term lime pretreatment of poplar wood, part I: Constant-pressure. Biotechnology Progress. https://doi.org/10.1002/btpr.590

Silveira, R.L., Stoyanov, S.R., Gusarov, S., Skaf, M.S., Kovalenko, A., 2013. Plant Biomass Recalcitrance: Effect of Hemicellulose Composition on Nanoscale Forces that Control Cell Wall Strength. Journal of the American Chemical Society 135, 19048–19051. https://doi.org/10.1021/ja405634k

Siyakatshana, N., Kudrna, V., Machoň, V., 2005. Incorporating Danckwerts' boundary conditions into the solution of the stochastic differential equation. Chemical Engineering Science. https://doi.org/10.1016/j.ces.2004.11.051

Sjostrom, E., 1993. Wood chemistry: fundamentals and applications.

Sluder, G., Wolf, D., 2013. Digital microscopy.

Stone, J.E., Scallan, A.M., 1965. Effect of component removal upon the porous structure of the cell wall of wood. Journal of Polymer Science Part C: Polymer Symposia 11. https://doi.org/10.1002/polc.5070110104

Stone, J.E., Scallan, A.M., Aberson, G.M.A., 1966. The wall density of native cellulose fibres. Pulp Paper Mag.Can 67, 263–268.

Suëtaka, W., 1995. Surface Infrared and Raman Spectroscopy, Surface Infrared and Raman Spectroscopy. Springer US. https://doi.org/10.1007/978-1-4899-0942-8

Sun, Y., Cheng, J., 2002. Hydrolysis of lignocellulosic materials for ethanol production: a review. Bioresource Technology 83, 1–11. https://doi.org/10.1016/S0960-8524(01)00212-7

Svedström, K., Lucenius, J., van den Bulcke, J., van Loo, D., Immerzeel, P., Suuronen, J.P., Brabant, L., van Acker, J., Saranpää, P., Fagerstedt, K., Mellerowicz, E., Serimaa, R., 2012. Hierarchical structure of juvenile hybrid aspen xylem revealed using X-ray scattering and microtomography. Trees - Structure and Function 26. https://doi.org/10.1007/s00468-012-0748-x

Szukiewicz, M.K., 2000. New approximate model for diffusion and reaction in a porous catalyst. AIChE Journal. https://doi.org/10.1002/aic.690460326

Thiele, E.W., 1939. Relation between Catalytic Activity and Size of Particle. Industrial and Engineering Chemistry 31. https://doi.org/10.1021/ie50355a027

Tomadakis, M.M., Rupani, D., 2007. Diffusion controlled reaction rate, survival probability, and molecular trajectory characteristics in the bulk, transition and Knudsen regime. Chemical Engineering Journal. https://doi.org/10.1016/j.cej.2006.10.005

Toriwaki, J., 2009. Fundamentals of three-dimensional digital image processing. Dordrecht ; London ; New York : Springer, Dordrecht ; London ; New York.

Torquato, S., 1991. Diffusion and reaction among traps: some theoretical and simulation results. Journal of Statistical Physics 65. https://doi.org/10.1007/BF01049606

Uju, Nakamoto, A., Shoda, Y., Goto, M., Tokuhara, W., Noritake, Y., Katahira, S., Ishida, N., Ogino, C., Kamiya, N., 2013. Low melting point pyridinium ionic liquid pretreatment for enhancing enzymatic saccharification of cellulosic biomass. Bioresource Technology. https://doi.org/10.1016/j.biortech.2012.06.096

Vainio, U., Maximova, N., Hortling, B., Laine, J., Stenius, P., Simola, L.K., Gravitis, J., Serimaa, R., 2004. Morphology of Dry Lignins and Size and Shape of Dissolved Kraft

Lignin Particles by X-ray Scattering. Langmuir 20, 9736–9744. https://doi.org/10.1021/la048407v

Vanholme, R., Demedts, B., Morreel, K., Ralph, J., Boerjan, W., 2010. Lignin biosynthesis and structure. Plant Physiology. https://doi.org/10.1104/pp.110.155119

Venkatesagowda, B., Dekker, R.F.H., 2019. Enzymatic demethylation of Kraft lignin for lignin-based phenol-formaldehyde resin applications. Biomass Conversion and Biorefinery. https://doi.org/10.1007/s13399-019-00407-3

Vickerman, J.C., Gilmore, I.S., 2009. Surface Analysis - The Principal Techniques: Second Edition, Surface Analysis - The Principal Techniques: Second Edition. https://doi.org/10.1002/9780470721582

Wang, D., Gou, S.Y., Axelrod, D., 1992. Reaction rate enhancement by surface diffusion of adsorbates. Biophysical Chemistry 43. https://doi.org/10.1016/0301-4622(92)80027-3

Wei, H., Donohoe, B.S., Vinzant, T.B., Ciesielski, P.N., Wang, W., Gedvilas, L.M., Zeng, Y., Johnson, D.K., Ding, S.Y., Himmel, M.E., Tucker, M.P., 2011. Elucidating the role of ferrous ion cocatalyst in enhancing dilute acid pretreatment of lignocellulosic biomass. Biotechnology for Biofuels 4. https://doi.org/10.1186/1754-6834-4-48

Williams, D.B., Carter, C.B., 2009. Transmission electron microscopy: A textbook for materials science, Transmission Electron Microscopy: A Textbook for Materials Science. https://doi.org/10.1007/978-0-387-76501-3

Wilson, R.H., Smith, A.C., Kacurakova, M., Saunders, P.K., Wellner, N., Waldron, K.W., 2000. The mechanical properties and molecular dynamics of plant cell wall polysaccharides studied by Fourier-transform infrared spectroscopy. Plant Physiology 124. https://doi.org/10.1104/pp.124.1.397

Wood, T.M., Saddler, J.N., 1988. Increasing the availability of cellulose in biomass materials. Methods in Enzymology 160, 3–11. https://doi.org/10.1016/0076-6879(88)60101-7

Yu, H., Liu, R., Shen, D., Wu, Z., Huang, Y., 2008. Arrangement of cellulose microfibrils in the wheat straw cell wall. Carbohydrate Polymers 72. https://doi.org/10.1016/j.carbpol.2007.07.035

Zalc, J.M., Reyes, S.C., Iglesia, E., 2004. The effects of diffusion mechanism and void structure on transport rates and tortuosity factors in complex porous structures. Chemical Engineering Science. https://doi.org/10.1016/j.ces.2004.04.028

Zalc, J.M., Reyes, S.C., Iglesia, E., 2003. Monte-Carlo simulations of surface and gas phase diffusion in complex porous structures. Chemical Engineering Science 58, 4605–4617.

Zhang, J., Cheng, Y., 2020. Despeckling Methods for Medical Ultrasound Images, Despeckling Methods for Medical Ultrasound Images. https://doi.org/10.1007/978-981-15-0516-4

Zhang, X., 2021. Visualising lignin quantitatively in plant cell walls by micro-Raman spectroscopy. RSC Advances 11. https://doi.org/10.1039/D1RA01825F

Zhang, X., Ji, Z., Zhou, X., Ma, J.F., Hu, Y.H., Xu, F., 2015. Method for automatically identifying spectra of different wood cell wall layers in Raman imaging data set. Analytical Chemistry. https://doi.org/10.1021/ac504144s

Zhang, X., Ma, J., Ji, Z., Yang, G.H., Zhou, X., Xu, F., 2014. Using confocal Raman microscopy to real-time monitor poplar cell wall swelling and dissolution during ionic liquid pretreatment. Microscopy Research and Technique. https://doi.org/10.1002/jemt.22379

Zhao, X., Li, S., Wu, R., Liu, D., 2017. Organosolv fractionating pre-treatment of lignocellulosic biomass for efficient enzymatic saccharification: chemistry, kinetics, and substrate structures. Biofuels, Bioproducts and Biorefining. https://doi.org/10.1002/bbb.1768

Zhao, X., Morikawa, Y., Qi, F., Zeng, J., Liu, D., 2014. A novel kinetic model for polysaccharide dissolution during atmospheric acetic acid pretreatment of sugarcane bagasse. Bioresource Technology. https://doi.org/10.1016/j.biortech.2013.10.036

Zheng, L.H., Chiew, Y.C., 1989. Computer simulation of diffusion- controlled reactions in dispersions of spherical sinks. The Journal of chemical physics 90, 322–327. https://doi.org/10.1063/1.456532

Zhou, X., Ma, J., Ji, Z., Zhang, X., Ramaswamy, S., Xu, F., Sun, R., 2014. Dilute acid pretreatment differentially affects the compositional and architectural features of Pinus bungeana Zucc. compression and opposite wood tracheid walls. Industrial Crops and Products 62, 196–203. https://doi.org/10.1016/J.INDCROP.2014.08.035

Zollfrank, C., Fromm, J., 2009. Ultrastructural development of the softwood cell wall during pyrolysis. Holzforschung 63, 248–253. https://doi.org/10.1515/HF.2009.031